DEPARTMENT OF MATHEMATICS
UNIVERSITY OF PISA
Doctorate Course in Mathematics (2011-2014)
SSD MAT/07

Ph.D. Thesis

The Yarkovsky Effect, Asteroid Dynamics and Impact Monitoring

Federica Spoto

Supervisor: *Prof. Andrea Milani*

Ph.D. director: *Prof. Rita Pardini*

Contents

1 Introduction **1**

2 General Theory **7**

2.1 Nongravitational perturbations 7

2.1.1 The Yarkovsky effect 7

2.2 Proper elements 12

2.2.1 Historical overview 12

2.2.2 Proper elements 13

2.2.3 The theories 15

2.3 Applications of the Yarkovsky effect 21

3 Yarkovsky and NEAs **25**

3.1 Methodology 26

3.1.1 Yarkovsky modeling and determination 26

3.1.2 Dynamical model 29

3.1.3 Observational error model 30

3.1.4 Treatment of precovery observations 32

3.1.5 Filtering spurious results 33

3.2 Results 34

3.2.1 2009 BD 34

3.2.2 Comparison with other published results 35

3.2.3 Lower SNR and small orbital drifts 37

3.3 Discussion 40

3.3.1 Connection with NEA feeding mechanisms 40

3.3.2 Spurious detections 42

3.3.3 Constraining physical quantities 44

3.3.4 Implications for impact predictions 45

3.4 Conclusions 47

4 (101955) Bennu **53**
4.1 Observational Data and Treatment 55
4.1.1 Optical Astrometry 55
4.1.2 Radar Astrometry 56
4.2 Orbit Determination and Dynamical Model 58
4.2.1 Yarkovsky Effect 58
4.2.2 Gravitational Perturbers 65
4.2.3 Relativity 66
4.2.4 Outlier Treatment 68
4.2.5 Numerics and Software Validation 68
4.3 Mass, Bulk Density and Implications 69
4.4 Earth Close Approaches 74
4.4.1 Impact Hazard Assessment 75
4.4.2 Statistical Close Approach Frequency 77
4.5 OSIRIS-REx Science 82
4.6 Discussion and Conclusions 83

5 (410777) 2009 FD **95**
5.1 Astrometry and physical observations of 2009 FD 97
5.2 Yarkovsky effect models 98
5.3 Line of variations in > 6 dimensions 101
5.4 Impact monitoring with a priori constraints 103
5.5 Monte Carlo impact monitoring 105
5.6 Scattering encounter 106
5.7 Conclusions 109
5.7.1 Comparison and reliability of the results 109
5.7.2 Future observability 111

6 Asteroid families **113**
6.1 Dataset 116
6.1.1 Proper elements 116
6.1.2 Absolute magnitudes 116
6.1.3 WISE and SDSS catalogs of physical observations . . . 117
6.1.4 Resonance identification 118
6.1.5 Amount of information 120
6.2 Method for large dataset classification 121
6.2.1 Step 1: Core families 123
6.2.2 Step 2: Attaching smaller asteroids to core families . . 125
6.2.3 Step 3: Hierarchical clustering of intermediate background 126
6.2.4 Step 4: Attaching background asteroids to all families . 127

6.2.5 Step 5: Merging satellite families with core families . . 127
6.2.6 Automatic update 128
6.2.7 Some methodological remarks 129
6.3 Results from dynamical classification 130
6.3.1 Large families 130
6.3.2 Medium families 135
6.3.3 Small families 138
6.3.4 Tiny families 141
6.4 Use of absolute magnitude data 143
6.4.1 The volume of the families 143
6.4.2 Family Ages 144
6.4.3 Size distributions 161
6.5 Refinement with physical data 163
6.5.1 The Hertha–Polana–Burdett complex family 163
6.5.2 Watsonia and the Barbarians 166
6.6 Cratering families 166
6.6.1 The Massalia family 167
6.6.2 The Vesta family substructures 168
6.6.3 Vesta Interlopers and lost Vestoids 170
6.6.4 The Eunomia Family 173
6.6.5 The missing Ceres family 173
6.7 Couples 177
6.8 Conclusions and Future Work 179
6.8.1 How to use HCM 179
6.8.2 Stability of the classification 179
6.8.3 Magnitudes 180
6.8.4 Yarkovsky effect and ages 180
6.8.5 Use of physical observations 181
6.8.6 Cratering vs. Fragmentation 181
6.8.7 Comparison with space mission data 182

7 Family ages **185**
7.1 Introduction 185
7.2 Least squares fit of the V-shape 187
7.2.1 Selection of the Fit Region 187
7.2.2 Binning and fit of the slopes 190
7.2.3 Error Model and Weights 191
7.2.4 Outlier Rejection and Quality Control 195
7.3 Results 196
7.3.1 Fragmentation Families 196
7.3.2 Cratering Families 198

7.3.3 Young Families . . . 199
7.3.4 One Side . . . 201
7.4 Age Estimation . . . 202
7.4.1 Yarkovsky Calibrations . . . 202
7.4.2 Ages and their Uncertainties . . . 206
7.5 Conclusions and future work . . . 213
7.5.1 Main results . . . 213
7.5.2 Open problems . . . 216
7.5.3 Family ages left to be computed . . . 217

8 Shadowing Lemma 219
8.1 Orbit determination for the standard map . . . 221
8.2 Shadowing Lemma . . . 223
8.2.1 Shadowing Lemma and orbit determination . . . 225
8.3 Numerical results . . . 228
8.3.1 Computability horizon . . . 228
8.3.2 Chaotic case . . . 231
8.3.3 Ordered case . . . 232
8.4 Discussion on the Wisdom hypothesis . . . 234
8.5 Examples from Impact Monitoring . . . 235

9 Short term impact monitoring 239
9.1 Method . . . 243
9.1.1 Synthetic asteroid populations . . . 243
9.1.2 Survey simulation . . . 245
9.1.3 Photometric & astrometric uncertainty . . . 247
9.1.4 Survey cadence . . . 248
9.1.5 Observability windows . . . 249
9.1.6 Orbit determination and impact probability . . . 249
9.2 Results & Discussion . . . 251
9.2.1 Observable characteristics of the impactor population . . . 252
9.2.2 Detection efficiency & rates . . . 254
9.2.3 Impact probability evolution for impacting asteroids . . . 256
9.2.4 Impact probability evolution for main belt and close-approaching asteroids . . . 261
9.3 Conclusions . . . 262

10 Appendix 265
10.1 Best power law . . . 265
10.2 Analytic estimate . . . 267

List of Figures

3.1 Relativistic accelerations of the Earth and Jupiter 30
3.2 Observed position, average observed position, and predicted postfit position both with and without the Yarkovsky perturbation in the dynamics 32
3.3 Same of Fig. 3.2 for asteroid 1999 FA. The uncertainty ellipses for predicted positions correspond to 3-σ levels, while the uncertainty for the observed position corresponds to 3". 37
3.4 Relative displacement of A_2 with respect to the nominal value as a function of the number of perturbers for (101955) Bennu and (4179) Toutatis. 38
3.5 Distribution of A_2 and its uncertainty, and prograde rotation and retrograde rotation 42
3.6 Inferred obliquity distribution based on 136 objects. 43
3.7 Histogram of $\mathcal{S}$ for different intervals of SNR 43
3.8 Density as a function of thermal inertia for asteroid (101955) Bennu 45
3.9 Density as a function of thermal inertia for asteroids Golevka, Apollo, Ra-Shalom, Toro, YORP, and Geographos. 52

4.1 Distribution of Bennu postfit residuals for JPL solution 87 . . 56
4.2 Arecibo delay-Doppler detections of Bennu from 2011-Sep-27,28,29 57
4.3 Time evolution of the osculating Bennu orbital elements, a, e and i, through 2136 61
4.4 Time history of the Bennu semimajor axis drift da/dt through 2136 62
4.5 Yarkovsky accelerations as a function of heliocentric distance . 63
4.6 The history of da/dt stemming from the transverse and radial components of the Yarkovsky acceleration 63
4.7 Comparison of the Yarkovsky effect with the relativistic perturbations on Bennu 67

4.8 Comparison of the transverse perturbations from the Yarkovsky effect and the relativistic component due to the Earth 67
4.9 Bulk density estimate 70
4.10 Yarkovsky effect enhancement due to 100% surface roughness as a function of thermal inertia. 72
4.11 Time history of the MOID 78
4.12 Uncertainty region on the b-plane of the 2135 encounter 78
4.13 A map of the Bennu impact keyholes on the 2135 b-plane . . . 79
4.14 Cumulative impact probability (upper) and cumulative number of keyholes found (lower) 80
4.15 Probability of having at least one close approach (CA) within a given distance for different time intervals 81

5.1 Comparisons of the colors of 2009 FD with the visible spectral shapes of the Ch and Cgh classes 99
5.2 Assumed distribution of the 2009 FD density 101
5.3 Distribution of the Yarkovsky parameter A_2 102
5.4 MOID and the distance at the descending node 105
5.5 Evolution of the longest semiaxis of the $1\,\sigma$ confidence ellipsoid 107
5.6 Left: LOV on the 2185 TP. Right: segment of the LOV on the 2185 TP 108
5.7 Map of the 2009 FD impact keyholes intersecting the trace of the LOV on the 2185 TP, computed both numerically and analitically 110

6.1 The family of (20) Massalia in the proper (a, e) plane. 131
6.2 The family of (1726) Hoffmeister in the proper $a, \sin I$ projection 134
6.3 V-shape of the family 20 145
6.4 V-shapes of the families of (847) Agnia, and (3395) Jitka . . . 146
6.5 V-shape of the family 4 150
6.6 V-shape of the family 15 151
6.7 V-shape of the family 158 153
6.8 Possible correlation spin–ejection velocity for a radial impact from the interior of the Solar System 159
6.9 Size distribution for the family 20 162
6.10 The Hertha dynamical family in the proper a, e plane 164
6.11 The distribution of WISE albedos for the 135 dynamical family with the locations of the three namesakes indicated by red lines 165
6.12 The family 4 in the proper a, e plane 168
6.13 Histogram of albedos measured by WISE with $S/N > 3$ 170

6.14 Asteroids complying with the Parker et al. [2008] criterion for V-type 172
6.15 Histogram of the albedos measured by WISE with $S/N > 3$ among the members of the family 93 174

7.1 Bins for the inner side of the family of (20) Massalia. 191
7.2 Bins for the outer side of the family of (20) Massalia. 192
7.3 Histogram of the significant WISE albedos for the dynamical family of (20) Massalia. 193
7.4 V-shape fit for the join of families of (163) Erigone and (5026) Martes. 200
7.5 Family ages and their uncertainties. 214

8.1 Orbits of the standard map for the perturbation parameter $\mu = 0.5$ 222
8.2 δ-pseudotrajectory. 224
8.3 ε-shadowing. 224
8.4 An example of a δ-pseudotrajectory. 227
8.5 Eigenvalues and determinant of the state transition matrix in double precision. 228
8.6 Eigenvalues and determinant of the state transition matrix in quadruple precision. 229
8.7 Standard deviation for the initial conditions and the dynamical parameter. 232
8.8 Uncertainty of the solution of the least squares fit for the initial conditions and for the dynamical parameter μ. 233
8.9 Standard deviation and actual error of the solutions for the initial conditions. 234
8.10 Top left: eigenvalues of the state transition matrices, for the chosen regular initial conditions and for ± 5000 iterations. Top right: solutions for the initial condition only, condition number of the normal matrix, standard deviation of y and for x. Bottom left: solutions for three parameters, condition number, standard deviation of x, of y, of μ. Bottom right: log-log plot of the 3 standard deviations, with very similar slopes. . . 237
8.11 Probability Density Functions for the trace of possible solutions on the TP of the close approach of the asteroid (410777) 2009 FD to the Earth in the year 2185. 238

9.1 Eccentricity and inclination vs. semi-major axis for synthetic impactors, close-approachers and main belt objects 243

9.2 Impact parameters of the synthetic close-approaching asteroids 244
9.3 Top: one night of the synthetic ATLAS survey covering the entire night sky visible from Haleakala, Maui, Hawaii. Bottom: time series for detections in tracklets for the 2-site 'no-shift', 'half-shift' and 'full-shift' scenarios 247
9.4 Observing window duration and average number of nights to closest approach or impact 250
9.5 Left: apparent rate of motion on the first night of observation for impactors with diameters of 10 m, 50 m and 300 m. Right: apparent rate of motion on the first night of observation for impacting, close-approaching and main belt asteroids 253
9.6 Time evolution of the sky plane position and apparent V magnitude for all the detected synthetic impactors at 4 different sizes: 10 m, 50 m, 100 m and 300 m 254
9.7 Left: detection efficiency for synthetic impactors and close approachers as a function of object diameter. Right: our predicted incremental number of detections per year of impactors, close-approachers, and false impactors 255
9.8 Impact probability time evolution for four synthetic objects of 10 m, 50 m, 100 m and 300 m diameter 257
9.9 Average impact probability as a function of the number of nights since discovery for impactors of 10 m, 50 m, 100 m and 300 m diameter 258
9.10 Impact warning time t_{warn} as a function of impactor diameter (D) for the ATLAS survey using the full-shift cadence 260
9.11 Fraction of close-approaching asteroids for which an impact is ruled out as a function of the number of days before close-approach for 7 different asteroid diameters 262

10.1 Dependency of transverse acceleration exponent 266

List of Tables

3.1 Gravitational parameters of perturbing asteroids 29
3.2 Semimajor axis, eccentricity, absolute magnitude, physical and Yarkovsky parameters, and observational information for selected NEAs. 48
3.3 Same as Table 3.2 for less reliable detections. 49
3.4 Same as Table 3.2 for small orbital drifts. 50
3.5 Probability of coming from one of the intermediate NEA source regions for the objects of Table 3.2. 51

4.1 Radar Astrometry for (101955) Bennu. 86
4.2 Radar observations of Bennu from 2011 87
4.3 JPL orbit Solns. 85 and 87 for Bennu, Ecliptic J2000 Frame. 88
4.4 Physical characteristics of (101955) Bennu and associated marginal uncertainty in estimate of bulk density ρ 89
4.5 Dynamical Effect of Several Model Variations 90
4.6 Main belt asteroid perturbers, associated GM values and the dynamical relevance of each as in the previous table. 91
4.7 Bennu bulk density and related quantities with 1σ uncertainties. 92
4.8 Bennu Deterministic Earth Approaches Closer than 0.05 AU (JPL solution 76). 92
4.9 Keyholes in 2135 b-plane and associated impact probabilities, JPL solution 76. 93
4.10 Resonances associated with the eight potential impacts with impact probability $> 10^{-5}$. 94
4.11 Formal uncertainties with and without simulated OSIRIS-REx pseudo-range measurements as described in the text. 94

5.1 Apparent V magnitude and optical colors (with error bars) of 2009 FD on 2014 April 02.0 UT. They are consistent with a primitive C-group taxonomy, most likely of the Ch or Cgh classes. 98

5.2 NEODyS risk file for 2009 FD 104
5.3 Sentry risk file 106

6.1 An estimate of the information content of catalogs 120
6.2 Summary of the relevant parameters for application of the HCM 122
6.3 Large families with > 1000 members sorted by # tot 130
6.4 The same as in Table 6.3 but for medium families with $100 < \# \leq 1000$ members 136
6.5 The same as in Table 6.3 but for small families with $30 < \# \leq 100$ members 139
6.6 The same as in Table 6.3 but for tiny families with < 30 members 142
6.7 Results of the fit for the low a (IN) and high a (OUT) sides for each considered family 149
6.8 Cratering families 152
6.9 Fragmentation families 154
6.10 Family age estimation 155
6.11 Very close couples 178

7.1 Fit region: family number and name, explanation of the choice, minimum value of proper a, minimum value of the diameter selected for the inner and the outer side. 188
7.2 Family albedos: number and name of the family, albedo of the parent body with standard deviation and code of reference, maximum and minimum value for computing mean, mean and standard deviation of the albedo 194
7.3 Slopes of the V-shape for the fragmentation families: family number/name, number of dynamical family members, side, slope (S), inverse slope ($1/S$), standard deviation of the inverse slope, ratio OUT/IN of $1/S$, and standard deviation of the ratio. 197
7.4 Slope of the V-shape for the cratering families. Columns as in Table 7.3. 199
7.5 Slope of the V-shape for the young families. Columns as in Table 7.3. 201
7.6 Slopes of the V-shape for the one-sided families: family number/name, number of dynamical family members, side, slope (S), inverse slope ($1/S$), standard deviation of the inverse slope. 201
7.7 Benchmark asteroids for the density of a taxonomic type: number/name, taxonomic type, densities as in [Carry, 2012] with their uncertainties, densities at 1 km. 203

7.8 Data for the Yarkovsky calibration: family number and name, proper semimajor axis a and eccentricity e for the inner and the outer side, 1-A, density value ρ at 1 km, taxonomic type, a flag with values m (measured) a (assumed) g (guessed), and the relative standard deviation of the calibration. 205
7.9 Age estimation for the fragmentation families: family number and name, da/dt, age estimation, uncertainty of the age due to the fit, uncertainty of the age due to the calibration, and total uncertainty of the age estimation. 207
7.10 Age estimation for the cratering families. Columns as in Table 7.9. 209
7.11 Age estimation for the young families. Columns as in Table 7.9. 211
7.12 Age estimation for the one-sided families. Columns as in Table 7.9. 212

10.1 The resonances with the mean motion of the Earth made accessible to 2009 FD by the 2185 close encounter. The lines in boldface show the resonances for which actual VIs are found numerically. 269

Chapter 1

Introduction

This thesis is a collection of the work carried out during the three years of Ph.D. studies at the University of Pisa with the Celestial Mechanics Groups.

The main topics of this thesis range from nongravitational perturbations, to asteroid orbit determination, and to the impact monitoring. The nongravitational perturbations arise because outer space is not empty, and they can affect not only the dynamics of Near Earth Asteroids (NEAs), but also the determination of the age of asteroid families. The main nongravitational perturbation is the Yarkovsky effect, a subtle nongravitational phenomenon related to the anisotropic thermal emission of Solar System objects. The nongravitational perturbations also affect the impact probabilities of NEAs, especially over long time span. For some special cases, we need to model the Yarkovsky effect to compute the long term propagation to the possible impacts and the intervening planetary encounters of NEAs.

In Chap. 2 we give a review of the general theory needed for the whole thesis. Sec. 2.1 is about nongravitational perturbations, as in [Milani and Gronchi, 2010, Chap. 14]. We focus our attention on the Yarkovsky effect, and on its modeling and formulations. Sec. 2.2 is a general description of the proper elements. Sec. 2.3 describes the applications of the Yarkovsky effect, expecially in the case of Near Earth Asteroids and in the case of the computation of the ages of asteroid families.

Then, in Chap. 3, we seek the evidence of the Yarkovsky effect among NEAs by measuring the Yarkovsky-related orbital drift from the orbital fit. To prevent the occurrence of unreliable detections we employ a high precision dynamical model, including the Newtonian attraction of 16 massive asteroids and the planetary relativistic terms, and a suitable astrometric data treatment. We find 21 NEAs whose orbital fits show a measurable orbital drift with a signal to noise ratio (SNR) greater than 3. The best determination is for asteroid (101955) Bennu, with a Signal to Noise Ratio (SNR) ~ 200. In

some cases it is also possible to constrain physical quantities otherwise unknown. Furthermore, the distribution of the detected orbital drifts shows an excess of retrograde rotators that can be connected to the delivery mechanism from the most important NEA feeding resonances and allows us to infer the obliquity distribution of NEAs. We discuss the implications of the Yarkovsky effect for impact predictions. This work is published in [Farnocchia et al., 2013b].

Among those NEAs, there are some special cases that need to be handled in a separate way. Two of these cases are the asteroid (29075) 1950 DA (see [Farnocchia and Chesley, 2014]), and (99942) Apophis (see [Farnocchia et al., 2013a]). Here we carefully analyze (101955) Bennu and (410777) 2009 FD. Chapter 4 is focused on (101955) Bennu: the asteroid with the best determined Yarkovsky effect, as explained in [Chesley et al., 2014]. (101955) Bennu is also the target of the OSIRIS-REx asteroid sample return mission. It is a half-kilometer near Earth asteroid with an extraordinarily well constrained orbit. An extensive data set of optical astrometry from 1999–2013 and high-quality radar delay measurements for Bennu in 1999, 2005, and 2011 reveal the action of the Yarkovsky effect, with a mean semimajor axis drift rate $da/dt = (-19.0 \pm 0.1) \times 10^{-4}$ au/Myr or 284 ± 1.5 m/yr. The accuracy of this result depends critically on the fidelity of the observational and dynamical model. The introduction of the Yarkovsky effect is crucial not only for the determination of the orbit, but also for the impact monitoring. Bennu's Earth close approaches are deterministic over the interval 1654–2135, beyond which the predictions are statistical in nature. In particular, the 2135 close approach is likely within the lunar distance and leads to strong scattering and therefore numerous potential impacts in subsequent years, from 2175–2196. The highest individual impact probability is 9.5×10^{-5} in 2196, and the cumulative impact probability is 3.7×10^{-4}, leading to a cumulative Palermo Scale value of -1.70.

Chapter 5 shows how the Yarkovsky effect is relevant for the asteroid (410777) 2009 FD. The results are from [Spoto et al., 2014].Asteroid 2009 FD could hit the Earth between 2185 and 2196. The long term propagation to the possible impacts and the intervening planetary encounters make 2009 FD one of the most challenging asteroids in terms of hazard assessment. To compute accurate impact probabilities we model the Yarkovsky effect by using the available physical characterization of 2009 FD and general properties of the near Earth asteroid population. We perform the hazard assessment with two independent methods: the first method is a generalization of the standard impact monitoring algorithms in use by NEODyS and Sentry, while the second one is based on a Monte Carlo approach. Both methods generate orbital samples in a seven-dimensional space that includes orbital elements and

the parameter characterizing the Yarkovsky effect. The highest impact probability is 2.7×10^{-3} for an impact during the 2185 Earth encounter. Impacts after 2185 corresponding to resonant returns are possible, the most relevant being in 2190 with a probability of 3×10^{-4}. Both numerical methods can be used in the future to handle similar cases. The structure of resonant returns and the list of the possible keyholes on the target plane of the scattering encounter in 2185 can be predicted by an analytic theory.

In Chap. 6 there is an overwiew of the asteroid families: their identification, the properties of their parent bodies, the collisional event(s) generating the family and the subsequent evolution due to chaotic dynamics. Note that the number of asteroids with accurately determined orbits increases fast, and this increase is also accelerating. The catalogs of asteroid physical observations have also increased, although the number of objects is still smaller than in the orbital catalogs. Thus it becomes more and more challenging to perform, maintain and update a classification of asteroids into families. To cope with these challenges we developed a new approach to the asteroid family classification by combining the Hierarchical Clustering Method (HCM) with a method to add new members to existing families. This procedure makes use of the much larger amount of information contained in the proper elements catalogs, with respect to classifications using also physical observations for a smaller number of asteroids. Our work is based on a large catalog of high accuracy synthetic proper elements (available from AstDyS), containing data for $> 330\,000$ numbered asteroids. By selecting from the catalog a much smaller number of large asteroids, we first identify a number of core families; to these we attribute the next layer of smaller objects. Then, we remove all the family members from the catalog, and reapply the HCM to the rest. This gives both satellite families which extend the core families and new independent families, consisting mainly of small asteroids. These two cases are discriminated by another step of attribution of new members and by merging intersecting families. This leads to a classification with 128 families and currently 87095 members. The number of members can be increased automatically with each update of the proper elements catalog; changes in the list of families are not automated (see [Knežević et al., 2014]). By using information from absolute magnitudes, we take advantage of the larger size range in some families to analyze their shape in the proper semimajor axis vs. inverse diameter plane. This leads to a new method to estimate the family age, or ages in cases where we identify internal structures. The results from the previous steps are then analyzed, using also auxiliary information on physical properties including WISE albedos and SDSS color indexes. This allows us to solve some difficult cases of families overlapping in the proper elements space but generated by different collisional events. The families

formed by one or more cratering events are found to be more numerous than previously believed because the fragments are smaller. We analyze some examples of cratering families (Massalia, Vesta, Eunomia) which show internal structures, interpreted as multiple collisions. We also discuss why Ceres has no family. This Chapter is from [Milani et al., 2014].

Chapter 7 is the continuation of the work carried out in Chap. 6 (see also [Spoto et al., 2015]). We have now a new family classification, based on a catalog of proper elements with $\sim$ 384 000 numbered asteroids and on the new methods described in Chap. 6. For the 45 dynamical families with > 250 members identified in this classification we present an attempt to obtain statistically significant ages, and we succeded in computing 37 collisional family ages. We used a rigorous method, which is an improvement of the method presented in Chap. 6. The ages of several families have been estimated for the first time, in other cases the accuracy has been improved.

Chap. 8 is the link among the chaotic orbit determination, the modeling of the Yarkovky effect, and the impact monitoring. Orbit determination is possible for a chaotic orbit of a dynamical system, given a finite set of observations, provided the initial conditions are at the central time. We test both the convergence of the orbit determination procedure and the behavior of the uncertainties as a function of the maximum number n of map iterations observed, by using a simple discrete model, namely the standard map. Two problems appear: first, the orbit determination is made impossible by numerical instability beyond a computability horizon, which can be approximately predicted by a simple formula containing the Lyapounov time and the relative round off error. Second, the uncertainty of the results is sharply increased if a dynamical parameter (contained in the standard map formula) is added to the initial conditions as parameter to be estimated. In particular the uncertainty of the dynamical parameter, and of at least one of the initial conditions, decreases like n^a with $a < 0$ but not large in absolute value (of the order of unity). If only the initial conditions are estimated, their uncertainty decreases exponentially with n, thus it becomes very small. All these phenomena occur when the chosen initial conditions belong to a chaotic orbit (as shown by one of the well known Lyapounov indicators). If they belong to a non-chaotic orbit the computational horizon is much larger, if it exists at all, and the decrease of the uncertainty appears to be polynomial in all parameters, like n^a with $a \simeq 1/2$; the difference between the case with and without dynamical parameter being also estimated disappears. These phenomena, which we can investigate in a simple model, have significant implications in practical problems of orbit determination involving chaotic phenomena, such as the chaotic rotation state of a celestial body and a chaotic orbit of a planet-crossing asteroid undergoing many close approaches. All these results

are from [Spoto and Milani, 2015].

In Chap. 9 we study the time evolution of the impact probability for synthetic but realistic impacting and close approaching asteroids detected in a simulated all-sky survey, see [Vereš et al., 2014]. Here we handle short term impacts, thus asteroids with poor orbits, while in the previous Chapters we were taking care of long term impacts and asteroids with accurate orbits. We use the impact probability to calculate the impact warning time (t_{warn}) as the time interval between when an object reaches a Palermo Scale value of -2 and when it impacts Earth. A simple argument shows that $t_{warn} \propto D^x$ with the exponent in the range $[1.0, 1.5]$ and our derived value was $x = 1.3 \pm 0.1$. The low-precision astrometry from a single simulated all-sky survey could require many days or weeks to establish an imminent impact for asteroids larger than 100 m diameter that are discovered far from the Earth. Most close-approaching asteroids are quickly identified as not being impactors but a size-dependent percentage, even for those larger than 50 m diameter, have a persistent impact probability greater than 10^{-6} on the day of closest approach. Thus, a single all-sky survey can be of tremendous value in identifying Earth impacting and close-approaching asteroids in advance of their closest approach but it can not solve the problem on its own: high-precision astrometry from other optical or radar systems is necessary to rapidly establish an object as an impactor or close-approacher. We show that the parallax afforded by surveying the sky from two sites is of benefit for only a small fraction of the smallest objects detected within a couple days before impact: probably not enough to justify the increased operating costs of a 2-site survey. Finally, the survey cadence within a fixed time span is relatively unimportant to the impact probability calculation. We tested three different reasonable cadences and found that one provided ~ 10 times higher (better) value for the impact probability on the discovery night for the smallest (10 m diameter) objects but the consequences on the overall impact probability calculation are negligible.

Chapter 2

General Theory

2.1 Nongravitational perturbations

The nongravitational perturbations arise because outer space is not empty. First, planetary atmospheres extent to large altitudes, where they can be thin enough to allow for a satellite orbit but still generate a significant aerodynamic drag, given the high relative velocity of the spacecraft.

Second, outer space is pervaded by electromagnetic radiation: the light arriving directly from the Sun, reflected by the Earth, and by the other planets. The photons exchange momentum with spacecraft when they are absorbed and reflected; spacecraft themselves emit infrared radiation and electromagnetic waves carrying away some momentum. The resulting accelerations are small, but at a level of accuracy of current tracking systems they are not negligible, hence the need to model and/or measure them. Even small natural bodies, such as asteroids with diameters in the km range, have orbits affected by non-gravitational perturbations in a measurable way.

2.1.1 The Yarkovsky effect

Historical overview

The Yarkovsy effect has a long and complex history. A Russian civil engineer, Ivan O. Yarkovsky, noted that if a prograde rotating body is heated, this should produce a transverse acceleration in its motion [Beekman, 2006; Yarkovsky, 1901]. Yarkovsky was only able to give a roughly estimate of the magnitude of the effect, but he gave rise to a new theory that has been developed a century later.

Öpik [1951] re-introduced the Yarkovsky effect, long after the original pamphlet had been lost. At about the same time, Radzievskii [1952a,b]

was the first to consider the effects of systematic photon thrust on a body's rotation, but he didn't find any strong evidence of large albedo variations over surfaces of asteroids or meteoroids.

During the years between 1969 and 1975, the Yarkovsky-O'Keefe-Radzievskii-Paddack effect (YORP effect) was born. It is based on the fact the the irregular shape and thermal radiation can change the meteoroid's spin rate [Paddack, 1969; Paddack and Rhee, 1975; Rubincam, 2000].

The work of Rubincam [1995, 1998], Farinella et al. [1998] and Vokrouhlický [1998a,b]; Vokrouhlický [1999] led to a major resurgence in the study of Yarkovsky and YORP effect. They realized a direct link between the orbital effects acting on the geodynamics artificial satellites such as LAGEOS and the orbital effects on small meteoroids.

It is also worth mentioning that the orbit analysis of some NEAs suggested evidence of non-gravitational phenomena by requiring an anomalous secular decrease of their semimajor axis [Sitarski, 1992, 1998].

Then, Bottke et al. [2002b, 2006]; Vokrouhlický et al. [2000a] showed new results on the modelling of the Yarkovsky effect, and on its applications to the dynamic of small asteroids and their population.

Classical models

The relevance of radiation pressure as a source of perturbations on the orbit of both spacecraft and asteroid depends upon the way it accumulates with time.

A passive celestial body exposed to solar radiation transforms the absorbed fractions into heat and reaches some thermal state. The surface temperature is not uniform and changes with time as a result of both the rotation and the orbital motion. Thus the entire surface re-emits thermal radiation anisotropically, carrying away linear momentum, and this results in a perturbative acceleration, affecting the orbit.

What matters is the fraction of the perturbing acceleration contributing to the secular change in the semimajor axis. Thermal emission can have secular effects in the semimajor axis for a heliocentric orbit, even for a spherical shape; this is called the Yarkovsky effect. A similar effect occurs for geocentric orbits, due to the uneven heating resulting from radiation emitted by both the Sun and the Earth. It is important to point out that there is no Yarkovsky force, but just thermal emission forces, which under suitable circumstances have a comparatively small, but significant, mean transversal component.

The Yarkovsky effect is very important as a source of secular perturbations to model the dynamical evolution of asteroids, e.g. it is relevant

for the transport of meteorites and asteroids to the Near Earth region: 15 $m/y \simeq 10^{-4} au/My$ accumulates to a large change over the age of the asteroids. For an orbit determination with a data span shorter that an orbital period they are very small, and anyway less relevant than the short period perturbations due to both direct radiation pressure and thermal emission. The exceptional cases are asteroids with a very long observed arc; very accurate observations may also be needed. As an example, the first asteroid for which the Yarkovsky effect has been measured by orbit determination is (6489) Golevka, which has been observed by radar during three separate close approaches to the Earth; the second case was (152563) 1992 BF.

With the accumulation of more data and also the expected improvements in astrometric accuracies, such cases has become more frequent, as it is clear from Chap. 3, 4, and 5.

Even if the Yarkovsky effect results in variations to all of the orbital elements, the most important one is the secular effect in the semimajor axis a.

Diurnal and seasonal Yarkovsky effect

The diurnal Yarkovsky effect arises because thermal inertia of the illuminated body results in a temperature maximum lagging some time after the maximum illumination. This effect depends upon the conductivity. This effect is always of the same order of magnitude, once the mass in known; of course it depends upon the obliquity ε, with the semimajor axis secularly increasing for prograde rotation ($\varepsilon < 90^o$) and decreasing for retrograde ($\varepsilon > 90^o$). The magnitude of this effect is larger than that of the seasonal effect.

If a body with a fixed rotation axis were in a constant thermal state as it orbits around the Sun, then the thermal emission force would be of constant size and direction, thus the mean transversal component is 0. This condition can be violated for two reasons. The first is when the obliquity ε, that is the angle between the spin axis and the orbital angular momentum, is not 0. Then the latitude of the Sun in the body equatorial frame is not constant, hence there is a thermal emission force changing with time, essentially with the frequency of the mean motion n. The second reason is that the isolation is a function of the distance from the Sun, thus it changes for an eccentric orbit, mostly with the frequency. There is a third possible reason: the rotation axis could be changing with time, for an asteroid not in a simple rotation state but tumbling, either regularly or chaotically as for (4179) Toutatis.

In the first two cases, the thermal emission force has an intensity which changes with a period equal to the orbital period (in a two-body approximation). This is called a seasonal effect because it depends on the fact that the heliocentric body has temperature variations depending upon the equatorial

obliquity and upon the orbital eccentricity, similarly to the major planet.

There are three basic assumptions of the model of the Yarkovsky effect:

- The linearization of the surface boundary condition;
- A rotation about a spin axis fixed in the inertial space (at least on a timescale comparable with the revolution about the Sun)
- A circular orbit about the Sun

The diurnal variant of the Yarkovsky acceleration can be written in the form:

$$\left(\frac{da}{dt}\right)_{diurnal} = -\frac{8}{9}\frac{\alpha\Phi}{n}W(R_\omega, \Theta_\omega)\cos\gamma$$

and the seasonal one:

$$\left(\frac{da}{dt}\right)_{seasonal} = \frac{4}{9}\frac{\alpha\Phi}{n}W(R_n, \Theta_n)\sin^2\gamma$$

where $\Phi = \pi R^2 F/(mc)$, R is the radius of the body, F is the solar radiation flux at the orbital distance a from the Sun, m is the mass of the body, c is the light velocity, n is the orbital mean motion and $\alpha = 1 - A$ with A denoting the Bond albedo Vokrouhlický and Bottke [2001]. The Φ factor is characteristic to any physical effect related to sunlight absorbed or scattered by the surface of the body. Since $m \propto R^3$, one obtain a simple scaling $\Phi \propto 1/R$. γ is the spin axis obliquity: the diurnal part is proportional to $\cos\gamma$, thus can make a positive or negative change of the semimajor axis, being maximum at 0^o and 180^o obliquity values. The seasonal part is $\propto \sin^2\gamma$, thus always results in a decrease in semimajor axis, being maximum at 90^o obliquity. The magnitude of the diurnal and seasonal Yarkovsky effect is clearly proportional to the function:

$$W(R_\nu, \Theta_\mu) = -\frac{\kappa_1(R_\nu)\Theta_\nu}{1 + 2\kappa_2(R_\nu)\Theta_\nu + \kappa_3(R_\nu)\Theta_\nu^2}$$

determined by the thermal parameters of the body and a frequency ν. This frequency is equal to the rotation frequency ω for the diurnal component, or to the orbital mean motion n for the seasonal component. The thermal parameters required by the model are:

- The surface thermal conductivity K;
- The surface heat capacity C;
- The surface density ρ.

These parameters, together with the frequency ν, do not appear in the equation of the function W individually, but in the process of solving the heat diffusion problem and determination of the orbital perturbations, they combine in two relevant parameters.

- They provide a scale length $l_\nu = \sqrt{K/(\rho C \nu)}$ which indicates the local value of the penetration depth of the diurnal thermal wave, assuming the surface irradiation is periodic with frequency ν. The non-dimensional radius of the body R_ν is defined by $R_\nu = R/l_\nu$;
- $\Theta_\nu = \Gamma\sqrt{\nu}/(\epsilon\sigma T^3)$ where Γ is the surface thermal inertia defined by $\Gamma = \sqrt{K\rho C}$, ϵ is the thermal emissivity of the surface, σ is the Stefan-Boltzmann constant and T the subsolar temperature ($\epsilon\sigma T^4 = \alpha F$).

Rubincam [1995] and Vokrouhlický [1998a] showed the behavior of the three κ-coefficients in the equation for W for an arbitrary value of R_ν, and in particular they noted that when the characteristic size R of the body is much larger than l_ν, the coefficients are equal to 1/2. Therefore, for large bodies the W-factor do not depend on the size R and

$$W \simeq W(\Theta_\nu) = -\frac{0.5\Theta_\nu}{(1 + \Theta_\nu + 0.5\Theta_\nu^2)}$$

Consequently, the Yarkovsky effect is maximum when $\Theta_\nu \simeq 1$; while for small or large values of Θ_ν the effect vanishes. In this case, the semimajor axis secular change da/dt due to the Yarkovsky effect scales as $\propto 1/R$ with the characteristic radius R. For small asteroids, either in the near-Earth space or in the main belt, Θ_ω is typically of the order of unity, while Θ_n is much smaller, which implies that the diurnal Yarkovsky component usually dominates the seasonal component.

Some models were developed to probe the role of each of the simplifying assumptions mentioned above using analytical, semi-analytical or fully numerical methods. These include:

- An inhomogeneity of the thermal parameters [Vokrouhlický and Brož, 1999];
- A coupling of the diurnal and seasonal components of the Yarkovsky effect [Sekiya and Shimoda, 2013, 2014; Vokrouhlický, 1999];
- Effects of a non-spherical shape for simple [Vokrouhlický, 1998b] or general geometries;
- A non-principal axis rotation state [Vokrouhlický et al., 2005a];

- The Yarkovsky effect for binary asteroids [Vokrouhlický et al., 2005b].

  Each of them was found to modify the results from the zero-approximation model by as much as several tens of percent without modifying the fundamental dependence of the Yarkovsky effect on obliquity, size or thermal parameters.

2.2 Proper elements

A classical definition states that proper elements are quasi-integrals of motion, and that they are nearly constant in time. The proper elements are obtained as a result of the elimination of short and long periodic perturbations from their instantaneous, osculating counterparts, and thus represent a kind of average characteristics of motion.

2.2.1 Historical overview

A concept of proper elements has been introduced by Hirayama [1918]. Even if not using the technical term proper, he employed Lagrange's classical linear theory of asteroid secular perturbations to demonstrate that certain asteroids tend to cluster around special values of the orbital elements, which very closely correspond to the constants of integration of the solutions of the equations of their motion, that is, to a sort of averaged characteristics of their motion over very long time spans. Hirayama [1923, 1928] explicitly computed just the proper elements (proper semimajor axis, proper eccentricity and proper inclination), and used them for the classification of asteroids into families.

Brouwer [1951] computed asteroid proper elements using a linear theory of secular perturbations, but in combination with an improved theory of motion of the perturbing planets.

Williams [1969] developed a semianalytic theory of asteroid secular perturbations which does not make use of a truncated development of the perturbing function, and which is applicable to asteroids of with arbitrary eccentricity and inclination. Williams' proper eccentricity and proper inclination are defined as values acquired when the argument of perihelion $\omega = 0$ (thus corresponding to the minimum of eccentricity and the maximum of inclination over a cycle of ω). The theory is linearized in the planetary masses, eccentricities and inclinations, so that the proper elements computed by means of this theory, even if much better that the previously available ones, were still of limited accuracy.

Kozai [1979] used his theory of secular perturbations for high inclination asteroids to define a set of proper parameters to identify the families. The selected parameters were semimajor axis, z-component of the angular momentum (integral of motion in a first order theory, with perturbing planets moving on circular, planar orbits), and the minimum value of inclination over the cycle of the argument of perihelion (corresponding to $\omega = \pi/2$).

Finally, Schubart [1982, 1991], Bien and Schubart [1987], Schubart and Bien [1987] tried to determine proper parameters for resonant groups, that is for Hildas and Trojans. Since the usual averaging methods do not apply in this case, they adopted slightly different definitions of the proper parameters, the most important difference being the substitution of a representative value measuring the libration of the critical argument instead of the usual proper semimajor axis.

2.2.2 Proper elements

The notion of proper elements is based upon the linear theory of secular perturbations. Linear theory neglets the short periodic perturbations, containing the anomalies in the arguments; this results in a constant semimajor axis which becomes the first proper element a_p. The long term evolution of the other variables is obtained by approximating the secular equation of motion with a system of linear differential equations. Because of the linearity assumption, the solutions can be represented in the planes $(k, h) = (e\cos\varpi, e\sin\varpi)$ as the sum of proper modes, one for each planet, plus one for the asteroid. Thus the solution can be represented by epicyclic motion: for the asteroid, the sum of the contributions from the planets represents the forced term, while the additional circular motion is the so called free oscillation and its amplitude is the proper eccentricity e_p. The same applies to the $(q, p) = (\sin I\cos\Omega, \sin I\sin\Omega)$ plane, with amplitude of the free term given by the (sine of) proper inclination $\sin I_p$. The approximation of linear secular perturbation theory is good enough for a time span of the order of the period of circulation for the longitude of perihelion ω. However, even over such a time span the linear theory is only an approximation, and over a much longer time span (e.g., millions of years) it would be a rather poor approximation in most cases.

Proper elements can also be obtained from the output of a numerical integration for the full equations of motion: the simplest method is to take averages of the action-like variables a, e, I, over times much longer that the periods of circulation of the corresponding angular variables. However, this method provides proper elements of low reliability: the dynamical state can change for unstable orbits and in such a case the simple average wipes out this

essential information. Thus, it is necessary to use much more complicated theories to compute proper elements stable to 1% of their value or better.

Whatever the type of theory, if it is to be accurate enough to represent the dynamics in the framework of a realistic model, its full-detail description requires to dwell into a very long list of often cumbersome technicalities. For this reason in the present thesis we only give a qualitative description of the computational procedures.

Several different sets of proper parameters have been introduced over the time, but the most common set, usually referred to as proper elements, includes proper semimajor axis a_p, proper eccentricity e_p, (sine of) proper inclination $\sin I_p$, proper longitude of perihelion ϖ_p, and proper longitude of node Ω_p, the latter two angles being accompanied with their precession rates, the fundamental frequencies g and s, respectively.

The analytical theories and the already mentioned theory by Williams [1969] use a different definition of proper eccentricity and inclination. Other authors introduced even completely different parameters to replace the standard proper elements. Still, the common feature of all these parameters is their stability over long time spans.

Lemaitre [1993] explains that, even if quite different in terms of the proper parameters and the ways to compute them, all the theories follow several basic steps, which can be summarized as follows:

- modelling of asteroid motion (N-body, restricted 3-body), and distinguishing the fast and slow angles, i.e. separating the perturbation depending on the mean longitudes from the rest;
- removal of the short periodic perturbations (analytical or numerical averaging, on-line filtering) and computation of the mean element;
- splitting of the resulting Hamiltonian into two parts, the integrable (secular) part, and the perturbation (the long-periodic part depending on slow angles). In the case of the synthetic theories this step corresponds to the removal of the forced terms;
- removal of the long-periodic terms and computation of the proper values. At this stage, analytic and semianalytic theories resort to the averaging over the slow angles and to the iterative procedures to compute the inverse map of canonical transformation, while in the case of synthetic theories this phase includes the Fourier analysis and extraction of the principal harmonics from the time series of mean elements;
- output of the proper values, possibly accompanied with their errors (standard deviations, maximum excursions), fundamental frequencies,

quality and resonant codes, chaotic behavior indicators and other information.

2.2.3 The theories

Analytical theory

The main problem in the manufacturing of fully analytical theories of proper elements is in the complete degeneracy of the unperturbed dynamics, the 2-body problem. Degeneracy means that some of the fundamental frequencies are zero, and indeed in the 2-body approximation both the perihelia and the nodes do not precess at all. In the Hamiltonian formalism, this is expressed by the statement that the unperturbed Hamiltonian function $H_0 = H_0(L)$ is a function only of one variable L, in turn a function of the semimajor axis. The perturbed problem with Hamiltonian $H_0(L) + \mu H_1(l, g, L, G)$ (the small parameter μ representing the ratio of the mass of the planets to the mass of the Sun) can be handled with different perturbative approaches, but they all have in common the use of a solution of the unperturbed 2-body problem to be substituted into the perturbing function H_1. Thus they also have in common the problem that the angle variable l, the mean anomaly conjugate to L, can be eliminated, but the angles g, conjugate to the other action variables not appearing in H_0, cannot be removed by averaging.

This implies that the procedure to compute proper elements must always be decomposed into two computational steps: the transformation from osculating orbital elements to mean elements, free from the short periodic perturbations (with arguments containing the fast variable l), and the transformations of the mean elements into proper elements. A fully analytical theory performs both steps by means of the computation of functions for which analytical expressions, in practice truncations of some series, are available. Note that it is possible to mix two different methods.

Different perturbations techniques can be used, the Lie series technique being the most convenient for theories pushed to higher order (and therefore based upon series with many terms). Analytical perturbation techniques exploit the approximation of the perturbing function H_1 by means of a finite sum of terms, each with a simple expression of the form,

$$\mu b(L) e^h e'^k I^j I'^m \cos(pl + ql' + \delta)$$

where h, k, j, m, p, q are integers, the primed elements refer to some perturbing planet, b is a known function and δ is some combination, with integer

coefficients, of the angles included in g, the perihelia and nodes of the asteroid and the planet. The truncation of the series is mostly based upon the degree in the small parameters eccentricity and inclination of both the asteroid and the planets, although truncation for large values of the integers p, q is also possible. Thus we can describe the degree of completeness of a theory by means of the order in the small parameter μ and of the degree in the eccentricities and inclinations. From this arises the main limitation of the analytical method: the accuracy, and stability with time, of the proper elements decreases as the asteroid eccentricity and inclination increase. There is a boundary between the region where the analytical proper elements are most suitable and the region where more computationally intensive methods, such as the semianalytic ones, need to be used; Knežević et al. [1995] have mapped this boundary. The simple analytical form of the terms implies that it is possible to perform both derivatives and integrals analytically; thus the corresponding operations can be applied to the series term by term. An analytical theory can be expressed by means of derivatives integrals and arithmetic operations on these series; thus they can be explicitly computed by means of a finite, although large, number of elementary operations. In practice, the current analytical theories use series with several tens of thousand of terms. The series used in the current theories are essentially based upon the expansions computed by Yuasa [1973] and corrected and completed by Knežević [1989, 1993]. These are complete to degree 4 in eccentricities and inclinations; only a few special terms of degree 6 have been added later Milani and Knežević [1994]. Yuasa [1973] defined an algorithm to compute proper elements with a theory containing the main terms of order 2 in μ and complete to degree 4 in eccentricity and inclination, but one essential step was missing. Milani and Knežević [1990] found that, at orders > 1 in μ, the formulas of perturbation theory explicitly provide a map between proper and mean elements, in the opposite direction from the one which we deal with in practice. Thus the computation of proper elements from mean elements requires the solution of an inverse function problem, and this is possible only by an iterative procedure. Later Milani and Knežević [1999] applied the same argument to the computation of mean elements from osculating ones.

The iterative procedures used in the computation of analytical proper elements can be divergent where a small divisor, resulting from the attempt to integrate one of the trigonometric terms with very slowly varying arguments, occurs. Difficulties in the computation of mean elements from the osculating ones are due to mean motion resonances, involving the anomalies of the asteroid and some planet. Difficulties in the convergence of the iterations for the computation of proper elements from mean elements indicate secular resonances, that is very small frequencies resulting from combinations of the

frequencies g, s of the perihelia and nodes with the corresponding frequencies for the perturbing planets. By the same theories it is possible to construct maps of secular resonances Knežević et al. [1995]; Milani and Knežević [1994], including combinations of up to four secular frequencies (and in some special cases also 6 and 8 frequencies).

Semianalytical theory

The semianalytic calculation of proper elements was initiated by Williams [1969] and then revisited by Lemaitre and Morbidelli [1994]. It is a classical perturbation method, where the two averaging processes (the first one on the mean longitudes and the second on the pericenters and nodes) are performed numerically. This avoids the expansion in the eccentricity (e) and inclination (I) of the asteroid, and makes the method particularly suitable for about 20% of the asteroids with large values of these elements.

The latest version of the theory is written in a Hamiltonian formalism and computed up to the second order in the perturbing masses (presently only Jupiter and Saturn) and up to the first degree in the eccentricities (e') and inclinations (I') of the perturbers.

The elimination of the short periodic terms is performed numerically by the calculation of the double integrals (over the two mean longitudes). After this averaging, the semi-major axis is constant and represent the first proper element. To compute the averaged Hamiltonian a Fourier series of the slow angles is used, with the coefficients evaluated on a three dimensional grid (in a, e, and I) and stored; a triple linear interpolation is used each time the Hamiltonian and its derivative have to be evaluated.

The averaged Hamiltonian is split in two parts, based upon the smallness of the parameters e' and I'; the integrable problem corresponds to circular and planar motion of the perturbing planets, while the perturbation part gathers all the first order contributions in e' and I'. The dynamics of the integrable problem has been analyzed already by Kozai [1962], and it reveals different behaviors for low and high inclinations; in the latter case a critical curve separates the phase space into two regions, corresponding to librations (about 90 or 270) and to circulations of the argument of the pericenter ω of the asteroid.

The removal of the long periodic terms is done by using the action angle variables and is based on the semianalytic method developed by Henrard [1990]. The resulting Hamiltonian K, after the second averaging process, depends only on two proper actions, J and Z, which are both constant. The result is a proper orbit of area proportional to J, located in a plane identified by the value of Z. Each point of the proper orbit is characterized by a value of the phase ψ, which can be considered as a proper argument of perihelion.

From the values of ψ, J and Z, the corresponding values of e, I and ω can be calculated. Any point can be chosen as a representant of this orbit: for example, $\psi = 0^o, 180^o$ corresponds to the minimum value of the eccentricity and the maximum of the inclination along the proper orbit. On the other hand, $\psi = 90^o, 270^o$ corresponds to the maximum of eccentricity and the minimum of the inclination; this option allows to define proper elements even for $\omega-$librators, since the libration center is either 90^o or 270^o.

The proper orbit is also characterized by the two basic frequencies, g and s, calculated as the partial derivatives of the Hamiltonian K with respect to the actions J and Z. The set a, g and s is also a set of proper elements and it is independent of the choice of the representative point on the proper orbit.

The existence of two high inclined groups of asteroids was shown by this method; a Pallas family at about 35^o of inclination Lemaitre and Morbidelli [1994], and a Hungaria family at 2 au Lemaitre [1994].

The precision is limited by the first order development in e' and I' and could not be easily improved. However this semianalytic procedure keeps some advantages, like the fact that it allows the calculation not only of the proper frequencies, but also of their derivatives with respect to the action variables.

Synthetic theory

The latest contribution to the field of asteroid proper element determination is the synthetic theory by Knežević and Milani [2000]. This is, in fact, a set of purely numerical procedures by means of which one can derive classical proper elements $(a_p, e_p, \sin I_p, \varpi_p, \Omega_p)$ and fundamental frequencies (g, s). The theory employs the approach used by Carpino et al. [1987] for the major planets, and consists of the following steps: first, one numerically integrates the asteroid orbits for a long enough time span, together with the orbits of perturbing planets included in the model (the indirect effects of the planets not included in the dynamical model are accounted for by applying the so-called barycentric correction to the initial conditions); the short periodic perturbations are removed by means of an online filtering of the osculating elements, performed in the course of the integration itself; simultaneously, the maximum Lyapounov Characteristic Exponents are derived from the variational equations to monitor the chaotic behaviors. The forced oscillations are then removed from the output of the integration and the resulting time series are spectrally resolved under the constraints set by the d'Alembert rules to extract principal harmonics (proper value) together with the associated fundamental frequencies and error estimates (standard deviations and maximum excursions).

The first proper element, the proper semimajor axis a_p, is obtained by

filtering out the short periodic perturbations from the time series of the osculating a. The definition is more complicated than the average of $a(t)$, because of the second order perturbations which contain both constant and long periodic terms [Milani et al., 1987]. However, the second order perturbations are very small and in practice they are seldom the main source of time variation of the proper semimajor axis: chaotic effects are dominant in most cases. Thus a_p has been computed as the mean of the values of $a(t)$ computed as output of the digital filter; that is a mean of the already smoothed data. There is also the associated third proper frequency, namely f_p, which is the slope of the angle $\lambda = l + \varpi$. The value of f_p can be obtained by a simple linear fit to the filtered $\lambda \in \mathbf{R}$, where the filter also preserves the number of revolutions. We can define a mean mean motion $n_p = f_p - g$ as the proper frequency of the mean longitude λ, but the frequency n_p is not related to a_p by Kepler's third law.

The procedure to extract proper eccentricity and inclination and the corresponding proper frequencies is a modified form of Fourier analysis introduced in [Carpino et al., 1987], and further improved [Knežević and Milani, 2000, 2003]. The procedure includes 3 steps.

First, the forced secular perturbations with known frequencies are removed from the filtered time series for the equinoctial elements:

$$\begin{aligned} k &= e\cos\varpi \\ h &= e\sin\varpi \\ q &= \tan(I/2)\cos(\Omega) \\ p &= \tan(I/2)\sin(\Omega) \end{aligned}$$

Given the fundamental frequencies g_5, g_6, g_7 of the precession of perihelia of Jupiter, Saturn and Uranus respectively, the Fourier components with these frequencies from (k, h) are removed. Given the fundamental frequencies s_6, s_7, s_8 of the precession of the nodes of Saturn, Uranus and Neptune respectively, the Fourier components with these frequencies from (q, p) are removed.

Second, there is the computation of the time series of the arguments ϖ_f, Ω_f, freed from short periodic computations, which are the phases of the oscillation in the planes (k, h) and (q, p), respectively. This is computed from the polar angles in these two planes, by adding multiples of 2π to obtain a continuous real function. Finally, by a linear least squares fit, we estimate the proper frequencies g, the slope of ϖ_f, and s, the slope of Ω_f.

Third, there is a Fourier extraction of the proper mode. This can be done in two ways, as discussed in [Milani and Knežević, 1994]. Either the Fourier component with period $2\pi/g$ is extracted from the time series $(k(t), h(t))$;

or the component with period 2π is extracted from the data expressed as functions of ϖ_f, that is $(k(\varpi_f), h(\varpi_f))$. The result would be identical if the proper oscillation was a linear one, but for non negligible e the higher order terms are important [Milani and Knežević, 1990] and the latter algorithm leads to more stable proper elements.

The same applies to the inclination related plane, and the extraction of the component with period 2π can be extracted from $(q(\Omega_f), p(\Omega_f))$. The amplitudes of these proper modes are the proper elements e_p and $\tan(I_p/2)$; the latter one is then converted to the more usual $\sin I_p$.

This theory furnishes results of a superior accuracy with respect to the analytical theory, and it provides a straightforward way to estimate errors of all the proper values and for each asteroid included in the computation.

Stability of proper elements

One of the main advantages of the synthetic method is the availability of a stability test for each single set of proper elements computed in this way. To compute synthetic proper elements, a numerical integration over a long enough time interval $[0, T]$ has to be performed. Given the output, the same algorithms can be applied to shorter time intervals $[t_j, t_j + \Delta T]$, beginning at initial times $t_j, j = 1, \ldots, N$, in such a way that $t_1 = 0$,$t_N = T + \Delta T$. For each of these running boxes a value of the proper elements $a_p, e_p, \sin I_p$ and of the proper frequencies is obtained, and the dispersion of these N values can be used to estimate the stability in time of the results. The dispersion of the values of some proper element in different boxes can be measured by the root mean square of the differences of the values computed in each box with respect to the value computed over the entire time span and by the maximum difference among the values computed in all the boxes.

The results obtained [Knežević and Milani, 2000] can be better described by distinguishing the stable and unstable orbits. A large majority of initial conditions correspond to ostensibly regular orbits (at least over the tested time span), and for these the synthetic proper elements can be determined with very good accuracy and stability in time: e.g., in 76% of the cases e_p and $\sin I_p$ had standard deviations less than 0.001, and a_p less than 0.0003 au. In 55% of the cases the Root Mean Square (RMS) was even less than 0.0003 in e_p and less than 0.0001 in $\sin I_p$. The typical improvement with respect to the analytically derived proper elements is by a factor of more than 3. In terms of the so-called standard metrics [Zappala et al., 1990] used to define asteroid families, this would imply a typical error of the relative velocity of family members with respect to the parent body on the order of ≈ 5 m/s, while for the analytical results the order is ≈ 17 m/s.

Lyapounov exponents

A well known indicator of chaotic motion is the maximum Lyapounov Characteristic Exponent (LCE). Although the LCE is rigorously defined as a limit for $t \to \infty$, an indicator can be obtained by a finite integration of both the equation of motion and the corresponding variational equation. An approximation of the LCE can be computed as the best fit slope of the function of time $\gamma(t) = \log[D(t)/D(0)]$ where $D(t)$ is the length of a variation vector (with initial conditions selected at random). Renormalization of the variations vector needs to be applied when it becomes too large, to avoid numerical instability and overflow. This method typically allows the detection of a positive LCE after $7 - 8$ Lyapounov times T_L. The approximate values of the LCE computed in this way are reliable as order of magnitude, unless a real state transition between two chaotic regions takes place; the exact values are not very significant, changes by 20% are typical when the integration time span is extended.

As a matter of principle, the chaotic orbits are found in the Arnold web of resonances. In the N-body type problems, because of the degeneracy of the unperturbed Hamiltonian, the frequencies are split in well separated groups, short periods, secular, and intermediate. Intermediate periods can occur only by forming comparatively slow arguments of the form $h\lambda - k\lambda_P + \ldots$ where P refers to some major planet (in practice in the asteroid belt only Jupiter and Mars resonance matter), and the dots indicate secular arguments. As an alternative, so called three-body resonances have slow arguments of the form $h\lambda - k\lambda_J + j\lambda_S + \ldots$. These are second order terms, produced by the beat of two terms in the perturbing function which happen to have close periods.

The LCE indicators, computed with only the major planets as perturbers, are a detector of resonances involving the mean motions of the asteroid and of the planets.

2.3 Applications of the Yarkovsky effect

The Yarkovsky effect has multiple applications ranging from the physical properties of asteroids to the meteorite transport issues and the spreading of asteroid families.

Physical properties of asteroids

An asteroid's Yarkovsky drift can be used to probe some physical properties of the asteroid itself. The most important physical properties are the obliquity, the size and mass of the asteroids, but also the thermal and reflective properties and the rotation rate should also be taken into account.

The weakest situations are the ones in which we only know da/dt and the absolute magnitude H. Even in these cases we can put meaningful constraints on the obliquity, because the Yarkovsky drift if proportional to $\cos\gamma$, as explained in Chap. 3.

If the spin state of the body is known, then $\cos\gamma$ is not unknown and the thermal parameter Θ_ω is better constrained.

The diameter D can also be directly measured by radar or can be derived from an assumed distribution of asteroid albedo, or inferred from taxonomic type or measured albedo. The measurement of the diameter allows the constraints to be cast in terms of the bulk density ρ and the thermal inertia Γ.

The degeneracy between ρ and Γ can be broken in two different ways:

- An independent estimate of ρ would allow a direct estimate of Γ;
- An use of measurable solar radiation pressure deviations on the orbit yields an area-to-mass ratio. With a size estimate, an independent mass estimate can lead to a double solution for the thermal inertia of the body.

This second approach has been applied in few special cases: observations of an asteroid's thermal emission can afford independent constraint on the thermal inertia.

The best cases of the Yarkovsky detection allow us to have a shape model, spin state and thermophysical characterization, thus we can infer the local gravity of the body.

The asteroid (101955) Bennu (see Chap. 4) is the Near Earth Asteroid with the best measured Yarkovsky effect, and the porosity has been computed using the second approach, as previously discussed.

Impact hazard assessment

If an asteroid has a very precise orbit, the Yarkovsky effect is crucial for the analysis of the risk posed by potential impacts on Earth. When the Yarkovsky effect is directly measured by the astrometric data, the analysis approach is straightforward as in the case for (101955) Bennu (see Chap. 4).

There are some cases where the astrometry provides little or no constraints on the Yarkovsky effect, and yet the Yarkovsky drift is a major contributor to uncertainties at a potentially threatening Earth encounter. In these cases we have to assume a distributions on albedo, obliquity, thermal inertia, etc., and from these we derive a distribution of A_2 or da/dt. These distributions allow us to better represent uncertainties at the threatening Earth encounter, and to compute more realistic impact probabilities, as in the case for (410777) 2009 FD (see Chap. 5).

Meteorite transport

The meteoroids are precursors of meteorites, which are believed to be fragments of larger asteroids located in the main belt between the orbits of Mars and Jupiter. The Yarkovsky effect was proposed to be main element driving meteorites to the Earth (see [Öpik, 1951]). The problem is that direct transport from the main belt required very long timescales and unrealistic values of the thermal parameters and rotation rates for meter size bodies.

The problem has been overcome: the transport routes that connect main belt objects to planet-crossing orbits are secular and mean motion resonances with giant planets, such as ν_6 secular resonance at the lower border of the main asteroid belt and/or the 3/1 mean motion resonance with Jupiter. Then meteoroids or their immediate precursor objects are collisionally born in the inner and/or central parts of the main belt, from where they are transported to the resonances by the Yarkovsky effect. However, some of the precursors may fragment and produce new swarms of daughter meteoroids which eventually reach the escape routes to planet crossing orbits. This model explains the distribution of the cosmic-ray exposure ages of stony meteorites as a combination of several timescales:

- The time it takes a meteoroid to collisionally break;
- The time it takes a meteoroid to travel to a resonance;
- The time it takes for that resonance to deliver the meteoroid to an Earth-crossing orbit;
- The time it takes the meteoroid on a planet-crossing orbit to hit the Earth.

This model contains a number of assumptions and potentially weak elements. For instance, one of the difficulties in refining the meteorite delivery models is the uncertainty in identification of the ultimate parent asteroid for a given meteorite class.

Spreading of asteroid families

The orbits in the main asteroid belt are affected by deterministic chaos over long timescales. It is not possible to reliably reconstruct past values of the orbital secular angles, with the proper values of the semimajor axis a, eccentricity e and inclination I being the only well-defined parameters at hand. The explanation of the new techniques used to compute these proper elements is in Chap. 6. While the deterministic chaos is still in action over long timescales and produces in most cases a slow diffusion of the proper e and I, the Yarkovsky effect is the principal phenomenon that changes the

proper a values of multi-kilometer-size asteroids. Knežević and Milani [2003] studying the structure of the Vesta family, presented a clear example of the Yarkovsky effect sculpting a large-scale shape of an asteroid family.

A new method for the age-determination is presented in Chap. 7. The method is based on the fact that small asteroids in some families are pushed towards extreme values of the proper semimajor axis and, if plotted in the proper a *vs* $1/D$ (diameter) diagram, they acquire a V-shape (see 7). This peculiar structure must result from a long-term dynamical evolution of the family: the Yarkovsky drift itself accounted for most of the family's extension in semimajor axis. Assisted by the YORP effect, the Yarkovsky effect is maximized, and pushes small family members towards the extreme values in proper a.

Chapter 3

NEAs with measurable Yarkovsky effect

It is well known that nongravitational forces should be considered as important as collisions and gravitational perturbations for the overall understanding of asteroid evolution [Bottke et al., 2006]. The most important nongravitational perturbation is the Yarkovsky effect, which is due to radiative recoil of anisotropic thermal emission and causes asteroids to undergo a secular semimajor axis drift da/dt. Typical values of da/dt for sub-kilometer NEAs are 10^{-4}–10^{-3} au/Myr [Vokrouhlický et al., 2000b].

The Yarkovsky acceleration depends on several physical quantities such as spin state, size, mass, shape, and thermal properties [Vokrouhlický, 1999]. Furthermore, Rozitis and Green [2012] show that surface roughness also plays an important role by enhancing the Yarkovsky related semimajor axis drift by as much as tens of per cent. Though no complete physical characterization is typically available to compute the Yarkovsky acceleration based on a thermophysical model, the orbital drift may be detectable from an astrometric dataset. As a matter of fact, purely gravitational dynamics could result in an unsatisfactory orbital fit to the observational data. This is especially true when extremely accurate observations are available, e.g., radar observations, or when the observational dataset spans a long time interval thus allowing the orbital drift to accumulate and become detectable.

Until recently, the Yarkovsky effect has been measured directly only in three cases, (6489) Golevka [Chesley et al., 2003], (152563) 1992 BF [Vokrouhlický et al., 2008], and recently for (101955) Bennu [Chesley et al., 2012]. For both Golevka and (101955) Bennu the Yarkovsky perturbation must be included to fit accurate radar observations spanning three apparitions. For 1992 BF the Yarkovsky effect is needed to link 4 precovery observations of 1953. Furthermore, in the case of (101955) Bennu the available

physical characterization, along with the estimate of the Yarkovsky effect, allows the estimate of the asteroid's bulk density.

Nugent et al. [2012b] find 54 detections of semimajor axis drift by performing a search for semimajor axis drift among NEAs similar to the one presented in this paper. However, there are differences in the observational data treatment, in the modeling, and in the selection filters. A description of the differences and a comparison of the results is provided in Sec. 3.2.2. Nugent et al. [2012a] use WISE-derived geometric albedos and diameters to predict orbital drifts for 540 NEAs. Even if none of these objects has an observational record that allows one to measure the predicted orbital drift, the authors list upcoming observing opportunities that may reveal the Yarkovsky signal.

The Yarkovsky effect plays an important role for orbital predictions such as those concerning Earth impacts. In particular, when an asteroid has an exceptionally well constrained orbit, the Yarkovsky effect may become the principal source of uncertainty. Milani et al. [2009] show how the size of the semimajor axis drift along with its uncertainty modifies impact predictions for the next century for (101955) Bennu. The cumulative impact probability is approximately 10^{-3}, while a Yarkovsky-free propagation would rule out any impact event. Chesley et al. [2012] improve the da/dt estimate by means of September 2011 Arecibo radar measurements and find a cumulative impact probability approximately 4×10^{-4}. Another remarkable case is (99942) Apophis. Though only a marginal da/dt estimate is available, Giorgini et al. [2008] and Chesley et al. [2009] prove that the occurrence of an impact in 2036 is decisively driven by the magnitude of the Yarkovsky effect. In the longer term, Giorgini et al. [2002] show that an impact between asteroid (29075) 1950 DA and the Earth in 2880 depends on the accelerations arising from thermal re-radiation of solar energy absorbed by the asteroid.

3.1 Methodology

3.1.1 Yarkovsky modeling and determination

The Yarkovsky effect depends on typically unknown physical quantities. As the primary manifestation is a semimajor axis drift, we seek a formulation depending on a single parameter to be determined simultaneously with the orbital elements from the observational dataset. To bypass the need of physical characterization we used a comet-like model [Marsden et al., 1973] for transverse acceleration $a_t = A_2 g(r)$, where g is a suitable function of the heliocentric distance r and A_2 is an unknown parameter.

For a given A_2 we estimate semimajor axis drift by means of Gauss' perturbative equations:

$$\dot{a} = \frac{2a\sqrt{1-e^2}}{nr} A_2 g(r) \tag{3.1}$$

where a is the semimajor axis, e is the eccentricity and n is the mean motion. By averaging we obtain

$$\bar{\dot{a}} = \frac{a\sqrt{1-e^2}A_2}{\pi} \int_0^T \frac{g(r)}{r} dt = \frac{A_2}{\pi n a} \int_0^{2\pi} r g(r) df \tag{3.2}$$

where T is the orbital period and f is the true anomaly. Let us now assume $g(r) = (r_0/r)^d$, where r_0 is a normalizing parameter, e.g., we use $r_0 = 1$ au. In this case the semimajor axis drift is

$$\bar{\dot{a}} = \frac{A_2(1-e^2)}{\pi n} \left(\frac{r_0}{p}\right)^d \int_0^{2\pi} (1 + e\cos f)^{d-1} df \ . \tag{3.3}$$

By Taylor expansion, we have

$$\int_0^{2\pi} (1 + e\cos f)^{d-1} df = \sum_{k=0}^{\infty} \binom{d-1}{k} e^k \int_0^{2\pi} \cos^k f df \ . \tag{3.4}$$

The odd powers of the cosine average out, so we obtain

$$\bar{\dot{a}} = \frac{2A_2(1-e^2)}{n} \left(\frac{r_0}{p}\right)^d J(e,d) \tag{3.5}$$

where

$$J(e,d) = \sum_{k=0}^{\infty} \alpha_k e^{2k} \quad , \quad \alpha_k = \binom{d-1}{2k} \binom{2k}{k} \frac{1}{2^{2k}} \ . \tag{3.6}$$

The ratio

$$\frac{\alpha_{k+1}}{\alpha_k} = \left(1 - \frac{d+1}{2k+2}\right)\left(1 - \frac{d}{2k+2}\right) \tag{3.7}$$

is smaller than 1 for $d > 0$ and k large enough. Therefore, α_k are bounded and $J(e,d)$ is convergent for any $e < 1$. Equation (3.7) can be used to recursively compute α_k starting from $\alpha_0 = 1$. For integer d the series J is a finite sum that can be computed analytically, e.g., $J(e,2) = 1$ and $J(e,3) = 1 + 0.5e^2$.

For a fixed d we have a transverse acceleration $a_t = A_2(r_0/r)^d$. To determine A_2 we used a 7-dimensional differential corrector: starting from the observational dataset we simultaneously determine a best-fitting solution for

both the orbital elements and A_2 along with an associated covariance matrix C describing the uncertainty of the nominal solution. The marginal uncertainty of A_2 is obtained from C: $\sigma_{A_2} = \sqrt{c_{77}}$, where c_{ij} is the generic element of C. This uncertainty is then mapped to the uncertainty of the semimajor axis drift by means of Eq. (3.5).

The proper value of d is not easily determined. From Vokrouhlický [1998a], we have

$$a_t \simeq \frac{4(1-A)}{9}\Phi(r) f(\Theta)\cos\gamma \quad , \quad f(\Theta) = \frac{0.5\Theta}{1+\Theta+0.5\Theta^2} \tag{3.8}$$

for the Yarkovsky diurnal component (which is typically dominant), where A is the Bond albedo, Θ is the thermal parameter, γ is the obliquity, and $\Phi(r)$ is the standard radiation force factor, which is inversely proportional to the bulk density ρ, the diameter D, and r^2. The thermal parameter Θ is related to the thermal inertia Γ by means of the following equation

$$\Theta = \frac{\Gamma}{\varepsilon\sigma T_*^3}\sqrt{\frac{2\pi}{P}} \tag{3.9}$$

where ε is the emissivity, σ is the Boltzmann's constant, T_* is the subsolar temperature, and P is the rotation period. In this paper we use $d = 2$ to match the level of absorbed solar radiation. Then, from Eq. (3.8) we have that

$$A_2 \simeq \frac{4(1-A)}{9}\Phi(1\text{au}) f(\Theta)\cos\gamma \ . \tag{3.10}$$

However, as $T_* \propto r^{-0.5}$ we have that $\Theta \propto r^{1.5}$, therefore the best value of d depends on the object's thermal properties:

- for $\Theta \gg 1$ we obtain $f \propto r^{-1.5}$, which gives $d = 3.5$;
- for $\Theta \ll 1$ we obtain $f \propto r^{1.5}$, which gives $d = 0.5$.

These are limit cases, the true d is always going to be between them. As a matter of fact, it turns out that most NEAs, whose rotation period is not excessively large and whose surface thermal inertia is not excessively small or large, have typically values of Θ near unity or only slightly larger, and we can thus expect d value in the range 2–3. As an example, Chesley et al. [2012] show that for (101955) Bennu the best match to the Yarkovsky perturbation computed by using a linear heat diffusion model is $d = 2.75$.

What matters to us is that da/dt does not critically depend on the chosen value of d. As an example for asteroid (101955) Bennu we have that $da/dt = (-18.99 \pm 0.10) \times 10^{-4}$ au/Myr for $d = 2$ and $da/dt = (-19.02 \pm 0.10) \times 10^{-4}$

Table 3.1: Gravitational parameters of perturbing asteroids. The masses of Ceres, Pallas, and Vesta are from Standish and Hellings [1989], the ones of Euphrosyne and Herculina are from the Institute of Applied Astronomy of RAS, St. Petersburg, Russia (http://www.ipa.nw.ru/PAGE/DEPFUND/LSBSS/engmasses.htm), the mass of Juno is from Konopliv et al. [2011], all the others are from Baer et al. [2011a].

Asteroid	Gm [km^3/s^2]
(1) Ceres	63.200
(2) Pallas	14.300
(4) Vesta	17.800
(10) Hygea	6.0250
(29) Amphitrite	1.3271
(511) Davida	3.9548
(65) Cybele	1.0086
(9) Metis	1.3669
(15) Eunomia	2.2295
(31) Euphrosyne	1.1280
(52) Europa	1.2952
(704) Interamnia	4.7510
(16) Psyche	1.7120
(3) Juno	1.9774
(532) Herculina	1.5262
(87) Sylvia	1.3138

au/Myr for $d = 3$. Another example is Golevka, for which we obtain $da/dt = (-6.62 \pm 0.64) \times 10^{-4}$ au/Myr for $d = 2$ and $da/dt = (-6.87 \pm 0.66) \times 10^{-4}$ au/Myr for $d = 3$. In both cases the difference in da/dt due to the different values assumed for d is well within one standard deviation.

3.1.2 Dynamical model

To consistently detect the Yarkovsky effect we need to account for the other accelerations down to the same order of magnitude. For a sub-kilometer NEA, typical values of a_t range from 10^{-15} to 10^{-13}au/d^2.

Our N-body model includes the Newtonian accelerations of the Sun, eight planets, the Moon, and Pluto that are based on JPL's DE405 planetary ephemerides [Standish, 2000]. Furthermore, we added the contribution of 16 massive asteroids, as listed in Table 3.1.

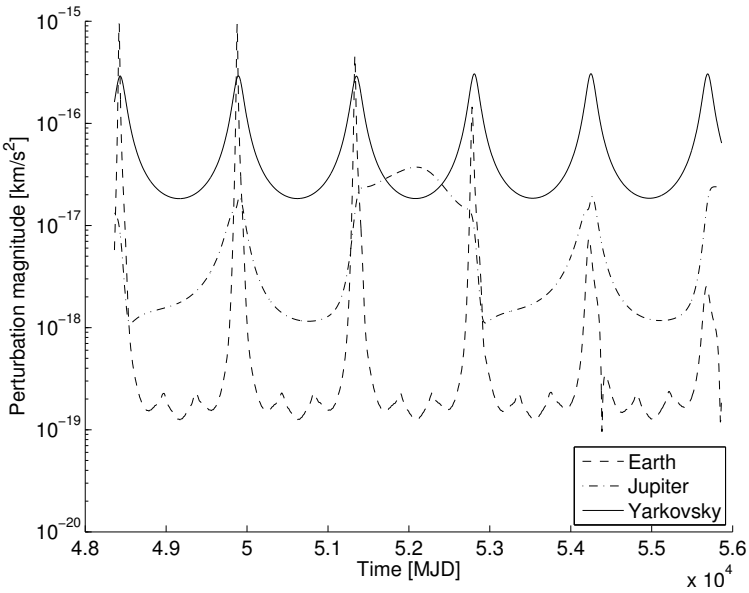

Figure 3.1: Relativistic accelerations of the Earth and Jupiter as they formallyappear in the EIH equations of motion compared to the transverse Yarkovsky acceleration acting on Golevka.

We used a relativistic force model including the contribution of the Sun, the planets, and the Moon. Namely, we used the Einstein-Infeld-Hoffman (EIH) approximation as described in Moyer [2003] or Will [1993]. As already noted in Chesley et al. [2012], the relativistic term of the Earth should not be neglected because of significant short range effects during Earth approaches that NEAs may experience. For asteroids with a large perihelion distance such as Golevka also Jupiter's term could be relevant. Figure 3.1 compares the relativistic accelerations of the Earth and Jupiter as they formally appear in the EIH equations of motion to the transverse Yarkovsky acceleration acting on Golevka.

3.1.3 Observational error model

The successful detection of the Yarkovsky effect as a result of the orbital fit strongly depends on the quality of the observations involved. In particular, the availability of radar data is often decisive due to the superior relative accuracy of radar data with respect to optical ones. Moreover, radar measurements are orthogonal to optical observations: range and range rate vs. angular position in the sky.

Since the Yarkovsky effect acts as a secular drift on semimajor axis we

have a quadratic effect in mean anomaly: the longer the time span the stronger the signal. However, the presence of biases in historical data and unrealistic weighting of observations may lead to inaccurate results. To deal with this problem we applied the debiasing and weighting scheme described in Chesley et al. [2010]. This scheme is a valid error model for CCD observations, while for pre-CCD data the lack of star catalog information and the very uneven quality of the observations represents a critical problem. In these cases the occurrence of unrealistic nominal values for Yarkovsky model parameters presumably point to bad astrometric treatments and have to be rejected.

To prevent outliers from spoiling orbital fits, we applied the outlier rejection procedure as described in Carpino et al. [2003].

Besides the astrometric treatment described above, in the following cases we applied an ad hoc observation weighting:

- (101955) Bennu: as already explained by Chesley et al. [2012], in some cases there are batches containing an excess of observations from a single observatory in a single night. In particular there are four nights, each with about 30 observations from observatory La Palma. To reduce the effect of these batches to a preferred contribution of 5 observations per night, we relaxed the weight by a factor $\sqrt{N/5}$, where N is the number of observations contained in the batch.

- 1992 BF: as the precovery observations of 1953 have been carefully remeasured in Vokrouhlický et al. [2008], these observations were given a weight at 0.5" in right ascension and 1" in declination.

- Apollo: the large dataset available for Apollo contains observations going back to 1930. Many pre-CCD era observation batches show unusually high residuals, especially during close Earth approches. To lower the effect of non-CCD observation, we used weights at 10" for observations from 1930 to 1950 and 3" from 1950 to 1990. By using weights at 10" we made sure we included all non-CCD observations, thus reducing the average error and avoiding to fit a possibly inaccurate subset only.

- 1989 ML: the discovery apparition contains observations from Palomar Mountain showing large residuals whether or not the Yarkovsky perturbation is included in the model. Even if this apparition increases the observed arc by three years only, we felt it safer to weight the corresponding observations at 3".

3.1.4 Treatment of precovery observations

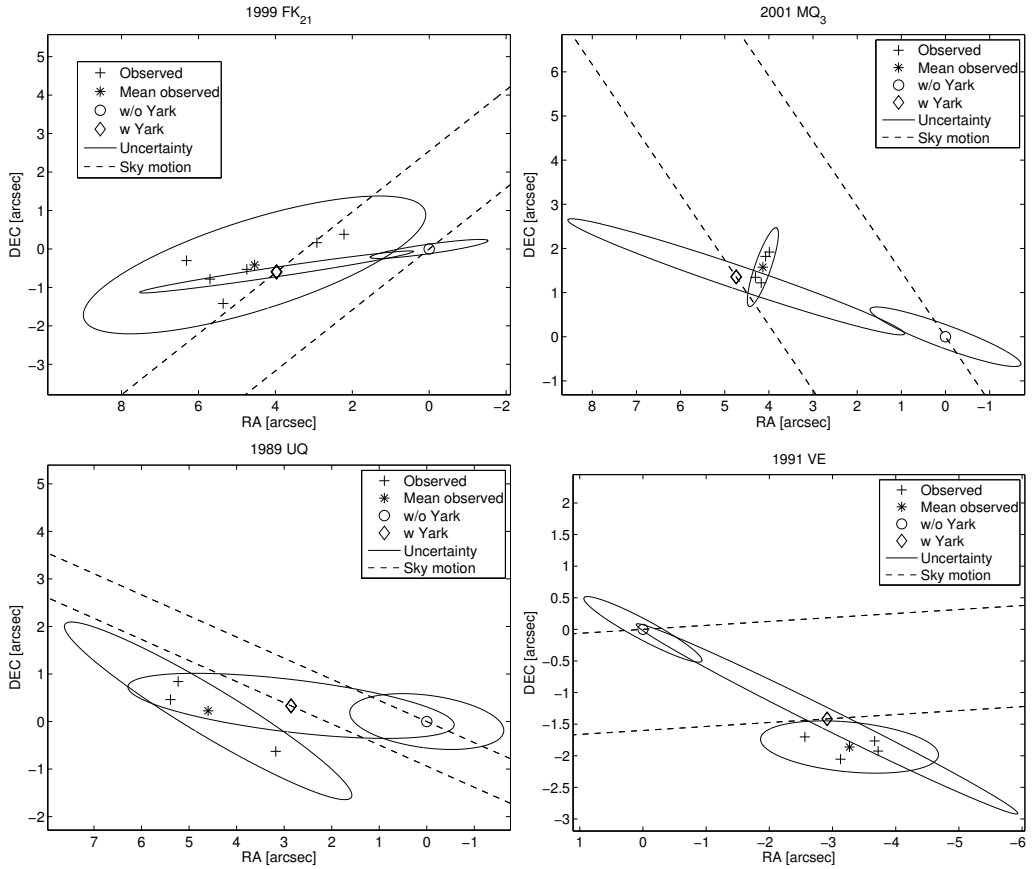

Figure 3.2: Observed position, average observed position, and predicted post-fit position both with and without the Yarkovsky perturbation in the dynamics. The uncertainty ellipses for the mean observed position and the predicted positions correspond to the 3-σ level. The dashed lines represent the predicted motion in the sky of the asteroid in the precovery apparition. Circles are the predicted positions, crosses are the measured positions, stars are the mean of the measured positions, while diamonds are the predicted positions when the Yarkovsky perturbation is included in the dynamics. The origin is arbitrarily set to the non-Yarkovsky prediction.

There are a few cases where the Yarkovsky signal is mainly contained in few isolated precovery observations. This is the case of the already mentioned asteroid 1992 BF, which has 4 isolated observations in 1953 from Palomar Mountain DSS. Other cases are

- 1999 FK_{21}, which has 6 isolated observations in 1971 from Palomar

Mountain;

- 2001 MQ_3, which has 4 isolated observations in 1951 from Palomar Mountain DSS;
- 1989 UQ, which has 3 isolated observations in 1954 from Palomar Mountain;
- 1991 VE, which has 4 isolated observations in 1954 from Palomar Mountain DSS.

For all these cases it would be desirable to remeasure the precovery observations as done for 1992 BF in Vokrouhlický et al. [2008], where precovery observations were corrected by an amount of up to 3.1". For this reason we conservatively gave weights at 3" to the precovery observations of the four asteroids above.

Besides the conservative weighting, we ruled out clock error as a possible cause of the Yarkovsky signal. Figure 3.2 shows the scenario for the four mentioned asteroids during the precovery apparition. We can see that it is not possible to match the observations by translating the non-Yarkovsky uncertainty ellipse on the along track direction. The Yarkovsky solution produces a shift in the weak direction that give a better match to the observations, in particular when we take the average of the observed positions.

3.1.5 Filtering spurious results

To assess the reliability of the Yarkovsky detections we computed an expected value for A_2 starting from the (101955) Bennu case, which is the strongest and most reliable detection, by scaling according to (3.10)

$$(A_2)_{exp} = (A_2)_{RQ36} \frac{D_{RQ36}}{D} \ . \tag{3.11}$$

For diameter D we used either the known value when available or an assumed value computed from the absolute magnitude H according to the following relationship [Pravec and Harris, 2007]:

$$D = 1329 \text{ km } \times \frac{10^{-0.2H}}{\sqrt{p_V}} \tag{3.12}$$

where p_V is the albedo, assumed to be 0.154 if unknown, in agreement with Chesley et al. [2002].

Some physical properties of (101955) Bennu maximize A_2 [Chesley et al., 2012]. In particular γ is nearly 180°, A is 0.01, and ρ is low (0.96 g/cm^3).

On the other hand $\Theta = 4.33$ for which $f(\Theta) \simeq 0.15$ while the maximum is $\simeq 0.21$. For these reasons we selected those Yarkovsky detections for which $\mathcal{S} = |A_2/(A_2)_{exp}|$ was smaller than 1.5. The selected threshold allows some tolerance as we are scaling only by D without accounting for other quantities such as bulk density, thermal properties, obliquity, spin rate, and surface roughness.

A high signal to noise ratio $\mathrm{SNR} = |A_2|/\sigma_{A_2}$ threshold is likely to produce robust detections with respect to the astrometric data treatment. With lower SNR the sensitivity to the observation error model increases and detections become less reliable. We decided that 3 was a sensible choice for minimum SNR, even if we analyze detections with smaller SNR in Sec. 3.2.3.

3.2 Results

We applied our 7-dimensional differential corrector to determine the parameter A_2 and the corresponding da/dt for all known NEAs. After applying the filters discussed in Sec. 3.1.5 we obtain 21 Yarkovsky detections that we consider reliable (Table 3.2). The reported uncertainties are marginal, i.e., they fully take into account the correlation between A_2 (and thus da/dt) and the orbital elements.

We cross-checked these detections by using two independent software suites: the JPL Comet and Asteroid Orbit Determination Package and OrbFit (http://adams.dm.unipi.it/orbfit/)[1]: in all cases we found agreement at better than the 1-σ level.

3.2.1 2009 BD

Despite the short observed arc, asteroid 2009 BD has a quite accurate orbit, e.g., the semimajor axis uncertainty of 5×10^{-8} au. The observational dataset contains some observation rejected as outliers from the Mauna Kea observatory. Micheli et al. [2012] show that including solar radiation pressure allows an improvement in the fit to the observations and the recovery of Mauna Kea observations. Therefore, we also included in the model a radial acceleration $a_r = A_1/r^2$. Along with the tabulated value of A_2, we obtained $A_1 = (62.05 \pm 8.85) \times 10^{-12}$ au/d^2. This results in an area to mass ratio $A/M = (2.72 \pm 0.39) \times 10^{-4}$ m^2/kg, which is consistent at the 1-σ level with the value reported by Micheli et al. [2012], i.e., $(2.97 \pm 0.33) \times 10^{-4}$ m^2/kg.

[1] OrbFit was used in the development version 4.3, currently in beta-testing.

After including A_1 and A_2 in the orbital solution, the uncertainty in semimajor axis is about 4.3×10^{-8} au, which is significantly smaller than the product between the detected semimajor axis drift and the observed arc time interval, i.e., 1.5×10^{-7} au.

The value of A_2 seems quite large, but it is consistent with the expected size of this object. From the absolute magnitude $H = 28.2$ we obtain an estimated diameter of 8 m and the parameter $\mathcal{S}$ computed accordingly is 0.4.

3.2.2 Comparison with other published results

The first three objects of Table 3.2 are the already known cases of Golevka, 1992 BF, and (101955) Bennu. While for (101955) Bennu there is a perfect match between our result and the one in Chesley et al. [2012], for Golevka and 1992 BF the values are different from Chesley et al. [2003] and Vokrouhlický et al. [2008], respectively. However, this can be easily explained by the availability of new astrometry and the fact that the present paper adopted the debiasing and weighting scheme by Chesley et al. [2010], which was not available at the time of the earlier publications.

As already mentioned, Nugent et al. [2012b] performed a search similar to the one presented in this paper and found 54 NEAs with a measurable semimajor axis drift. The main differences are the following:

- They selected only numbered objects, while we included all known NEAs.

- Their observation dataset was slightly different as they used observations until 2012 January 31, while we have data until 2012 October 31. This difference does not really matter for optical data, but it does for radar data, e.g., for Aten and Toro. Moreover, they did not use single apparition radar observations, while we did as we think they represent an important constraint.

- They solved for constant da/dt while we used constant A_2 and then convert to da/dt. These techniques are equivalent when the semimajor axis and eccentricity are constant, but there could be differences as we cannot assume da/dt constant for objects experiencing deep planetary close approaches. However, the error due to close encounter is generally smaller than the da/dt standard deviation.

- They searched for the best-fit da/dt by means of the golden section algorithm, i.e., they computed the RMS of the residuals corresponding to the best fitting orbital elements for fixed values of da/dt, then

the minimum is obtained by interpolation. In this paper we used a full 7-dimensional differential corrector. The two methods should be equivalent.

- They used 1 as lower bound for SNR, while we use 3 that gives detections more robust against changes in the observation weighting. Also, they used the "sensitivity" parameter, i.e., a metric to measure the sensitivity of a dataset to the presence of a semimajor axis drift. We did not use such a metric as we think that an SNR$\geq$ 3 is already a good metric in that respect.

- We kept only those objects for which the measured orbital drift can be related to the Yarkovsky perturbation presuming that inconsistencies stem from astrometric errors, while they also considered the possibility of other nongravitational effects such as a loss of mass.

Table 3.2 contains a comparison between our orbital drifts and the ones reported by Nugent et al. [2012b]. 2009 BD, 1999 MN, and 2005 ES_{70} are present only in our list as they are not numbered, while 2001 MQ_3, 1989 UQ, 1991 VE, and Illapa are eliminated by their filters. It is worth pointing out that also (101955) Bennu, Golevka, and YORP have been filtered out by Nugent et al. [2012b] criteria, even though they report the corresponding detections for a comparison with Chesley et al. [2008]. This is likely to be due to the lack of radar information in the computation of the sensitivity parameter.

Among the cases that Nugent et al. [2012b] report with SNR > 3 we did not include the following three:

- (1036) Ganymed for which we found $A_2 = (-16.54 \pm 4.35) \times 10^{-15}$ au/d^2, corresponding to $da/dt = (-6.06 \pm 1.59) \times 10^{-4}$ au/Myr. However, the nominal A_2 is 28 times larger than $(A_2)_{exp}$, so we marked this detection as spurious. As Ganymed observations go back to 1924, this unreliable detection might be due to bad quality astrometry.

- (4197) 1982 TA for which we used the radar apparition of 1996, which reduced the SNR below 1. For this object we found $A_2 = (5.61 \pm 14.26) \times 10^{-15}$ au/d^2, corresponding to $da/dt = (3.88 \pm 9.86) \times 10^{-4}$ au/Myr. For comparison Nugent et al. [2012b] report $da/dt = (30.9 \pm 9.2) \times 10^{-4}$ au/Myr.

- (154330) 2002 VX_4 for which we found $A_2 = (102.36 \pm 36.34) \times 10^{-15}$ au/d^2, corresponding to $da/dt = (43.10 \pm 15.25) \times 10^{-4}$ au/Myr. Again, the value of A_2 was ~ 4 times larger than $(A_2)_{exp}$, so also this detection was marked as spurious.

Besides the differences outlined above, there is an overall agreement for the common cases. As a matter of fact by computing the σ of the difference, i.e., $\sigma^2 = \sigma_1^2 + \sigma_2^2$, there are only two cases that are not consistent at the 1-σ level:

- 1992 BF, for which we applied suitable weights (see Sec. 3.1.3) for the remeasured observations [Vokrouhlický et al., 2008] of the 1953 apparition. By using the Chesley et al. [2010] standard weights the uncertainty in da/dt of our detection increases to 0.97×10^{-4} au/Myr, and therefore we are consistent with Nugent et al. [2012b] at the 1-σ level.
- Apollo, for which we applied a suitable manual weighting as described in Sec. 3.1.3.

3.2.3 Lower SNR and small orbital drifts

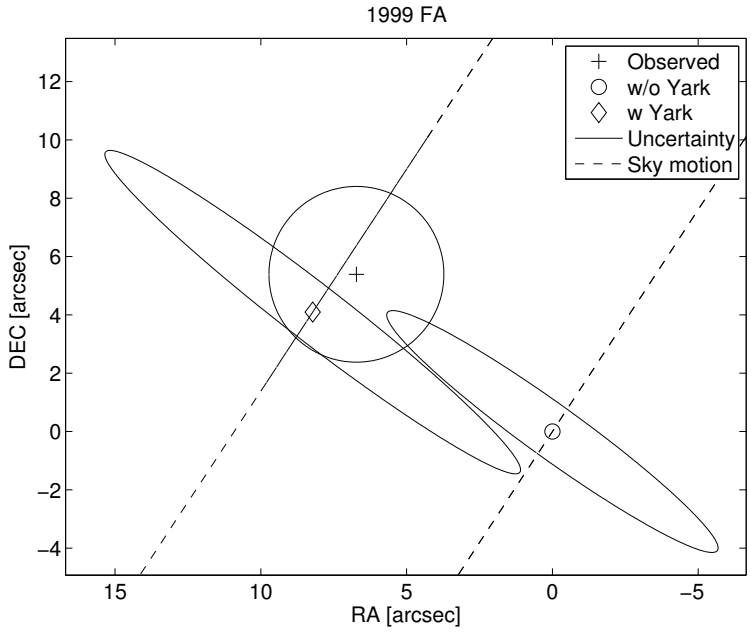

Figure 3.3: Same of Fig. 3.2 for asteroid 1999 FA. The uncertainty ellipses for predicted positions correspond to 3-σ levels, while the uncertainty for the observed position corresponds to 3".

Table 3.3 contains detections that we rate as non-spurious on the basis of the $\mathcal{S}$ ratio between expected and measured value, down to SNR = 2 plus the following remarkable cases:

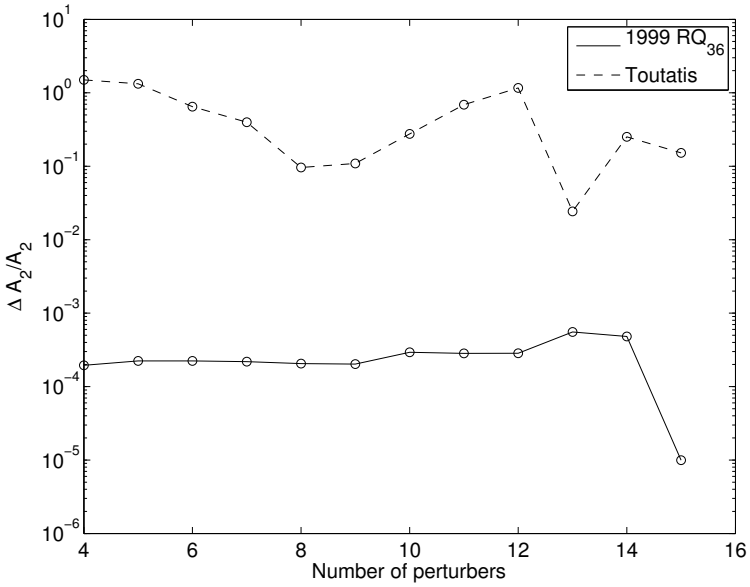

Figure 3.4: Relative displacement of A_2 with respect to the nominal value as a function of the number of perturbers for (101955) Bennu and (4179) Toutatis.

- 1999 FA, which has 1 isolated observation in 1978 from Siding Spring Observatory. By performing the same analysis of Sec. 3.1.4 (see Fig. 3.3) we see no clear improvement due to Yarkovsky as the observation is 3.5–4 σ away from the prediction either way. In this case a clock error may bring the Yarkovsky solution close to the observation. As this detection depends on a lone, isolated observation we would rather be cautious and consider this detection reliable only if the 1978 observation is remeasured.

- Eros, which looks like a reliable detection as $\mathcal{S} = 0.75$. However, the obliquity is known to be 89° [Yeomans et al., 2000] and then we enter the regime where the seasonal component of the Yarkovsky effect is dominant. As the seasonal component is typically 10 times smaller then the diurnal one [Vokrouhlický et al., 2000b] we mark this detection as spurious. This points to possible bad astrometric treatment, especially for historical observations dating back to 1893.

- Toutatis, which enters the Main Belt region because of the 4.12 au aphelion and the low inclination (0.44°). Therefore, it is important to account for the uncertainty in the masses of the perturbing asteroids. By taking into account the uncertainty of the perturbing asteroid

masses the actual uncertainty in A_2 increases by 11% with a commensurable drop in SNR. Figure 3.4 shows the evolution of A_2 as a function of the number of perturbers for asteroids (101955) Bennu and Toutatis. While for (101955) Bennu (aphelion 1.36 au) we reach convergence with just four perturbers, for Toutatis we have a quite irregular behavior suggesting that we may need to include more perturbers.

- 1994 XL_1, whose observations in 1994 from Siding Spring Observatory show high residual so we relaxed weights at 3".
- 2005 QC_5 and 2000 NL_{10} have been included despite the low SNR. Similarly to the cases described in Sec. 3.1.4, we applied weights at 3" to precovery observations and this data treatment weakened the Yarkovsky detection. However, we think that remeasuring the precovery observations may lead to reliable Yarkovsky detections for these objects.
- 1950 DA, for which the Yarkovsky effect plays an important role for impact predictions, e.g., see Sec. 3.3.4.

There are other objects with an even lower SNR for which the Yarkovsky signal might be revealed if precovery observations were remeasured: (11284) Belenus, (66400) 1999 LT_7, (4688) 1980 WF, (67399) 2000 PJ_6, (267759) 2003 MC_7, and (88710) 2001 SL_9.

Though these detections have to be considered less reliable, some of them may be good candidates for becoming stronger detections in the future if high quality astrometry is obtained, e.g., by radar or Gaia [Mignard, 2003].

The results presented so far do not capture those cases for which the orbital drift truly is small. In fact, when $da/dt \sim 0$ the SNR is unlikely to be greater than 1. Table 3.4 contains detections with SNR < 2 such that

$$\frac{|(A_2)_{exp}| - |A_2|}{\sigma_{A_2}} > 3 \ . \tag{3.13}$$

This inequality ensures that the possible magnitude of the Yarkovsky effect is significantly smaller (3-σ level) than expected. In particular, for Icarus we obtain a strong constraint on A_2 and thus da/dt, which is consistent with Vokrouhlický et al. [2000b, Fig. 5] where $|da/dt| < 3 \times 10^{-4}$ au/Myr. These cases are interesting as they might be an indication of obliquities near 90° (e.g., Icarus' obliquity is 103°), excessively slow rotations, high bulk density, or small thermal inertias.

3.3 Discussion

3.3.1 Connection with NEA feeding mechanisms

The diurnal Yarkovsky effect produces a semimajor axis drift proportional to $\cos\gamma$ [Vokrouhlický et al., 2000b]. As the diurnal term is typically the dominant one, the sign of da/dt can be related to the asteroid spin orientation, i.e., a negative da/dt corresponds to a retrograde rotator while a positive da/dt corresponds to a prograde rotator. This conclusion is supported by the eight known obliquities for the asteroids in the sample that are listed in Table 3.2: in all cases the spin axis obliquity is consistent with the sign of da/dt.

We can now use this interpretation and our solution for the Yarkovsky semimajor axis drift values for NEAs in the following way. Table 3.2 contains four prograde rotators and seventeen retrograde rotators. This excess of retrograde rotators can be explained by the nature of resonance feeding into the inner Solar System [Bottke et al., 2002a]. Most of the primary NEA source regions (e.g., the 3:1 resonance, JFCs, Outer Belt, etc.) allow main belt asteroids to enter by drifting either inwards or outwards, but the ν_6 resonance is at the inner edge of the main belt and so asteroids can generally enter only by inwards drift, i.e., with retrograde rotation. Bottke et al. [2002a] report that 37% of NEAs with absolute magnitude $H < 22$ arrive via ν_6 resonance. La Spina et al. [2004] point out that this implies 37% of NEAs have retrograde spin (via ν_6), plus half of the complement (via other pathways). Thus, the retrograde fraction should be $0.37 + 0.5 \times 0.63 = 0.69$, while La Spina et al. [2004] report 67% retrograde for their sample, which is dominated by large NEAs.

Table 3.2 contains 81% retrograde rotators, which is larger than 69% and thus, at face value, appears to be inconsistent with the theory. The sample of asteroids shown in Table 3.2, however, is based on measured Yarkovsky mobility and is not a representative sample of the debiased NEA population as described by Bottke et al. [2002a]. For example, the sample is dominated by small PHAs (MOID < 0.05 AU) on fairly deep Earth-crossing orbits. We find that 9 of the 21 objects are Aten asteroids (43%), compared to the 6% fraction predicted for the debiased NEA population. Bottke et al. [2002a] suggest that the majority of Atens ($\sim 79\%$) should come from the innermost region of the main belt where the ν_6 resonance is located. That would indicate the sampled objects are predisposed to have retrograde spin vectors.

To further quantify this, we used the debiased NEA model from Bottke et al. [2002a] to determine the probability that the objects in Table 3.2 came

from one of five intermediate source regions: the ν_6 secular resonance, the intermediate source Mars-crossing region (MC), the 3:1 mean motion resonance with Jupiter, the outer main belt (OB), and the transneptunian disk (which provides active and inactive Jupiter-family comets, JFC). Our results are shown in Table 3.5. Next, we multiplied these values by a second set of probabilities corresponding to whether a given intermediate source would produce NEAs with prograde or retrograde spin vectors. Here we assumed the ν_6 resonance would only produce NEAs with retrograde spin vectors, while the other sources would provide a 50-50 mix of objects with prograde and retrograde spin vectors. Adding these probabilities together and normalizing by the number of objects in our sample, we predict that 79.3% of the objects in Table 3.2 should have retrograde spins. We therefore find an excellent match to the $81\% \pm 8\%$ value provided by observations.

Asteroid 1999 MN represents a mismatch to the assumption that the ν_6 resonance produce NEAs with retrograde spin only. However, 1999 MN has a very peculiar orbit as it might have been evolving in the planet-crossing space for more than 50 Myr. During this time various things might have occurred, including a situation that the spin went over the end of a YORP cycle. Moreover, this body is a prime candidate for being affected by tidal forces during a close planetary encounter (i.e., high eccentricity Aten with low inclination). As a matter of fact, Hicks et al. [2010] already suggested the possibility of YORP and/or tidal spin-up. From its orbit, 1999 MN has a very high probability of encountering both Earth and Venus.

To assess the behavior of the fraction of retrograde rotators as a function of the SNR, we took all of the objects with $\mathcal{S} < 1.5$. The left panel of Fig. 3.5 shows the distribution of A_2 and its uncertainty. The excess of retrograde rotators is clearly visible for SNR > 3 and also between 2 and 3, where small PHAs dominate. For lower SNR we have a more uniform distribution. The right panel of Fig. 3.5 is a running mean of the fraction of retrograde rotators as a function of the SNR. For SNR < 1 (372 objects) we are in a noise dominated regime for which we have a rough 50% fraction of retrograde rotators, for $1 <$ SNR < 2 (51 objects) we have a transition from noise-dominated to signal dominated, and for SNR > 2 (43 objects) we have a signal dominated regime with around 80% retrograde rotators.

We can also try to use the detected values to infer the obliquity distribution. From Eq. (3.10) we have that

$$A_2 \propto \frac{\cos\gamma}{D}. \tag{3.14}$$

and so we can estimate γ by using the either known or estimated by Eq. (3.12) diameter and using (101955) Bennu. By taking both the detections with

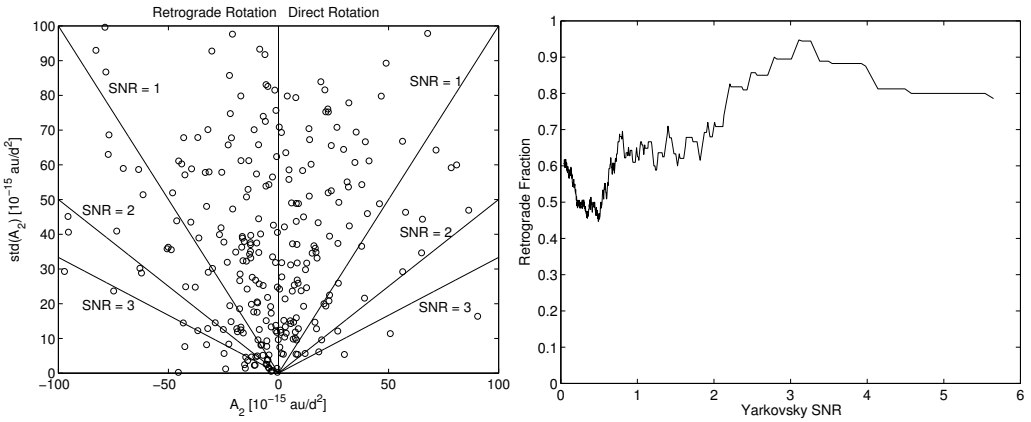

Figure 3.5: Left panel: distribution of A_2 and its uncertainty. Right side of plot is prograde rotation and left side is retrograde rotation. Right panel: running box mean in SNR for the fraction of asteroids with indication of retrograde spin. Cases with SNR > 2 show a consistent 4:1 retrograde ratio, cases with little or no signal are split 50–50.

SNR > 1 and those satisfying Eq. (3.13) with 1 as right hand side, and assuming a fixed $\rho = 1500$ kg/m^3 we obtain the distribution of Fig. 3.6, where the cases with $|\cos\gamma| > 1$ have been placed in the extreme obliquity bins. For the detections with SNR < 1 the nominal value of A_2 is not very reliable, so we added a random component corresponding to σ_{A_2}. Despite the low number of bins, we can see the excess of retrograde rotators and the abundance of objects with an extreme obliquity, as expected from the YORP effect [Čapek and Vokrouhlický, 2004]. While this distribution should be considered only approximate due to the numerous assumptions (e.g., neglecting dependence on bulk density, shape and thermal properties) we consider it to be a significant improvement over what is otherwise known. However, we find it interesting that it appears to be consistent with the observed obliquity distribution of the NEAs [La Spina et al., 2004].

3.3.2 Spurious detections

Our search for Yarkovsky signal produced a large number of spurious detections, i.e., semimajor axis drifts far larger than the Yarkovsky effect would cause. Figure 3.7 contains the histograms of $\mathcal{S}$ for different SNR intervals. For SNR > 3 we have 67% spurious detections, for $2 <$ SNR < 3 we have 88%.

It is worth trying to understand the reason of these spurious solutions.

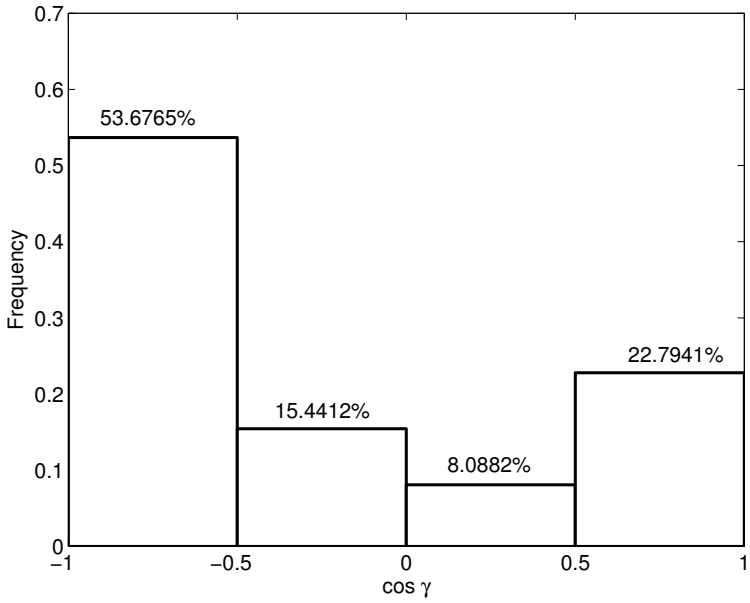

Figure 3.6: Inferred obliquity distribution based on 136 objects.

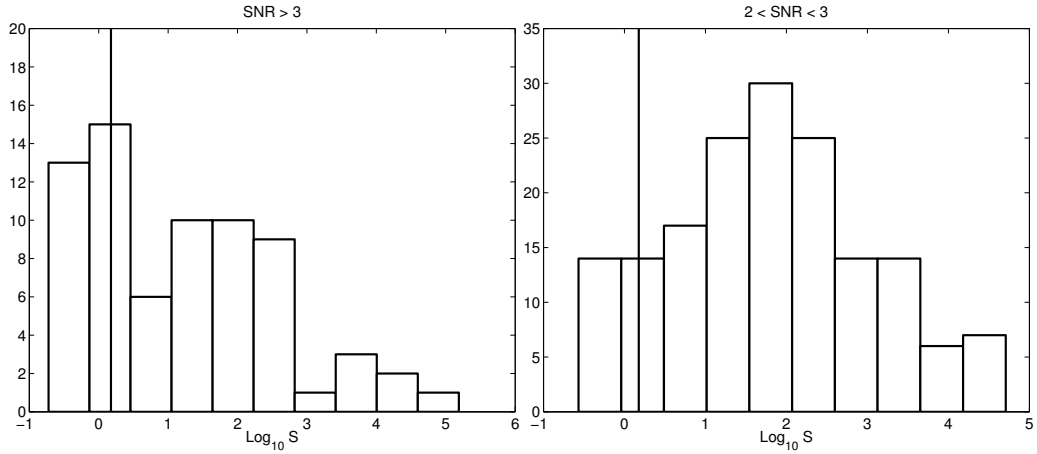

Figure 3.7: Histogram of $\mathcal{S}$ for different intervals of SNR. The vertical lines correspond to the selected threshold 1.5.

We think there are two possible causes:

- Bad astrometry treatment: as discussed in Sec. 3.1.3 and Sec. 3.1.4, non-CCD observations may contain errors that are difficult to model. If an ad hoc weighting is not used we may have misleading results. Indeed, spot checking of such cases generally confirmed isolated astrometry as source of spurious detections.

- Incompleteness or inconsistency in the dynamical model: the formulation proposed in Sec. 3.1.1 is a simplified model of the Yarkovsky perturbation that might be poor in some cases. A more sophisticated formulation would require a rather complete physical characterization that is typically unavailable and thus cannot be used for a comprehensive search as done in this paper. Moreover, as discussed in Sec. 3.2.3 for Toutatis, we may need to include more perturbing asteroids (and the uncertainty in their masses) in the model. Finally, we cannot rule out the possibility of nongravitational perturbations different from Yarkovsky as also discussed by Nugent et al. [2012b].

3.3.3 Constraining physical quantities

The results reported in Table 3.2 can be used to constrain physical quantities. When A, D, and γ are known Eq. (3.10) provides a simple relationship between ρ and Θ. This relationship can be easily translated into a relationship between ρ and the thermal inertia Γ by means of Eq. (3.9). As a benchmark of this technique we can use asteroid (101955) Bennu (Fig. 3.8), for which the known values of Γ and ρ [Chesley et al., 2012] match the plotted contraint. Figure 3.9 shows the possible values of ρ as a function of Γ for asteroids Golevka, Apollo, Ra-Shalom, Toro, YORP, and Geographos. For the latter two objects we assumed slope parameter $G = 0.15$. Our findings are consistent with the taxonomic type. For instance, Golevka, Apollo, Toro, YORP, and Geographos are S/Q-type asteroids with an expected density between 2000 and 3000 kg/m^3, while Ra-Shalom is a C-type so we expect a bulk density from 500 and 1500 kg/m^3. Figure 3.9 suggests that Golevka has thermal inertia $150 < \Gamma < 500$ J m^{-2} s$^{-0.5}$ K^{-1} and Apollo has a rather large thermal inertia $400 < \Gamma < 1000$ J m^{-2} s$^{-0.5}$ K^{-1}. According to Delbó et al. [2003] Ra-Shalom has an unusually high thermal inertia. In fact, by taking the right side of the plotted rectangle we obtain a density closer to 1000 kg/m^3, similar to the one (101955) Bennu, which belongs to a similar taxonomic class. For Toro, Mueller [2012] reports a thermal inertia $200 < \Gamma < 1200$ J m^{-2} s$^{-0.5}$ K^{-1} but likely lower, which would result in a bulk density between 2000 and 4000 kg/m^3.

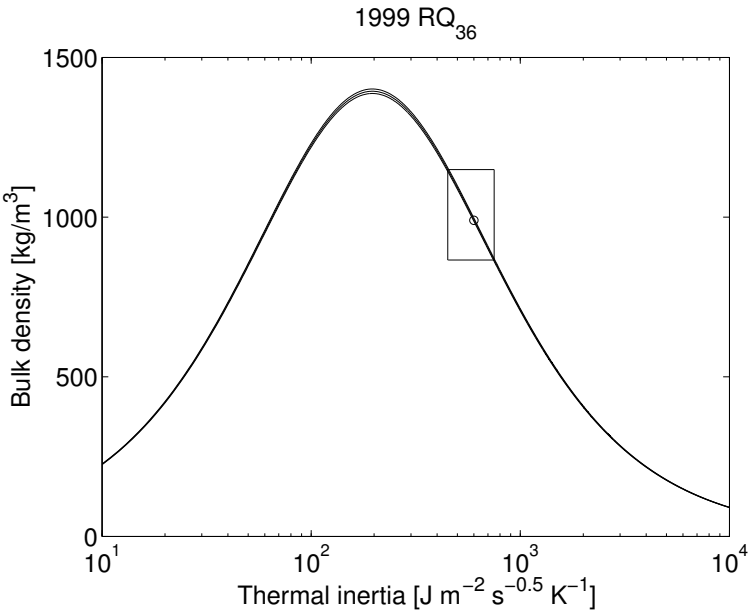

Figure 3.8: Density as a function of thermal inertia for asteroid (101955) Bennu. The three lines corresponding to the nominal value and the 1-σ levels are extremely narrow because of the high SNR. The circle corresponding to the nominal observed value of Γ and thus inferred nominal value of ρ [Chesley et al., 2012] matches the plotted curves. The enclosed region corresponds to the 1-σ interval for Γ [Emery et al., 2012] and indicates how it maps onto the 1-σ limits of ρ.

3.3.4 Implications for impact predictions

There are three known asteroids, namely Apophis, (101955) Bennu, and 1950 DA, for which Yarkovsky perturbations are relevant and need to be accounted for in the impact risk assessment. For Apophis and (101955) Bennu this is due to the presence of a strongly scattering planetary close approach between now and the epochs of the possible impacts. These encounters transform a very well determined orbit into a poorly known one for which chaotic effects are dominant [Milani et al., 2009]. Apophis will have a close approach in April 2029 with minimum distance of $\sim$ 38000 km from the geocenter. As a consequence the orbital uncertainty will increase by a factor $>$ 40000. (101955) Bennu will have a close approach to Earth in 2135 with nominal minimum distance about the same as the distance to the Moon, with an increase in uncertainty by a factor $\sim$500. The minimum possible distance for this close approach is three times smaller and would result in an increase of the uncertainty by a factor $\sim$1500 [Chesley et al., 2012]. In both cases the

Yarkovsky effect is large enough to shift the position at the scattering close approach by an amount much larger than the distance between the keyholes [Chodas, 1999] corresponding to impacts in later years (2036, 2037, 2068 for Apophis; 2175, 2180, 2196 for (101955) Bennu). Thus, the occurrence of these later impacts is determined by the Yarkovsky perturbation in the years between now and the scattering encounter. For 1950 DA the influence of the Yarkovsky effect for the possible impact in 2880 is due to long time interval preceding the impact that allows the orbital displacement to accumulate [Giorgini et al., 2002].

Currently, (101955) Bennu is the case with the best determined Yarkovsky effect (SNR ~ 200), while Apophis and 1950 DA have only a marginal detection (SNR < 1 and SNR ~ 1.4, respectively). Therefore, the impact monitoring for (101955) Bennu fully takes into account the Yarkovsky effect [Chesley et al., 2012]. On the contrary, the current estimate of impact probabilities for Apophis is based on a Monte Carlo model of the Yarkovsky perturbation based on a priori knowledge of the statistical properties of this effect [Chesley et al., 2009]. 1950 DA benefits from a similar approach [Farnocchia and Chesley, 2014].

We investigated the possibility that our identification of asteroids with measurable Yarkovsky effect produces new cases such as the two above, that is of impact monitoring affected by the Yarkovsky perturbation . The answer to this question is negative, in that the intersection between the current list of NEA with possible impacts on Earth (404 according to Sentry, 337 according to NEODyS) and the list with detected Yarkovsky orbital drifts contains only (101955) Bennu.

However, this conclusion depends on the fact that our monitoring of possible future impacts is done for only about one century (currently 100 for Sentry, 90 years for NEODyS). (101955) Bennu was a special case, related to an intensified effort for the OSIRIS-REx mission target (http://osiris-rex.lpl.arizona.edu). If this time span were generally increased to 150–200 years, there could well be other cases similar to (101955) Bennu.

For asteroid 1950 DA Busch et al. [2007] report a minimum density around 3000 km/m^3 and two possible solutions for pole orientation and effective diameter:

1. $\gamma = 24.47^\circ$ and $D = 1.16$ km;
2. $\gamma = 167.72^\circ$ and $D = 1.30$ km.

By scaling from the (101955) Bennu case, we obtain $A_2 = 7.01 \times 10^{-15}$ au/d^2 for the direct solution and $A_2 = -5.83 \times 10^{-15}$ au/d^2 for the retrograde solution. Even if we found a low SNR detection, our result strongly favors

the retrograde solution, which is at 0.6 σ, than the direct solution, which is more than 3 σ away.

3.4 Conclusions

High precision orbit estimation for asteroids is important in several applications such as linking old observations to a newly discovered and assessing the risk of an Earth impact. In these cases, the Yarkovsky perturbation is a critical component as it is usually unknown.

We measured reliable orbital drifts for 23 objects and we expect to have more as new high precision data, e.g., radar and Gaia observations, are available.

Inaccurate astrometric treatments can lead to unrealistic results, especially when the Yarkovsky drift significantly depends on isolated observations.

When a rather complete physical model is available, the measured orbital drifts can be used to measure unknown physical quantities such as the bulk density.

The distribution of the detected orbital drifts can be connected to the NEA delivery mechanism and serve as a validation of future NEA models.

For asteroids experiencing deep close approaches, the occurrence of an impact can be decisively driven by the magnitude of the Yarkovsky perturbation.

Table 3.2: Semimajor axis, eccentricity, absolute magnitude, physical and Yarkovsky parameters, and observational information for selected NEAs. The physical quantities for Bennu are from Chesley et al. [2012]. Golevka's obliquity γ is from Hudson et al. [2000], Apollo's from Ďurech et al. [2008b], Nyx's from Drummond and Wisniewski [1990], Ra-Shalom's from Ďurech et al. [2012], YORP's from Taylor et al. [2007], Geographos' from Ďurech et al. [2008a], and Toro's from Ďurech (personal communication). Diameters D and rotation periods P are from the European Asteroid Research Node (EARN) database (http://earn.dlr.de/nea/). Bond albedo A was computed from geometric albedo p_V and slope parameter G (both from the EARN database when available) by $A = (0.290 + 0.684G)p_V$ [Bowell et al., 1989].

Asteroid	a [au]	e	H	D [km]	P [hr]	A	γ	A_2 [10^{-15} au/d^2]	SNR	$\mathcal{S}$	da/dt [10^{-4} au/Myr]	da/dt Nugent et al.	Diff. σ	Observed arc	Radar apparitions
(101955) Bennu	1.13	0.20	20.6	0.49	4.29	0.01	175°	-45.49 ± 0.23	197.7	1.0	-18.99 ± 0.10	-18.9 ± 0.2	0.4	1999-2012	1999, 2005, 2011
(152563) 1992 BF	0.91	0.27	19.6	0.51	NA	0.02	NA	-24.01 ± 1.21	19.8	0.5	-11.55 ± 0.58	-12.84 ± 1	1.1	1953-2011	NA
(6489) Golevka	2.52	0.60	19.1	0.27	6.03	0.23	137°	-15.88 ± 1.52	10.4	0.2	-6.62 ± 0.64	-5.74 ± 0.7	0.9	1991-2011	1991, 1995, 2003
2009 BD	1.01	0.04	28.2	NA	NA	NA	NA	-1164.01 ± 138.76	8.3	0.4	-493.39 ± 58.81	NA	NA	2009-2011	NA
(1862) Apollo	1.47	0.56	16.0	1.40	3.06	0.12	162°	-3.34 ± 0.52	6.4	0.2	-1.70 ± 0.26	-2.3 ± 0.2	1.8	1930-2012	1980, 2005
(2062) Aten	0.97	0.18	16.9	1.30	40.77	NA	NA	-15.41 ± 2.45	6.3	0.9	-6.29 ± 1.10	-7.5 ± 2.4	0.4	1955-2012	1995, 2012
(3908) Nyx	1.93	0.46	17.3	1.00	4.43	NA	20°	29.95 ± 5.39	5.6	1.3	11.61 ± 2.09	12.9 ± 2.7	0.4	1980-2012	1988, 2004
(2100) Ra-Shalom	0.83	0.44	16.1	2.24	19.80	0.05	162°	-10.97 ± 2.25	4.9	1.1	-6.31 ± 1.30	-5.4 ± 1.5	0.5	1975-2012	1981, 1984, 2000, 2003
(10302) 1989 ML	1.27	0.14	19.4	0.25	19	NA	NA	90.48 ± 16.38	4.6	1.0	34.71 ± 6.28	35.3 ± 7.1	0.0	1989-2012	NA
1999 MN	0.67	0.67	21.4	NA	5.49	NA	NA	50.79 ± 11.39	4.5	0.4	47.12 ± 10.56	NA	NA	1999-2010	NA
(2340) Hathor	0.84	0.45	19.9	0.30	NA	0.24	NA	-24.71 ± 5.66	4.4	0.3	-14.33 ± 3.28	-14.5 ± 3.5	0.0	1976-2012	NA
(6037) 1988 EG	1.27	0.50	18.7	0.40	2.76	NA	NA	-32.66 ± 8.19	4.0	0.6	-16.39 ± 4.11	-14.2 ± 4.3	0.4	1988-2011	1988
(37655) Illapa	1.48	0.75	17.8	NA	2.66	NA	NA	-13.99 ± 3.65	3.8	0.6	-11.27 ± 2.94	NA	NA	1994-2012	2012
(85953) 1999 FK_{21}	0.74	0.70	18.0	0.59	NA	NA	NA	-10.62 ± 2.33	3.7	0.3	-10.38 ± 2.28	-10.44 ± 1.5	0.0	1971-2012	NA
(1685) Toro	1.37	0.44	14.3	3.00	10.20	0.05	144°	-2.83 ± 0.77	3.7	0.4	-1.27 ± 0.34	-1.4 ± 0.7	0.2	1948-2012	1980, 1988 2012
2005 ES_{70}	0.76	0.39	23.6	NA	NA	NA	NA	-97.23 ± 29.27	3.3	0.3	-55.58 ± 16.73	NA	NA	2005-2011	NA
(54509) YORP	1.00	0.23	22.6	0.10	0.20	NA	178°	-74.93 ± 23.68	3.2	0.3	-33.60 ± 10.61	-35.63 ± 10.5	0.1	2000-2005	2001, 2004
(283457) 2001 MQ_3	2.23	0.46	18.9	NA	NA	NA	NA	-44.63 ± 14.33	3.1	1.1	-16.02 ± 5.14	NA	NA	1951-2011	NA
(1620) Geographos	1.25	0.34	15.2	2.47	5.22	NA	153°	-4.25 ± 1.40	3.0	0.5	-1.82 ± 0.60	-2.5 ± 0.6	0.8	1951-2012	1983, 1994
(65679) 1989 UQ	0.91	0.26	19.3	0.73	7.73	NA	NA	-36.66 ± 12.23	3.0	1.2	-17.51 ± 5.84	NA	NA	1954-2011	NA
(162004) 1991 VE	0.89	0.66	18.0	NA	NA	NA	NA	18.30 ± 6.13	3.0	0.7	14.75 ± 4.94	NA	NA	1954-2012	NA

Table 3.3: Same as Table 3.2 for less reliable detections. Eros' obliquity is from Yeomans et al. [2000], Nereus' from Brozović et al. [2009], and Betulia's from Drummond and Wisniewski [1990]. All the other physical quantities are from the EARN database.

Asteroid	a [au]	e	H	D [km]	P [hr]	A	γ	A_2 [10^{-15} au/d^2]	SNR	$\mathcal{S}$	da/dt [10^{-4} au/Myr]	da/dt Nugent et al.	Diff. σ	Observed arc	Radar apparitions
1999 FA	1.07	0.13	20.6	0.30	10.09	NA	NA	-98.69 ± 6.15	3.2	1.3	-41.07 ± 13.02	NA	NA	1978-2008	NA
(433) Eros	1.46	0.22	10.8	23.30	5.27	0.10	89°	-0.72 ± 0.23	3.1	0.7	-0.26 ± 0.09	-0.3 ± 0.2	0.2	1893-2012	1975, 1988
(230111) 2001 BE_{10}	0.82	0.37	19.0	NA	4.20	NA	NA	-38.72 ± 14.00	2.8	0.9	-20.98 ± 7.59	NA	NA	2001-2013	2004
(4660) Nereus	1.49	0.36	18.1	0.34	15.16	NA	11°	28.58 ± 11.72	2.4	0.4	11.43 ± 4.69	10.9 ± 4.8	0.1	1981-2012	2001, 2002
2007 PB_8	0.88	0.45	21.2	NA	NA	NA	NA	-156.01 ± 66.45	2.3	1.4	-88.05 ± 37.50	NA	NA	2002-2012	NA
2004 BG_{41}	2.52	0.61	24.4	NA	NA	NA	NA	-598.99 ± 255.87	2.3	1.2	-256.03 ± 109.37	NA	NA	2004-2011	NA
(4179) Toutatis	2.53	0.63	15.1	2.80	176.00	0.05	NA	-3.32 ± 1.43	2.3	0.4	-1.49 ± 0.63	-5.0 ± 0.6	4.1	1976-2012	1992, 1996, 2000, 2004, 2008
(138911) 2001 AE_2	1.35	0.08	19.0	0.35	NA	NA	NA	-62.23 ± 28.84	2.2	1.0	-22.90 ± 10.61	-22.9 ± 11.2	0.0	1984-2012	NA
(326290) 1998 HE_3	0.88	0.44	21.7	0.10	NA	NA	NA	-70.57 ± 33.01	2.1	0.3	-39.68 ± 18.56	NA	NA	1993-2012	2012
(3361) Orpheus	1.21	0.32	18.9	0.50	3.51	NA	NA	12.07 ± 5.67	2.1	0.3	5.20 ± 2.44	5.7 ± 2.5	0.1	1982-2010	NA
(154590) 2003 MA_3	1.11	0.40	21.7	NA	NA	NA	NA	-95.60 ± 45.11	2.1	0.7	-46.06 ± 21.74	NA	NA	1998-2012	NA
1994 XL_1	0.67	0.53	20.8	NA	NA	NA	NA	-31.22 ± 15.32	2.0	0.3	-22.38 ± 10.98	NA	NA	1994-2011	NA
(1580) Betulia	2.19	0.49	14.3	4.57	6.13	0.03	117°	-4.65 ± 2.31	2.0	0.9	-1.75 ± 0.87	-1.3 ± 0.9	0.4	1950-2012	1976, 1989, 2002
(29075) 1950 DA	1.70	0.51	17.0	1.4	2.12	0.08	NA	-5.00 ± 3.47	1.4	0.3	-2.20 ± 1.52	NA	NA	1950-2012	2001
(250680) 2005 QC_5	0.89	0.36	19.7	NA	NA	NA	NA	26.44 ± 22.01	1.2	0.5	13.70 ± 11.40	NA	NA	1978-2011	NA
(105140) 2000 NL_{10}	0.91	0.82	15.5	1.72	6.93	NA	NA	-11.78 ± 10.49	1.1	0.9	-15.73 ± 14.02	NA	NA	1951-2012	NA

Table 3.4: Same as Table 3.2 for small orbital drifts. Icarus' obliquity is from De Angelis [1995]. All the other physical quantities are from the EARN database.

Asteroid	a [au]	e	H	D [km]	P [hr]	A	γ	A_2 [10^{-15} au/d^2]	SNR	$\mathcal{S}$	da/dt [10^{-4} au/Myr]	da/dt Nugent et al.	Diff. σ	Observed arc	Radar apparitions
(1566) Icarus	1.08	0.83	16.7	1.30	2.27	0.04	103°	-0.66 ± 1.39	0.5	0.04	-0.86 ± 1.80	-3.2 ± 2.0	0.9	1949-2012	1968, 1996
(3757) 1982 XB	1.84	0.45	19.1	0.39	9.00	NA	NA	-17.06 ± 13.25	1.3	0.30	-6.68 ± 5.19	-13.7 ± 6.8	0.8	1982-2012	1987
(6239) Minos	1.15	0.41	18.3	0.47	3.56	0.26	NA	-9.34 ± 9.59	1.0	0.20	-4.45 ± 4.57	NA	NA	1983-2010	2004
(99907) 1989 VA	0.73	0.59	17.8	0.55	2.51	0.11	NA	8.71 ± 5.40	1.6	0.21	6.70 ± 4.15	NA	NA	1989-2012	NA
(161989) Cacus	1.12	0.21	17.1	0.6	3.75	NA	NA	7.97 ± 5.48	1.5	0.21	3.35 ± 2.30	2.6 ± 2.3	0.2	1978-2010	NA
(306383) 1993 VD	0.88	0.55	21.6	NA	NA	NA	NA	-16.01 ± 11.58	1.4	0.11	-10.43 ± 7.55	NA	NA	1993-2011	NA
2003 XV	1.92	0.55	26.6	NA	NA	NA	NA	-187.40 ± 272.02	0.7	0.14	-82.37 ± 119.56	NA	NA	2003-2011	NA
2004 FG_{11}	1.59	0.72	20.9	0.15	20.0	NA	NA	-29.98 ± 30.16	1.0	0.20	-21.24 ± 21.36	NA	NA	2004-2012	2012
2004 SC_{56}	0.77	0.43	22.8	NA	NA	NA	NA	-61.54 ± 51.38	1.2	0.26	-36.56 ± 30.52	NA	NA	2004-2010	NA
2005 ST_1	1.45	0.37	20.3	NA	NA	NA	NA	-12.31 ± 19.82	0.6	0.16	-5.03 ± 8.10	NA	NA	1991-2012	NA

Table 3.5: Probability of coming from one of the intermediate NEA source regions for the objects of Table 3.2.

Asteroid	ν_6	MC	3:1	OB	JFC
(101955) Bennu	81.5%	18.5%	0.0%	0.0%	0.0%
1992 BF	70.2%	27.5%	2.3%	0.0%	0.0%
Golevka	15.9%	21.7%	39.6%	22.8%	0.0%
2009 BD	78.8%	21.2%	0.0%	0.0%	0.0%
Apollo	60.3%	21.1%	18.6%	0.0%	0.0%
Aten	68.6%	28.8%	2.7%	0.0%	0.0%
Nyx	65.0%	20.2%	5.3%	9.5%	0.0%
Ra-Shalom	29.2%	7.0%	63.8%	0.0%	0.0%
1989 ML	5.7%	94.3%	0.0%	0.0%	0.0%
1999 MN	100.0%	0.0%	0.0%	0.0%	0.0%
Hathor	75.2%	19.2%	5.6%	0.0%	0.0%
1988 EG	60.2%	26.7%	13.1%	0.0%	0.0%
Illapa	45.6%	24.3%	30.1%	0.0%	0.0%
1999 FK_{21}	72.1%	27.9%	0.0%	0.0%	0.0%
Toro	62.9%	27.7%	9.4%	0.0%	0.0%
2005 ES_{70}	63.3%	10.8%	25.9%	0.0%	0.0%
YORP	72.0%	24.4%	3.6%	0.0%	0.0%
2001 MQ_3	17.9%	73.9%	5.2%	3.0%	0.0%
Geographos	60.4%	27.8%	11.7%	0.0%	0.0%
1989 UQ	64.2%	15.0%	20.8%	0.0%	0.0%
1991 VE	63.8%	1.3%	34.9%	0.0%	0.0%
Average	58.7%	25.7%	13.9%	1.7%	0.0%

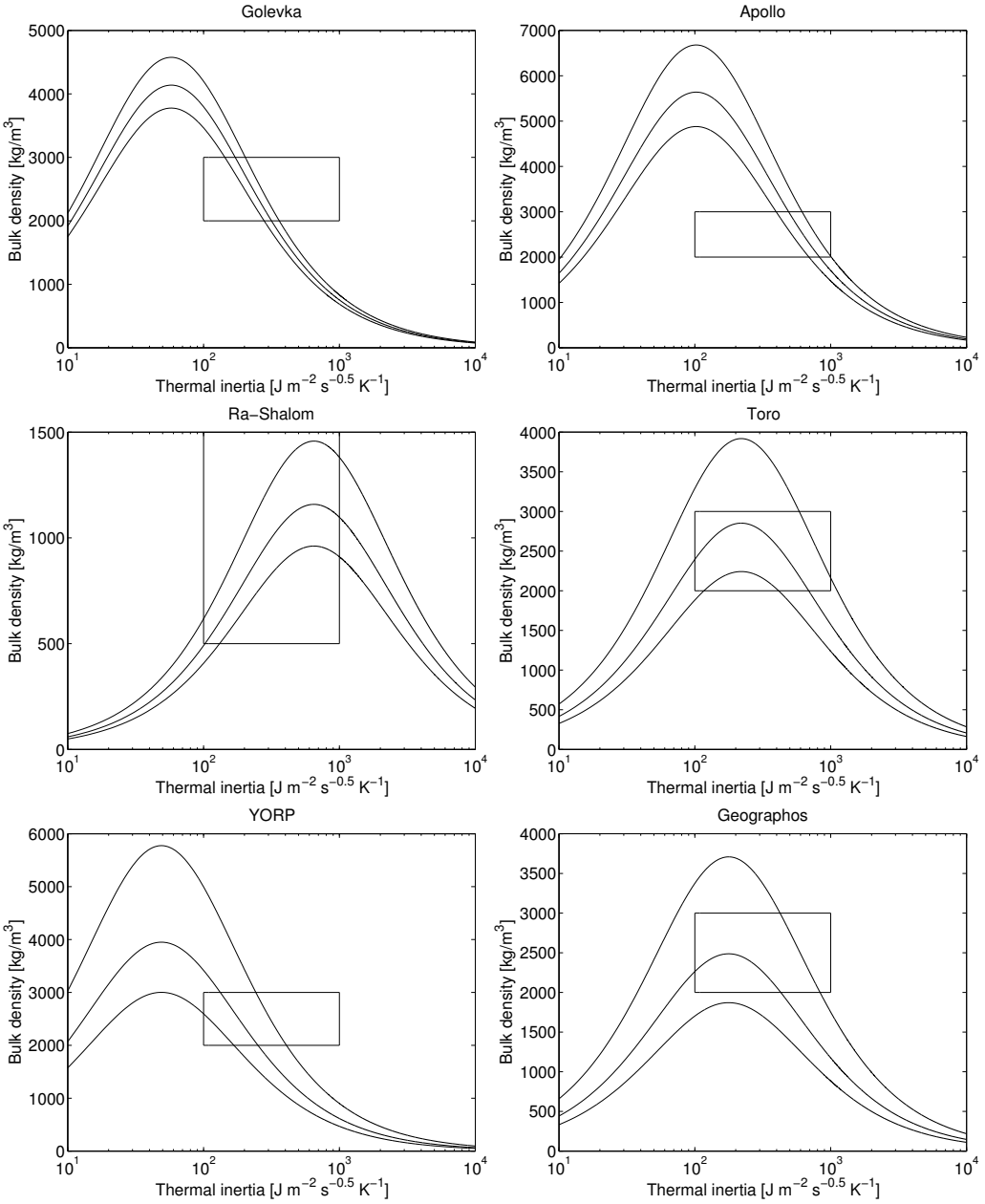

Figure 3.9: Density as a function of thermal inertia for asteroids Golevka, Apollo, Ra-Shalom, Toro, YORP, and Geographos. The rectangles correspond to reasonable values of ρ according to the taxonomic type and to a reasonable range of Γ [Delbó et al., 2007].

Chapter 4

Orbit and Bulk Density of the OSIRIS-REx Target Asteroid (101955) Bennu

The Apollo asteroid (101955) Bennu, a half-kilometer near-Earth asteroid previously designated 1999 RQ_{36}, is the target of the OSIRIS-REx sample return mission. A prime objective of the mission is to measure the Yarkovsky effect on this asteroid and constrain the properties that contribute to this effect. This objective is satisfied both by direct measurement of the acceleration imparted by anisotropic emission of thermal radiation, the first results of which are reported here, and by constructing a global thermophysical model of the asteroid to confirm the underlying principles that give rise to this effect.

Bennu was discovered by the LINEAR asteroid survey in September 1999. Since then, more than 500 optical observations have been obtained for this Potentially Hazardous Asteroid (PHA). Moreover, the asteroid was observed using radar by the Arecibo and Goldstone radio telescopes during three different apparitions. Thanks to this rich observational data set, Bennu has one of the most precise orbits in the catalog of known near-Earth asteroids. The exceptional precision of the Bennu orbit allows one to push the horizon for predicting possible Earth impacts beyond the 100 years typically used for impact monitoring Milani et al. [2005a], and indeed Milani et al. [2009] showed that Earth impacts for Bennu are possible in the second half of the next century. In particular, the cumulative impact probability they found was approximately 10^{-3}, about half of which was associated with a possible impact in 2182. However, the occurrence of an impact depends decisively on the Yarkovsky effect because the prediction uncertainty due to this non-gravitational perturbations dominates over the orbital uncertainty associated

with astrometric errors.

The Yarkovsky effect is a subtle nongravitational perturbation that primarily acts as a secular variation in semimajor axis and thus causes a runoff in orbital anomaly that accumulates quadratically with time Bottke et al. [2006]. The computation of the Yarkovsky perturbation requires a rather complete physical model of the asteroid, including size, shape, density, spin rate and orientation, thermal properties, and even surface roughness Rozitis and Green [2012]. Though such a complete profile is rarely available, the orbital drift due to the Yarkovsky effect can sometimes be determined from an asteroid observational data set. For example, Chesley et al. [2003] managed to directly estimate the Yarkovsky effect for asteroid (6489) Golevka by using three radar apparitions. Vokrouhlický et al. [2008] employ the Yarkovsky effect to match precovery observations of asteroid (152563) 1992 BF that are incompatible with purely gravitational dynamics. More recently Nugent et al. [2012b] and Farnocchia et al. [2013b] have estimated the Yarkovsky effect for a few tens of near-Earth asteroids by using a formulation that depends on a single parameter to be determined from the orbital fit.

Besides Bennu, there are two other asteroids for which possible impacts are known to be driven by the Yarkovsky effect: (29075) 1950 DA Giorgini et al. [2002] and (99942) Apophis Chesley [2006]; Giorgini et al. [2008]. The relevance of the Yarkovsky effect for Apophis is due to a scattering close approach in 2029 with minimum geocentric distance ∼38000 km. For 1950 DA the influence of the Yarkovsky effect for an impact in 2880 is due to the long time interval preceding the potential impact. However, no estimate of the Yarkovsky perturbation acting on these two asteroids is currently available. To analyze such cases one can use the available physical constraints for the specific objects, along with general properties of near-Earth asteroids (e.g., albedo, thermal inertia, bulk density, etc.) to statistically model the Yarkovsky effect. The orbital predictions and the impact hazard assessment are then performed by a Monte Carlo simulation that accounts for both the Yarkovsky effect distribution and the orbital uncertainty Farnocchia and Chesley [2014]; Farnocchia et al. [2013a]. For Bennu, no such heroics are required. As we shall see, we now have a precise estimate of the orbital deviations caused by the Yarkovsky effect, as well as a comprehensive physical model distilled from numerous investigations.

While the Yarkovsky effect requires a priori knowledge of several physical parameters to be computed directly, its detection through orbital deviations can be used to constrain the otherwise unknown physical parameters. When the spin state is unknown, one can derive weak constraints on obliquity, as was first shown by Vokrouhlický et al. [2008] for 1992 BF. In cases where the spin state is well characterized, usually through the combination of radar

imaging and photometric light curves, the bulk density of the object is correlated with the thermal properties and mutual constraints can be inferred, as was the case for Golevka Chesley et al. [2003]. Rozitis et al. [2013] were able to jointly model the measured Yarkovsky and YORP effects on (1862) Apollo, and thereby constrain a number of the body's physical characteristics, including axis ratios, size, albedo, thermal inertia and bulk density. In the case of Bennu, the thermal inertia is known from infrared observations Emery et al. [2014]; Müller et al. [2012], and so we are able to directly estimate the mass and bulk density.

4.1 Observational Data and Treatment

4.1.1 Optical Astrometry

We use the 569 RA-DEC astrometric measurements available from the Minor Planet Center from 1999-Sep-11.4 to 2013-Jan-20.1. We apply the star catalog debiasing algorithm introduced by Chesley et al. [2010], and data weights are generally based on the astrometric weighting scheme proposed in Sec. 6.1 of that paper. In some cases there is an excess of observations from a single observatory in a single night. In such cases we relax the weights by a factor of about $\sqrt{N/5}$, where N is the number of observations in the night. This reduces the effect of the particular data set to a level more consistent with the typical and preferred contribution of 3–5 observations per night.

Considerable care was taken in identifying outlier observations to be deleted as discordant with the bulk of the observations. From among the 569 available observations from 43 stations, we reject 91 as outliers, leaving 478 positions from 34 stations in the fits. Figure 4.1 depicts the postfit plane of sky residuals, highlighting the deleted data. There are an additional 14 observations, all deleted, that are not depicted in Fig. 4.1 because they fall beyond the limits of the plot. The manual rejection approach often deletes an entire batch of data if it appears biased in the mean, thus some of the deleted points in Fig. 4.1 do not show significant residuals. On the other hand, some observations are de-weighted relative to the others, and in some cases these are not deleted, despite the raw residuals being larger than some rejected observations. In Sec. 4.2.4 we discuss the dependency of the ephemeris prediction on the outlier rejection approach.

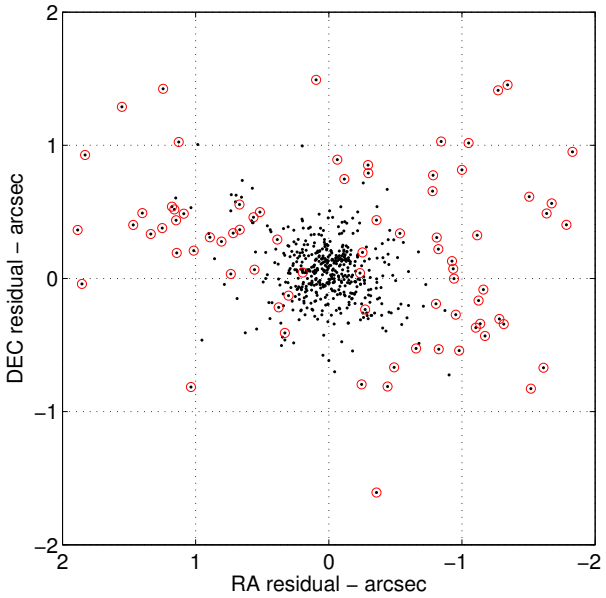

Figure 4.1: Depiction of Bennu postfit residuals for JPL solution 87. Deleted observations are depicted with circles around the points. In addition to the observations shown here, there are 14 deleted observations outside the plot boundaries.

4.1.2 Radar Astrometry

The time delay and Doppler shift of radar echoes from Bennu were measured in 1999, 2005 and 2011. Radar astrometry was obtained at both Arecibo and Goldstone as detailed in Table 4.1. The delay observations in the table correspond to the round-trip light travel time from the nominal telescope position to the center of mass of the object, and thus they are often referred to as range measurements. Doppler measurements in the table reflect the frequency shift between the transmit and receive signals due to the line-of-sight velocity of the object. The use of radar delay and Doppler measurements in asteroid orbit determination was introduced by Yeomans et al. [1992].

Delay uncertainties arise from the finite resolution of the imaging of 0.05-0.125 μs/px Nolan et al. [2013], uncertainty in the shape modeling (to determine the center of mass from the observed echo power) of 10-20 m, equivalent to about 0.1 μs, and systematic calibration, including uncertainties in the position of the telescope and light travel within the telescope optics. Because we have a shape model of Bennu that directly relates the individual range observations to the center of figure of the model Nolan et al. [2013], the systematic uncertainties dominate the range uncertainty in the 1999 and 2005 observations, and are assigned conservative values of 1.0 and 0.5 μs (respectively).

In 2011, Bennu was much farther away than the previous observations, and the uncertainty of 2 μs is from the pixel scale of the observations. Doppler uncertainties are taken to be 1 Hz at 2380 MHz, about 1/4 of the total rotational Doppler width of the object, and are based on the uncertainty of estimating the position of the center of mass of the spectra.

The 2011 observations (Fig. 4.2 and Table 4.2) were of too low resolution and SNR to be useful for shape modeling and were obtained solely for improving our knowledge of the orbit of Bennu. The 2-μs (300 m) resolution was chosen to be the finest resolution that would maximize the SNR of the observations by including all of the echo power from the 250-m radius asteroid in one or two range bins. The asteroid was visible with a SNR > 3 on each of the three observing dates at consistent delay and Doppler offsets from the a priori ephemeris used in the data taking.

The 2011 radar observations of Bennu, which enabled the results of the present paper, almost never happened. The two-million-Watt, 65,000-Volt "power brick" that supplies the electricity for the Arecibo Planetary Radar system failed in late 2010, and was finally repaired on September 15, 2011. Because of the critical schedule for Bennu observations, in a space of seven days the 16-ton unit was trucked 800 miles from Pennsylvania to Florida, shipped to Puerto Rico, trucked again, and lifted into place with a crane. The system was reconnected and recommissioned in four days, after nearly a year of down-time, just in time to perform the observations on the last possible dates of September 27–29, and just as the prime contractor managing the Arecibo Observatory was changing (on October 1), after 45 years of operation by Cornell University, so that most observatory operations were frozen for the transition.

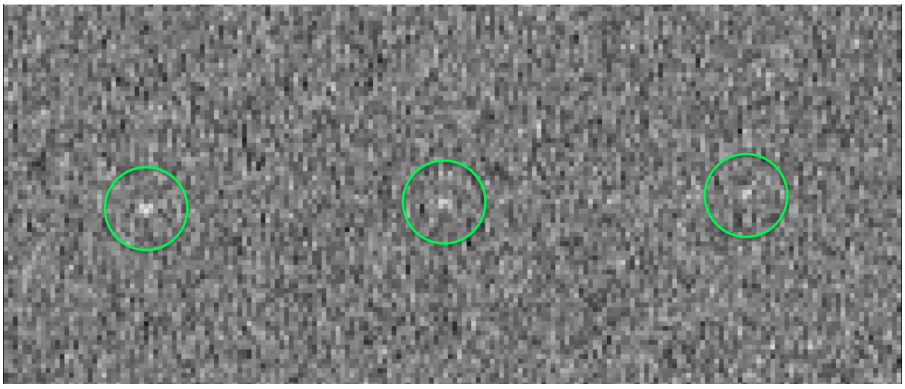

Figure 4.2: Arecibo delay-Doppler detections of Bennu from 2011-Sep-27,28,29. Doppler frequency increases to the right and delay increases upwards. Image resolution is $1\,\mathrm{Hz} \times 1\,\mu$s.

4.2 Orbit Determination and Dynamical Model

We have updated the orbit determination for Bennu based on the observational data set described above. These orbital position measurements place extraordinary constraints on the orbit determination, and thus we must pay careful attention to the fidelity of force models, observation models and numerical integration. Our dynamical model includes direct solar radiation pressure and the thermal re-emission of absorbed solar radiation (i.e., the Yarkovsky effect). Besides the gravitational acceleration of the Sun, we include Newtonian perturbations by the eight planets, the Moon, Pluto and 25 selected main belt asteroids. We consider the oblateness term of the Earth's geopotential and full relativistic perturbations from the Sun, eight planets and the Moon.

As shown by Giorgini et al. [2002], who studied the potential impact of 29075 (1950 DA) in the year 2880, other potential dynamical perturbations, such as galactic tide, solar mass loss and solar oblateness, are too slight to affect our results. This is because these small effects, which were not important for 1950 DA, will be even less significant for Bennu due to the much shorter time interval.

4.2.1 Yarkovsky Effect

The Yarkovsky effect is a key consideration when fitting an orbit for Bennu Milani et al. [2009]. This slight nongravitational acceleration arises from the anisotropic re-emission at thermal wavelengths of absorbed solar radiation Bottke et al. [2006]. The component of the thermal recoil acceleration in the transverse direction acts to steadily increase or decrease the orbital energy, leading to a drift in semimajor axis da/dt that accumulates quadratically with time in the orbital longitude of the asteroid. For a uniform, spherical asteroid on a known orbit, the drift rate depends on the physical characteristics of the asteroid according to

$$\frac{da}{dt} \propto \frac{\cos\gamma}{\rho D},$$

where γ is the obliquity of the asteroid equator with respect to its orbital plane, ρ is the bulk density of the asteroid, and D is the effective diameter. Additionally, da/dt depends in a nonlinear and often nonintuitive way on the asteroid rotation period P and the surface material properties, namely thermal inertia Γ, infrared emissivity ϵ and Bond albedo A Vokrouhlický et al. [2000a].

We have three models available to us for computing thermal accelerations on Bennu. The first, and most straightforward, is to simply apply a trans-

verse acceleration of the form $A_T \times (r/1\,\mathrm{au})^{-d}$, where A_T is an estimable parameter, r is the heliocentric distance and the exponent is typically assumed as $d = 2$ to match the level of absorbed solar radiation. Given an estimated value of A_T and the assumed value of d, one can readily derive the time-averaged da/dt using Gauss' planetary equations Farnocchia et al. [2013b]. This approach, which we term the *transverse model*, is computationally fast and captures the salient aspects of the thermal recoil acceleration. Importantly, it requires no information about the physical characteristics or spin state of the asteroid, and so it can be implemented readily in cases where only astrometric information is available Chesley et al. [e.g., 2008]; Farnocchia et al. [e.g., 2013b]; Nugent et al. [e.g., 2012b]; Vokrouhlický et al. [e.g., 2008].

For Bennu we find numerically that the exponent $d = 2.25$ provides the best match to the transverse thermal acceleration derived from the thermal re-emission models described below. This result can also be computed analytically using a simplified model with the technique described in Appendix A. Using the transverse model with $d = 2.25$ we derive JPL solution 87 (Table 4.3), which serves as a reference solution as we investigate the effect of various model variations on the orbit.

JPL solution 87 yields a Yarkovsky drift estimate that compares well with the corresponding result from Milani et al. [2009], who used observations only through mid-2006 and found $da/dt = (-15 \pm 9.5) \times 10^{-4}$ au/Myr, which was judged to be a weak detection of the nongravitational acceleration. Using the same fit span (1999–2006) from the current data set we now find $da/dt = (-22.9 \pm 5.3) \times 10^{-4}$ au/Myr. The change in the estimate relative to that of Milani et al. [2009] is due in large part to the use of star catalog debiasing Chesley et al. [2010], while the improved precision is due to the higher accuracy and quantity of radar delay measurements obtained through re-measurement of the 1999 and 2005 Arecibo observations, as well through as the use of tighter weights on the optical data proposed by Chesley et al. [2010]. Incorporating the subsequent optical observations through 2013 leads to $da/dt = (-21.3 \pm 4.6) \times 10^{-4}$ au/Myr. Finally, adding the 2011 Arecibo radar astrometry reduces the uncertainty by nearly a factor 50, leading to the current best estimate $da/dt = (-19.0 \pm 0.1) \times 10^{-4}$ au/Myr. We note that the new formal uncertainty on da/dt is 0.5%, by far the most precise Yarkovsky estimate available to date. As well, the uncertainty on the semimajor axis a is 6 m, the lowest value currently found in the asteroid catalog. This low uncertainty is primarily a reflection of the current precision of the orbital period (2 ms) rather than an indication of the uncertainty in the predicted asteroid position, which is at the level of a few kilometers during the fit span.

Both our second (linear) and third (nonlinear) Yarkovsky acceleration

models employ heat transfer models of different levels of fidelity in order to predict the surface temperature and associated re-emission of thermal energy. The *linear model* utilizes linearized heat transfer equations on a rotating homogeneous sphere, closely following the development given by Vokrouhlický et al. [2000b] for both the diurnal and seasonal components of the Yarkovsky effect. The linear model requires knowledge of the spin orientation and rate, asteroid diameter and thermal inertia, but does not allow for shape effects such as self-shadowing and self-heating, which are generally considered minor. The linear model assumes a sphere, and so oblateness effects are not captured. This is relevant because the cross-sectional area receiving solar radiation is increased for an equal volume sphere relative to that of an oblate body, and thus the force derived with the linear model is enhanced relative to the nonlinear model. This in turn leads to an increased estimate of the bulk density as we shall see later.

The *nonlinear model* is the highest fidelity Yarkovsky force model that we apply to the orbit determination problem. This approach solves the nonlinear heat transfer equation on a finite-element mesh of plates or facets that models the Nolan et al. [2013] asteroid shape. The approach is described in more detail by Čapek and Vokrouhlický [2005], but we summarize it here. For each facet on the asteroid shape model, the nonlinear heat transfer problem is solved while the asteroid rotates with a constant spin rate and orientation and revolves along a frozen, two-body heliocentric orbit. A uniform temperature distribution is assumed at start-up and the temperature and energy balance between absorbed, conducted and re-radiated radiation for each facet is solved as a function of time. The heat transfer problem is treated as one-dimensional, i.e., the temperature for a given facet depends only on the depth below the facet. There is no conduction across or between facets. After several orbital revolutions the temperature profile from revolution to revolution converges for each plate. Following convergence, diurnal averaging of the vector sum of the thermal emission over the body yields the force of thermal emission as a function of orbital anomaly. Given the shape model volume and an assumed bulk density, the mass can be computed and from this the thermal recoil acceleration. This ultimately leads to a lookup table of acceleration as a function of true anomaly that is interpolated during the high-fidelity orbital propagation.

The nonlinear model was previously used with asteroid (6489) Golevka Chesley et al. [2003], but at that time the acceleration table was for a frozen orbit, which turns out to be an unacceptable approximation for Bennu. Figure 4.3 shows the orbital element variations into the future due to planetary perturbations and Fig. 4.4 reveals the associated variation in the average da/dt, which is clearly significant relative to the 0.10×10^{-4} au/Myr uncer-

tainty. As a result of this analysis we have implemented an enhancement to the nonlinear model that corrects the tabulated accelerations for variations in orbital elements. The approach is to compute the Yarkovsky force vector from a linearized expansion about a central, reference orbit according to

$$\vec{F}_Y(a,e;f_i) = \vec{F}_Y(a_0,e_0;f_i) + \frac{\partial \vec{F}_Y(a_0,e_0;f_i)}{\partial a}(a-a_0) + \frac{\partial \vec{F}_Y(a_0,e_0;f_i)}{\partial e}(e-e_0).$$

Here $\vec{F}_Y$ is the thermal acceleration in the orbit plane frame so that variations of the Keplerian Euler angle orbital elements (ω, Ω, i) do not affect the computation; $\vec{F}_Y$ is rotated to the inertial frame during the propagation. The f_i are the true anomaly values in the tabulation, a_0 and e_0 are the values for the reference orbit. The partial derivatives are also tabulated after they are derived by finite differences based on a series of pre-computed lookup tables for varying orbits $\vec{F}_Y(a_0 \pm \delta a, e_0 \pm \delta e; f_i)$.

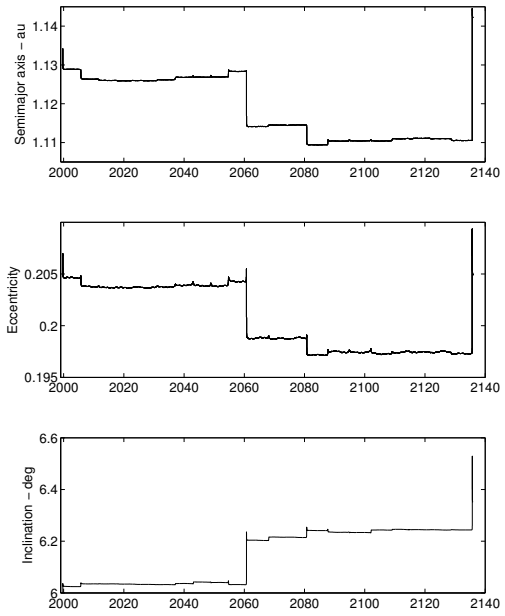

Figure 4.3: Time history of the osculating Bennu orbital elements, a, e and i, through 2136. The effects of Earth encounters are evident and can be cross-referenced with Table 4.8.

When computing an orbit with the linear or nonlinear model we use the physical parameters listed in Table 4.4, and for the nonlinear model we also use the Nolan et al. [2013] shape model. The bulk density ρ is estimated as a free parameter. Because the semimajor axis drift da/dt is constrained by the observations at the 0.5% level, any variations in the force computed by

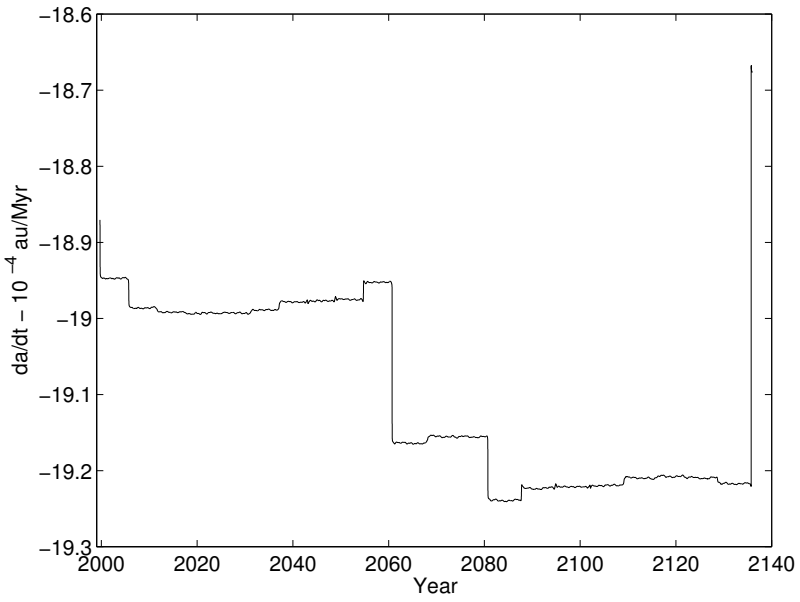

Figure 4.4: Time history of the Bennu semimajor axis drift da/dt through 2136. The variations arise from orbital changes induced by Earth encounters as depicted in Fig. 4.3.

the thermal models manifests as a variation in the estimated bulk density. This is discussed in greater detail in Sec. 4.3.

JPL solution 85 (Table 4.3) uses the nonlinear model, and is assumed to be our most accurate orbital solution. To indicate the differences between the two models, Fig. 4.5 depicts the estimated thermal recoil accelerations from the nonlinear and linear models. The plot reveals an excellent agreement between the two models in the transverse acceleration, which is to be expected since the transverse component is constrained by the observed orbital runoff and the associated semimajor axis drift. The radial and normal (out-of-plane) accelerations show a good but imperfect agreement, with linear model accelerations being noticeably reduced relative to the nonlinear model.

Figure 4.6 shows how the radial and transverse accelerations in the linear model affect the instantaneous and average values of da/dt, as derived from the classical Gauss planetary equations. During a given orbit, the variations in the instantaneous drift rate are much larger from the transverse component. The normal component of acceleration does not affect the semimajor axis. While the radial component of acceleration does lead to variations in semimajor axis during an orbital period, in the mean the radial term does not contribute to semimajor axis drift, which is a classical result if the radial

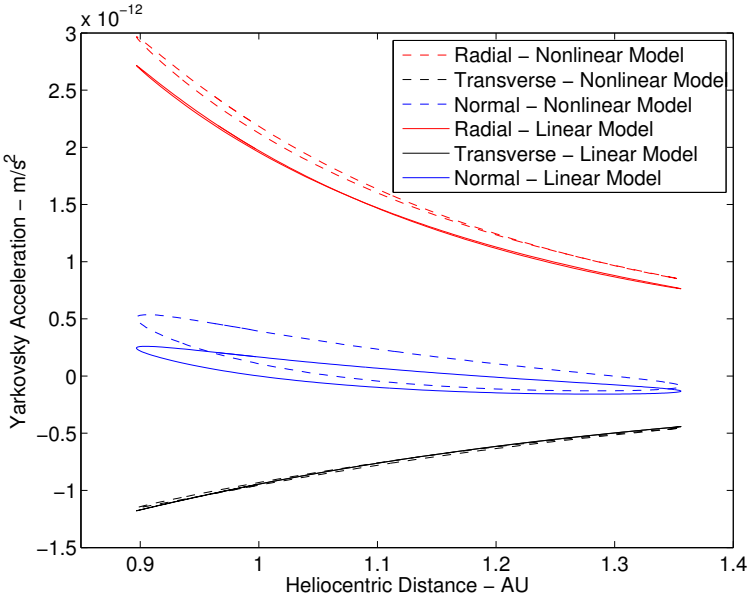

Figure 4.5: Yarkovsky accelerations as a function of heliocentric distance, according to the linear and nonlinear Yarkovsky models.

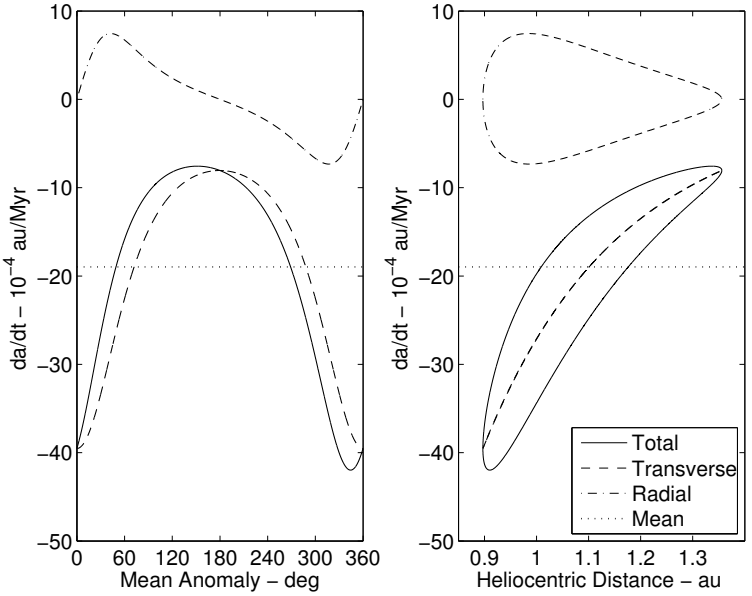

Figure 4.6: The variation of da/dt stemming from the transverse and radial components of the Yarkovsky acceleration. The linear Yarkovsky model is depicted.

accelerations are symmetric about perihelion. However, Fig. 4.5 reveals that symmetry is not necessarily present in this case. There is a slight hysteresis in the radial acceleration profile for the linear model, but because the curve crosses itself the integrated area under the curve in one orbit nets to approximately zero. In contrast, the nonlinear radial acceleration has a more significant hysteresis that does not sum to zero, and thus the radial component of acceleration actually contributes to da/dt in the mean. This behavior is presumably associated with the fact that thermal energy penetrates more deeply below the asteroid surface around perihelion when the absorbed radiation is greatest, which leads to greater thermal emission post-perihelion that pre-perihelion. We find that in the nonlinear model the radial acceleration increases da/dt by 0.3%, which is not negligible relative to the 0.5% precision of the estimate. The result is that the transverse component must contribute 0.3% more in magnitude to compensate. With the linear model the radial contribution to da/dt is 60 times less.

Table 4.5 shows the variation in estimated da/dt associated with the different Yarkovsky models. JPL solution 87 ($d = 2.25$) is the reference solution for the comparison, and the linear and nonlinear models yield da/dt values within 0.03%, less than a tenth of the formal uncertainty. The result for the typical default value $d = 2$ is also tabulated and agrees well. This is not surprising since the astrometry provides a strong constraint on da/dt that the models must accommodate. At this level of precision, the averaged da/dt may not be the best means of quantifying the Yarkovsky effect because the mean value changes as the orbit undergoes strong planetary perturbations (Figs. 4.3 and 4.4). Nonetheless, it is informative when comparing objects and assessing the scale of the Yarkovsky effect and so we continue to use it here.

As discussed in Sec. 4.4, Bennu will have a close approach to Earth in 2135 at around the lunar distance. Table 4.5 also lists the variation in the 2135 b-plane coordinates $(\xi_{2135}, \zeta_{2135})$ associated with the different Yarkovsky models. We describe these coordinates more fully later, but the salient point is that $\Delta\zeta_{2135}$ reveals the importance of the model variation for long term predictions, while $\Delta da/dt$ reflects the relevance to the orbital estimate over the fit span from 1999-2013.

In addition to the Yarkovsky effect, our dynamical model also includes another nongravitational perturbation related to solar radiation, namely direct solar radiation pressure Vokrouhlický and Milani [SRP, 2000]. Based on the Nolan shape model and the mass estimate discussed in Sec. 4.3, we assume an area-to-mass ratio of $2.59 \times 10^{-6}\,\mathrm{m^2/kg}$, which leads to an acceleration of $1.2 \times 10^{-11}\,\mathrm{m/s^2}$ at 1 au, an order of magnitude greater than the radial acceleration from thermal re-emissions (see Fig. 4.5). Reflected

radiation pressure is negligible due to the 1.7% Bond albedo of the body Emery et al. [2014]. Even though the acceleration of SRP is several times greater than that from thermal re-emission, it has little effect on the orbital predictions as it is perfectly aliased with the solar gravity. Turning SRP on and off changes the estimated semimajor axis (by $\sim 67\sigma$) but leaves the mean motion unchanged. Thus there is only a minor effect on the trajectory from eliminating solar radiation pressure from the force model (by assuming an area-to-mass ratio of zero), as can be seen in Table 4.5 under the entry labeled Area/Mass= 0.

4.2.2 Gravitational Perturbers

The gravitational effects of the Sun, eight planets, the Moon and Pluto are based on JPL's DE424 planetary ephemeris Folkner [2011]. The use of the older DE405 planetary ephemeris Standish [2000] leads to a modest variation in the estimated da/dt and the predicted ζ_{2135} as indicated in Table 4.5.

When Bennu is near the Earth we modeled the gravitational perturbation due to Earth oblateness. Table 4.5 indicates the effect of varying the distance within which the oblateness model is included. We found that unless the effect was included whenever the asteroid is closer than 0.3 au there is a modest but discernible effect on the orbit determination and propagation. As a result we used a 1 au cutoff as our baseline.

Perturbing asteroids were also included in the force model. Using DE424, we developed mutually perturbed trajectories of the four largest asteroids (1 Ceres, 2 Pallas, 4 Vesta and 10 Hygeia) and designated this perturber model the CPVH small body ephemeris. We then computed the orbits for the next 12 largest main belt asteroids, each of which was perturbed only by DE424 and CPVH. The combination of these 12 additions with CPVH formed a perturber list of the 16 most massive asteroids (based on current mass estimates), and we refer to this perturber model as BIG-16. Finally, we added nine more asteroids, which were selected according to an analysis of which perturbers could most significantly influence the orbit of Bennu. The final nine asteroid ephemerides, each perturbed by DE424 and BIG-16, were combined with BIG-16 to form our final, baseline perturber set of 25 asteroids.

Table 4.5 indicates the effect on the estimated value of da/dt due to changing the perturber model to either BIG-16 or CPVH. In either case the effect is small and far less than the 0.5% formal uncertainty. Table 4.6 lists the assumed masses for each of the asteroid perturbers, as well as the effect of deleting each one of them from the perturber model. From this table one can see that, besides the very large contribution of 1 Ceres, 2 Pallas and 4 Vesta,

only two other asteroids affect da/dt at more than 0.1σ, namely 6 Hebe and 7 Iris. Beyond CPVH, the accumulation of smaller and smaller contributions tends toward a zero mean. This is not surprising, and is a fortuitous result of the low aphelion distance (1.36 au) of Bennu, which limits the perturbations of the main asteroid belt.

4.2.3 Relativity

We used a full relativistic force model including the contribution of the Sun, the planets, and the Moon. More specifically, we used the Einstein-Infeld-Hoffman (EIH) approximation Moyer [2003]; Soffel et al. [2003]; Will [1993]. Table 4.5 shows the variations in da/dt and ζ_{2135} associated with different relativistic models. We found a 1.6% difference in da/dt with respect to the basic Sun-only Schwarzschild term [Damour et al., 1994, Sec. 4]. This is only in small part due to the switch to the improved model for the Sun, as the contribution of some of the planets is not negligible. In particular, the Earth's relativistic terms are responsible for a 1.5% ($\sim 3\sigma$) variation because of significant short range effects during Bennu Earth approaches in 1999 and 2005. Figure 4.7 shows the main relativistic terms and compares them to the Yarkovsky perturbation. Clearly, the relativistic effects of the Sun are very important, about two orders of magnitude greater than Yarkovsky, though it matters little whether the Schwarzschild or EIH approximation is used. The Earth's relativistic terms are at the same level as Yarkovsky during the Earth encounters in 1999 and 2005. At other times, Jupiter and Venus perturbations are generally more significant, although even the lunar term can briefly exceed them during close Earth encounters.

The Yarkovsky effect is primarily a transverse acceleration and thus the transverse component of the relativistic perturbations can alias as Yarkovsky if not properly modeled. Figure 4.8 depicts how the transverse component of Earth relativistic perturbation during the 1999 close approach is several times greater than the transverse acceleration associated with the Yarkovsky effect. Because the modeled semimajor axis drift is an integral of the two curves in Fig. 4.8, neglecting Earth relativity leads to significant errors.

Table 4.5 indicates that Earth's relativity term is the most significant factor among all of those considered, at least on longer timescales as indicated by $\Delta\zeta_{2135}$. On shorter timescales, i.e., during the fitspan, Table 4.6 reveals that the perturbation of Vesta leads to a greater change in $\Delta da/dt$ than Earth relativity, although Earth relativity is still more important than Vesta for longer integrations. The uncertainty in both of these perturbations is negligible.

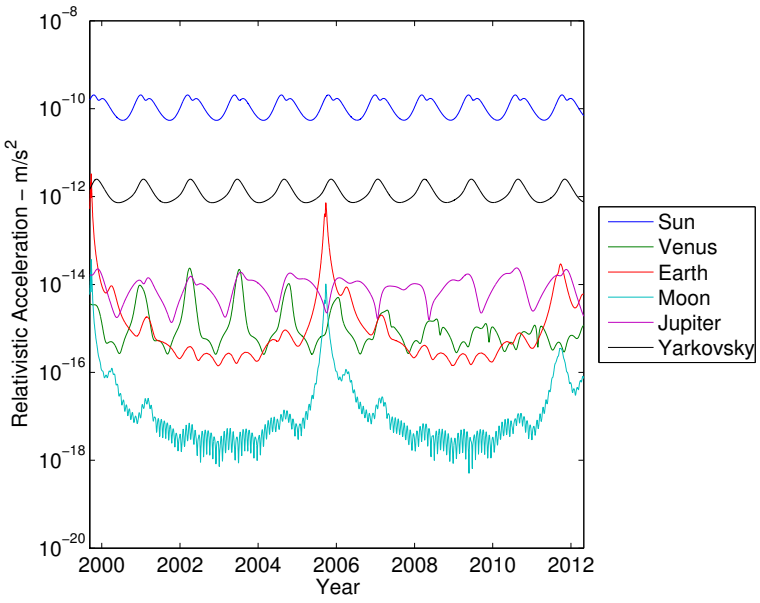

Figure 4.7: Comparison of the Yarkovsky effect with the relativistic perturbations on Bennu. The magnitude of the respective accelerations is plotted.

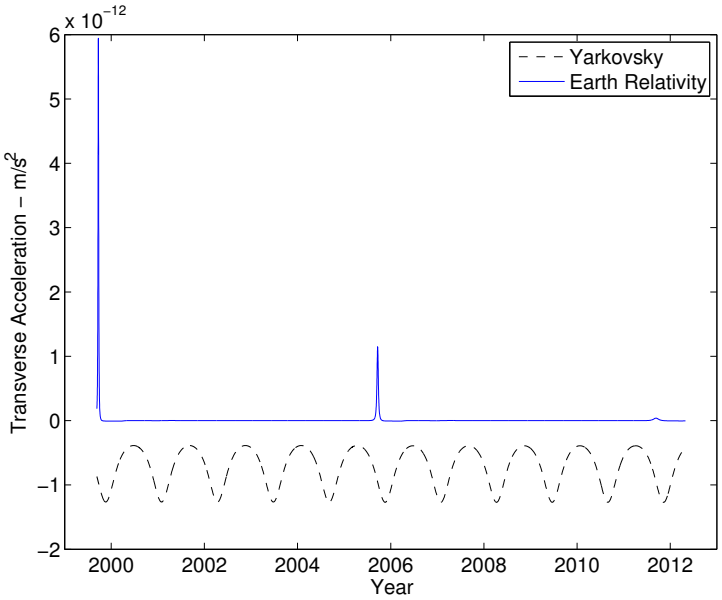

Figure 4.8: Comparison of the transverse perturbations from the Yarkovsky effect and the relativistic component due to the Earth. Earth relativity can be significantly greater in magnitude than the Yarkovsky effect during Earth encounters, and thus provides a statistically significant change in semimajor axis that must be accounted for in the dynamical model.

4.2.4 Outlier Treatment

The selection of outliers has a statistically significant effect on the orbital prediction. To explore this sensitivity, we have generated for comparison several orbital solutions with a variety of automatic outlier rejection parameter settings. These are summarized in Table 4.5, which lists the $\chi_{\rm rej}$ parameter value used in the algorithm described by Carpino et al. [2003]. The outlier rejection threshold $\chi_{\rm rej}$ is similar to the sigma level at which outlier rejection takes place, but the algorithm is more sophisticated than simple sigma clipping. The number of observations deleted in the various cases is also tabulated. The importance of careful attention to statistical outliers is indicated by the fact that the solutions are seen to progress steadily towards solution 87 as progressively more stringent requirements are placed on the outlier selection. In terms of estimated da/dt, the most inclusive approach to outliers falls about 0.5σ from the solution 87 estimate. However, even a cursory inspection of the data indicates that numerous spurious points remain in the fit for that solution. While the manual outlier rejections in solution 87 are more aggressive than even the most stringent automatic selections (e.g., $\chi_{\rm rej} = 1$), the separation between these two solutions is slight, and both are very well constrained by the observational data, with 478 and 519 optical observations, respectively. Most of the movement in the orbital predictions due to outlier treatment can be traced to a small handful of observatories with significantly biased observations. In general, the manual approach deletes more observations because it often removes the entire contribution from a problematic observatory, rather than only those that are clearly discordant with the bulk of the data.

4.2.5 Numerics and Software Validation

Giorgini et al. [2002] show that numerical integration errors are not significant for the case of the year 2880 potential impact of 1950 DA. We reach the same conclusion for Bennu by varying the integration error tolerance used in our software. Table 4.5 shows that the estimated value of da/dt is not materially affected by integrator tolerance values $\leq 10^{-14}$.

All of the results in this paper are based on the outputs of the JPL orbit determination and propagation software package. We have verified our primary JPL results by careful cross-referencing with comparable results obtained with the OrbFit orbit determination and integration package[1]. We compared the orbital solutions, the sensitivity to different settings of the dy-

[1]See http://adams.dm.unipi.it/orbfit; we used the OrbFit version 4.3, which is still in beta testing.

namical model, and the orbit propagation, and we found that these two independent software packages reproduce each other's results very well. Indeed, the comparison with the OrbFit software package revealed to us the critical importance of the Earth general relativity terms in the dynamical model. After resolving modeling discrepancies, we found that the determinations of A_T from the orbital fits was consistent to better than 0.1%, corresponding to $< 0.2\sigma$ in da/dt. We are therefore confident that our findings are not corrupted by software bugs.

4.3 Mass, Bulk Density and Implications

The linear and nonlinear Yarkovsky models both require the asteroid bulk density ρ, which was initially unknown. However, since all other parameters in the model are independently known, we can estimate this quantity. We used the linear model to compute JPL solution 86, with an associated bulk density estimate of 1314 kg/m^3. Similarly, we used the more accurate nonlinear model to obtain JPL solution 85 (Table 4.3), which includes an associated bulk density estimate $\rho = 1181$ kg/m^3. The discrepancy between the two models is a combination of factors, but overall implies that the linear model overestimates the transverse Yarkovsky force by about 11% and thus the estimated value of ρ is increased to maintain the required mean da/dt. Of particular importance is the oblateness of the Bennu shape model. This flattening leads to a diminished cross-sectional area, which tends to reduce the energy input and thereby reduce the thermal recoil acceleration in the nonlinear model. According to the theory of Vokrouhlický [1998a] this should account for a 5–10% error. Additionally, the linearization of the heat transfer problem tends to slightly increase the thermal emissions Čapek and Vokrouhlický [2005], which readily accounts for the remaining discrepancy.

The uncertainty in the bulk density estimate is a complex story due to the numerous parameters that are used in formulating the estimate. The formal uncertainty that is obtained directly from the orbit determination (Table 4.3) captures only the 0.5% uncertainty in the semimajor axis drift, and does not account for the more significant sources of uncertainty outlined in Table 4.4. The final column of that table indicates how the associated parameter uncertainty maps into the bulk density uncertainty, from which we conclude that the uncertainty in thermal inertia and asteroid size dominate over other error sources.

As described in Sec. 4.2.1, for a sphere we are sensitive to the product ρD and so the density estimate varies inversely with the asteroid size, in contrast to other density estimates that are derived from the asteroid volume. For

a non-spherical shape the Yarkovsky acceleration actually depends on the quotient of the radiative cross-sectional area and the volume A/V, rather than $1/D$, and yet the contribution to bulk density is still linear.

In contrast, the bulk density dependence on thermal inertia is markedly nonlinear (Fig. 4.9). The thermal inertia of Bennu is $\Gamma = 310 \pm 70$ J m^{-1} s$^{-0.5}$ K^{-1} Emery et al. [2014]. This value is derived from analysis of a suite of observations of thermal flux, consisting of 8–20 μm spectra of opposite hemispheres and photometry at 3.6, 4.5, 5.8, 8.0, 16, and 22 μm of 10 different longitudes using the Spitzer Space Telescope. The thermophysical modeling that results in this thermal inertia estimate incorporates the detailed shape and spin information derived from radar imaging and visible light curve photometry, and explicitly includes the effects of macroscopic surface roughness.

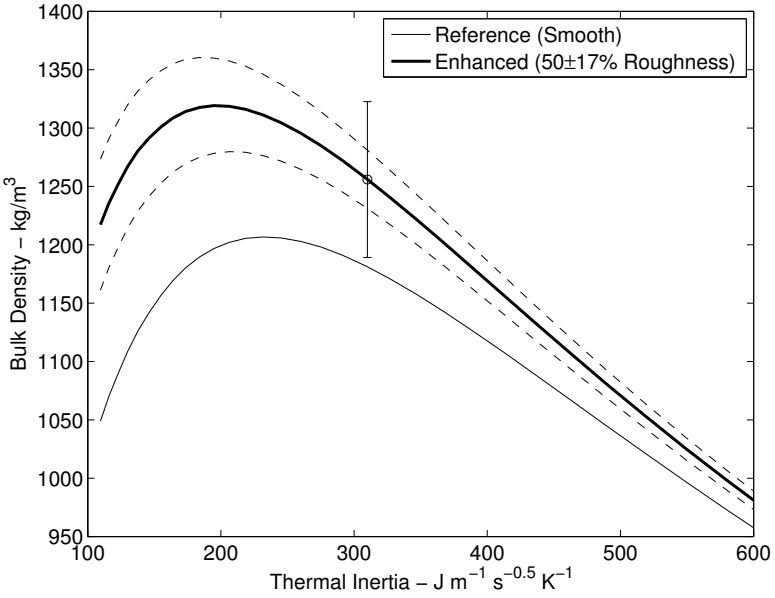

Figure 4.9: The bulk density estimate for Bennu depends nonlinearly on the estimated thermal inertia Γ. Neglecting surface roughness, we obtain a bulk density estimate of 1180 kg/m^3. However, taking into account the assumed Yarkovsky enhancement from roughness, as well as uncertainties in obliquity, diameter and thermal inertia, we obtain 1260 ± 70 kg/m^3 as depicted here.

Previous estimates of Bennu's thermal inertia Emery et al. [2010, 2012]; Müller et al. [2012] are somewhat higher (~ 600 J m^{-1} s$^{-0.5}$ K^{-1}), and have led to correspondingly lower bulk density estimates Chesley et al. [e.g., 970 kg/m^3, 2014]. There are two primary reasons for the different thermal inertia values. First, the earlier studies used only a subset of the Spitzer data, namely the spectra. Those spectra are noisy, making it difficult to scale

the different segments of the full spectra relative to each other. Different scale values affect the best-fit model surface temperature distribution, and therefore the derived thermal inertia. In contrast, Emery et al. [2014] include the large set of photometric data, which have much higher signal-to-noise than the spectral data, leading to results that are both more accurate and have significantly smaller uncertainties. Note that if the uncertainties in scale factors are included in the uncertainty estimates from the spectral data, the error bars overlap the Emery et al. [2014] estimate given above. Second, the earlier estimates assumed a spherical shape for Bennu. However, Bennu is actually fairly oblate Nolan et al. [2013]. The oblateness causes surface facets to be tilted farther away from the Sun as compared to a sphere. The models assuming spherical shape compensate for the more direct viewing geometry with a lower thermal inertia. For these reasons, we rely here on the updated thermal inertia from Emery et al. [2014].

The effects of surface roughness on Bennu are not incorporated into the ρ estimates so far, and yet Rozitis and Green [2012] used a sophisticated thermophysical model to show that the thermal effects of surface roughness always tend to increase the Yarkovsky effect. For the Bennu shape model with the roughest surface model the increase in ρ is 12.7% at the nominal thermal inertia (see Fig. 4.10), pointing to roughness as the dominant source of uncertainty.

Although we have no rigorous estimates of Bennu's roughness, it is unlikely to be either remarkably smooth or extremely rough. The thermal inertia from Emery et al. [2014] is somewhat lower than that derived for (25143) Itokawa Müller et al. [2005], which suggests that Bennu could have a somewhat smoother surface texture than Itokawa. Elsewhere, Nolan et al. [2013] find that the radar circular polarization ratio, which is a proxy for near-surface roughness at the scale of the radar wavelength (12.6 and 3.5 cm), indicates a relatively smooth surface compared to other bodies that are not particularly rough. In particular, they find Bennu has significantly lower polarization ratios than Itokawa at both wavelengths and conclude that Bennu is likely smoother than Itokawa. However, Nolan et al. [2013] did identify a boulder on Bennu with a size of 10–20 m, suggesting the presence of smaller boulders below the resolution limit of 7.5 m and a surface that is not perfectly smooth. In the absence of reliable estimates, we assume that the roughness is $50 \pm 17\%$, which covers the full range 0–100% at 3σ. This yields the "Enhanced" curve in Fig. 4.9. Inflating the reference value $\rho = 1181$ kg/m^3 by 50% of the 12.7% enhancement yields our best estimate of 1255 kg/m^3.

To develop a comprehensive estimate of the uncertainty in the presence of the nonlinearity evident in Fig. 4.9 we take a Monte Carlo approach.

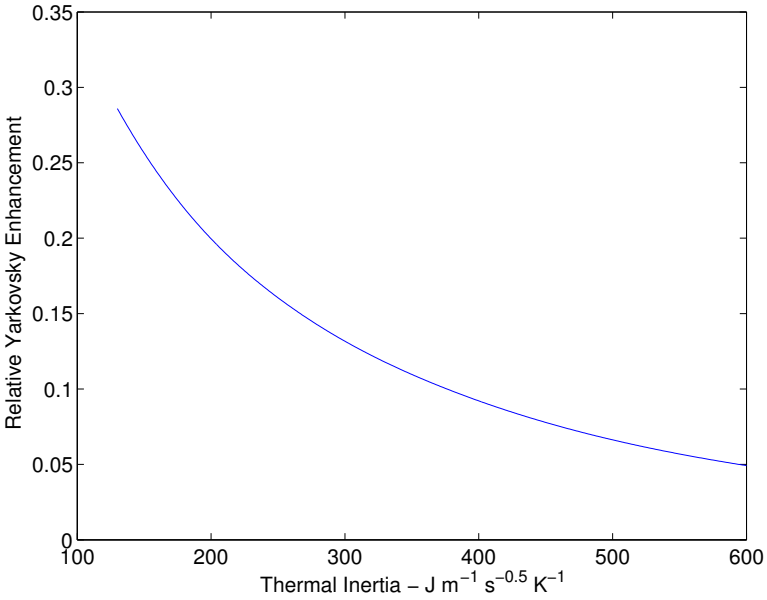

Figure 4.10: Yarkovsky effect enhancement due to 100% surface roughness as a function of thermal inertia.

We sample Γ, A/V and γ according to the normal distributions given by Table 4.4. We obtain the Yarkovsky enhancement for each case by sampling a roughness from $50 \pm 17\%$ and using it to scale the 100%-rough enhancement (from Fig. 4.10) at the sampled thermal inertia. This leads to our final bulk density estimate of $\rho = 1260 \pm 70$ kg/m^3. The associated mass, GM and area-to-mass ratio values are listed in Table 4.7.

We assume that the Yarkovsky effect is the only significant source of non-gravitational acceleration on Bennu, and in particular we do not account for the possibility of outgassing, which would corrupt our bulk density estimate if it were significant. If the direction of any hypothetical outgassing is skewed towards the evening terminator, which might be expected as the diurnal thermal wave penetrates to release buried volatiles, then it would combine to increase the magnitude of the transverse acceleration on the asteroid. In this case, the bulk density estimate should be increased to account for outgassing. Conversely, if the outgassing tends to cancel the transverse thermal recoil acceleration then our bulk density estimate will be an overestimate.

3200 Phaethon, a B-type asteroid like Bennu, has long been identified as the parent body of the Geminid meteor shower Whipple [1983]. This suggests that at least some objects of this taxonomic type have the possibility of shedding material, possibly as fine-grained material entrained in gasses released by the sublimation of volatiles. However, the only report of possible

dust release on Phaethon took place at a heliocentric distance of 0.14 au, and it has been suggested that the Geminids are shed from Phaethon due to fracturing associated with fatigue from thermal cycling and the decomposition of hydrated minerals Jewitt and Li [2010]. There is no evidence that Bennu is shedding material and, with $q \simeq 0.9\,\mathrm{au}$, solar heating is markedly lower than that experienced by Phaethon. Therefore, we do not consider it likely that outgassing is significantly affecting our results.

Is the estimated GM in Table 4.7 consistent with loose material on the equator being gravitationally bound to the surface? Nolan et al. [2013] report that the maximum equatorial diameter is 565 m. From this and the known spin rate we find a lower bound of $GM = 3.7\,\mathrm{m}^3/\mathrm{s}^2$ if we assume that the gravitational attraction exceeds the centrifugal acceleration. This is a reasonable expectation because, as discussed above, we consider it likely that Bennu's surface is dominated by cm-scale and smaller regolith. However, it is difficult to rule out the possibility that some regions along the equator are devoid of loose material, or that induration or cohesion provides sufficient binding to keep material on the surface that would otherwise depart. Even so, the assumption that material is gravitationally bound to the surface would imply $\rho > 890\,\mathrm{kg/m}^3$ which is satisfied here with a high degree of confidence.

One can compute the macroporosity, $P = 1 - \rho/\rho_M$, of an asteroid if the bulk densities of the body ρ and the appropriate meteorite analog ρ_M are known. Bennu has been identified as a B-type asteroid, and CI and CM carbonaceous chondrite meteorite samples provide the best spectral match Clark et al. [2011]. Consolmagno et al. [2008] report that CM meteorite samples have average bulk densities of $2130 \pm 190\,\mathrm{kg/m}^3$, which, taken together with our asteroid bulk density estimate and uncertainty from Table 4.7, suggests P in the range 30–50%. For CI meteorites the data are fewer and less conclusive, with different measurement techniques leading to sample bulk densities similar to those of CM meteorites or as low as $1600\,\mathrm{kg/m}^3$, which would allow P to be as low as 20% Consolmagno et al. [2008]. Overall, our judgement is that the macroporosity of Bennu is likely to be in the range $40 \pm 10\%$, but could be as low as 20%.

Bennu's estimated bulk density is comparable to values obtained for other low-albedo asteroids, from large asteroids in the main asteroid belt to smaller asteroids in the inner solar system. The average C-type asteroid in the main belt, according to estimates derived from the gravitational perturbations on the planets, predominantly Mars, is $\rho = 1290 \pm 60\,\mathrm{kg/m}^3$ Standish [2000]. This estimate is biased toward asteroids with diameters much larger than 100 km, which contain the majority of the mass among C-types. However, a flyby of the 53-km, C-type asteroid (253) Mathilde by the NEAR spacecraft

also yielded a similar density $\rho = 1300 \pm 200\,\mathrm{kg/m^3}$ Yeomans et al. [1997]. Furthermore, Marchis et al. [2008a,b] report densities of several C-complex binary asteroids in the main belt. The summary given by Marchis et al. [2008a, Table 8] suggests that the density distribution of large, C-complex binaries is $\rho = 1100 \pm 300\,\mathrm{kg/m^3}$. Among the near-Earth asteroid population, Shepard et al. [2006] report that the low-albedo binary system (276049) 2002 CE_{26} has a 3.5-km primary with bulk density $900^{+500}_{-400}\,\mathrm{kg/m^3}$, which is comparable within the error bars to that of Bennu.

What do Bennu's density and porosity tell us? To say anything useful here, we need to put Bennu into context. Our best estimates suggest Bennu is a fragment of a larger body that experienced a collision Campins et al. [2010]; Walsh et al. [2013]. Similarly, the large multiple systems examined by Marchis et al. [2008a,b] were presumably formed by large collision events [e.g., Durda et al., 2004]. One would expect these smashed up target worlds, with porosity added by the fragmentation and ejecta re-assembly process, to have low bulk densities in comparison to their meteorite analogs, and that the smallest bodies should tend to still lower density due to self-gravitation and compaction on the large bodies Baer and Chesley [2008]; Baer et al. [2011b]. However, this size dependence seems to vanish at sizes below roughly 250–300 km, below which no obvious size trend exists in macroporosity, an observation reinforced by Bennu. With this background, we argue that Bennu's porosity was produced by a similar mechanism, consistent with our hypothesis that void space and porosity were added into Bennu by its formation and/or by post-formation processes. Taken together, these arguments allow us to infer that Bennu has a heavily fractured or shattered internal structure combined with a substantial porosity. These characteristics fit the definition of a rubble pile asteroid provided by Richardson et al. [2002].

4.4 Earth Close Approaches

The deterministic prediction interval for the trajectory of Bennu extends for 481 years, from 1654 to 2135. Earth close approaches within 0.05 au during this time interval are listed in Table 4.8. Close encounters outside of this interval have encounter time uncertainties well in excess of a day. The closest approach in this interval is the nominally sub-lunar distance encounter in 2135. This deep close approach leads to strong scattering of nearby orbits, and so the subsequent impact hazard can only be explored through statistical means.

Figure 4.3 shows the time history of Bennu's orbital elements from 2000 to 2136. There are variations of a few percent due to Earth close approaches,

especially in 2135. As the Yarkovsky induced orbital drift depends on the osculating orbital elements ,see Sec. 3 there are also commensurable variations in the da/dt evolution (see Fig. 4.4).

Table 4.5 details the effect of various differing models on the b-plane coordinates $(\xi_{2135}, \zeta_{2135})$ of the close approach at the last reliably predicted Earth encounter for Bennu, which takes place in 2135. The b-plane is oriented normal to the inbound hyperbolic approach asymptote and is frequently used in encounter analysis. The (ξ, ζ) coordinates on the b-plane are oriented such that the projected heliocentric velocity of the planet is coincident with the $-\zeta$-axis. In this frame the ζ coordinate indicates how much the asteroid is early ($\zeta < 0$) or late ($\zeta > 0$) for the minimum possible distance encounter. In absolute value, the ξ coordinate reveals the so-called Minimum Orbital Intersection Distance (MOID), which is the minimum possible encounter distance that the asteroid can attain assuming only changes to the timing of the asteroid encounter. For a more extensive discussion of these coordinates see Valsecchi et al. [2003] and references therein. In Table 4.5, the tabulated da/dt differences are indicative of the importance of the effect on the 1999–2012 time frame of the observation set, while ζ_{2135} provides an indication of how important the term is for the much longer integration from 2011 to 2135.

4.4.1 Impact Hazard Assessment

The geometry of Bennu's orbit allows deep close approaches to the Earth, which require a careful assessment of the associated potential collision hazard. Figure 4.11 shows the dependence on time of the Minimum Orbit Intersection Distance Gronchi [MOID, see, e.g., 2005]. According to the secular evolution, the MOID reaches its minimum near the end of the next century while short periodic perturbations make it cross the Earth impact cross section threshold at different epochs from 2100 to 2300, which is therefore the time period for which we must analyze possible close approaches. This objective is similar to that discussed by Milani et al. [2009], however we bring new analysis tools to bear on the problem and we have the benefit of crucial astrometric data not available in 2009. We recall that Milani et al. [2009] based much of their analysis on the variability of the 2080 encounter circumstances, finding that, for the observational data then available, this was the last encounter that was well constrained, and after which chaotic scattering made linear analysis infeasible. With the current data set, future encounter uncertainties remain modest until after 2135 (Table 4.8), and nonlinear analysis techniques are necessary for subsequent encounters. Thus the 2135 encounter is the central focus in our current impact hazard assessment.

We performed a Monte Carlo sampling Chodas and Yeomans [1999] in the

7-dimensional space of initial conditions and bulk density. Figure 4.12 shows the distribution of the Monte Carlo samples on the 2135 b-plane. The b-plane plot depicts the geocentric locations of the incoming hyperbolic asymptote of the Monte Carlo samples on the plane orthogonal to the asymptote, indicating the distance and direction of the closest approach point of a fictitious unperturbed trajectory Valsecchi et al. [see, e.g., 2003]. The linear mapping of the uncertainty region is a poor approximation as we can see from the asymmetry of the distribution. As expected, the uncertainty region gets stretched along ζ, which reflects time of arrival variation and is thus related to the along-track direction.

By propagating the Monte Carlo samples through year 2250 we can determine the Virtual Impactors (VIs), i.e., the Virtual Asteroids (VAs) compatible with the orbital uncertainty corresponding to an impacting trajectory. The positions of the VIs in the 2135 b-plane define the 2135 keyholes, which are the coordinates on the b-plane corresponding to a subsequent impact Chodas [1999]. On the b-plane of a given post-2135 encounter we can interpolate among nearby samples to identify the minimum possible future encounter distance. When this minimum distance is smaller than the Earth radius, the keyhole width is obtained by mapping the chord corresponding to the intersection between the line of variations and the impact cross section back to the 2135 b-plane. This procedure allows us to develop a map of the keyholes in the b-plane. For Bennu we found about 200 keyholes in the 2135 b-plane with widths ranging from 1.6 m to 54 km.

Figure 4.13 shows the probability density function (PDF) of ζ_{2135} resulting from the Monte Carlo sampling. As already noted, the linear approximation is not valid in this case, and so the PDF is distinctly non-gaussian. The figure also reveals the keyhole map in ζ_{2135}, where the vertical bars correspond to the keyholes > 100 m in width and the height of the bars is proportional to the width. For a given keyhole the impact probability (IP) is simply the product of the PDF and the keyhole width. For each of the 78 keyholes larger than 100 m and with an IP $> 10^{-10}$, Table 4.9 reports the impact year, the keyhole width, the impact probability, and the associated Palermo Scale Chesley et al. [2002]. The cumulative IP is 3.7×10^{-4} and the cumulative Palermo Scale is -1.70. There are eight keyholes corresponding to an IP larger than 10^{-5}. Among these, the year 2196 has the highest IP, 1.3×10^{-4}, which arises primarily from two separate but nearby keyholes.

Figure 4.14 shows the dependence of the number of keyholes and the cumulative IP on the minimum keyhole width. Although the number of keyholes increases with decreasing minimum width, the cumulative IP is essentially captured already by only the largest $\sim 10\%$ of keyholes, i.e., those with width $\gtrsim 1$ km.

Post-2135 Earth encounters correspond to resonant returns Valsecchi et al. [2003]. Table 4.10 describes the main features of the resonant returns corresponding to an IP $> 10^{-5}$.

It is important to assess the reliability of our results. On one hand, the keyholes are essentially a geometric factor that does not depend on the modeling of Bennu's orbit. On the other hand, the PDF on the 2135 b-plane can be strongly affected by the dynamical model and the statistical treatment applied to the observations. Table 4.5 reports the 2135 b-plane coordinates as a function of the different configurations of the dynamical model and different settings for the removal of outliers from the observational data set. It is worth pointing out that neglecting the Earth relativistic term produces a large error comparable to a 3σ shift in the orbital solution. In contrast, the contribution of solar radiation pressure is rather small. As already discussed in Sec. 4.2.1, this can be explained by the fact that the action of solar radiation pressure is aliased with the solar gravitational acceleration, and neglecting solar radiation pressure in the model is therefore compensated when fitting the orbital solution to the observations. The different Yarkovsky models give ζ_{2135} predictions within several thousand kilometers of each other. Interestingly, the shift due to the different astrometric outlier treatment is comparable to the one due to the relativistic term of the Earth and much larger than any shift due to the other dynamical configurations. Table 4.6 shows the effect of removing each of the 24 perturbing asteroids included in the dynamical model. Ceres, Pallas, and Vesta give the largest contributions. Among smaller perturbers, Hebe and Iris turn out to be the most important.

We used OrbFit (see Sec. 4.2.5) to cross-check the keyhole locations and widths, the PDF of Fig. 4.13, and the sensitivity to the different configurations of the dynamical model. We found good overall agreement with only one noticeable difference related to the PDF: while the PDF shapes are similar, the peaks are separated by about 40000 km in ζ_{2135}. This difference is related to the 0.2σ shift in the nominal solution (see Sec. 4.2.5) and is in part due to the fact that OrbFit presently uses JPL's DE405 planetary ephemeris rather than DE424, which is used in our analysis.

4.4.2 Statistical Close Approach Frequency

We now want to characterize the Earth encounter history for Bennu's orbital geometry. The first step is to understand the statistical properties of Earth encounters during a node crossing cycle (see Fig. 4.11). For this we generated a dense sampling of 20,000 Virtual Asteroids on the Solution 87 orbit (Table 4.3), but with a uniform sampling of the mean anomaly from the full range, 0 to 2π, to randomize the node crossing trajectory. For each VA

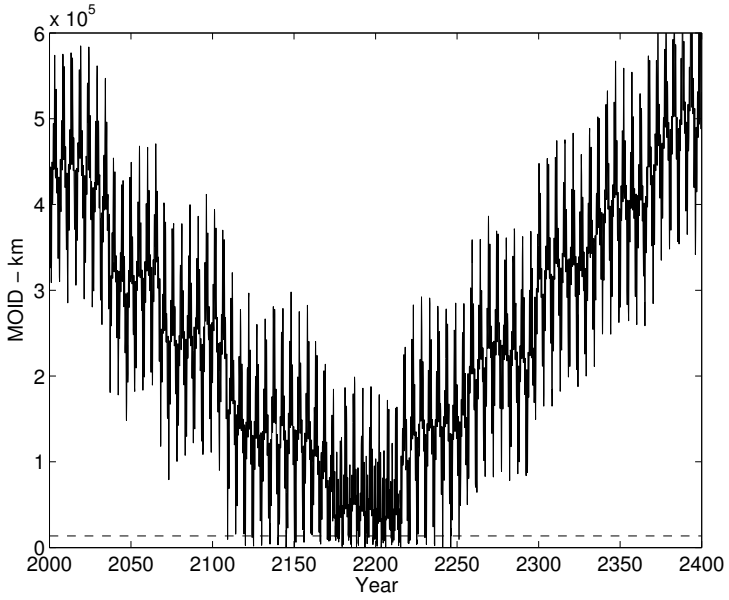

Figure 4.11: Time history of the MOID. The Earth impact cross-section (2.1 Earth radii) is marked by the dashed line.

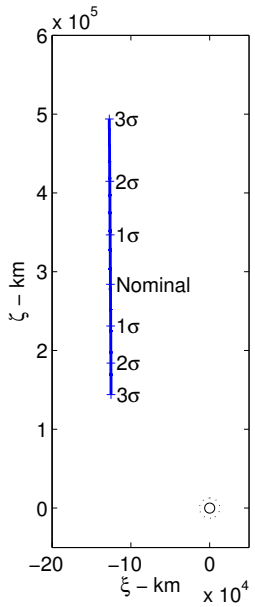

Figure 4.12: Uncertainty region on the b-plane of the 2135 encounter. The Earth is plotted to scale at the origin, and the impact cross-section is indicated by the dots.

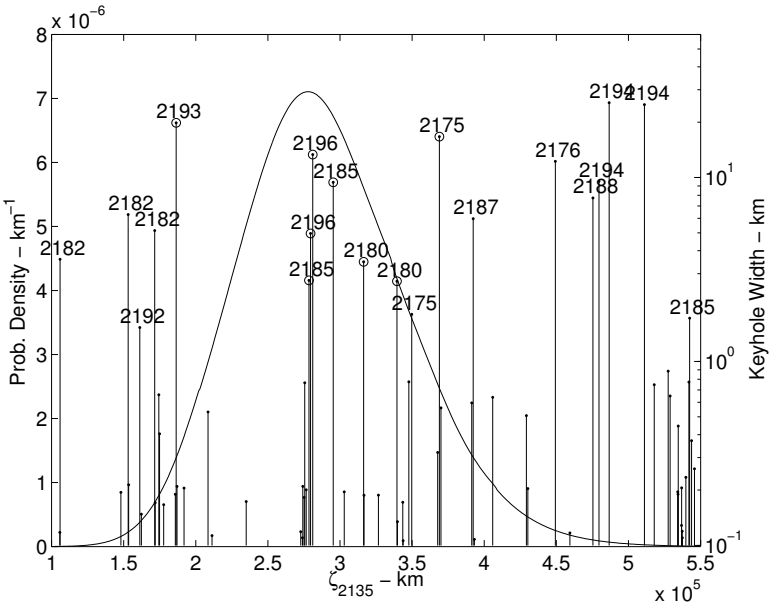

Figure 4.13: A map of the Bennu impact keyholes on the 2135 b-plane. The probability density is given by the curve with the left ordinate, and the keyholes are indicated by the vertical lines at their respective ζ_{2135} positions with their widths given on the right ordinate. For clarity only keyholes wider than 1 km are labeled with the year of impact and only keyholes > 100 m in width are depicted. Potential impacts with impact probability greater than 10^{-5} are marked with a circle at the top of the vertical bar.

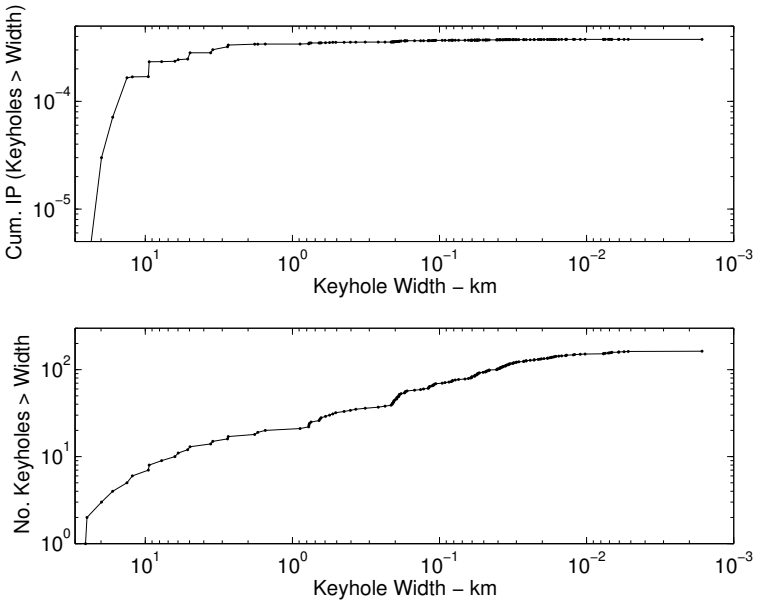

Figure 4.14: Cumulative impact probability (upper) and cumulative number of keyholes found (lower), each as a function of diminishing keyhole width. The cumulative impact probability over all potential impacts is 3.7×10^{-4}.

we recorded all of the close approaches within 0.015 au during JPL's DE424 ephemerides time interval, i.e., from year −3000 to year 3000, which contains only one node crossing cycle.

We modeled the number of Earth approaches within a given distance in a given time frame as a Poisson random variable. We estimated the Poisson parameter λ by averaging over the trajectories of the VAs. Figure 4.15 shows the probability of having at least one close approach within a given geocentric distance during a node crossing cycle (dashed line). For instance, during each node crossing cycle we have 38% probability of a close approach within the lunar distance and a 6×10^{-4} probability of an impact. This is consistent with our predictions for the next node crossing taking place around 2200, for which we have similar probabilities of impact and sub-lunar distance encounters.

To analyze the long-term history we need to account for the secular evolution of Bennu's orbit. As reported by NEODyS[2], Bennu's perihelion precession period is 28100 yr and each precession period contains four node crossings. For a given time interval we can compute the expected number of node crossings and suitably scale the probability of an encounter within a given distance during a single node crossing cycle. The solid lines in Fig. 4.15

[2]http://newton.dm.unipi.it/neodys/index.php?pc=1.1.6&n=bennu

show the probability of at least one Earth encounter within a given distance for time intervals of 1 yr, 1000 yr, and 1,000,000 yr. For example, in a 1000 yr time interval the probability of a close encounter within a lunar distance is 7% while the probability of an impact is 9×10^{-5}. This indicates that for Bennu's current orbital configuration the mean Earth impact interval is ~ 10 Myr. Note that the precession period assumed here is for the nominal orbit of Table 4.3, while the precession period does change due to planetary interactions. For instance, the nominal semimajor axis increases and the uncertainty grows after the 2135 encounter, causing the post-2135 precession period to be in the range 28900–33400 years. Delbò and Michel [2011] analyze the orbital evolution of Bennu on a much longer time frame than a single node crossing and find that the median lifetime of Bennu could be ~ 34 Myr, but their study allowed for substantial orbital evolution to take place, while our results are valid for the present-day, un-evolved orbit.

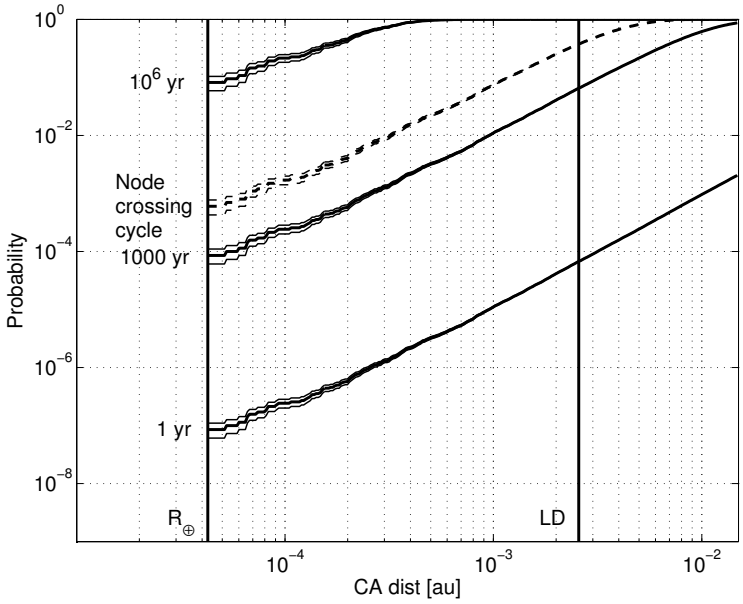

Figure 4.15: Probability (with corresponding 1σ error bars) of having at least one close approach (CA) within a given distance for different time intervals. The dashed curve is for a node crossing cycle, while solid line are for 1 yr, 1000 yr, and 1,000,000 yr. The Earth radius ($R_\oplus$) and lunar distance (LD) are marked by vertical lines.

4.5 OSIRIS-REx Science

Continued study of Bennu's trajectory is a significant element of the OSIRIS-REx science investigation. In particular, the characterization of the Yarkovsky effect is planned to be conducted on two tracks. On one track, Earth-based radio tracking of the spacecraft and optical navigation images of the asteroid from the spacecraft will be used to derive high-precision asteroid position measurements. These position updates will afford refined estimates of the nongravitational accelerations that the asteroid experiences. On the other track, science observations by the OSIRIS-REx spacecraft will allow the development of a complete thermophysical model of the asteroid, yielding a precise estimate of the thermal recoil acceleration, as well as direct and reflected solar radiation pressure acting on the body. A comparison of the acceleration profile from these two independent approaches will provide significant insight into the quality of current thermophysical models, and, for example, the extent to which surface roughness affects the net thermal recoil acceleration Rozitis and Green [2012].

But first the OSIRIS-REx must rendezvous with Bennu, and knowledge of the asteroid position is required for accurate navigation of the spacecraft during the initial encounter. Our current prediction calls for Radial-Transverse-Normal (RTN) position uncertainties of (3.3, 3.8, 6.9) km on 2018-Sep-10, during the planned OSIRIS-REx rendezvous. These are formal 1-sigma error bars, and may not account for some unmodelled systematic effects, although we are not aware of any that are significant. In any case, such low uncertainties suggest that asteroid ephemeris errors will not be a significant complicating factor during the OSIRIS-REx rendezvous with Bennu.

To characterize the Bennu ephemeris improvement provided by the OSIRIS-REx mission, we simulate 8 post-rendezvous, pseudo-range points from the geocenter to the asteroid center of mass. The simulated measurements are placed at monthly intervals from 2018-Dec-01 to 2019-Jul-01, and they assume an a priori uncertainty of 0.1 μs in time delay, which translates to 15 m in range. The trajectory constraints from the OSIRIS-REx radio science effort are likely to be somewhat better than assumed for this study. Table 4.11 lists the uncertainties obtained before and after the inclusion of these simulated OSIRIS-REx radio science data. We find that the uncertainty in the transverse nongravitational acceleration parameter A_T, and by extension the uncertainty in the mean da/dt, drops by roughly a factor 6–7, bringing the precision to better than 0.1%.

The OSIRIS-REx radio science observations will not only refine the Yarkovsky acceleration acting on the asteroid, but also enable significantly improved future predictions. Table 4.11 reveals that our current predictions call for

position uncertainties of a few km at the end of proximity operations on 2020-Jan-04, which could be reduced to under 100 m with the simulated mission data. The associated velocity uncertainties are of order 1 mm/s with current information, but could fall by a factor 50 or more with the OSIRIS-REx data.

Similarly, we find that the OSIRIS-REx radio science data could narrow the ζ_{2135} uncertainty region on the 2135 b-plane by a factor ~ 60. This would be similar to the reduction in uncertainty seen between the Milani et al. [2009] paper and the present paper. The implication is that the hazard assessment will be dramatically altered by the OSIRIS-REx radio science effort. The self-similar nature of the keyholes on the 2135 b-plane suggest that the cumulative probability is likely to remain around 10^{-4}, although if the nominal ζ_{2135} prediction does not change appreciably the cluster of relatively wide keyholes near the current nominal (Fig. 4.13) could lead to a cumulative probability of impact in excess of 10^{-2}.

Besides providing direct radio science position measurements of the asteroid, OSIRIS-REx will refine and test other aspects of the Bennu ephemeris problem. The mission objectives include

- a search for outgassing and the incorporation of any activity into force models,
- direct measurement of the asteroid mass, providing ground truth for the mass determination technique presented here,
- precision radiometry of both reflected and thermally emitted radiation with high spatial resolution, providing ground truth for the thermal accelerations presented in this paper, and
- analysis of the returned sample, which will provide a direct measurement of the thermal, dielectric, and bulk density of the asteroid surface.

4.6 Discussion and Conclusions

Understanding of an asteroid's physical properties becomes essential whenever the Yarkovsky effect or other nongravitational accelerations are a crucial aspect of the orbit estimation problem. Radar astrometry of asteroids can provide surprising and important constraints, not only on an asteroid's orbit, but also on its physical properties. In the case of Bennu, this information has immense value for space mission designers. We have seen that the availability of well-distributed radar astrometry over time spans of order a decade can

constrain asteroid orbits to the extent that precise estimates of the Yarkovsky effect can be derived. When coupled with thermal inertia information derived from other sources, such as the Spitzer Space Telescope, important parameters such as mass, bulk density and porosity can be derived. Combining Yarkovsky detections with thermal inertia measurements to infer the asteroid mass can be implemented on other near-Earth asteroids, including potential space mission targets. This technique is the focus of ongoing work. Indeed, Bennu clearly demonstrates that even weak radar detections can have considerable science value, raising the imperative to aggressively pursue every available radar ranging opportunity for potential Yarkovsky candidates.

Our bulk density estimate for Bennu implies a primitive body with high porosity of $40 \pm 10\%$. The implication is that Bennu must be comprised of a gravitationally bound aggregate of rubble, a conclusion that is reinforced by its shape, which is spheroidal with an equatorial bulge consistent with the downslope movement and accumulation of loose material at the potential minimum found at the equator [Nolan et al., 2013]. This bodes well for the OSIRIS-REx sample collection effort, which requires loose material at the surface for a successful sample collection, although nothing in this study constrains the size distribution of the surface material.

The statistical encounter frequency with Earth (Fig. 4.15) can be used to understand the rate of encounters that could alter the shape and spin state of a body through tidal interactions [e.g., Nesvorný et al., 2010; Walsh and Richardson, 2008]. Scheeres et al. [2005] have shown that tidal interactions at a distance of 6 Earth radii can appreciably alter the spin state of 99942 Apophis. More distant encounters could still excite the spin state enough to induce seismic activity, leading to a periodic resurfacing of the asteroid that may have implications for interpretation of Bennu samples returned by OSIRIS-REx.

We have seen that the current levels of uncertainty in Bennu's orbit are low enough that unprecedented levels of accuracy are required in the dynamical model that governs the trajectory. For example, the relativistic perturbation of planetary gravity fields, in particular that of Earth, must be incorporated to obtain reliable results. The future addition of OSIRIS-REx radio science data will again decrease the orbital uncertainties by 1–2 orders of magnitude, which will likely require even finer scale refinements to our dynamical model than used here. However, difficulties in understanding the proper statistical treatment of asteroid optical astrometry, and in particular the identification of statistical outliers, will likely remain a dominant source of uncertainty that is not properly captured by a posteriori covariance analysis.

Thus our findings for the post-OSIRIS-REx orbital uncertainties of Bennu

may be illusory. The finding that ζ_{2135} uncertainties may be reduced as low as 1000 km with the OSIRIS-REx radio science data assumes that our Yarkovsky model, including the asteroid spin state, holds through 2135. Thus a host of model refinements may be necessary to properly characterize the trajectory out to 2135. Notwithstanding the next radar observation opportunity in January 2037, we may reach an uncertainty limit that prevents us from improving predictions any further until models can improve or the prediction interval is significantly reduced. As an example, the post-2135 predictability will markedly improve after the 0.005 au Earth close approach in 2060, and it is reasonable to expect that at least some potential impacts will persist until that time.

Table 4.1: Radar Astrometry for (101955) Bennu.

Date & Time (UTC - Receive)	Measurement (μsec or Hz)	Uncertainty (μsec or Hz)	Station
Delay			
2011-09-29 11:55:00	202378520.04	2.0	Arecibo
2011-09-28 11:08:00	199711477.27	2.0	Arecibo
2011-09-27 11:39:00	197293588.79	2.0	Arecibo
2005-10-02 14:10:00	57762582.67	0.5	Arecibo
2005-10-02 12:55:00	57594268.2	0.5	Arecibo
2005-09-28 13:35:00	45734943.4	0.5	Arecibo
2005-09-28 11:57:00	45550976.4	0.5	Arecibo
2005-09-20 11:24:00	33024222.68	0.5	Arecibo
2005-09-20 09:09:00	33024251.3	0.5	Arecibo
2005-09-19 12:50:00	33215505.86	1.0	Goldstone
2005-09-18 12:20:00	33873463.	1.0	Goldstone
2005-09-16 09:27:00	36609699.09	0.5	Arecibo
2005-09-16 08:45:00	36658796.03	0.5	Arecibo
1999-10-01 13:40:00	35441297.	1.0	Goldstone
1999-09-25 12:55:00	17785960.83	1.0	Arecibo
1999-09-25 11:09:00	17634668.28	1.0	Arecibo
1999-09-24 12:23:00	15955075.55	1.0	Arecibo
1999-09-24 10:26:00	15838961.63	1.0	Arecibo
1999-09-23 11:28:00	14846130.16	1.0	Arecibo
1999-09-23 09:36:00	14800106.19	1.0	Arecibo
1999-09-23 09:30:00	14820631.	5.0	Goldstone
1999-09-21 10:20:00	15418454.	10.0	Goldstone
Doppler			
2011-09-29 11:55:00	-72841.0156	1.0	Arecibo
2011-09-28 11:08:00	-68554.7858	1.0	Arecibo
2011-09-27 11:39:00	-66400.2088	1.0	Arecibo
2005-09-28 12:00:00	-73137.0697	1.0	Arecibo
2005-09-20 09:06:00	2631.7168	1.0	Arecibo
2005-09-16 08:44:00	47170.7359	1.0	Arecibo
1999-09-21 09:00:00	135959.	5.0	Goldstone

Notes:

- Transmit frequency is 2.38 GHz at Arecibo and 8.56 GHz at Goldstone.
- All measurements are referenced to the body center of mass.
- Measurements are also available online at `http://ssd.jpl.nasa.gov/?radar`.

Table 4.2: Radar observations of Bennu from 2011. Each line gives the UTC date and start/stop times, the number of transmit-receive cycles (runs), and the direction and distance to Bennu at the mid-epoch on each date. All observations used a 2 microsecond baud (corresponding to a range resolution of 300 meters), an 8191-length code, and JPL/Horizons orbital solution 70.

UTC Date	Start Time	Stop Time	Runs	RA (°)	DEC (°)	Distance (au)
2011-Sep-27	10:30:36	12:53:45	21	114.3	+28.3	0.1977
2011-Sep-28	10:34:40	12:56:31	10	116.2	+28.5	0.2002
2011-Sep-29	10:38:31	13:02:29	18	118.1	+28.6	0.2028

Table 4.3: JPL orbit Solns. 85 and 87 for Bennu, Ecliptic J2000 Frame.

Solution 85 (Nonlinear Yarkovsky Model)	
Epoch	2011-Jan-1.0 TDB
Semimajor axis (a)	1.126391025996(42) au
Eccentricity (e)	0.203745112(21)
Perihelion dist. (q)	0.896894360(24) au
Perihelion time (t_p)	2010-Aug-30.6419463(30) TDB
Long. of Asc. Node (Ω)	2.0608668(37)°
Arg. of perihelion (ω)	66.2230699(55)°
Inclination (i)	6.0349391(27)°
Bulk Density (ρ)	1181.1(6.3) kg/m^3†
χ^2 ‡	68.37
Solution 87 (Transverse Yarkovsky Model, $d = 2.25$)	
Epoch	2011-Jan-1.0 TDB
Semimajor axis (a)	1.126391026404(40) au
Eccentricity (e)	0.203745114(21)
Perihelion dist. (q)	0.896894358(24) au
Perihelion time (t_p)	2010-Aug-30.6419468(30) TDB
Long. of Asc. Node (Ω)	2.0608670(37)°
Arg. of perihelion (ω)	66.2230705(55)°
Inclination (i)	6.0349388(27)°
Transverse accel. (A_T)	$-4.618(24) \times 10^{-14}$ au/d^2
χ^2 ‡	68.73

Notes:
Numbers in parentheses indicate the 1σ formal uncertainties of the corresponding (last two) digits in the parameter value.
† The bulk density uncertainty is marginal only with respect to the orbital elements, and is conditional with respect to the physical parameters that can affect the thermal modeling. In particular, the uncertainties in effective diameter, thermal inertia and obliquity are not captured here, and these lead to a marginal uncertainty an order of magnitude greater. See Fig. 4.9 and the discussion in Sec. 4.3.
‡ χ^2 denotes the sum of squares of normalized postfit residuals.

Table 4.4: Physical characteristics of (101955) Bennu and associated marginal uncertainty in estimate of bulk density ρ. Tabulated error bars represent assumed 1σ uncertainties.

Parameter	Value & Uncertainty	Ref.	ρ Uncert.
Thermal inertia	$\Gamma = 310 \pm 70\ \mathrm{J\,m^{-1}\,s^{-0.5}\,K^{-1}}$	A	+2.1%/−4.1%
Cross-sectional Area/Volume	$A/V = 3.06 \pm 0.06 \times 10^{-3}\ \mathrm{m^{-1}}$	B	±2.0%
Obliquity of equator	$\gamma = 175^\circ \pm 4^\circ$	B	+0.4%/−0.9%
Surface emissivity	$\epsilon = 0.90 \pm 0.05$	A	±0.3%
Bond albedo	$A = 0.017 \pm 0.002$	A	±0.2%
Rotation period	4.29746 ± 0.002 h	B	±0.0%

References: A— Emery et al. [2014], B— Nolan et al. [2013]

Table 4.5: Dynamical Effect of Several Model Variations. The columns indicate the type of model variation and the associated change in semimajor axis drift rate da/dt or 2135 b-plane coordinates $(\xi_{2135}, \zeta_{2135})$. Tabulated Δ values are with respect to JPL solution 87 (Table 4.3), for which $da/dt = -18.973 \times 10^{-4}$ au/My at epoch 2011-Jan-1.0 and $(\xi_{2135}, \zeta_{2135}) = (-125\,932\,\text{km}, 281\,597\,\text{km})$.

Model	$\Delta da/dt$ (10^{-4} au/My)	$\Delta\xi_{2135}$ (km)	$\Delta\zeta_{2135}$ (km)	Remarks
Yarkovsky Model				
Nonlinear	-0.004	-43	6251	Soln. 85
Linear	0.006	-16	2096	Soln. 86
$d = 2.25$	0.000	0	0	Soln. 87
$d = 2.00$	0.006	-21	3423	
Asteroid Perturbations				
25 Perturbers	0.000	0	0	Soln. 87
BIG-16 only	-0.004	2	-409	
CPVH only	-0.010	22	-3714	
Earth Oblateness Limit				
10. au	0.000	0	-70	
1. au	0.000	0	0	Soln. 87
0.1 au	0.000	0	-25	
0.01 au	-0.004	11	-1822	
0.001 au	-0.004	10	-1703	
Relativity Model				
Full EIH	0.000	0	0	Soln. 87
Basic Sun Model	0.305	-1128	168469	
EIH Sun only	0.295	-1069	160086	
w/o Mercury	-0.001	1	-240	
w/o Venus	0.017	-54	8954	
w/o Earth	0.291	-1059	159130	
w/o Mars	0.000	0	-43	
w/o Jupiter	-0.012	46	-7652	
w/o Saturn	-0.004	11	-1859	
w/o Uranus	0.000	-1	168	
w/o Neptune	0.000	-0	60	
w/o Moon	0.004	-11	1801	
Outlier Rejection				
$\chi_{\text{rej}} = 3$	0.049	-537	84670	7 del.
$\chi_{\text{rej}} = 2$	0.026	-414	65916	15 del.
$\chi_{\text{rej}} = 1.5$	0.018	-243	39502	24 del.
$\chi_{\text{rej}} = 1$	0.003	-13	2220	49 del.
Manual	0.000	0	0	91 del., Soln. 87
Integration Tolerance				
10^{-16}	0.000	-0	60	
10^{-15}	0.000	0	0	Soln. 87
10^{-14}	-0.002	4	-721	
10^{-13}	-0.003	-5	831	
Other				
Area/Mass= 0	-0.001	5	-1122	
DE405 w/BIG-16	-0.048	84	-14160	

Note: For reference, the formal uncertainty in the da/dt estimate is 0.100×10^{-4} au/My and in ζ_{2135} is roughly 60,000 km.

Table 4.6: Main belt asteroid perturbers, associated GM values and the dynamical relevance of each as in the previous table.

Count	IAU No.	Name	GM (km^3/s^2)	$\Delta da/dt$ (10^{-4} au/My)	$\Delta\xi_{2135}$ (km)	$\Delta\zeta_{2135}$ (km)
CPVH						
1	1	Ceres	63.13[a]	-0.118	298	-51351
2	2	Pallas	13.73[b]	-0.109	295	-50754
3	4	Vesta	17.29[c]	0.437	-893	136194
4	10	Hygiea	5.78[a]	0.002	-11	1661
Additions for BIG-16						
5	3	Juno	1.82[d]	0.002	-8	1126
6	6	Hebe	0.93[d]	0.019	-65	10790
7	7	Iris	0.86[d]	-0.014	57	-9532
8	15	Eunomia	2.10[d]	-0.001	1	-260
9	16	Psyche	1.81[d]	-0.005	16	-2615
10	29	Amphitrite	0.86[d]	0.000	-0	30
11	52	Europa	1.59[d]	0.001	-5	643
12	65	Cybele	0.91[d]	0.000	1	-188
13	87	Sylvia	0.99[d]	0.000	-1	66
14	88	Thisbe	1.02[d]	-0.007	19	-3099
15	511	Davida	2.26[d]	0.000	1	-114
16	704	Interamnia	2.19[d]	0.000	0	-7
Additions for Bennu						
17	11	Parthenope	0.39[d]	-0.006	18	-3031
18	14	Irene	0.19[d]	-0.002	6	-1013
19	56	Melete	0.31[d]	-0.002	-6	1070
20	63	Ausonia	0.10[d]	-0.002	4	-731
21	135	Hertha	0.08[d]	0.001	-6	872
22	259	Aletheia	0.52[d]	0.000	0	-31
23	324	Bamberga	0.69[d]	-0.001	-4	628
24	419	Aurelia	0.12[d]	0.002	2	-259
25	532	Herculina	0.77[d]	0.005	-13	2200

Refs.: [a]Baer et al. [2011b], [b]Konopliv et al. [2011], [c]Russell et al. [2012], [d]Carry [2012].

Table 4.7: Bennu bulk density and related quantities with 1σ uncertainties.

Bulk density ρ (kg/m^3)	1260 ± 70
Mass M (10^{10} kg)	7.8 ± 0.9
GM (m^3/s^2)	5.2 ± 0.6
Area-to-mass ratio (10^{-6} m^2/kg)	2.4 ± 0.1

Table 4.8: Bennu Deterministic Earth Approaches Closer than 0.05 AU (JPL solution 76).

Date (TDB)	Nom. Dist. (AU)	3σ Min. (AU)	3σ Max. (AU)	1σ Time Uncert. (s)	1σ ζ Uncert. (km)
1654 Sep 17.89194	0.022033	0.010586	0.035240	49590	816253
1788 Sep 20.56364	0.009771	0.009304	0.010254	2237	32739
1848 Sep 21.91904	0.007915	0.007892	0.007938	105	1573
1911 Sep 22.88762	0.014178	0.014177	0.014179	2.4	38
1970 Sep 27.10790	0.021403	0.021403	0.021403	1.6	16
1999 Sep 22.76422	0.014686	0.014686	0.014686	$\ll 1$	1.1
2005 Sep 20.44528	0.033130	0.033130	0.033130	$\ll 1$	1.2
2054 Sep 30.04163	0.039299	0.039299	0.039299	1.6	11
2060 Sep 23.02530	0.005008	0.005008	0.005008	1.0	15
2080 Sep 22.02378	0.015560	0.015427	0.015693	360	7318
2135 Sep 25.40942	0.002009	0.000819	0.003549	4746	79674

Table 4.9: Keyholes in 2135 b-plane and associated impact probabilities, JPL solution 76.

Year	ζ_{2135} (km)	ζ-width (km)	Impact Prob.	Palermo Scale	Year	ζ_{2135} (km)	ζ-width (km)	Impact Prob.	Palermo Scale
2192	92981	0.17	1.04×10^{-10}	−8.27	2195	343783	0.11	4.15×10^{-07}	−4.67
2187	93280	0.32	2.01×10^{-10}	−7.97	2181	347699	0.78	2.86×10^{-06}	−3.80
2198	99162	0.25	3.33×10^{-10}	−7.78	2175	349704	1.80	6.43×10^{-06}	−3.43
2187	105731	0.12	3.44×10^{-10}	−7.74	2186	367729	0.32	8.12×10^{-07}	−4.36
2182	105945	3.59	1.08×10^{-08}	−6.23	**2175**	**368877**	**16.67**	$\mathbf{4.13 \times 10^{-05}}$	**−2.63**
2197	148127	0.19	3.08×10^{-08}	−5.81	2181	370007	0.56	1.35×10^{-06}	−4.13
2182	153125	6.29	1.42×10^{-06}	−4.11	2193	391326	0.60	8.52×10^{-07}	−4.36
2187	153481	0.21	4.94×10^{-08}	−5.58	2187	392308	5.97	8.34×10^{-06}	−3.35
2192	161203	1.53	5.83×10^{-07}	−4.52	2198	393200	0.11	1.47×10^{-07}	−5.13
2193	162322	0.15	6.04×10^{-08}	−5.51	2181	405893	0.64	6.27×10^{-07}	−4.46
2182	171554	5.15	3.55×10^{-06}	−3.71	2187	429187	0.51	2.43×10^{-07}	−4.89
2187	171842	0.17	1.19×10^{-07}	−5.20	2181	430234	0.20	9.41×10^{-08}	−5.28
2187	174357	0.66	5.25×10^{-07}	−4.55	2176	449272	12.23	3.07×10^{-06}	−3.76
2192	174935	0.40	3.31×10^{-07}	−4.76	2193	459392	0.12	2.09×10^{-08}	−5.97
2194	177766	0.17	1.57×10^{-07}	−5.09	2188	475391	7.74	7.99×10^{-07}	−4.37
2199	185793	0.19	2.56×10^{-07}	−4.89	2194	479545	9.54	8.50×10^{-07}	−4.36
2193	**186415**	**19.84**	$\mathbf{2.75 \times 10^{-05}}$	**−2.85**	2194	486578	25.51	1.77×10^{-06}	−4.04
2198	186996	0.21	2.97×10^{-07}	−4.83	2194	511097	24.90	6.94×10^{-07}	−4.45
2199	191883	0.20	3.53×10^{-07}	−4.75	2188	517881	0.75	1.61×10^{-08}	−6.07
2198	208524	0.53	1.53×10^{-06}	−4.11	2193	527510	0.89	1.30×10^{-08}	−6.17
2190	211276	0.11	3.50×10^{-07}	−4.74	2181	528840	0.65	9.06×10^{-09}	−6.30
2199	235014	0.17	8.69×10^{-07}	−4.36	2193	534125	0.20	2.21×10^{-09}	−6.94
2192	272823	0.12	8.39×10^{-07}	−4.36	2193	534310	0.19	2.13×10^{-09}	−6.96
2198	273950	0.11	7.79×10^{-07}	−4.41	2198	534527	0.45	4.96×10^{-09}	−6.60
2186	274243	0.21	1.48×10^{-06}	−4.10	2198	536801	0.13	1.30×10^{-09}	−7.18
2191	275096	0.18	1.29×10^{-06}	−4.17	2198	536823	0.21	2.08×10^{-09}	−6.98
2191	275569	0.77	5.44×10^{-06}	−3.55	2196	537259	0.12	1.19×10^{-09}	−7.22
2191	276541	0.20	1.42×10^{-06}	−4.13	2189	537324	0.11	1.09×10^{-09}	−7.24
2185	**278479**	**2.76**	$\mathbf{1.96 \times 10^{-05}}$	**−2.98**	2199	539780	0.23	2.11×10^{-09}	−6.98
2196	**279590**	**4.96**	$\mathbf{3.52 \times 10^{-05}}$	−2.75	2185	541921	0.77	6.37×10^{-09}	−6.46
2196	**281070**	**13.32**	$\mathbf{9.45 \times 10^{-05}}$	**−2.32**	2185	542397	1.72	1.39×10^{-08}	−6.12
2185	**295318**	**9.42**	$\mathbf{6.33 \times 10^{-05}}$	**−2.47**	2185	543753	0.37	2.84×10^{-09}	−6.81
2190	302940	0.20	1.24×10^{-06}	−4.18	2197	545747	0.26	1.84×10^{-09}	−7.03
2180	**316352**	**3.48**	$\mathbf{1.95 \times 10^{-05}}$	**−2.96**	2190	558169	11.57	4.86×10^{-08}	−5.59
2191	316680	0.19	1.05×10^{-06}	−4.26	2196	561278	12.31	4.54×10^{-08}	−5.64
2186	326599	0.19	9.38×10^{-07}	−4.30	2196	565865	20.20	6.12×10^{-08}	−5.51
2180	**339506**	**2.73**	$\mathbf{1.14 \times 10^{-05}}$	**−3.20**	2190	618399	17.45	4.95×10^{-09}	−6.59
2191	339838	0.13	5.60×10^{-07}	−4.53	2184	636299	54.23	6.51×10^{-09}	−6.45
2190	343541	0.17	6.74×10^{-07}	−4.45	2184	651571	4.35	2.45×10^{-10}	−7.88

Note: Impact probabilities $> 10^{-5}$ are highlighted in bold.

Table 4.10: Resonances associated with the eight potential impacts with impact probability $> 10^{-5}$.

Year	ζ_{2135} (km)	Post-2135 Period (yr)	Resonance	Res. Period (yr)	ΔP (yr)
2193	186415	1.2342	58 yr/47 rev	1.2340	+0.0002
2185	278479	1.2215	50 yr/41 rev	1.2195	+0.0020
2196	279590	1.2213	61 yr/50 rev	1.2200	+0.0013
2196	281070	1.2211	61 yr/50 rev	1.2200	+0.0011
2185	295318	1.2194	50 yr/41 rev	1.2195	−0.0001
2180	316352	1.2169	45 yr/37 rev	1.2162	+0.0007
2180	339506	1.2144	45 yr/37 rev	1.2162	−0.0018
2175	368877	1.2116	40 yr/33 rev	1.2121	−0.0005

Table 4.11: Formal uncertainties with and without simulated OSIRIS-REx pseudo-range measurements as described in the text.

	Uncertainties	
	Reference	With sim. obs.
A_T (10^{-16} au/d)	2.52	0.38
2020-Jan-04 Position (km)		
Radial	1.539	0.008
Transverse	0.855	0.033
Normal	2.461	0.098
2020-Jan-04 Velocity (mm/s)		
Radial	0.662	0.005
Transverse	0.400	0.002
Normal	1.388	0.029
ζ_{2135} (km)	58000	1000

Chapter 5

Nongravitational perturbations and virtual impactors: the case of asteroid (410777) 2009 FD

For many years we have been operating impact monitoring systems at the University of Pisa[1] and the Jet Propulsion Laboratory (JPL)[2]. These online information systems continually and automatically update the list of asteroids that can hit our planet in the next 100 years.

The attempt to extend the monitoring time span to a longer interval, e.g., 200 years, is on the contrary at the frontier of research on the theory of chaos, nongravitational perturbations, and observational error models. Thus, we are not surprised to find that new cases need to be handled in a different way from the previous ones. So far we have successfully handled the special cases (99942) Apophis [Farnocchia et al., 2013a], (101955) Bennu [Chesley et al., 2014], and 1950 DA [Farnocchia and Chesley, 2014]. Each of these cases required us to model and/or solve for parameters appearing in the nongravitational perturbations, especially the Yarkovsky effect [Vokrouhlický et al., 2000a].

Recently, asteroid 2009 FD (discovered by the La Sagra survey on 2009 March 16) appeared as a new case with the following new characteristics. We previously had 182 optical observations (from the years 2009 and 2010) and a very precise orbit solution, with a purely gravitational model, leading to several Virtual Impactors (VIs) (patches of initial conditions leading to possible impacts with Earth [Milani et al., 2005a]) in the years 2185–2196. 2009 FD was reobserved between 2013 November and 2014 April: 109 additional op-

[1] http;//newton.dm.unipi.it/neodys since 1999; operated by SpaceDyS srl. from 2011.
[2] http://neo.jpl.nasa.gov/risk/ since 2002.

tical observations were obtained, plus one radar Doppler measurement was performed on April 7 from Arecibo (see Sec. 5.1). As a consequence, the uncertainty of the orbit with the same model become small enough to exclude the main VI in 2185, the one with largest Impact Probability (IP).

However, this result was inaccurate because it did not properly account for the uncertainties of the dynamical model. The available astrometry, even with the radar data point, is not sufficient to determine the strength of the Yarkovsky effect. The Yarkovsky effect order of magnitude, as estimated by models, increases the uncertainty of the long term prediction and therefore the main VI in 2185 is still within the range of possible orbits.

If new observations are added without modeling the Yarkovsky effect, it is possible that no VIs will be included, although we know this is not correct. Therefore, rather than removing the risk file (list of VIs) we need to be able to compute a risk file taking fully into account the Yarkovsky effect. Otherwise the observers would decrease the priority of observing 2009 FD. To solve this problem we started an intensive effort to compute the appropriate solution; in the meantime we decided not to update the online risk files[3] to avoid giving a false "all clear".

In this paper we report how we solved this problem, in two different ways, in Pisa and at JPL. Both solutions use theories, most of which are presented in the papers cited, but some are new, and the known tools have to be combined in an innovative way to solve this specific case. Of course our hope is to have accumulated enough expertise (and well-tested software) to be able to handle new difficult cases, but this is yet to be determined.

The computation of a Yarkovsky model is based on the available physical properties of 2009 FD, as well as general properties of the Near Earth Asteroid (NEA) population, with uncertainties propagated nonlinearly to generate a Probability Density Function (PDF) for the Yarkovsky parameter A_2 [Farnocchia et al., 2013b] (see Sec. 5.2). We used this model in two different ways.

The Pisa solution is to generalize the method of the Line Of Variations (LOV) [Milani et al., 2005a,b] already in use (both in Pisa and at JPL) to a higher dimensional space, e.g., to vectors containing six initial conditions and at least one nongravitational parameter. We obtained the appropriate metric for defining the LOV by mapping on the 2185 scatter plane (Sec. 5.3). We control the weakness in the determination of the Yarkovsky parameter by adding an a priori observation (Sec. 5.4). The JPL solution is based on a Monte Carlo method applied to propagate the orbital PDF (including the Yarkovsky parameter) to the target planes of the encounters with Earth in

[3]This decision was applied both at University of Pisa/SpaceDyS and at JPL.

the late 22nd Century (Sec. 5.5).

In Sec. 5.6 we discuss the role of the 2185 close approach in scattering the alternative orbits and consequently in giving access to resonant returns. The analytic theory, based on Valsecchi et al. [2003], provides approximate locations for the possible keyholes is given in Appendix 10.2.

The results obtained by the two methods are compared in Sec. 5.7, where we dicuss the trade-off between the two. We also discuss the future observability of 2009 FD.

5.1 Astrometry and physical observations of 2009 FD

The observational coverage of 2009 FD available to date is composed of three separate apparitions. More than 150 astrometric positions were reported during its discovery apparition in 2009, when 2009 FD reached a magnitude of V=16 just before disappearing into solar conjunction, making it an easy target for many observers. A slightly less favorable opportunity in late 2010 resulted in a handful of additional observations, including a Near Infrared (NIR) detection by the WISE spacecraft [Mainzer et al., 2014]. The object then entered a phase of almost prohibitive observational geometry, which resulted in a lack of coverage for a three year period, until late 2013.

In an effort to secure the maximum observational coverage for this important target, in November 2013 we decided to attempt an early third-opposition recovery using the 8.2 meter ESO Very Large Telescope (VLT) on Cerro Paranal, Chile. Observations collected starting from 2013 November 30 with the FORS2 optical imager resulted in a faint but unambiguous detection inside the uncertainty region, confirmed by consistent detections achieved over the two subsequent nights; at that time the object was estimated to have a magnitude of approximately V=25.5, making it a challenging target even for a large aperture telescope like VLT. From early 2014 various other professional and amateur-level sites began reporting optical observations, guaranteeing a dense astrometric coverage until early April, when the object reached its close approach with Earth and then entered solar conjunction.

As an additional attempt to extend the observational coverage, we tried to locate unreported precovery observations of 2009 FD in existing archival data, using the image search engine made available by the Canadian Astronomy Data Centre [Gwyn et al., 2012]; all the available images covering the ephemeris position of 2009 FD corresponded to times when the object was

fainter than V=24, unlikely to result in a detection in non-targeted sidereal exposures.

Just before the end of the observability window, and close to the time of peak brightness for the apparition, we were able to obtain BVRI colorimetric observations using the EFOSC2 instrument mounted on the 3.6 meter ESO New Technology Telescope (NTT) at La Silla, Chile. The exposure time was of 200 s for each of the images, which were reduced using standard procedures with the MIDAS software: after subtraction of the bias from the raw data and flat-field correction, the instrumental magnitudes were measured via aperture photometry. For the R filter, we considered the mean value of two different images, while only one image was taken with the other photometric filters. The absolute calibration of the magnitudes was obtained by means of the observation of standard fields from the [Landolt, 1992] catalog. Although exposed at high airmass (around 1.9) and under not ideal (but stable) seeing conditions (1.4"), the dataset was sufficient to extract accurate optical colors for the asteroid (see Table 5.1), which suggest a C-group primitive composition, most likely (based on chi-square minimization) of the Ch or Cgh classes [DeMeo et al., 2009] (see Fig. 5.1). These observations were obtained only a few days before the radar Doppler detection by the Arecibo radiotelescope, which marked the end of the 2013-2014 apparition of 2009 FD.

Table 5.1: Apparent V magnitude and optical colors (with error bars) of 2009 FD on 2014 April 02.0 UT. They are consistent with a primitive C-group taxonomy, most likely of the Ch or Cgh classes.

Band	Value [mag]
V	20.258 ± 0.063
B – V	0.816 ± 0.091
V – R	0.298 ± 0.070
V – I	0.704 ± 0.083

5.2 Yarkovsky effect models

As already discussed, the Yarkovsky effect [Vokrouhlický et al., 2000a] needs to be taken into account to make reliable impact predictions for 2009 FD. Including the Yarkovsky accelerations in the force model is tricky because such accelerations are unknown.

One way to constrain the Yarkovsky effect is to look for deviations from a gravitational trajectory in the astrometric dataset. The Yarkovsky effect is

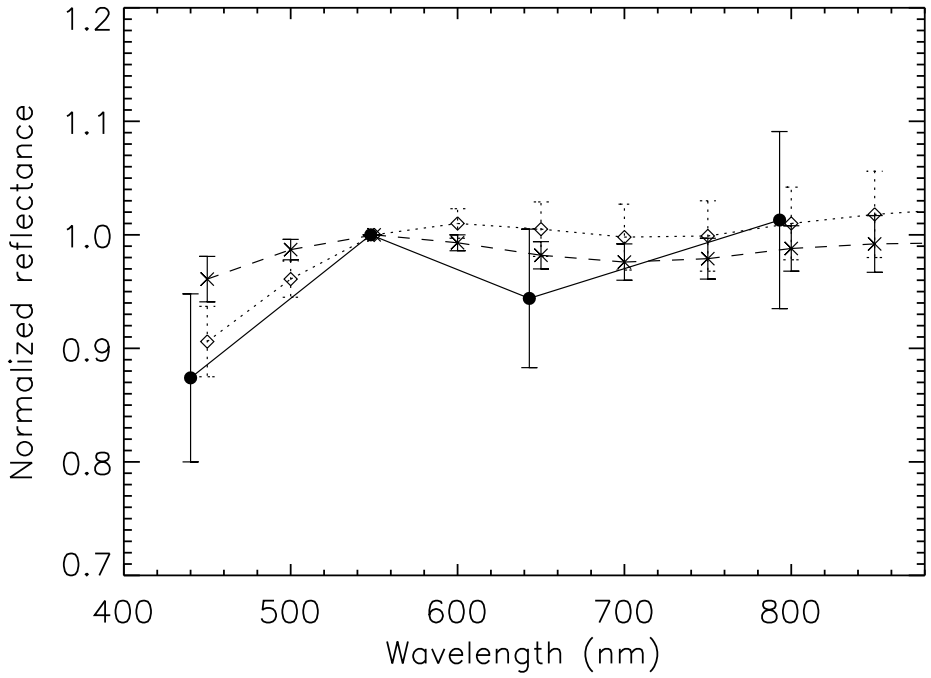

Figure 5.1: Comparisons of the colors of 2009 FD with the visible spectral shapes of the Ch and Cgh classes. Continous line: 2009 FD measurements; dashed: Ch taxonomic class; dotted: Cgh class.

modeled as a purely transverse acceleration A_2/r^2 and A_2 is determined by the orbital fit to the observations [Farnocchia et al., 2013b]. [Chesley et al., 2014] successfully used this approach for asteroid (101955) Bennu. However, for 2009 FD we have a relatively short observed arc and only one Doppler radar observation. Therefore, the astrometry provides no useful constraint on A_2.

Another option is to use the available physical model as well as general properties of the near-Earth asteroid population to constrain the Yarkovsky effect. [Chesley et al., 2009] and [Farnocchia and Chesley, 2014] applied this technique to perform the risk assessment of asteroids (99942) Apophis and (29075) 1950 DA. The situation for 2009 FD is similar to that discussed by [Chesley et al., 2009] for Apophis. The available information for 2009 FD is as follows.

- [Mainzer et al., 2014] use WISE observations to constrain the diameter and albedo of 2009 FD as (472±45) m and (0.010±0.003), respectively.

This value of the albedo is extreme, lower by a factor of > 3 than any other known albedo for asteroids of similar taxonomic classes. Such a large anomaly cannot be due to the error in absolute magnitude, thus even the diameter could be unreliable. We use the published data: when better data is available we can easily repeat the procedure described in this paper.

- The known rotation period is (5.9 ± 0.2) h [Carbognani, 2011].

The slope parameter G, the obliquity, density, and thermal inertia are unknown. Therefore, we resort to general properties of the asteroid population:

- From the JPL small-body database[4], we obtain $G = (0.18 \pm 0.13)$ for the whole asteroid population. This distribution for G was also used by [Mommert et al., 2014] for asteroid 2009 BD.

- For the spin axis orientation we use the obliquity distribution by [Farnocchia et al., 2013b], which was obtained from a list of Yarkovsky detections.

- The density is unknown, but as discussed in Sec. 5.1 spectral properties suggest a C-type asteroid and therefore a density typically smaller than 2 g/cm^3. We used a distribution as in Fig. 5.2, i.e., a lognormal with mean 1.5 g/cm^3 and standard deviation 0.5 g/cm^3.

- For thermal inertia we adopt the [Delbó et al., 2007] relationship between diameter and thermal inertia.

For more details see [Farnocchia et al., 2013b] and [Chesley et al., 2009].

Figure 5.3 shows the distribution of A_2 obtained by combining the physical parameters described above. Since we do not know whether 2009 FD is a retrograde or a direct rotator, the A_2 distribution has a bimodal behavior. In general, a retrograde rotation is more likely as discussed in [La Spina et al., 2004] and [Farnocchia et al., 2013b]. We did not model a complex rotation state. However, the overall uncertainty is well captured since a complex rotation would decrease the size of the Yarkovsky effect and thus A_2, thereby providing no wider dispersion. Figure 5.3 also shows a normal distribution with zero mean and the same 3σ level of the distribution obtained from the physical model, i.e., 97.5×10^{-15} au/d^2.

[4] http://ssd.jpl.nasa.gov/sbdb_query.cgi

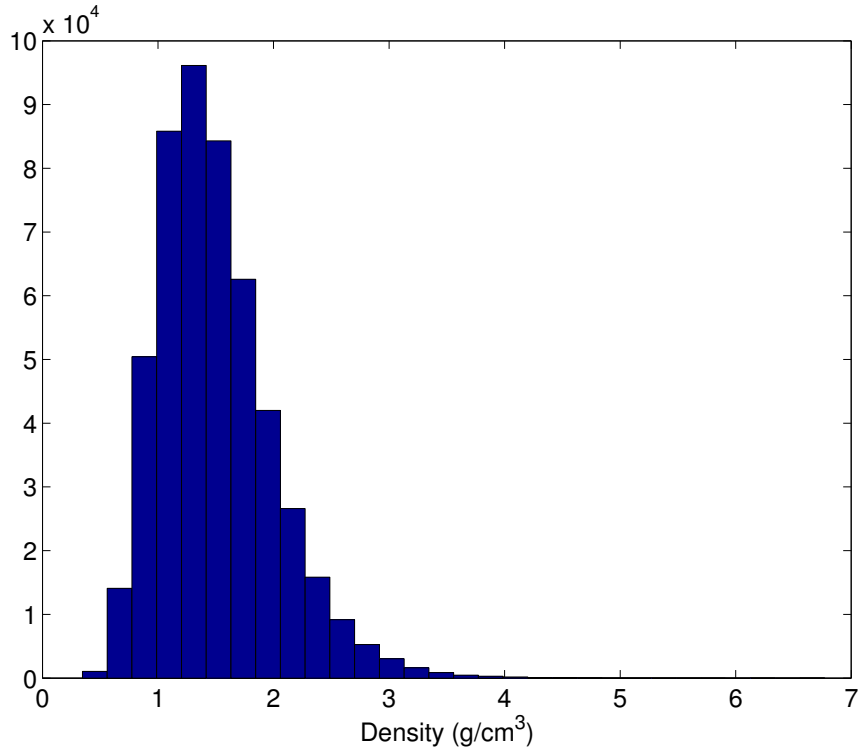

Figure 5.2: Assumed distribution of the 2009 FD density.

From the described physical model we also obtain a nominal mass of 8.3×10^{10} kg, which we use in Sec. 5.4 and 5.5 to estimate the energy released by a possible impact.

If we were to assume that the albedo was 0.06 ± 0.015, with absolute magnitude $H = 22.1 \pm 0.3$, then the $3\,\sigma$ uncertainty would grow to 215.3. This would imply lower IPs and lower mass estimates in the results in Sects. 5.4 and 5.5, but the overall structure of the VIs would be preserved, possibly with some additional VIs in the distribution tails.

5.3 Line of variations in > 6 dimensions

The most common parameter when modeling the Yarkovsky effect is A_2, i.e., the coefficient appearing in the average transverse acceleration: $T = A_2/r^2$, where r is the distance from the Sun. The result is obtained by fitting the available astrometry (optical and radar) to the initial conditions and the A_2 parameter. Thus all the orbit determination process has to be done with seven parameters, the normal matrix C is 7×7, and the eigenvector V_1 of

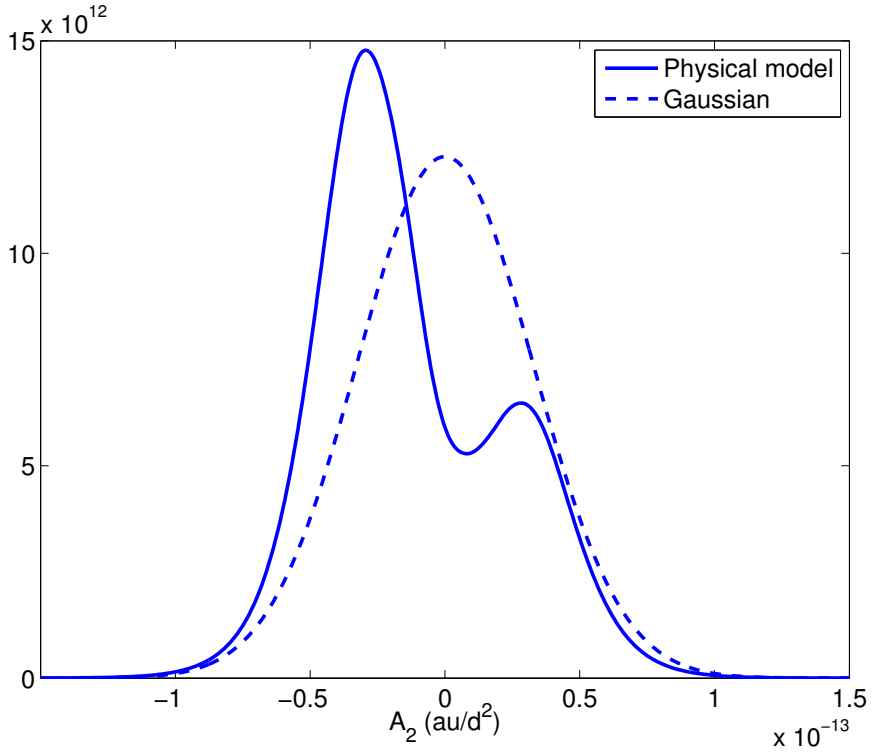

Figure 5.3: Distribution of the Yarkovsky parameter A_2. The solid curve corresponds to the distribution obtained from the physical model; the dashed line is a normal distribution with the same 3σ limits.

C with smallest eigenvalue is seven-dimensional [Milani and Gronchi, 2010, Chap. 5, 10]. The theory of the line of variations [Milani et al., 2005b] can be generalized to dimension > 6: the LOV is defined as the set of the local minima of the target function restricted to hyperplanes orthogonal to V_1. The actual computation of the LOV uses a constrained differential correction process operating on this hyperplane. This change is conceptually straightforward, but in terms of programming it is a complicated task. As a result, version 4.3 of the software system OrbFit, implementing a full seven-dimensional LOV and seven-dimensional impact monitoring, is still undergoing testing and has not yet replaced the operational version 4.2 [5].

However, the impact monitoring processing chain including Yarkovsky effect has already been tested, in particular on the case of (99942) Apophis. The comparison with results obtained with Monte Carlo method has confirmed that the method gives satisfactory results, provided one problem is solved. As discussed in [Milani et al., 2005b], the notion of smallest eigen-

[5] http://adams.dm.unipi.it/orbfit/

value depends on a metric in the parameter space, thus it is not invariant for coordinate changes. For comparatively short term impact monitoring (a few tens of years) we can select an appropriate coordinate system depending on the astrometry available (e.g., Cartesian coordinates for short observed arcs, equinoctal elements [Broucke and Cefola, 1972] for longer arcs).

The best choice of LOV, applicable to a much longer time span, would need to have the following property. If there is a planetary encounter that scatters the LOV solutions into qualitatively different orbits such that they can result in successive encounters in different years, then we select the Target Plane (TP) of this encounter as scattering plane [Chesley et al., 2014]. The best LOV in the space of initial conditions and parameters is such that the spread of corresponding TP points is maximum. In this way, all the dynamical pathways after the scattering encounter, which could lead to succesive impacts, are represented on the LOV.

To achieve this result, before computing the LOV we propagated the nominal orbit to the scattering plane, where we found the major axis vector $W \in \mathbb{R}^2$ of the confidence ellipse obtained by linear propagation of the orbit covariance. Among the possible inverse images of W by the differential of the propagation to the TP, we selected $Z \in \mathbb{R}^7$ corresponding to the minimum increase in the quadratic approximation to the target function, as given by the appropriate regression line. We then used Z as the direction of the LOV. For very well determined orbits such as the one of 2009 FD, given the direction Z, the LOV can be computed as a straight line: a full nonlinear computation would give negligible changes in the selected sample points.

5.4 Impact monitoring with a priori constraints

We carefully analyzed the available astrometry and manually weighted the observations to account for the uncertainty information provided by some of the observers and to mitigate the effect of correlations for nights with a large number of observations.

When solving for the six orbital elements the orbit is very well constrained. For instance, the standard deviation for the semimajor axis a is $STD(a) = 1.8 \times 10^{-9}$ au $= 270$ m. However, if the seventh parameter A_2 is also determined its uncertainty is too large and the nominal value does not provide useful information. Thus, we decided to assume an a priori value $A_2 = (0 \pm 32.5) \times 10^{-15}$ au/d^2, consistent with the discussion in Sec. 5.2. The a priori observation was added to the normal equation with the standard formula [Milani and Gronchi, 2010, Sec. 6.1].

In these conditions, the best fit value is $A_2 = (-2 \pm 32.5) \times 10^{-15}$au/d^2,

which is not significantly different from 0. The $STD(a) = 2.3 \times 10^{-9}$ au is not much higher that the six-parameter fit. We then run the computation of the LOV defined by the 2185 scattering plane, with 2 401 points up to $|\sigma| = 3$, the propagation to the year 2250 of all the sample points on the LOV, and the search for virtual impactors, all in the seven-dimensional version; apart from the change in dimension, the method is not different from [Milani et al., 2005a].

These computations were done with DE430 planetary ephemerides from JPL [Folkner et al., 2014], 17 perturbing asteroids including Pluto, and appropriate relativistic dynamics as discussed in [Chesley et al., 2014]. To assess the risk level, we computed the Palermo Scale (PS) by using the expected value of the mass as estimated in Sec. 5.2.

Table 5.2: Risk file for 2009 FD: calendar year, month, and day for the potential impact; approximate location along the LOV in σ space; minimum distance (the lateral distance from the LOV to the center of the Earth with the 1 σ semi-width of the TP confidence region); stretching factor (how much the confidence region at the epoch has been stretched by the time of impact); probability of Earth impact; and Palermo Scale. The width of the TP confidence region is always few km. For all VIs the LOV directly intersects the Earth.

date yyyy-mm-dd .dd	sigma	dist ($r_\oplus$)	stretch	$IP_\oplus$	PS
2185-03-29.75	−1.069	0.52	184	2.71×10^{-3}	−0.43
2186-03-29.98	−1.049	0.58	1450000	3.50×10^{-7}	−4.32
2190-03-30.08	0.005	0.57	2960	2.92×10^{-4}	−1.41
2191-03-30.21	−0.962	0.89	377000	1.24×10^{-6}	−3.78
2192-03-29.51	−1.003	0.87	1110000	3.96×10^{-7}	−4.28
2194-03-30.02	−1.025	0.93	3110000	1.58×10^{-7}	−4.68
2196-03-29.44	−0.872	0.54	225000	2.68×10^{-6}	−3.46

Table 5.2 includes the main 2185 VI with the highest $PS = -0.43$ among all asteroids currently on our Risk Page. Its $IP \simeq 1/369$ is quite high, especially for an impact with an estimated energy of $\simeq$ 3 700 Mt of TNT. On the contrary, the IP in 2190 is lower than that computed with a purely gravitational model, although the current VI is very close to the nominal solution. The computations with the Yarkovsky effect were crucial for a reliable assessment of the impact risk.

We performed the impact monitoring with limit date in 2250 and we found many close approaches in every single year until 2250, but none leading to impact because of the secular increase in the Minimum Orbit Intersection

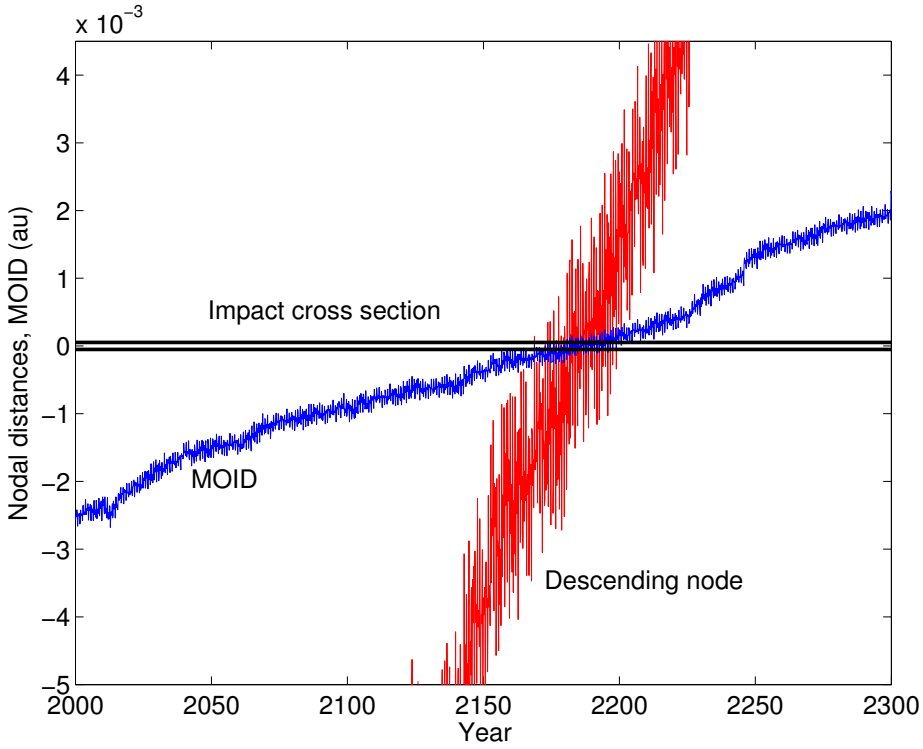

Figure 5.4: From the orbit of 2009 FD propagated until year 2300, we have computed the MOID and the distance at the descending node (in au). A MOID smaller than the radius of the impact cross-section occurs between 2166 and 2197.

Distance (MOID) (see Fig. 5.4); the closest one is in 2198 with a close approach of 1.4 Earth radii.

5.5 Monte Carlo impact monitoring

The JPL Sentry risk assessment was independently performed by means of a Monte Carlo simulation. First, we computed a seven-dimensional orbital solution, with $A_2 = 0$ au/d^2. The a priori uncertainty on A_2 was set to obtain a postfit uncertainty of 32.5 au/d^2. Then, we used the resulting seven-dimensional covariance to randomly generate a million samples thus getting a resolution of $\sim 10^{-6}$ for the impact probability. Finally, we propagated each sample, recorded the future close approaches, and counted the impacts occurring before 2200. The dynamical model is the same used for the computations in Sec. 5.4.

Table 5.3 lists the possible impacts found by the Monte Carlo method.

The values of σ are computed by taking the distribution of the Monte Carlo samples on the 2185 b-plane. The impact probabilities do not change very much if we use the most complete information about the A2 distribution in the Monte Carlo method. The ratio between the A2 distribution from the physical model and the normal A2 distribution is about 2, except the left tails of the distribution. However, the impacts found in the Monte Carlo simulations are for $|A2| < 5 \times 10^{-15}$ au/d^2 and are therefore far from the distribution tails.

Table 5.3: The JPL Sentry risk file for 2009 FD obtained from the Monte Carlo simulation: date for the potential impact; approximate location along the LOV in sigma space; minimum distance; stretching factor; probability of Earth impact; and Palermo Scale.

date yyyy-mm-dd.dd	sigma	dist ($r_\oplus$)	stretch	$IP_\oplus$	PS
2185-03-29.75	−1.048	0.52	160	2.6×10^{-3}	−0.44
2190-03-30.08	0.028	0.57	2580	2.7×10^{-4}	−1.43
2191-03-30.24	−0.993	0.40	209000	2.0×10^{-6}	−3.57
2192-03-29.51	−0.986	0.83	364000	1.0×10^{-6}	−3.87
2196-03-29.44	−0.864	0.76	496000	1.0×10^{-6}	−3.88

5.6 Scattering encounter

Figure 5.5 shows the increase of the position uncertainty (longest semiaxis of the $1\,\sigma$ confidence ellipsoid, as deduced from the linearly propagated confidence matrix) with time. This increase is by no means a gradual increase, but mostly occurs within short time intervals corresponding to close approaches to the Earth. In particular, the position uncertainty increases as Δt^2 far from the close approaches, while it increases much more quickly during the close approaches. The deepest close approaches are marked by dotted lines. After the close approach in 2009, there is another at a minimum distance of 0.418 au in 2015, then the pair in 2063 (at 0.0130 au) and 2064 (at 0.0266 au). The last two are near different nodes, connected by a nonresonant return [Milani et al., 1999]. Another nonresonant return connects the close approach of 2136 (at 0.0218 au) with the shallower one of 2137 (at 0.0815 au). In all cases, the divergence of nearby orbits fluctuates, but overall increases by a factor of $\simeq 3 \times 10^5$ over 176 years (from 2009 to 2185), corresponding to a Lyapounov time $176/\log(3 \times 10^5) \simeq 14$ years. Over this timespan the Yarkovsky effect is very important, because the prediction uncertainty is not dominated by the chaotic effects.

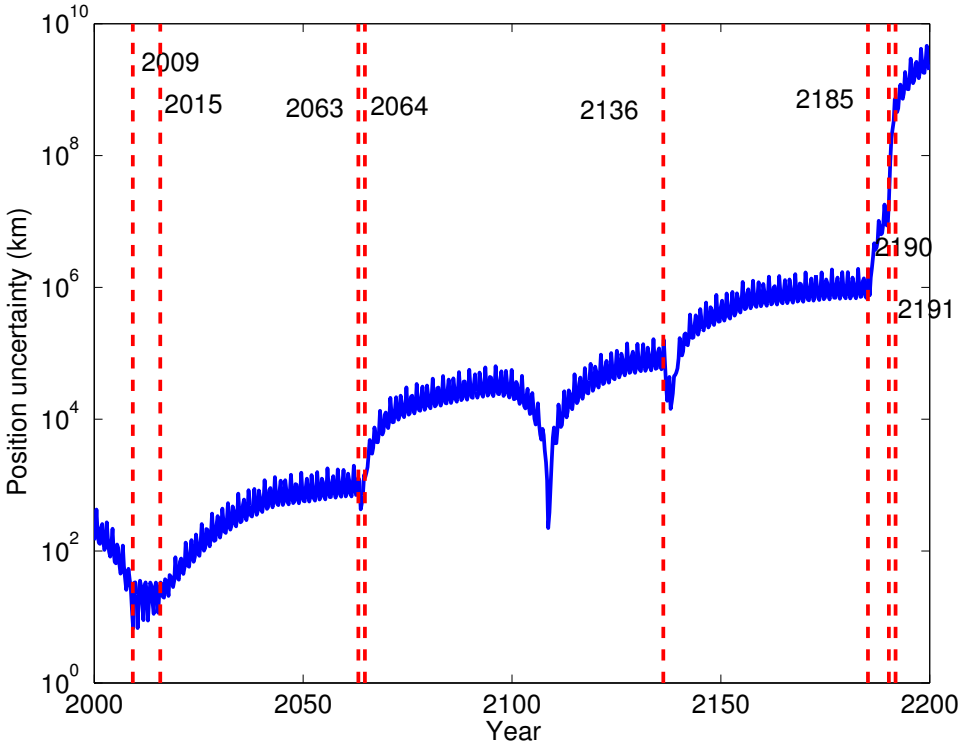

Figure 5.5: Evolution of the longest semiaxis of the $1\,\sigma$ confidence ellipsoid. The vertical dashed lines correspond to close approaches with the Earth within 0.05 au.

Finally, as Fig. 5.6 shows, at the time of the 2185 encounter the LOV (plotted over the interval from $\sigma = -3$ to $+3$) spans more than 7 million km on the b-plane, and straddles the Earth. As a consequence, a very wide range of close approach distances is possible, from actual Earth collision up to very distant encounters. The 2185 VI is similar to a direct impact, with a very low stretching, hence the comparatively large IP.

After 2185, the divergence grows to much larger values, of course different for the different LOV sample orbits, depending on how close the 2185 encounter is, and the prediction uncertainty becomes dominated by chaos. The later VI detected have higher stretching, thus lower IP, and are resonant returns [Milani et al., 1999] from comparatively close approaches in 2185, occurring at the same date after 1, 5, 6, 7, 11 years. They correspond to resonances between the mean motions $n, n_\oplus$ of the asteroid and the Earth, respectively:

$$\frac{n}{n_\oplus} = \frac{1}{1}\,,\ \frac{4}{5}\,,\ \frac{5}{6}\,,\ \frac{6}{7}\,,\ \frac{8}{9}\,,\ \frac{9}{11}\quad .$$

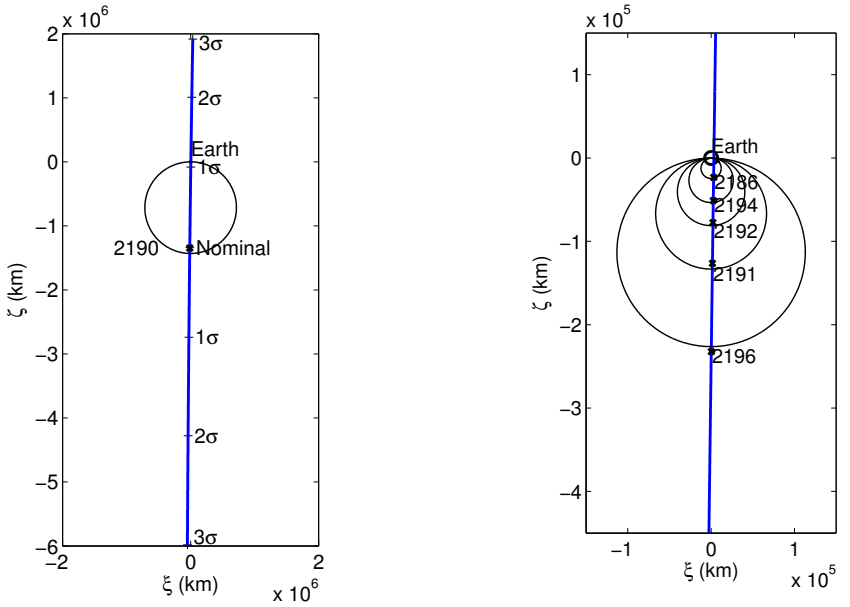

Figure 5.6: The left figure shows the LOV on the 2185 TP: the VI of 2190 is marked with a cross. The right figure shows a segment of the LOV on the 2185 TP: the keyholes for impact in (from top to bottom) 2186, 2194, 2192, 2191, and 2196 are marked with crosses; also shown are the b-plane circles associated with the respective mean motion resonances (1/1, 8/9 6/7, 5/6, 9/11).

Figure 5.6 shows the location of the VI on the LOV and the Valsecchi circles corresponding to the resonances, according to an approximate analytic theory [Valsecchi et al., 2003]. The 4/5 resonance corresponds to the weakest perturbation in 2185 since the orbit is currently close to it: thus the circle for returns in 2190, shown in the left plot of Fig. 5.6, is much larger than the others, shown at a larger scale in the right plot.

It can be shown with formulas derived from [Valsecchi et al., 2003] that the values of the semimajor axis after the 2185 encounter could range between 0.82 and 2.10 au, these values being obtained for grazing encounters (see Appendix 10.2). This semimajor axis gives access to all the resonances with ratio of mean motions ranging from 4/3 to 1/3. In the propagation of the LOV orbits we find close approaches to the Earth occurring in each single year after 2185 until the growth of the MOID prevents the possibility of impact after 2196.

Thus the analytic theory allows us to predict the approximate location of possible keyholes [Chodas, 1999]. Figure 5.7 compares the analytical and the numerical computations of locations and widths of the keyholes, from

which the IPs can be computed. However, the analytical theory does not take into account the short periodic changes in the MOID (see Fig. 5.4), thus it can only provide upper bounds for the widths and the IPs: it is expected that the number of potential keyholes computed analytically will be greater than the actual keyholes found numerically. It is also interesting to compare the probability density distributions computed with or without the Yarkovky effect. As a result of this comparison, the $3\,\sigma$ value for the distribution obtained with the Yarkovsky effect is $\sim 10^6$ km, while the same value for the distribution without the Yarkovky effect is $\sim 10^5$ km.

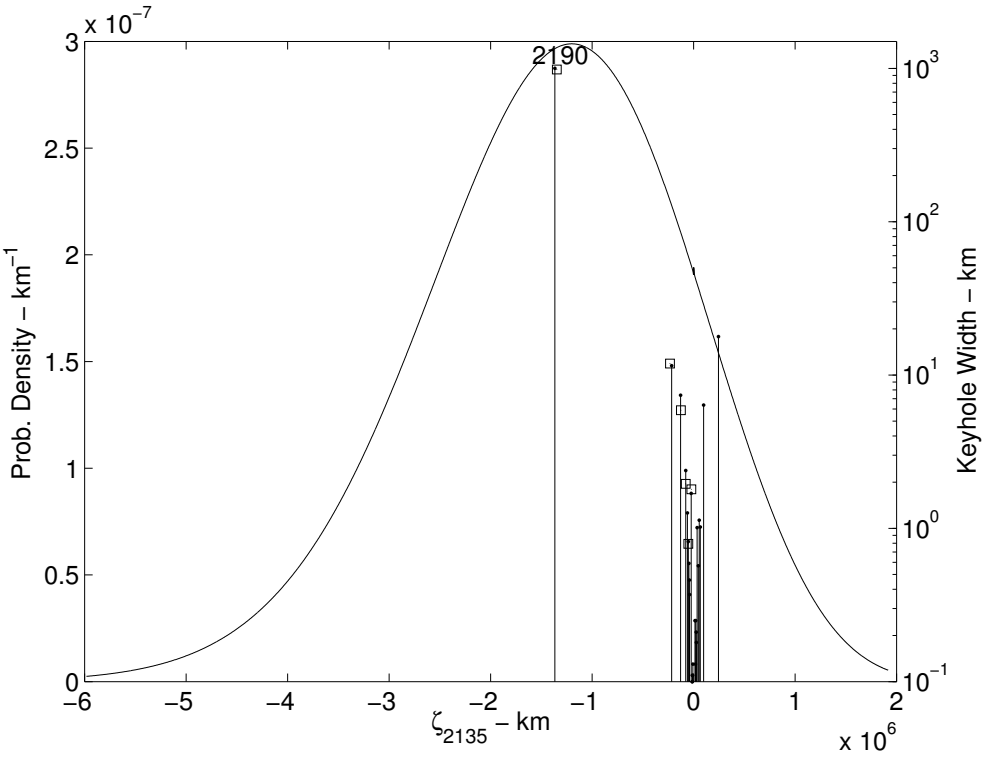

5.7 Conclusions

5.7.1 Comparison and reliability of the results

Given the use of the same dynamical model, it is no surprise that the results are very similar: still, they are remarkably close. The LOV method finds seven VIs, while the Monte Carlo method finds five, but the two missing VIs have IPs of 3.5×10^{-7} and 1.6×10^{-7}, below the sensitivity of the Monte Carlo method with a million samples. The five common VIs have consistent

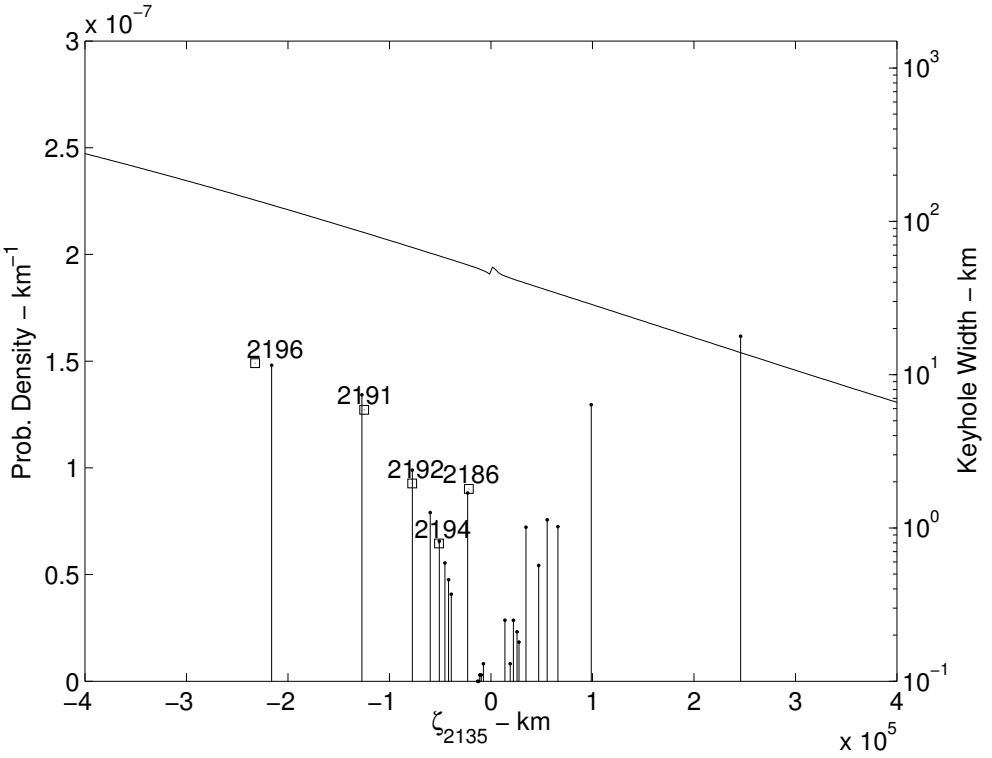

Figure 5.7: Map of the 2009 FD impact keyholes intersecting the trace of the LOV on the 2185 TP, computed both numerically and analitically. The probability density is given by the curve with the left scale, and the analytically computed keyholes are indicated by the vertical lines with their widths given by the height of the bar (right scale). The 7 actual VIs found numerically (from Table 5.2) are marked with a square.

IP estimates: the higher ones, for 2185 and 2190, are in agreement within a few percentage points; the three lower ones are different (as expected) because of Poisson statistics.

Thus the Monte Carlo method detects VI down to its sensitivity limit, which is 1×10^{-6}; the LOV method detects VI close to its generic completeness limit [Milani et al., 2005a][Sec. 2.5], which is $IP \simeq 2.5\times10^{-7}$. We note that it would not be difficult to upgrade these sensitivity limits, with both methods, by increasing the resolution and therefore the computational load. The seven dimensional LOV method is more efficient from the computational point of view for a given resolution. On the other hand, the Monte Carlo method is simpler from the software perspective and is generally more reliable, e.g., in the case of off–LOV VIs.

Thus, the problem we had with the computation of the possibilities of

impact and the values of the IP was solved, and we posted the new results on our online services NEODyS and Sentry.

The results obtained with the analytical theory despite the approximations it must contain are remarkably good, to the point that they can be used as a check of the numerical results. However, they cannot replace numerical computations to verify that some VIs actually exists in an accurate orbital computation.

5.7.2 Future observability

2009 FD could be optically observable again during its next apparition in early 2015. 2009 FD should become detectable with a large-aperture telescope (8-meter class) in October 2014, and even with smaller apertures (2-meter class) around January 2015, when it is expected to reach a peak magntiude of $V = 23$ near opposition. However, the very small skyplane uncertainty of this apparition ($0.15''$ at the 3σ level, even including the contribution due to Yarkovsky) will prevent any significant improvement in the overall orbital uncertainty.

The next valuable opportunity to collect useful information will begin in late October 2015, when 2009 FD will emerge from solar conjunction immediately after its closest approach, already at $V = 19$. The magnitude will then reach a peak magnitude of $V = 18$ within a few days, making 2009 FD an easy target for physical observations from the ground even with modest apertures. On 2015 November 1 the $3\,\sigma$ uncertainty ellipse will have semiaxes 2.34" and 0.69" (most uncertainty is in declination, while proper motion is mostly along right ascension). This uncertainty will give significant leverage for orbital improvement with ground-based astrometry.

Since the late October 2015 close approach will be at about 0.04 au from the geocenter, there could be radar observations, hopefully including range measurements (which were not possible in 2014, with minimum distance 0.1 au).

If these radar and optical observations improve the constraints on the Yarkovsky parameter A_2, then the Impact Monitoring will need to be recomputed. Our methods and software now allow us to do this, although a manual procedure is still required: it involves a limited amount of manpower and some computing time.

The object will then slowly approach solar conjunction during the first half of 2016, and will not become easily observable from the ground until late 2018 (apart from a couple of very challenging low-elongation opportunities in early and late 2017 of very limited astrometric relevance). Unless the 2015 observations rule out the two dangerous segments of the current LOV,

observations may need to be continued for a long time, before the 2009 FD impact problem is resolved.

Chapter 6

The Yarkovsky Effect and Asteroid families

Asteroid families are a powerful tool to investigate the collisional and dynamical evolution of the asteroid belt. If they are correctly identified, they allow to describe the properties of the parent body, the collisional event(s) generating the family and the subsequent evolution due to chaotic dynamics, non-gravitational perturbations, and secondary collisions.

However, asteroid families are statistical entities. They can be detected by density contrast with respect to a background in a space of appropriate parameters, but their reliability strongly depends upon the number of members, the accuracy of the parameters and the method used for the classification. The exact membership cannot be determined, because the portion of phase space filled by the family can have already been occupied by some background asteroids, thus every family can and usually does have interlopers Migliorini et al. [1995]. Moreover, the boundary of the family corresponds to marginal density contrast and thus cannot be sharply defined.

The problem is, the purpose of a classification is not just to get as many families as possible, but to obtain families with enough members, with a large enough spread in size, and accurate enough data to derive quantities such as number of family generating collisional events, age for each of them, size of parent bodies, size distribution of fragments, composition, and flow from the family to Near Earth Asteroid (NEA) and/or cometary type orbits.

This has three important implications. First, the quality of a family classification heavily depends on the number of asteroids, and the accuracy of the parameters used. The number of asteroids is critical, because small number statistics masks all the information content in small families. There is no way of excluding that families currently with few members are statistical flukes, even if they are found likely to be significant by statistical tests.

Second, different kinds of parameters have very different value in a family classification. This can be measured by the information content, which is, for each parameter, the base 2 logarithm of the inverse of relative accuracy, summed for all asteroids for which such data are available; see Section 6.1. By using this measure, it is easy to show that the dynamical parameters, such as the proper elements[1] a, e, I have a much larger information content than the physical observations, because the latter are available either for much smaller catalogs of asteroids, or with worse relative accuracy, or both. As an example, absolute magnitudes are available for all asteroids with good orbits and accurate proper elements, but they are computed by averaging over inhomogeneous data with poorly controlled quality. There are catalogs with albedos such as WISE, described in Mainzer et al. [2011a]; Masiero et al. [2011], and color indexes such as the Sloan Digital Sky Survey (SDSS), described in Ivezić et al. [2001], but the number of asteroids included is smaller by factors 3 to 5 with respect to proper elements catalogs, and this already includes many objects observed with marginal S/N, thus poor relative accuracy.

Third, catalogs with asteroid information grow with time at a rapid and accelerating pace: e.g., we have used for this paper a catalog, distributed from AstDyS[2] with 336 219 numbered asteroids with synthetic proper elements computed up to November 2012. By April 2013 the same catalog had grown to 354 467 objects, i.e., 5.4% in 5 months. If the rate of asteroid numbering was to continue at this rate, a pessimistic assumption, in less than 8 years the catalog would be doubled. Catalogs of physical observations are also likely to grow, although in a less regular and predictable way. Thus the question is whether the increase of the catalogs will either confirm or contradict the conclusions we draw at present; or better, the goal should be to obtain robust conclusions which will pass the test of time.

As a consequence our purpose in this paper is not to make "yet another asteroid family classification", but to setup a classification which can be automatically updated every time the dataset is increased. We are going to use the proper elements first, that is defining "dynamical families", then use information from absolute magnitudes, albedos and generalized color indexes, when available and useful, as either confirmation or rejection, e.g, identification of interlopers and possibly of intersections of different collisional families. We will continue to update the classification by running at short intervals (few months) a fully automated "classification" computer program

[1] As an alternative the corresponding frequencies n, g, s can be used, the results should be the same if the appropriate metric is used Carruba and Michtchenko [2007].

[2] http://hamilton.dm.unipi.it/astdys2/index.php?pc=5

which attaches newly numbered objects to existing families.

This will not remove the need to work on the identification of new families and/or on the analysis of the properties of the already known families. Every scientist will be practically enabled to do this at will, since for our dataset and our classification we follow a strict open data policy, which is already in place when this paper is submitted: all the data on our family classification is already available on AstDyS, and in fact it has already been updated with respect to the version described in this paper[3].

We have also recently made operational a new graphic interface on AstDyS providing figures very much like the examples shown in this paper[4]. Data tabulations in papers have now been abolished, it is now time to reduce the number of figures, especially in color, and replacing them with "graphic servers" providing figures composed upon request from the users: this is what the AstDyS graphic tool is about.

The main purpose of this paper is to describe and make available some large data sets, only some of the interpretations are given, mostly as examples to illustrate how the data could be used. We would like to anticipate one major conceptual tool, which will be presented in the paper. This concerns the meaning of the word "family", which has become ambiguous because of usage by many authors with very different background and intent.

We shall use two different terms: since we believe the proper elements contain most of the information, we perform a family classification based only upon them, thus defining *dynamical families*. A different term *collisional families* shall be used to indicate a set of asteroids which have been formed at once by a single collision, be it either a catastrophic fragmentation or a cratering event. Note that there is no reason to think that the correspondence between dynamical families and collisional families should be one to one. A dynamical family may correspond to multiple collisional events, both on the same and on different parent bodies. A collisional family may appear as two dynamical families because of a gap due to dynamical instability. A collisional family might have dissipated long ago, leaving no dynamical family. A small dynamical family might be a statistical fluke, with no common origin. In this paper we shall give several examples of these non-correspondences.

[3]We acknowledge that D. Nesvorný was the first to implement such an open data policy, by making the membership list of his classification(s) available on PDS (NASA Planetary Data System, EAR-A-VARGBDET-5-NESVORNYFAM-V2.0). We think such an open data policy should be standard from now on.

[4]http://hamilton.dm.unipi.it/astdys2/Plot/index.html

6.1 Dataset

6.1.1 Proper elements

Proper elements $a, e, \sin I$ are three very accurate parameters, and we have computed, over many years up to November 2012, synthetic proper elements Knežević and Milani [2000, 2003] for 336 319 asteroids. We made a special effort to recompute synthetic proper elements missing in our database because of different reasons: asteroids close to strong resonances, suffering close encounters with major planets, with high e and I. In particular we aimed at increasing the sparse statistics in the high e, I regions, in order to improve the reliability of small families therein. We thus integrated orbits of a total of 2 222 asteroids: the proper elements computation failed for only 62 of them. The rest are now included in the AstDyS synthetic proper elements files. This file is updated a few times per year.

For each individual parameter in this dataset there are available both standard deviation and maximum excursion obtained from the analysis of the values computed in sub-intervals Knežević and Milani [2000]. If an asteroid has large instabilities in the proper elements, as it happens for high proper $e, \sin I$, then the family classification can be dubious.

The same catalog contains also absolute magnitudes and estimates of Lyapounov Characteristic Exponents, discussed in the following subsections.

6.1.2 Absolute magnitudes

Another piece of information is the set of absolute magnitudes H available for all numbered asteroids computed by fitting the apparent magnitudes obtained incidentally with the astrometry, thus stored in the Minor Planet Center (MPC) astrometric database. The range of values for all numbered asteroids is 15.7 magnitudes, the accuracy is difficult to be estimated because the incidental photometry is very inhomogeneous in quality, and the information on both S/N and reduction method is not available.

The sources of error in the absolute magnitude data are not just the measurement errors, dominant only for dim asteroids, but also star catalog local magnitude biases, the conversion from star-calibrated magnitudes to the assumed V magnitude used in absolute magnitudes, and the light curve effect. The brightness of an asteroid changes at different apparitions as an effect of shape and spin axis orientation, so the absolute magnitude does not appear constant. Last but not least, the absolute magnitude is defined at zero phase angle (ideal solar opposition) thus some extrapolation of observations obtained in different illumination conditions is always needed, and this

introduces significant errors, especially for high phase angles. The standard deviation of the apparent magnitude residuals has a distribution peaked at 0.5 mag: since numbered asteroids have in general many tens of magnitude observations, the formal error in the absolute magnitude, which is just a corrected average, is generally very small, but biases can be very significant. Thus we do not have a reliable estimate of the accuracy for the large dataset of 336 219 absolute magnitudes H computed by AstDyS, we can just guess that the standard deviations should be in the range $0.3 - 0.5$ magnitudes.

The more optimistic estimate gives a large information content (see Table 6.1), which would be very significant, but there are many quality control problems. Other databases of photometric information with better and more consistent information are available, but the number of objects included is much smaller, e.g., 583 asteroids with accuracy better than 0.21 magnitudes Pravec et al. [2012]: these authors also document the existence of serious systematic size-dependent biases in the H values.

6.1.3 WISE and SDSS catalogs of physical observations

The WISE catalog of albedos[5] has information on 94 632 numbered asteroids with synthetic proper elements, but the relative accuracy is moderate: the average standard deviation (STD) is 0.045, the average ratio between STD and value is 0.28; e.g., the asteroids in the WISE catalog for which the albedo measured is < 3 times the STD are 26% (we are going to use measure > 3 times STD as criterion for using WISE data in Section 6.5).

This is due to the fact that WISE albedos, for small asteroids, have been derived from a *measured* infrared flux and *an estimated* visible light flux derived from an adopted nominal value of absolute magnitude. Both terms are affected by random noise increasing for small objects, and by systematics in particular in the visible, as outlined in the previous subsection. In principle one should use a value of absolute magnitude not only accurate, but also corresponding to the same observation circumstances of the thermal IR observations, which is seldom the case. For large asteroids, the albedo can be constrained from the ratios between different infrared channels of WISE, thus the result are less affected by the uncertainty of the absolute magnitude.

The 4th release of the SDSS MOC[6] contains data for 471 569 moving objects, derived from the images taken in five filters, u, g, r, i, and z, ranging from 0.3 to 1.0 μm. Of those, 123 590 records refer to asteroids present in

[5]Available at URL http://wise2.ipac.caltech.edu/staff/bauer/NEOWISE_pass1

[6]Available at URL http://www.astro.washington.edu/users/ivezic/sdssmoc/

our catalog of proper elements. As many of these objects have more than one record in the SDSS catalog, the total number of asteroids is 61 041. The latter number was then further decreased by removing objects having error in magnitude larger than 0.2 mag in at least one band (excluding the u-band which was not used in our analysis): this is used to remove only obviously degenerate cases. Thus, we used the SDSS MOC 4 data for 59 975 numbered asteroids.

It is well known that spectrophotometric data is of limited accuracy, and should not be used to determine colors of single objects. Still, if properly used, the SDSS data could be useful in some situations, e.g. to detect presence of more than one collisional family inside a dynamical family, or to trace objects escaping from the families, see Section 6.5.

Following Parker et al. [2008] we have used a^*, the first principal component[7] in the $r-i$ versus $g-r$ color-color plane, to discriminate between C-complex asteroids ($a^* < 0$) and S-complex asteroids ($a^* \geq 0$). If ($a^* \geq 0$) the $i-z$ values can be used to discriminate between S- and V-type, with the latter one characterized by the $i-z < -0.15$. The average standard deviation of the data we have used is 0.04 for a^*, 0.08 for $i-z$.

6.1.4 Resonance identification

Another source of information available as an output of the numerical integrations used to compute synthetic proper elements is an estimate of the maximum Lyapounov Characteristic Exponent (LCE). The main use of this is to identify asteroids affected by chaos over comparatively short time scales (much shorter than the ages of the families)[8]. These are mostly due to mean motion resonances with major planets (only resonances with Jupiter, Saturn and Mars are affecting the Main Belt at levels which are significant for family classification). Thus we use as criterion to detect these "resonant/chaotic" asteroids the occurrence of at least one of the following: either a LCE > 50 per Million years (that is a Lyapounov time $< 20\,000$ years) or standard deviation or proper $a > 3 \times 10^{-4}$ au.

Note that the numerical integrations done to compute proper elements use a dynamical model not including any asteroid as perturber. This is done for numerical stability reasons, because all asteroids undergo mutual close approaches and these would need to be handled accurately, which is difficult while integrating hundreds of asteroids simultaneously. Another reason for

[7] According to Ivezić et al. [2001] the first principal component in the $r-i$ vs $g-r$ plane is defined as $a^* = 0.89(g-r) + 0.45(r-i) - 0.57$.

[8] Every asteroid is strongly affected by chaotic effects over timescales comparable to the age of the solar system, but this does not matter for family classification.

this choice is that we wish to identify specifically the chaos which is due to mean motion resonances with the major planets. As shown by Laskar et al. [2011], if even a few largest asteroids are considered with their mass in the dynamical model, then all asteroids are chaotic with Lyapounov times of a few 10 000 years. However, the long term effect of such chaos endogenous to the asteroid belt is less important than the chaos generated by the planetary perturbations Delisle and Laskar [2012].

The asteroid perturbers introduce many new frequencies, resulting in an enormous increase of the Arnold web of resonances, to the point of leaving almost no space for conditionally periodic orbits, and the Lyapounov times are short because the chaotic effects are driven by mean motion resonances. However, these resonances are extremely weak, and they do not result in large scale instability, not even over time spans of many thousands of Lyapounov times, the so called "stable chaos" phenomenon Milani and Nobili [1992]. In particular, locking in a stable resonance with another asteroid is almost impossible, the only known exception being the 1/1 resonance with Ceres, see the discussion about the Hoffmeister family in Section 6.3.1 and Figure 6.2. This implies that the (size-dependent) Yarkovsky effect, which accumulates secularly in time in semimajor axis, cannot have secular effects in eccentricity and inclination, as it happens when there is capture in resonance.

We have developed a sensitive detector of mean motion resonances with the major planets, but we would like to know which resonance, which is the integer combination of mean motions forming the "small divisor". For this we use the catalog of asteroids in mean motion resonances by Smirnov and Shevchenko [2013], which has also been provided to us by the authors in an updated and computer readable form. This catalog will continue to be updated, and the information will be presented through the AstDyS site.

Asteroid families are also affected by secular resonances, with "divisor" formed with an integer combination of frequencies appearing in the secular evolution of perihelia and nodes, namely g, g_5, g_6 for the circulation of the perihelia of the asteroid, Jupiter and Saturn, and s, s_6 for the circulation of the nodes of the asteroid and Jupiter-Saturn[9]. The data on the asteroids affected by secular resonances can be found with the analytic proper elements, computed by us with methods developed in the 90s Milani and Knežević [1990, 1992, 1994]. In these algorithms, the small divisors associated with secular resonances appear as obstruction to the convergence of the iterative algorithm used to compute proper elements, thus error codes corresponding to the secular resonances are reported with the proper elements[10].

[9]In the Hungaria region even some resonances involving the frequencies g_3, g_4, s_4 for Earth and Mars can be significant Milani et al. [2010].

[10]We must admit these codes are not user friendly, although a Table of conversion from

Note that we have not used analytic proper elements as a primary set of parameters for family classification, since they are significantly less accurate (that is, less stable in time over millions of years) than the synthetic ones, by a factor about 3 in the low e and I portion of the main belt. The accuracy becomes even worse for high e, I, to the point that for $\sqrt{e^2 + \sin^2 I} > 0.3$ the analytical elements are not even computed Knežević et al. [1995]; they are also especially degraded in the outer portion of the main belt, for $a > 3.2$ au, due to too many mean motion resonances. On the other hand, analytic proper elements are available for multiopposition asteroids, e.g., for 98 926 of them in November 2012, but these would be more useful in the regions where the number density of numbered asteroids is low, which coincide with the regions of degradation: high e, I and $a > 3.2$ au. It is also possible to use proper elements for multiopposition asteroids to confirm and extend the results of family classification, but for this purpose it is, for the moment, recommended to use ad hoc catalogs of synthetic proper elements extended to multiopposition, as we have done in Milani et al. [2010]; Novaković et al. [2011].

6.1.5 Amount of information

Table 6.1: An estimate of the information content of catalogs. The columns give: parameters contained in the catalogs, minimum and maximum values and range, average information content in bits for a single entry, number of records and total information content.

parameter	min	max	range	av.bits	number	tot Mb
a (au)	1.80	4.00	2.20	16.7	336219	5.63
e	0.00	0.40	0.40	10.7	336219	3.59
sin I	0.00	0.55	0.55	15.1	336219	5.08
total						14.39
H	3.30	19.10	15.8	5.7	336219	1.92
albedo	0.00	0.60	0.60	4.5	94632	0.43
a*	-0.30	0.40	0.70	4.4	59975	0.26
i-z	-0.60	0.50	1.10	4.0	59975	0.24
total						0.50

For the purpose of computing the information content of each entry of the catalogs mentioned in this section, we use as definition of inverse relative accuracy the ratio of two quantities: 1) for each parameter, the useful range,

the error codes to the small divisors is given in [Milani and Knežević, 1990, table 5.1]. We shall try to improve the AstDyS user interface on this.

within which most ($> 99\%$) of the values are contained; 2) the standard deviation, as declared in each catalog, for each record.

Then the content in bit of each individual parameter is the base 2 logarithm of this ratio. These values are added for each asteroid in the catalog, thus forming a total information content, given in the last column of Table 6.1 in Megabits. For statistical purposes we give also the average number of bits per asteroid in the catalog.

For H we have assumed a standard deviation of 0.3 magnitudes for all, although this might be optimistic.

With the numbers in Table 6.1 we can estimate the information content of our synthetic proper element catalog to be about 14 Megabits, the absolute magnitudes provide almost 2 megabits with somewhat optimistic assumptions, the physical data catalogs WISE and SDSS are $\sim$ 1 Megabit together.

6.2 Method for large dataset classification

Our adopted procedure for family identification is largely based on applications of the classical Hierarchical Clustering Method (HCM) already adopted in previous families searches performed since the pioneering work by Zappala et al. [1990], and later improved in a number of papers Milani et al. [2010]; Novaković et al. [2011]; Zappalà et al. [1995]; Zappala et al. [1994]. Since the method has been already extensively explained in the above papers, here we will limit ourselves to a very quick and basic description.

We have divided the asteroid belt in zones, corresponding to different intervals of heliocentric distance, delimited by the most important mean-motion resonances with Jupiter. These resonances correspond to Kirkwood gaps wide enough to exclude family classification across the boundaries.

As shown in Table 6.2, our "zone 1" includes objects having proper semi-major axes between 1.6 and 2 au. In this region, only the so-called Hungaria objects at high inclination ($\sin I \geq 0.3$) are dynamically stable Milani et al. [2010]. Our "zone 2" includes objects with proper orbital elements between 2.067 and 2.501 au. The "zone 3" is located between 2.501 and 2.825 au, and "zone 4" between 2.825 and 3.278 au. Finally, we use also a "zone 5", corresponding to the interval between 3.278 and 3.7 au., and a "zone 6", extending between 3.7 and 4.0 au (mostly asteroids locked in the 3/2 resonance with Jupiter).

Moreover, some semi-major axis zones have been also split by the value of proper sin I, between a moderate inclination region $\sin I < 0.3$ and a high inclination region $\sin I > 0.3$. Note that in zone 1 the moderate inclination

Table 6.2: Summary of the relevant parameters for application of the HCM.

Zone	$\sin I$	range a	N (total)	H_{comp}	$N(H_{comp})$	N_{min}	QRL (m/s)	bins (a)	bins (e)	bins ($\sin I$)
1	> 0.3	$1.600 - 2.000$	4249			15	70	20	6	12
2	< 0.3	$2.065 - 2.501$	115004	15.0	15888	17	70	20	10	10
2	> 0.3	$2.065 - 2.501$	2627			11	130	8	2	2
3	< 0.3	$2.501 - 2.825$	114510	14.5	16158	19	90	20	10	10
3	> 0.3	$2.501 - 2.825$	3994			9	140	8	3	3
4	< 0.3	$2.825 - 3.278$	85221	14.0	14234	17	100	15	10	10
4	> 0.3	$2.825 - 3.278$	7954			12	80	6	3	3
5	all	$3.278 - 3.700$	991			10	120	20	10	15
6	all	$3.700 - 4.000$	1420			15	60	1	10	15

region is almost empty and contains very chaotic objects (interacting strongly with Mars). In zone 2 the $g - g_6$ secular resonance clears a gap below the Phocaea region. In zones 3 and 4 there is no natural dynamical boundary which could be defined by inclination only, and indeed we have problems with families found in both regions. In zones 5 and 6 there are few high inclination asteroids, and a much smaller population.

To compute the mutual distances of objects in the proper element space we used the "standard metric" d adopted by Zappala et al. [1990], and in subsequent HCM-based family investigations. We remind that using this metric means that the distances between objects in the proper element space are expressed as differences of velocity and are given in m/s.

The HCM algorithm identifies all groups of objects existing at any given value of mutual distance. This means that for each member i belonging to a group found at distance d, there is at least one other member whose distance from i is $\leq d$. The basic idea of the HCM is to identify groups which are sufficiently populous, dense and compact to be reasonably confident, in a statistical sense, that their existence cannot be due to random fluctuations of the distribution of objects in the proper element space.

In HCM-based analysis, the most important parameters are the minimum number of objects N_{min} required for groups to be considered as candidate families, and the critical level of distance adopted for family identification. The choice of N_{min} depends on the total number of objects present in a given region of the phase space. $N_{min} = 5$ was chosen at the epoch of the pioneering study by Zappala et al. [1990], when the inventory of main belt asteroids with computed proper elements included only about 4,000 objects. In subsequent analyzes of increasingly bigger datasets, the N_{min} values were scaled as the square root of the ratio between the new and old numbers of objects present in the same volume of the proper element space. We follow

this procedure also in the present paper. We chose the new N_{min} values by scaling with respect to the values adopted by Zappalà et al. [1995] for the low-I portions of zones 2, 3, and 4, and Novaković et al. [2011] for the high-I portions of the same zones. Zones 5 and 6 contain relatively low numbers of objects, and for them we adopted N_{min} values close to 1% of the sample, after checking that this choice did not affect severely the results.

As for the critical distance level, it is derived by generating synthetic populations (Quasi-Random Populations) of fictitious objects occupying the same volume of proper element space, and generated in such a way as to have *separately* identical, uncorrelated distributions of a, e and $\sin I$ as the real asteroids present in the same volume. An HCM analysis of these fictitious populations is performed to identify critical values of mutual distance below which groupings of at least N_{min} quasi-random objects are not found. All groups of real objects which include N_{min} members at distance levels below the critical threshold are then considered as dynamical families. Note that we look at groupings found at discrete distance levels separated by steps of 10 m/s, starting from a minimum value of 10 m/s.

It is a rare case, in the domain of astronomical disciplines, that the abundance of data, and not their scarcity, produces technical problems. The reason is that the catalogs of asteroid proper elements are today so large that difficult problems of overlapping between different groupings must be faced, especially the phenomenon of *chaining* by which obviously independent families get attached together by a thin chain of asteroids.

For these reasons, when necessary (i.e., in the most populous zones of the asteroid belt) we have adopted in this paper a new, multistep procedure, allowing us to deal at each step with manageable numbers of objects, and appropriate procedures to combine the results obtained in different steps.

6.2.1 Step 1: Core families

In order to cope with the challenge posed by very big samples of objects in the low-inclination portions of zones 2, 3 and 4, we first look for the cores of the most important families present in these regions.

We thus take into account that small asteroids are subject to comparatively fast drifts in semi-major axis by the Yarkovsky effect, and to some other effects (including low-energy collisions, see Dell'Oro et al. [2012]). The cloud of smallest members of a newly born family expands therefore in the proper element space and the family borders tend to "blur" as a function of time. Hence, we first removed from our HCM analysis of the most populous regions all objects having absolute magnitudes H fainter than H_{comp} roughly corresponding to the completeness limit in each of the low-I portions of zones

2, 3 and 4. The completeness limits listed in Table 6.2 were derived from the cumulative distributions of H; for the purposes of our analysis, the choice of this threshold value is not critical. Having removed the faint objects, we were left with a much more manageable numbers of asteroids, see Table 6.2.

To these samples, we applied the classical HCM analysis procedures. As a preliminary step we considered in each zone samples of N completely random synthetic objects (N being the number of real objects present in the zone), in order to determine a distance value RL at which these completely random populations could still produce groups of N_{min} members. Following Zappalà et al. [1995], groups of the real population with $> 10\%$ of the total population at RL were then removed and substituted by an equal number of fully-random objects. The reason of this preliminary operation is to avoid that in the real population, a few very big and dense groups become exceedingly dominant and affect the distributions of proper elements in the zone by over-populating some bins of the $a, e, \sin I$ distribution, from which the Quasi-Random population is next built (see below) [11]. Only one group in Zone 3 and two in Zone 4 were removed and then substituted by equal number of randomly generated clones. In Zone 2, however, the RL turned out to be exceedingly high: 160 m/s, a distance level at which practically the whole real population merges in a unique group. Removing real objects at that level would have meant to substitute nearly the whole real population by fully-random objects. So this substitution was *not* done in Zone 2.

After that, we performed the classical generation of quasi-random populations. In each zone, the distributions of proper a, e, and $\sin I$ to be mimicked by the quasi-random populations were subdivided in number of bins (see Table 6.2), and the minimum distance for which groupings of N_{min} objects could be found are determined. We considered as the critical Quasi Random level QRL in each zone the minimum value obtained in ten runs. The QRL values adopted in each zone are given in Table 6.2.

Finally, we run the HCM algorithm on the real proper elements. Families were defined as the groups having at least N_{min} members at distance levels 10 m/s lower than QRL, or just reaching QRL, but with a number of members $N \geq N_{min} + 2\sqrt{N_{min}}$.

The families obtained in this first step of our procedure include only a small subset, corresponding to the largest objects, of the asteroids present in the low-I portion of zones 2, 3 and 4. For this reason, we call them "core families": they represent the inner "skeletons" of larger families present in

[11] As a matter of fact, such an over-representation could affect the generation of Quasi-Random objects, producing an exceedingly deep (low) Quasi-Random level (QRL) of distance, leading to a too severe criterion for family acceptance

these zones, whose additional members are to be identified in the following steps of the procedure (see Figure 6.3). In the case of the high-I portions of zones 2, 3 and 4, and the entire zones 1, 5 and 6, the number of asteroids was not that large, and we identified families by the direct application of the HCM procedure, without the multistep approach. For each family, the members were simply all the objects found to belong to it at the QRL value common to the zone. In other words, we did not adopt a case-by-case approach based on looking at the details of the varying numbers of objects found within each group at different distance levels, as was done by Novaković et al. [2011] to identify members of the high-inclination families.

6.2.2 Step 2: Attaching smaller asteroids to core families

The second step of the procedure in the low-I portions of zones 2, 3 and 4 was to *classify* individual asteroids which had not been used in the core classification, by attaching some of them to the established family cores. For this we used the same QRL distance levels used in the identification of the family cores, but we allowed only single links for attachment, because otherwise we would get chaining, with the result of merging most families together. In other words, in step 2 we attribute to the core families the asteroids having a distance from at least one member (of the same core family) not larger than the QRL critical distance. The result is that the families are extended in the absolute magnitude/size dimension, not much in proper elements space, especially not in proper a (see Figure 6.3).

Since this procedure has to be used many times (see Section 6.2.6), it is important to use an efficient algorithm. The distances between M proper element sets are $M \cdot (M-1)/2$, we could compute all of them then select the ones $< QRL$. The computational load is reduced by the partition into zones, but with zones containing $> 100\,000$ asteroids with proper elements it is anyway a time consuming procedure.

This problem has a solution which is well known, although it may not have been used previously in asteroid family classification. Indeed, the problem is similar to the one of comparing the computed ephemerides of a catalog of asteroids to the available observations from a large survey [Milani and Gronchi, 2010, Section 11.3]. We select one particular dimension in the proper elements space, e.g, $\sin I$; we sort the catalog by the values of this proper element. Then, given the value of $\sin I_0$ for a given asteroid, we find its position in the sorted list, and scan the list starting from this position up and down, only until the values $\sin I_0 + QRL$ and $\sin I_0 - QRL$, respectively, are

exceeded. In this way the computational complexity for the computation of the distances $< QRL$ for M asteroids is of the order of $M \log_2(M)$, instead of M^2. The large distances are not computed, even less stored in the computer memory.

6.2.3 Step 3: Hierarchical clustering of intermediate background

As an input to the third step in the low-I portion of zones 2, 3, and 4, we use the "intermediate background" asteroids, defined as the set of all the objects not attributed to any family in steps 1 and 2. The HCM procedure was then applied to these objects, separately in each of the three zones.

The numbers of objects left for step 3 of our analysis were 99399 in zone 2, 94787 in zone 3 and 57422 in zone 4. The corresponding values of N_{min} were 42, 46 and 34, respectively, adopting the same criterion Zappalà et al. [1995] already used for core families. The same HCM procedures were applied, with only a few differences. In computing the critical QRL distance threshold, we did not apply any preliminary removal of large groupings of real objects, because *a priori* we were not afraid to derive in this step of our procedure rather low values of the QRL distance level threshold. The reason is that, dealing with very large numbers of small asteroids, we have to adopt quite strict criteria for family acceptance, in order to minimize the possible number of false grouping, and to reduce the chance of spurious family merging. We obtained the following QRL values: 50, 60 and 60 m/s for zones 2, 3 and 4, respectively. Following the same criteria used for core families, step 3 families were supposed to be found as groupings having at least N_{min} members at 40 m/s in zone 2, and 50 m/s in the zones 3 and 4.

On the other hand, as mentioned above, in identifying step 3 families we are forced to be quite conservative because of overlapping between different families due either to the intrinsic mobility of their smallest members in the proper element space, as a consequence of (mostly) Yarkovsky, or to the family-forming collisional events which also can produce overlapping of members of different families in the proper element space. For these reasons, we eventually adopted a value of 40 m/s for step 3 family identification in all three zones. We also checked that adopting a distance level of 50 m/s in zones 3 and 4 would tend to produce an excessive effect of chaining, which would suggest merging of independent families.

Families identified at this step are formed by the population of asteroids left after removing from the proper elements data set family members identified in steps 1 and 2 of our procedure. There are therefore essentially two

possible cases: "step 3" families can either be fully independent, new families having no relation with the families identified previously, or they may be found to overlap "step 1+2" families, and to form "satellite families" of smaller objects surrounding some family cores. The procedure adopted to distinguish between these two cases is described in the following.

6.2.4 Step 4: Attaching background asteroids to all families

After adding the step 3 families to the list of core families of step 1, we repeat the procedure of attribution with the same algorithm of step 2. The control value of distance d for attribution to a given family is the same used in the HCM method as QRL for the same family; thus values are actually different for step 1 and step 3 families, even in the same zone.

If a particular asteroid is found to be attributed to more than one family, it belongs to an "intersection". A small number of these asteroids with double classification is unavoidable, but the concentration of multiple intersections between particular families requires some explanation.

One possible explanation is due to the presence of families at the boundaries between high and low inclination regions in zones 3 and 4, where there is no gap between them. Indeed, the classification has been done for proper $\sin I > 0.29$ for the high I regions, for $\sin I < 0.30$ for low I. This implies that some couples of families are found with intersection in the overlap strip $0.29 < \sin I < 0.30$, e.g., family 729. This is an artifact of our decomposition in zones and needs to be corrected by merging the intersecting families.

6.2.5 Step 5: Merging satellite families with core families

Some cases of family intersections, created by step 4, lead to the "satellite families". This is when a new family appears as an extension of a family already identified at steps 1 and 2, with intersections near the boundary.

In general for the merging of two families we require multiple intersections. Visual inspection of the three planar projections of the intersecting families proper elements is used as a check, and can allow to assess ambiguous cases.

Of the 77 families generated by HCM in step 3, we have considered 34 to be satellite. Even 2 core families have been found to be satellite of other core families and thus merged. There are of course dubious cases, with too few intersections, as discussed in Section 6.3.1. Still the number of asteroids belonging to intersections decreases sharply, e.g., in the two runs of single-

step linkage before and after the step 5 mergers, the number of asteroids with double classification decreased from 1 042 to 29.

The other 43 families resulting from step 3 have been left in our classification as independent families, consisting mostly of smaller asteroids. As discussed in Sections 6.3.2 and 6.3.3, some of them are quite numerous and statistically very significant, some are not large enough and may require confirmation, but overall the step 3 families give an important contribution.

6.2.6 Automatic update

The rapid growth of the proper elements database results in any family classification becoming quickly outdated. Thus we devised a procedure for an automatic update of this family classification, to be performed periodically.

The procedure consists in repeating the attribution of asteroids to the existing families every time the catalog of synthetic proper elements is updated. What we repeat is actually step 4, thus the lists of core families members (found in step 1), of members of smaller families (from step 3), and also the list of mergers (from step 5) are kept unchanged.

There is a step which currently we have not automated, and that is step 5: in principle, as the list of asteroids attached to established families grows, the intersection can increase. As an example, with the last update of the proper elements catalog with 18 149 additional records, we have added 3 586 new "step 4" family members. Then the number of intersections, that is members of two families, grows from 29 to 36. In some cases the new intersections support some merge previously not implemented because considered dubious, some open new problems, in any case to add a new merger is a delicate decision which at the moment we are unable to automatize.

As time goes by, there will be other changes, from the confirmation/contradiction of some of our interpretations by new data: as an example, some small families will be confirmed by the attribution of new members and some will not. At some point we may conclude that some small families are flukes and decide to remove them from the classification, but this is a complicated decision based on the statistical significance of the lack of increase.

In conclusion we are committed to monitor as the classification is updated and to perform non-automated changes whenever we believe there is enough evidence to justify them. The purpose of both automated and non-automated upgrades of the classification is to maintain the validity of the information made public for many years, without the need for repeating the entire procedure. This is also to avoid confusing the users with the need of continuously resetting their perception of the state of the art.

6.2.7 Some methodological remarks

As it should be clear after the description above, our approach to asteroid family identification is based on procedures which are quite different from other possible approaches previously adopted by other authors.

In particular, we do not use any systematic family classifications in > 3 dimensional spaces, such as the ones based either upon proper elements and albedo, or proper elements and color indexes, or all three data sets. We make use in our procedure, when dealing with very populous zones, of the absolute magnitude, but only as a way to decompose into steps the HCM procedure, see Subsection 6.2.1. Any other available data are used only *a posteriori*, as verification and/or improvement, after a purely dynamical classification has been built. The reasons for this are explained in Table 6.1: less objects, each with a set of $4 - 6$ parameters, actually contain less information.

We acknowledge that other approaches can be meaningful and give complementary results. The specific advantage of our methods is in the capability of handling large numbers of small asteroids. This allows to discover, at least to measure better, different important phenomena. The best example of this is the radical change in perception about the cratering families, which have been more recently discovered and are difficult to appreciate in an approach biased against the information provided by small asteroids, as in classifications requiring the availability of physical data (see Section 6.6).

We do not make use of naked eye taxonomy, that is of purely visual perception as the main criterion to compose families. We agree that the human eye is an extremely powerful instrument, but we want to provide the users with data as little as possible affected by subjective judgments. We have no objection on the use of visual appreciation of our proposed families by the users of our data, as shown by the provision of a dedicated, public graphic tool. But this needs to be kept separate, after the classification has been computed by objective methods.

The reader who may may wish to compare our results with other recent classifications such as Brož et al. [2013a]; Carruba et al. [2013]; Masiero et al. [2013]; Mothé-Diniz et al. [2005]; Parker et al. [2008] should note that such comparison are not easy. One reason is that the families are conventionally based on the lowest numbered member, and a family which is statistically the same might have a different name. Thus comparisons should be based on the full lists of members, not just on summary tables: of the above cited classifications, as far as we know only Brož et al. [2013a] makes full lists available[12].

[12]http://sirrah.troja.mff.cuni.cz/~mira/mp/fams/

6.3 Results from dynamical classification

6.3.1 Large families

By "large families" we mean those having, in our classification, $> 1\,000$ members. There are 19 such families: some of their properties are in Table 6.3.

Table 6.3: Large families with > 1000 members sorted by # tot. The columns give: family, zone, QRL distance (m/s), number of family members classified in steps 1, 3, 2+4 and the total number of members, family boundaries in terms of proper a, e and $\sin I$.

family	no	z	QRL	1	3	$2+4$	tot	a_{min}	a_{max}	e_{min}	e_{max}	sI_{min}	sI_{max}
Hertha	135	2	70	1141	5001	5286	11428	2.288	2.478	0.134	0.206	0.032	0.059
Eos	221	4	100	3060	310	6966	10336	2.950	3.146	0.022	0.133	0.148	0.212
Vesta	4	2	70	1599	925	5341	7865	2.256	2.482	0.080	0.127	0.100	0.132
Eunomia	15	3	90	2713	0	4132	6845	2.521	2.731	0.117	0.181	0.203	0.256
Koronis	158	4	100	930	0	4671	5601	2.816	2.985	0.016	0.101	0.029	0.047
Massalia	20	2	70	86	3546	1126	4758	2.335	2.474	0.145	0.175	0.019	0.033
Themis	24	4	100	1208	0	2742	3950	3.062	3.240	0.114	0.192	0.009	0.048
Hygiea	10	4	100	511	50	1841	2402	3.067	3.241	0.100	0.166	0.073	0.105
Astrea	5	3	90	27	1743	350	2120	2.552	2.610	0.146	0.236	0.054	0.095
Agnia	847	3	90	176	175	1682	2033	2.713	2.819	0.063	0.083	0.056	0.076
Maria	170	3	90	785	0	1245	2030	2.523	2.673	0.067	0.128	0.231	0.269
Minerva	93	3	90	641	0	1192	1833	2.720	2.816	0.115	0.155	0.147	0.169
Adeona	145	3	90	327	0	1072	1399	2.573	2.714	0.153	0.181	0.193	0.213
Hoffmeister	1726	3	90	84	159	1072	1315	2.754	2.818	0.041	0.053	0.066	0.088
Levin	2076	2	70	140	528	477	1145	2.254	2.323	0.130	0.153	0.088	0.106
Veritas	490	4	100	187	46	903	1136	3.143	3.196	0.049	0.079	0.151	0.172
Hungaria	434	1	70	662	0	455	1117	1.883	1.988	0.051	0.097	0.344	0.378
Dora	668	3	90	259	0	842	1101	2.744	2.811	0.188	0.204	0.129	0.143
Klumpkea	1040	4	100	226	0	870	1096	3.083	3.174	0.176	0.217	0.279	0.298

The possibility of finding families with such large number of members results from our method to attach to the *core families* either families formed with smaller asteroids or individual asteroids which are suitably close to the core. The main effect of attaching individual asteroids is to extend the family to asteroids with higher H, that is smaller. The main effect of attaching satellite families is to extend the families in proper a, as a consequence of the Yarkovsky secular drift da/dt, inversely proportional to the diameter D.

As the most spectacular increase in the family size, the core family of (5) Astraea is very small, with only 27 members, growing to 2 120 members with steps 2-5: almost all the family members are small, i.e., $H > 14$.

Among the largest families, the ones of (135) Hertha and (4) Vesta are increased significantly in both ways, by attaching satellite families on the low

a side (the high a side being eaten up, in both cases, by the 3/1 resonance with Jupiter) and by attaching smaller asteroids to the core. The shape of both families, when projected on the proper a, e plane, clearly indicates a complex structure (Figures 6.10 and 6.12). There are two different reasons for these complex shapes: family 135 actually contains the outcome of the disruption of two different parents (see Section 6.5); family 4 is the product of two or more cratering events, but on the same parent body (see Section 6.6).

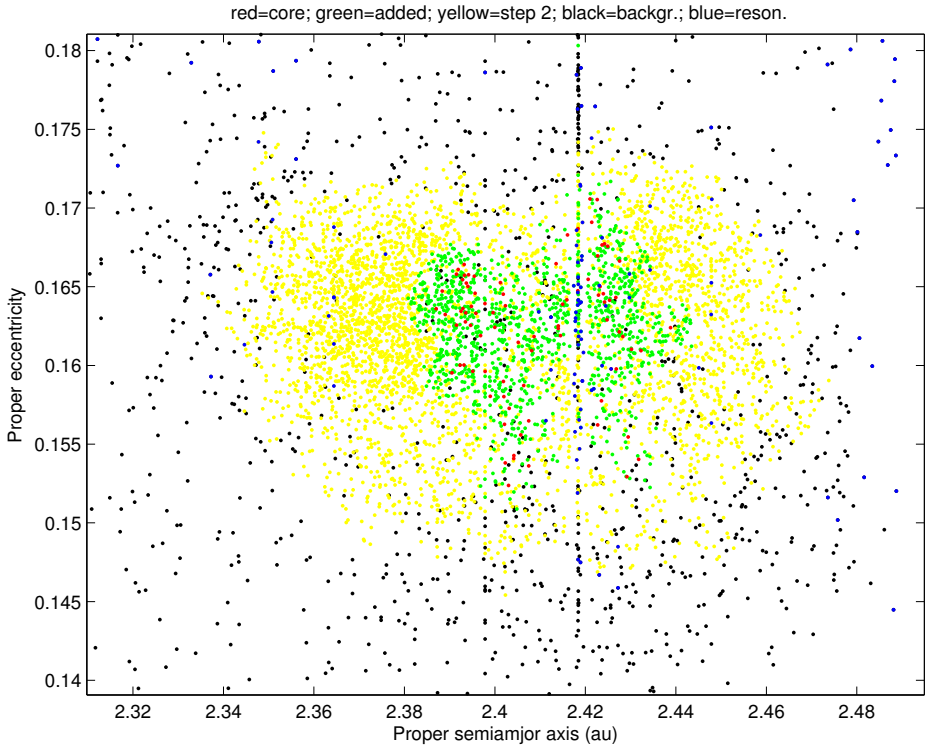

Figure 6.1: The family of (20) Massalia in the proper (a, e) plane. Red dots indicate members of the family core, green dots objects added in step 2 and 4 of the classification procedure, while yellow points refer to members of satellite families added at step 5, see Table 6.3. Black dots are not recognized as family members, although some of them might be, while others are background objects. Blue dots are chaotic objects, affected by the 2/1 resonance with Mars.

Another spectacular growth with respect to the core family is shown by the family of (20) Massalia, which is also due to a cratering event. The region of proper elements space occupied by the family has been significantly expanded by the attribution of the satellite families, in yellow in Figure 6.1, on both the low a and the high a side. The shape is somewhat bilobate, and this, as already reported by Vokrouhlický et al. [2006b], is due to the 1/2

resonance with Mars indicated by chaotic orbits (marked in blue) and by the line of diffusion along the resonance. The border of the family on the high proper a side is very close to the 3/1 resonance with Jupiter; the instability effects due to this extremely strong resonance may be responsible for the difficulties of attributing to the family a number of objects currently classified as background (marked in black). Anyway Massalia can be a significant source of NEA and meteorites through a chaotic path passing though the 3/1. On the contrary, there is no resonance affecting the low a border.

The families of (221) Eos and (15) Eunomia have also been increased significantly by our procedure, although the core families were already big. In both cases there is a complex structure, which makes it difficult to properly define the family boundaries.

The family of (158) Koronis was produced by an impact leading to complete disruption of the original parent body, since there is no dominant largest member. Family 158 has no satellite families: this is due to being sandwiched between the 5/2 resonance and the 7/3 resonance with Jupiter. The same lack of satellite families occurs for the family of (24) Themis: the 2/1 resonance with Jupiter explains the lack on the high a, the 11/5 resonance affects the low a boundary.

There has been some discussion on the family 490, but as pointed out already in Milani and Farinella [1994] the asteroid (490) Veritas is in a strongly chaotic orbit resulting in transport along a resonance (later identified as $5J - 2S - 2A$), thus it currently appears to be far away in proper e from the center of the family, but still can be interpreted as the parent body. A significant fraction of family members are locked in the same resonance, giving the strange shape of the family. To exclude (490) Veritas from the other group with largest member (1086) Nata, as proposed by Michel et al. [2011], the cutoff distance should be as low as 28 m/s Mothé-Diniz et al. [2005]; we are using 100 m/s for the core and 40 for step 3, thus we have no reason to exclude (490) from the family. Both spectroscopic data Mothé-Diniz et al. [2005] and the albedo data from WISE and IRAS confirm that the family is homogeneous in composition.

We note that in our analysis we do not identify a family associated with (8) Flora. A Flora family was found in some previous family searches, but always exhibited a complicated splitting behavior which made the real membership quite uncertain Zappalà et al. [1995]. We find (8) Flora to belong to a step 1 grouping which is present at a distance level of 110 m/s, much higher than the adopted QRL for this zone (70 m/s). This grouping merges with both (4) and (20) at 120 m/s, obviously meaningless. In a rigorous HCM analysis, the QRL cannot be increased arbitrarily just to accept as a family groupings like this one, not compliant with statistical reliability criteria.

Satellite problems

We are not claiming that our method of attaching "satellite" families to larger ones can be applied automatically and/or provide an absolute truth. There are necessarily dubious cases, most of which can be handled only by suspending our judgment. Here we are discussing the problem cases, resulting in a total of 29 asteroids belonging to family intersections.

For the family of (15) Eunomia, the 3/1 resonance with Jupiter opens a wide gap on the low a side. The 8/3 resonance controls the high a margin, but there is a possible appendix beyond the resonance, the family of (173) Ino: we have four intersections 15–173. There is a problem in merging the two families: the proper $a = 2.743$ au of the large asteroid (173) appears incompatible with the dynamical evolution of a fragment from (15). A solution could be to join to family 15 only the smaller members of 173, but such a merge cannot be considered reliable at the current level of information.

The family of (221) Eos appears to end on the lower a side at the 7/3 resonance with Jupiter, but the high a boundary is less clear. There are two families 507 and 31811 having a small number (six) of intersections with 221: they could be interpreted as a continuation of the family, which would have a more complex shape. However, for the moment we do not think there is enough information to draw this conclusion. Other families in the same region have no intersections and appear separate: the $a, \sin I$ projection shows well the separation of core families 179, 490, 845, and small families 1189 and 8737, while 283 is seen to be well separate by using an $e, \sin I$ projection.

The family of (135) Hertha has few intersections (a total of four) with the small families 6138 (48 members) 6769 (45 members) 7220 (49 members). All three are unlikely to be separate collisional families, but we have not yet merged them with 135 because of too little evidence.

The family of (2076) Levin is limited on the low a side by the 7/2 resonance with Jupiter. It has few (three) intersections with families 298 and 883. 883 is at lower a than the 7/2 resonance, and could be interpreted as a satellite, with lower density due to the ejection of family members by the resonance. Although this is a reasonable interpretation, it cannot be considered proven, thus we have not merged 2076–883. As for the family of (298) Baptistina, again the merge with 2076 could be correct, but the two families in all three proper element planes appear rather as close, possibly partly overlapping, neighbors, than as a single homogeneous structure (the Baptistina family exhibits a low density of members and a complete lack of satellites, while the Levin family has densely packed members and a significant satellite family, lowest numbered (4375), with 38 intersection), implying different formation circumstances; thus we have not implemented the merge.

The family of (1040) Klumpkea has an upper bound of the proper $\sin I$ very close to 0.3, that is to the boundary between the moderate inclination and the high inclination zones, to which the HCM has been applied separately. This boundary also corresponds to a sharp drop in the number density of main belt asteroids (only 5.3% have proper $\sin I > 0.3$), which is one reason to separate the HCM procedure because of a very different level of expected background density. The small family of (3667) Anne-Marie has been found in a separate HCM run for high proper $\sin I$, but there are ten intersections with family 1040. However, a merged family would have a strange shape, with a sharp drop in number density inside the family. This could have explanation either because of a stability boundary or because of an observational bias boundary. However, this would need to be proven by a very detailed analysis, thus we have not implemented this merge.

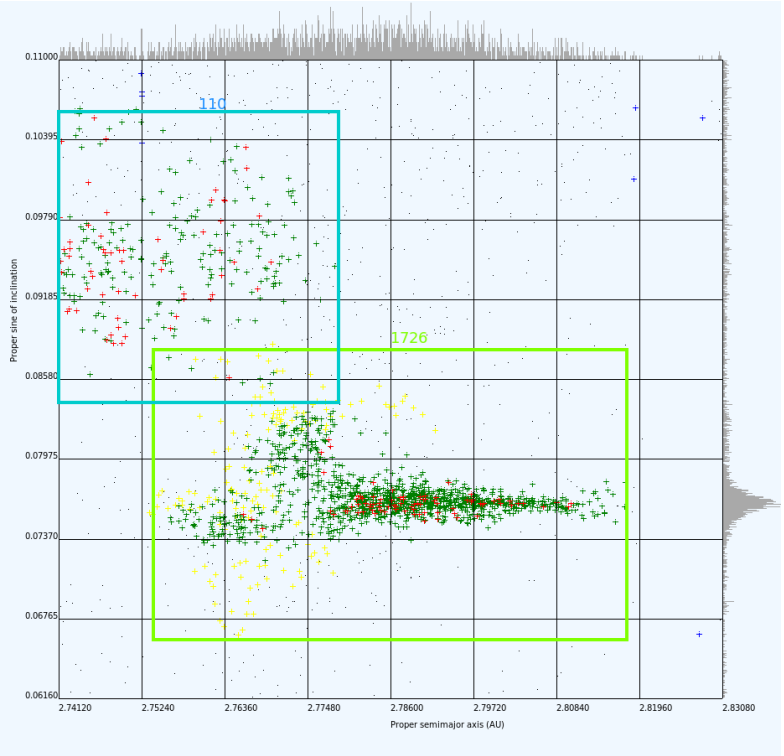

Figure 6.2: The strange shape of the family of (1726) Hoffmeister in the proper $a, \sin I$ projection. Some perturbations affect the low a portion of the family, including the halo family 14970. The family of (110) Lydia is nearby, but there is no intersection.

The family of (10) Hygiea has two intersections with family 1298, but the two are well separated in the $e, \sin I$ plane, thus they have not been merged.

The family of (1726) Hoffmeister has twenty intersection with the family 14970, formed with much smaller asteroids. Given such an overlap, merging the two families appears fully consistent with our procedure as defined in Section 3. However, the merged family has a strange shape, see Figure 6.2, in particular with a protuberance in the $\sin I$ direction which would not be easy to reconcile with a standard model of collisional disruption followed by Yarkovsky effect. Moreover, the strange shape already occurs in the core family, that is for the few largest asteroids, and thus should be explained by using perturbations not depending upon the size, that is gravitational ones.

Indeed, by consulting the database of analytic proper elements, it is possible to find that (14970) has a "secular resonance flag" 10, which can be traced to the effect of the secular resonance $g + s - g_6 - s_6$, see also [Milani and Knežević, 1994, Figure 7]; the same flag is 0 for (1726). Indeed, the value of the "divisor" $g + s - g_6 - s_6$ computed from the synthetic proper elements is 0.1 arcsec/y for (14970), 0.65 for (1726). On top of that, the proper semimajor axis of (1) Ceres is 2.7671 au, which is right in the range of a of the protuberance in proper $\sin I$, thus it is clear that close approaches and the 1/1 resonance with Ceres can play a significant role in destabilizing the proper elements Delisle and Laskar [2012]. We do not have a rigorous answer fully explaining the shape of the family, but we have decided to apply this merger because the number of intersection is significant and the strange shape did not appear as a result of the procedure to enlarge the core family.

From these examples, we can appreciate that it is not possible to define some algorithmic criterion, like a fixed minimum number of intersections, to automatize the process. All of the above cases can be considered as still open problems, to be more reliably solved by acquiring more information.

6.3.2 Medium families

By "medium families" we mean families found to have more than 100 and no more than 1 000 members; the properties of the 41 families in this group are given in Table 6.4. The exact boundaries 100 and 1 000 are chosen just for convenience: still the distinction between families based on these boundaries has some meaning. The medium families are such that the amount of data may not be enough for detailed studies of the family structure, including family age determination, size distribution, detection of internal structures and outliers. They are unlikely to be statistical flukes, they represent some real phenomenon, but some caution needs to be used in describing it.

In this range of sizes it is necessary to analyze each individual family to find out what can be actually done with the information they provide. As for the ones near the lower boundary for the number of members, they are

Table 6.4: The same as in Table 6.3 but for medium families with $100 < \# \leq 1000$ members.

family	no	z	QRL	1	3	2 + 4	tot	a_{min}	a_{max}	e_{min}	e_{max}	sI_{min}	sI_{max}
Euphrosyne	31	4	80	968	0	0	968	3.082	3.225	0.150	0.231	0.431	0.459
Phocea	25	2	130	944	0	0	944	2.261	2.415	0.160	0.265	0.366	0.425
Hansa	480	3	140	839	0	0	839	2.538	2.721	0.008	0.101	0.364	0.385
Merxia	808	3	90	72	166	567	805	2.705	2.805	0.125	0.143	0.080	0.093
Juno	3	3	90	45	257	462	764	2.623	2.700	0.228	0.244	0.225	0.239
Lydia	110	3	90	168	0	561	729	2.696	2.779	0.026	0.061	0.084	0.106
Zdenekhorsky	3827	3	90	29	310	332	671	2.705	2.768	0.082	0.096	0.080	0.094
Gantrisch	3330	4	100	63	0	537	600	3.123	3.174	0.184	0.212	0.171	0.184
Inness	1658	3	90	98	172	288	558	2.546	2.626	0.165	0.185	0.123	0.142
Ursula	375	4	100	229	0	273	502	3.096	3.241	0.059	0.130	0.264	0.299
Brasilia	293	4	100	38	0	405	443	2.832	2.872	0.119	0.133	0.256	0.264
Harig	10955	3	40	0	428	0	428	2.671	2.739	0.005	0.026	0.100	0.113
Erigone	163	2	40	0	392	0	392	2.332	2.374	0.200	0.218	0.081	0.098
Misa	569	3	40	0	389	0	389	2.623	2.693	0.169	0.183	0.035	0.045
Astrid	1128	3	40	0	389	0	389	2.754	2.817	0.045	0.053	0.008	0.018
Emma	283	4	100	49	0	320	369	3.029	3.084	0.107	0.124	0.155	0.166
Klytaemnestra	179	4	100	60	0	306	366	2.955	3.015	0.053	0.080	0.148	0.159
Martes	5026	2	40	0	346	0	346	2.368	2.415	0.200	0.217	0.082	0.096
Konig	3815	3	40	0	283	0	283	2.563	2.583	0.138	0.143	0.145	0.164
Schubart	1911	6	60	280	0	0	280	3.964	3.967	0.159	0.222	0.041	0.055
Naema	845	4	100	29	0	224	253	2.917	2.953	0.029	0.041	0.205	0.209
Prokne	194	3	140	235	0	17	252	2.522	2.691	0.154	0.196	0.293	0.315
Aeolia	396	3	40	0	242	0	242	2.731	2.750	0.164	0.170	0.057	0.062
1992DY7	12739	3	40	0	240	0	240	2.682	2.746	0.047	0.060	0.031	0.041
Struveana	778	4	100	29	0	200	229	3.158	3.191	0.240	0.261	0.243	0.253
Barcelona	945	3	140	219	0	0	219	2.599	2.659	0.190	0.289	0.506	0.521
Luthera	1303	4	80	179	0	0	179	3.193	3.236	0.106	0.144	0.310	0.337
Sulamitis	752	2	70	27	90	41	158	2.421	2.484	0.084	0.095	0.085	0.092
1995SU37	18466	3	40	0	155	0	155	2.763	2.804	0.171	0.182	0.229	0.236
Ino	173	3	90	29	0	125	154	2.708	2.770	0.159	0.180	0.229	0.239
Brangane	606	3	40	0	153	0	153	2.573	2.594	0.179	0.183	0.166	0.168
Laodica	507	4	100	38	0	111	149	3.124	3.207	0.049	0.075	0.181	0.198
1998RH71	13314	3	40	0	146	0	146	2.756	2.801	0.170	0.183	0.069	0.078
Clarissa	302	2	40	0	143	0	143	2.385	2.418	0.104	0.111	0.056	0.060
Nocturna	1298	4	100	69	0	74	143	3.088	3.220	0.105	0.123	0.104	0.123
Sylvia	87	5	120	119	0	20	139	3.459	3.564	0.046	0.073	0.162	0.179
Matterania	883	2	70	46	0	86	132	2.213	2.259	0.140	0.151	0.092	0.102
Baptistina	298	2	70	43	0	88	131	2.261	2.288	0.146	0.161	0.100	0.114
Darcydiegel	19466	3	40	0	125	0	125	2.724	2.761	0.007	0.020	0.103	0.111
Nele	1547	3	40	0	108	0	108	2.641	2.650	0.267	0.270	0.211	0.212
Duponta	1338	2	70	38	0	66	104	2.259	2.302	0.119	0.130	0.075	0.091

expected to grow as the family classification procedure is applied automatically by the AstDyS information system to larger and larger proper elements datasets. As a result, they should over a time span of several years grow to the point that more information on the collisional and dynamical evolution process is available. The only other expected outcome is that some of them can become much stronger candidates for merging with big families (e.g., family 507 cited above as a possible appendix to 221). If some others were not to grow at all, even over a timespan in which there has been a significant increase in number density (e.g, 50%) in the region, this would indicate a serious problem in the classification and would need to be investigated.

Note that 14 of the medium families have been generated in step 3, that is they are formed with the intermediate background after removal of step 1 and 2 family members, roughly speaking with "smaller" asteroid.

Some remarkable medium families

The families of (434) Hungaria, (25) Phocaea, (31) Euphrosyne, and (480) Hansa, clustered around the 1 000 members boundary, are the largest high inclination families, one for each semimajor axis zone[13]. Given the lower number density for proper $\sin I > 0.3$ the numbers of members are remarkably high, and suggest that it may be possible to obtain information on the collisional processes at higher relative velocities. These four were already known Carruba [2009]; Knežević and Milani [2003]; Milani et al. [2010]; Novaković et al. [2011], but now it is possible to investigate their structure.

For family 480 the proper e can be very small: this results in a difficulty in computing proper elements (especially e and the proper frequency g) due to "paradoxical libration". We need to fix our algorithm to avoid this problem, but it has no influence on family membership, since $e = 0$ is not a boundary.

The largest family in zone 5 is the one of (87) Sylvia, which is well defined, but with a big central gap corresponding to the resonance 9/5 with Jupiter. This family has in (87) such a dominant largest member that it can be understood as a cratering event, even if we do not have a good idea of how many fragments have been removed by the 9/5 and other resonances[14].

The largest family found in zone 6, that is among the Hilda asteroid locked in the 3/2 resonance with Jupiter, is the one of (1911) Schubart. Proper elements for Hildas, taking into account the resonance, have been computed by Schubart [1991], but we have used as input to the HCM (step 1) procedure

[13]Zones 5 and 6 have essentially no stable high inclination asteroids

[14]This family is interesting also because (87) Sylvia has been the first recognized triple asteroid system, formed by a large primary and two small satellites Marchis et al. [2005]

the synthetic proper elements computed without taking into account the resonance, thus averaging over the libration in the critical argument. This is due to the need to use the largest dataset of proper elements, and is a legitimate approximation because the contribution of even the maximum libration amplitude to the modified metrics d, to be used for resonant asteroids, is more than an order of magnitude smaller than the one due to eccentricity.

We have not identified a family of (153) Hilda Brož et al. [2011], and this can be understood because they use for determining the Hilda family members a distance truncation level 140 m/s, as opposed to our QRL of 60 m/s. In our HCM procedure the Hilda family would appear and gobble up our small family 6124 (at a truncation level of $d = 80$ m/s) and absorb also the tiny family 3561 (at $d = 120$ m/s). Thus the Hilda family is too sparse to be a statistically significant concentration, even being a large structure perfectly visible in a plot in the proper $(e, \sin I)$ plane. According to Brož et al. [2011] its age is ~ 4 Gy, which means the family has lost all the small members, thus it has become too sparse to detect with a rigorous application of HCM. The smaller families 6124 and 3561 could be interpreted as the results of fragmentations, younger by an order of magnitude, of some Hilda family members.

6.3.3 Small families

The families we rate as "small" are those in the range between 30 and 100 members; data for 43 such families are in Table 6.5. Out of these, 29 are "small families" added in step 3, and not absorbed as satellite families.

The families in this category have been selected on the basis of statistical tests, which indicates they are unlikely to be statistical flukes. Nevertheless, most of them need some confirmation, which may not be available due to small number statistics. Thus most of these proposed families are there waiting for confirmation, which may require waiting for more data.

The possible outcomes of this process, which requires a few years, are as follows: (i) the family is confirmed by growing in membership, as a result of automatic attachment of new numbered asteroids; (ii) the family is confirmed by the use of physical observations and/or modeling; (iii) the family grows and become attached as satellite to a larger family; (iv) the family is found not to exist as collisional family because it does not increase with new smaller members; (v) the family is found not to exist as collisional family because of enough physical observations showing incompatible composition.

Thus the tables published in this paper are to be used as reference and compared, at each enlargement of the proper elements database, with the automatically generated new table based on more asteroids, to see which

Table 6.5: The same as in Table 6.3 but for small families with $30 < \# \leq 100$ members.

family	no	z	QRL	1	3	2 + 4	tot	a_{min}	a_{max}	e_{min}	e_{max}	sI_{min}	sI_{max}
Aegle	96	4	100	38	0	62	100	3.036	3.070	0.176	0.189	0.280	0.289
Gallia	148	3	140	95	0	0	95	2.712	2.812	0.116	0.150	0.420	0.430
Chloris	410	3	90	55	0	38	93	2.713	2.761	0.238	0.265	0.146	0.160
Leonidas	2782	3	90	21	0	71	92	2.657	2.701	0.185	0.197	0.061	0.072
1999NA41	31811	4	40	0	89	1	90	3.096	3.138	0.060	0.075	0.178	0.188
Wagman	3110	3	40	0	86	0	86	2.554	2.592	0.134	0.145	0.049	0.065
1993FY12	18405	4	40	0	85	0	85	2.832	2.858	0.103	0.110	0.158	0.162
1986QA1	7744	3	40	0	78	0	78	2.635	2.670	0.069	0.075	0.042	0.049
Hanskya	1118	4	100	47	0	30	77	3.145	3.246	0.035	0.059	0.252	0.266
Watsonia	729	3	90	73	0	2	75	2.720	2.814	0.110	0.144	0.294	0.305
1981EY40	17392	3	40	0	75	0	75	2.645	2.679	0.059	0.070	0.036	0.042
Ikenozenni	4945	3	40	0	71	0	71	2.570	2.596	0.235	0.244	0.087	0.096
Ausonia	63	2	40	0	70	0	70	2.383	2.401	0.118	0.127	0.107	0.118
4057P-L	16286	4	40	0	68	0	68	2.846	2.879	0.038	0.047	0.102	0.111
Tina	1222	3	140	68	0	0	68	2.769	2.803	0.068	0.113	0.350	0.359
1990RA3	11882	3	40	0	66	0	66	2.683	2.708	0.059	0.066	0.031	0.040
1997EM	21344	3	40	0	62	0	62	2.709	2.741	0.150	0.159	0.046	0.050
Lottie	3489	2	40	0	57	0	57	2.390	2.413	0.090	0.096	0.103	0.109
Mecklenburg	6124	6	60	57	0	0	57	3.966	3.967	0.186	0.212	0.146	0.159
1999FO14	29841	3	40	0	53	0	53	2.639	2.668	0.052	0.059	0.033	0.040
1999AZ8	25315	3	40	0	53	0	53	2.575	2.596	0.243	0.251	0.090	0.096
Ashkova	3460	4	100	28	0	24	52	3.159	3.218	0.187	0.209	0.016	0.028
Vladisvyat	2967	4	80	52	0	0	52	3.150	3.224	0.092	0.124	0.295	0.303
Bankakuko	8905	3	40	0	49	0	49	2.599	2.620	0.181	0.190	0.084	0.091
Philnicholson	7220	2	40	0	48	1	49	2.418	2.424	0.183	0.195	0.026	0.036
Karma	3811	3	40	0	49	0	49	2.547	2.579	0.101	0.110	0.185	0.190
1991JH1	6138	2	40	0	46	2	48	2.343	2.357	0.204	0.215	0.039	0.045
2000RD33	32418	3	40	0	48	0	48	2.763	2.795	0.255	0.261	0.152	0.156
2000BY6	53546	3	40	0	47	0	47	2.709	2.735	0.170	0.174	0.247	0.251
1999XM196	43176	4	40	0	47	0	47	3.109	3.152	0.065	0.074	0.174	0.183
Elfriede	618	4	40	0	46	0	46	3.177	3.200	0.056	0.059	0.270	0.277
2000HC81	28804	3	40	0	46	0	46	2.589	2.601	0.146	0.156	0.063	0.070
Anfimov	7468	4	40	0	45	0	45	3.031	3.075	0.087	0.091	0.060	0.061
Brokoff	6769	2	40	0	44	1	45	2.398	2.431	0.148	0.155	0.051	0.056
Aemilia	159	4	40	0	45	0	45	3.091	3.131	0.111	0.117	0.084	0.090
Traversa	5651	4	100	20	0	22	42	3.097	3.166	0.112	0.128	0.231	0.241
1999UY27	21885	4	40	0	42	0	42	3.079	3.112	0.026	0.035	0.184	0.188
Armenia	780	4	80	41	0	0	41	3.085	3.129	0.060	0.074	0.310	0.314
4072T-3	22241	4	40	0	40	0	40	3.082	3.096	0.126	0.133	0.087	0.096
Pallas	2	3	140	38	0	0	38	2.756	2.791	0.254	0.283	0.531	0.550
Terentia	1189	4	40	0	38	0	38	2.904	2.936	0.071	0.075	0.192	0.194
Takehiro	8737	4	40	0	37	0	37	3.116	3.141	0.112	0.121	0.207	0.211
Inarradas	3438	4	100	20	0	14	34	3.036	3.067	0.176	0.186	0.249	0.255

family is growing[15].

However, there are cases in which some of these outcomes appear more likely, and we shall comment on a few of them.

Small but convincing families

The family of (729) Watsonia has been obtained by joining a high I and a low I families. We are convinced that it is robust, but it may grow unevenly in the high I and in the low I portions because of the drop in number density, whatever its cause. Other results on this family are given in Section 6.5.

The family of (2) Pallas has only 38 members, but it is separated by a gap in proper a from the tiny family 14916. The gap is the effect of 3-body resonances, the main one being $3J-1S-1A$. Given the large escape velocity from Pallas (~ 320 m/s) an ejecta from (2) Pallas could be directly injected in an orbit with proper elements in the region of family 14916. We have not merged these two families because this argument, although we believe it is correct, arises from a model, not from the data as such.

Small families which could be satellites of large families

On top of the small families already listed in Subsection 6.3.1, which are considered as possible satellites because of intersections, there are other cases in which small families are very close to large ones, and thus could become candidates for merging as the size of the proper elements catalog increases.

To identify these cases we have used for each family the "box" having sides corresponding to the ranges in proper $a, e, \sin I$ listed in Tables 6.3–6.6, and we analyzed all the overlaps between them. The parameter we use as an alert of proximity between two families is the ratio between the volume of the intersection to the volume of the box for the smaller family. If this ratio is 100% then the smaller family is fully included within the box of the larger one; we have found 12 such cases. We found another 17 cases with ratio $> 20\%$. By removing the cases with intersections, or anyway already discussed in Sections 6.3.1 and 6.3.2, we are left with 17 cases to be analyzed.

One case of these overlapping-box families is about two medium families, namely family 10955 (with 428 members the largest of the step 3 families) and family 19466, which has 40% of its box contained in the box of 10955. The possibility of future merger cannot be excluded.

Among small/tiny families with boxes overlapping larger ones, we have found 10 cases we think could evolve into mergers with more data: 4-3489,

[15] At http://hamilton.dm.unipi.it/~astdys2/propsynth/numb.famtab you can download the current family table.

5-8905, 5-28804, 10-159, 10-22241, 221-41386, 375-2967, 480-34052, 1040-29185.

In two of the above cases there is already, from the first automatic update, supporting evidence: of the 7 new intersections, one is 10-22241 and another is 375-2967. We are not claiming this is enough evidence for a merge, but it shows how the automatic upgrade of the classification works.

In three cases we do not think there could be future mergers: 15-145, 15-53546, 221-21885. In another three cases the situation is too complicated to make any guess: 24-3460, 31-895, 4-63.

The conclusion from this discussion is clear: a significant fraction of the small families of Table 6.5, and few from Table 6.6, could be in the future included as satellites of larger families. Others could be confirmed as independent families, and some could have to be dismissed.

6.3.4 Tiny families

The "tiny families" are the ones with < 30 members; their number is critically dependent upon the caution with which the small clusters have been accepted as families. In Table 6.6 we describe 25 such families.

Given the cautionary statements we have given about the "small families", what is the value of the "tiny" ones? To understand this, it is useful to check the zones/regions where these have been found: 3 tiny families belong to zone 5, 1 to zone 6, 12 to zone 4 high inclination, 9 to zone 3 high inclination. Indeed, groupings with such small numbers can be statistically significant only in the regions where the number density is very low.

These families satisfy the requirements to be considered statistically reliable according to the standard HCM procedure adopted in the above zones. It should be noted that, due to the low total number of objects present in these regions, the adopted minimum number N_{min} of required members to form a family turns out to be fairly low, and its choice can be more important with respect to more densely populated regions. In the case of high-I asteroids, Novaković et al. [2011] included in their analysis a large number of unnumbered objects which we are not considering in the present paper. The nominal application of the HCM procedure leads to accept the groups listed in Table 6.6 as families, but it is clear that their reliability will have to be tested in the future when larger numbers will be available in these zones.

Thus, each one of these groups is only a proposed family, in need of confirmation. There is an important difference with most of the small families listed in Table 6.5: there are two reasons why the number densities are much lower in these regions, one being the lower number density of actual asteroids, for the same diameters; the other being the presence of strong observational

Table 6.6: The same as in Table 6.3 but for tiny families with < 30 members.

family	no	z	QRL	1	3	$2+4$	tot	a_{min}	a_{max}	e_{min}	e_{max}	sI_{min}	sI_{max}
Anne-Marie	3667	4	80	25	0	3	28	3.087	3.125	0.184	0.197	0.294	0.301
Helio	895	4	80	25	0	0	25	3.202	3.225	0.169	0.183	0.438	0.445
Ulla	909	5	120	23	0	1	24	3.524	3.568	0.043	0.058	0.306	0.309
Reich	29185	4	80	23	0	0	23	3.087	3.116	0.196	0.209	0.295	0.304
Brucato	4203	3	140	22	0	0	22	2.590	2.648	0.124	0.135	0.473	0.486
2000OL37	34052	3	140	21	0	0	21	2.641	2.687	0.073	0.087	0.368	0.377
Zhvanetskij	5931	4	80	19	0	0	19	3.174	3.215	0.160	0.172	0.302	0.313
1999RR2	22805	4	80	17	0	0	17	3.136	3.159	0.165	0.175	0.301	0.308
Clematis	1101	4	80	17	0	0	17	3.229	3.251	0.030	0.037	0.363	0.375
Sinden	10369	3	140	17	0	0	17	2.551	2.609	0.105	0.118	0.470	0.482
Higson	3025	4	80	16	0	0	16	3.192	3.221	0.059	0.066	0.368	0.378
1993VV7	14916	3	140	16	0	0	16	2.710	2.761	0.270	0.282	0.537	0.542
Devine	3561	6	60	15	0	0	15	3.962	3.962	0.127	0.133	0.149	0.156
2000EW12	45637	5	120	14	0	1	15	3.344	3.369	0.103	0.123	0.142	0.151
Huberta	260	5	120	11	0	4	15	3.410	3.464	0.081	0.088	0.100	0.108
1998HT148	58892	4	80	14	0	0	14	3.121	3.154	0.153	0.162	0.300	0.308
Univermoscow	6355	4	80	13	0	0	13	3.188	3.217	0.088	0.097	0.374	0.378
1998QO53	40134	3	140	13	0	0	13	2.715	2.744	0.223	0.235	0.429	0.438
2004EW7	116763	3	140	13	0	0	13	2.621	2.652	0.236	0.246	0.463	0.468
Bontekoe	10654	4	80	13	0	0	13	3.207	3.244	0.051	0.056	0.368	0.374
Myriostos	10000	3	140	13	0	0	13	2.562	2.623	0.260	0.273	0.316	0.325
1995FR1	7605	4	80	12	0	0	12	3.144	3.153	0.065	0.073	0.447	0.453
1997UG5	69559	4	80	12	0	0	12	3.202	3.219	0.196	0.201	0.299	0.305
1999PM1	20494	3	140	12	0	0	12	2.653	2.690	0.119	0.132	0.470	0.480
2000YD17	23255	3	140	10	0	0	10	2.655	2.688	0.095	0.113	0.460	0.469

biases which favor discovering only objects of comparatively large size. In the case of the high inclination asteroids the observational bias is due to most asteroid surveys looking more often near the ecliptic, because there more asteroids can be found with the same observational effort. For the more distant asteroids the apparent magnitude for the same diameter is fainter because of both larger distance and lower average albedo.

If a family is small because of observational bias, it grows very slowly in membership unless the observational bias is removed, which means more telescope time is allocated for asteroid search/recovery at high ecliptic latitude and more powerful instruments are devoted to find more distant/dark asteroids. Unfortunately, there is no way to be sure that these resources will be available, thus some "tiny" families may remain tiny for quite some time. In conclusion, the list of Table 6.6 is like a bet to be adjudicated in a comparatively distant future. We can already confirm that many of these tiny families are slowly increasing in numbers. As already mentioned, while this paper was being completed, the proper elements catalog has already been

updated, the automatic step 4 was completed, resulting in a new classification with a 4% increase in family membership. In this upgrade 14 out of 25 tiny families have increased their membership, in most cases by just $1 - -2$.

6.4 Use of absolute magnitude data

For most asteroids a direct measurement of the size is not available, whereas all the asteroids with an accurate orbit have some estimated value of absolute magnitude. To convert absolute magnitude data into diameter D we need the albedo, thus D can be estimated only for the objects for which physical observations, such as WISE data or polarimetric data, are available. However, families are generally found to be quite homogeneous in terms of albedo and spectral reflectance properties Cellino et al. [2002]. Therefore, by assuming an average albedo value for all the members of a given family, we can derive the size of each object from its value of absolute magnitude. This requires that a family has one or more members with a known albedo, and we have reasons to exclude that they are interlopers.

The main applications of the statistical information on the diameter D of family members are three: estimation of the total volume of the family, of the age of a collisional family, and of the size distribution.

6.4.1 The volume of the families

In case of a total fragmentation, the total volume of a collisional family, computed as the sum of the volume of known family members (estimated from absolute magnitude and some assumed common albedo), can be used to give a lower bound for the size of the parent body. For cratering, the volume computed without considering the parent body can be used to constrain from below the size of the corresponding crater. In case of dubious origin, the total volume can be used to discard some possible sources if they are too small.

As an example let us choose the very large family of (4) Vesta. The albedo of Vesta has been measured as 0.423 Tedesco et al. [2002], but more recently an albedo of 0.37 has been reported by Shevchenko and Tedesco [2006], while a value around 0.30 is found by the most recent polarimetric investigations Cellino et al. [2012][16].

Before computing the volume of fragments we need to remove the biggest interlopers, because they could seriously contaminate the result: asteroids (556) and (1145) are found to be interlopers because they are too big for their

[16]By using WISE albedos, it can be shown that the most frequent albedos for members of family 4 are in the range spanning these measurements, see Figure 6.13

position with respect to the parent body, as discussed in the next subsection, see Figure 6.5.

If we assume albedo 0.423 for all family 4 members, we can compute the volume of all the family members at 32 500 km^3. The volume would be 54 500 km^3 with albedo 0.3, thus the volume of the known family can be estimated to be in this range. On Vesta there are two very large craters, Rheasilvia and Veneneia, with volumes of $>$ 1 million km^3 Schenk et al. [2012]. Thus it is possible to find some source crater.

Another example of cratering on a large asteroid is the family of (10) Hygiea. After removing Hygiea and interlopers with $D > 40$ km which should be too large for being ejected from a crater[17], and assuming a common albedo equal to the IRAS measure for (10), namely 0.072, we get a total volume of the family as 550 000 km^3. This implies on the surface of (10) Hygiea there should be a crater with a volume at least as large as for Rheasilvia. Still the known family corresponds to only 1.3% of the volume of (10) Hygiea.

6.4.2 Family Ages

The computation of family ages is a high priority goal. As a matter of principle it can be achieved by using V-shape plots such as Figure 6.3, for the families old enough to have Yarkovsky effect dominating the spread of proper a. The basic procedure is as follows: as in the previous section by assuming a common geometric albedo p_v, from the absolute magnitudes H we can compute[18] the diameters D. The Yarkovsky secular effect in proper a is $da/dt = c\ \cos(\phi)/D$, with ϕ the obliquity (angle of the spin axis with the normal to the orbit plane), and c a calibration depending upon density, thermal conductivity, spin rate, and other parameters. As a matter of fact c is weakly dependent upon D, but this cannot be handled by a general formula since the dependence of c from thermal conductivity is highly nonlinear [Vokrouhlický et al., 2000b, Figure 1]. Thus, as shown in 10.1, the power law expressing the dependence of c upon D changes from case to case. For cases in which we have poor information on the thermal properties (almost all cases) we are forced to use just the $1/D$ dependency.

Then in a plot showing proper a vs. $1/D$ for asteroids formed by the same collisional event we get straight lines for the same ϕ. We can try to fit to the data two straight lines representing the prograde spin and retrograde spin states ($\phi = 0°$ and $\phi = 180°$). The slopes of these lines contain information on the family age. Note that this procedure can give accurate results only

[17] Asteroids (100), (108), (758) also have WISE albedo at least double that of Hygiea.
[18] $D = 1\,329 \times 10^{-H/5}\ \times 1/\sqrt{p_v}$

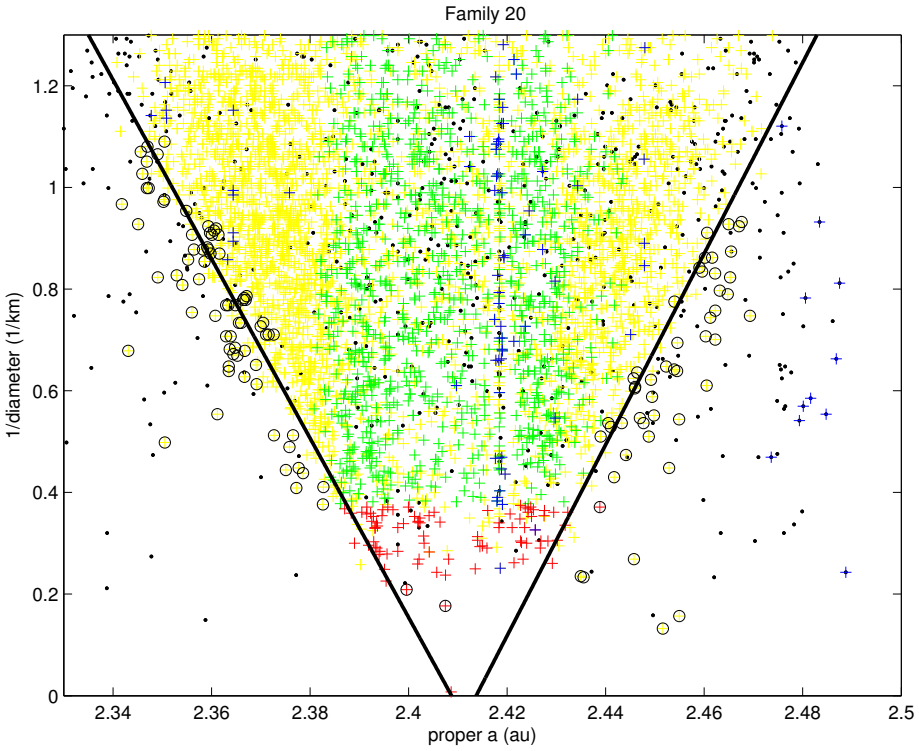

Figure 6.3: V-shape of the family 20 in the proper a vs. $1/D$ plane. The black lines are the best fit on the two sides; the black circles indicate the outliers. Black dots are background asteroids, crosses are colored according to the same conventions as in the previous Figures.

if the family members cover a sufficient interval of D, which now is true for a large set of dynamical families thanks to the inclusion of many smaller objects (represented by green and yellow points in all the figures).

As an example in Figure 6.3 we show two such lines for the Massalia family on both the low proper a and the high proper a side, that is representing the above mentioned retrograde and direct spin rotation state, respectively. This is what we call *V-shape*, which has to be analyzed to obtain an age estimate.

A method of age computation based on the V-shape has already been used to compute the age of the Hungaria family [Milani et al., 2010, Figure 20]. A similar method could be applied to all the large (and several medium) families; however, a procedure to handle cases with different properties needs to be more robust, taking into account the following problems.

The method assumes all the family members have the same age, that is, the coincidence of the dynamical family with the collisional family. If this is not the case, the procedure is more complicated: see in Figure 6.4

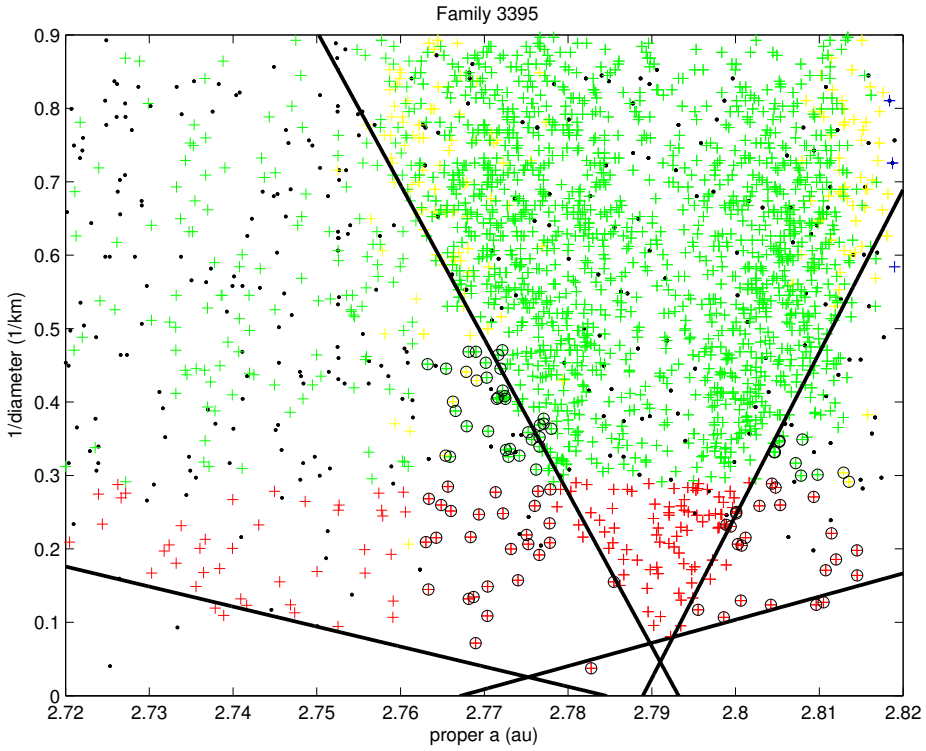

Figure 6.4: V-shapes, in the proper a vs. $1/D$ plane, for the family of (847) Agnia and for the subfamily of (3395) Jitka, which appears as a much denser substructure. All the members marked as outliers are for the Jitka slope fit.

two V-shapes, with a fit for the boundary, in the Agnia family, indicating at least two collisional events with different ages. Thus a careful examination of the family shape, in the $a, 1/D$ plot and in other projections, is required to first decide on the minimum number of generating collisional events. If substructures are found, with shape suggesting separate collisional events, their ages may in some cases be computed.

To compute the age we use the inverse slope $\Delta a(D)/(1/D)$ (D in km) of one of the two lines forming the V-shape, the same as the value of Δa for an hypothetical asteroid with $D = 1$ km along the same line. This is divided by the secular drift da/dt for the same hypothetical asteroid, giving the estimated age. However, the number of main belt asteroids for which we have a measured value of secular da/dt is zero. There are > 20 Near Earth Asteroids (NEA) for which the Yarkovsky drift has been reliably measured (with $S/N > 3$) from the orbit determination (see Sec. 3, Table 2.2). We can estimate the calibration c, and the expected value of da/dt for an asteroid with a given D, a, e, ϕ, by scaling the result for a NEA with different

D, a, e, ϕ. However, to derive an error model for this scaling is complicated; see Farnocchia et al. [2013a] for a full fledged Monte Carlo computation.

The data points $(1/D, a)$ in the V-shape are not to be taken as exact measurements. The proper a coordinate is quite accurate, with the chaotic diffusion due to asteroid-asteroid interaction below 0.001 au Delisle and Laskar [2012], and anyway below the Yarkovsky secular contribution for $D < 19$ km; the error in the proper elements computation (with the synthetic method) gives an even smaller contribution. To the contrary, the value of D can have a relative error of 0.2 (see the column $RMS(resid)$ in Table 6.7). Thus a point in the $1/D, a$ plane has to be considered as measurement with a significant error, especially in $1/D$, and the V-shape needs to be determined by a least squares fit, allowing also for outlier rejection.

Most families are bounded, on the low-a side and/or on the high-a side, by resonances strong enough to eject most of the family members reaching the resonant value of a by Yarkovsky, into unstable orbits. Thus the V-shape is cut by vertical lines at the resonant values of a. Thus the slope fit must be done for values of $1/D$ below the intersection of one of the slanted sides of the V and the vertical line at the resonant value of a. For many families this restricts the range of $1/D$ for which the V-shape can be measured.

The dynamical families always contain interlopers, few in number, but not representing a small fraction of the mass (the size distribution of the background asteroids is less steep). The removal of large interlopers is necessary not to spoil the computation of the slopes, and also of centers of mass.

For the common albedo we use the average of the WISE albedos with $S/N > 3$, cutting tails such as albedo < 0.15 and > 0.6 for V-types. The values used are in Table 6.7.

As a consequence of the above arguments, we have decided to develop a new method, which is more objective than the previous one we have used, because the slope of the two sides of the V-shape is computed in a fully automated way as a least squares fit, with equally automatic outlier rejection. The following points explain the main features of this new method.

1. For each family we set up the range of values for the proper a, and for the diameter D (we may use a different range of values for D for the inner and the outer side of the V, taking into account the interaction with resonances). Note this is the only "manual" intervention.

2. The computer code divides the $1/D$-axis into bins, which are created in such a way to contain about the same number of objects. Hence: the bins, which correspond to small values of $1/D$ are wider than the ones which correspond to large values of $1/D$; the inner and the outer side of the family may have different bins.

3. We select the minimum value (inner side) and the maximum value (outer side) of the proper a and the corresponding 1/D value in each bin. The variables of the fit are (proper a,1/D).

4. The computer code implements a linear regression for both sides. The method is iterative: for each iteration we calculate the residuals, the outliers and the kurtosis of the residuals. The outliers are the residuals greater than 3σ, where the control values σ should be the a priori standard deviation of the residuals in $1/D$. However, we do not have an a priori error model for the measurment of D. Thus we replace it with a quantity which is fixed in the iteration, our current choice is $\sigma = STD(a)$. After removing the outliers we repeat the linear regression. Note that the outliers for the fit can be interlopers in the family, but also family members with low accuracy diameters.

5. The method has converged if either the kurtosis of the residuals is 3 ± 0.3 or there is an iteration without additional outliers.

6. The standard deviation of the slope S is computed from the STD of the residuals σ and from the formal variance of the slope $\Gamma_{S,S}$ as found in the covariance matrix of the fit: $STD(S) = \sqrt{\Gamma_{S,S}} \times \sigma$. For the inverse slope $STD(1/S) = STD(S) \times (1/S^2)$.

7. The two straight lines on the sides of the V-shape are computed independently, thus they do not need to cross in a point on the horizontal axis. We compute the *V-base* as the difference in the a coordinate of the intersection with the a axis of the outer side and of the inner side. This quantity has an interpretation we shall discuss in Section 6.4.2.

The goal in this paper is to introduce objective methods taking into account the problems above. We pay a special attention to the computation of quantities like the slopes, used to estimate the family age; the ages themselves, involving the complicated calibration of the Yarkovsky effect, are given only as examples, to demonstrate what we believe should be a rigorous procedure.

Massalia

One of the best examples of dynamical family for which the computation of a single age for a crater is possible is the one of (20) Massalia, see Figure 6.1. The two slopes of the inner and outer side of V-shape (Figure 6.3) have opposite sign, with the absolute value different by 7.5%, see Table 6.7. This indicates an accurately determined slope, as confirmed by the formal STD of the fit.

Table 6.7: Results of the fit for the low a (IN) and high a (OUT) sides for each considered family: number of iterations, minimum diameter D (in km) used in the fit, number of bins, number of outliers, value of the kurtosis and standard deviation of the residuals in $1/D$, and the value of the inverse of the slope (in au).

family	albedo		iter.	Dmin	bins	outliers	kurtosis	RMS(resid)	1/slope	STD(1/slope)
20	0.250	IN	7	0.9	21	74	2.96	0.049	-0.057	0.003
20		OUT	6	1.0	13	48	3.12	0.062	0.053	0.004
4	0.353	IN	2	2.2	23	7	2.87	0.039	-0.299	0.045
4		OUT	2	3.9	7	2	1.49	0.035	0.588	0.251
15	0.260	IN	2	4.5	13	1	2.83	0.019	-0.550	0.085
15		OUT	2	5.9	16	1	2.84	0.016	0.447	0.050
158	0.235	IN	2	7.8	9	2	3.03	0.018	-0.346	0.090
158		OUT	2	4.6	11	0	2.16	0.027	0.445	0.080
847	0.238	IN	1	5.2	7	0	1.87	0.013	-0.367	0.070
847		OUT	1	7.2	7	0	1.36	0.011	0.317	0.050
3395	0.238	IN	10	2.1	9	63	2.78	0.038	-0.048	0.007
3395		OUT	7	2.9	8	33	2.81	0.024	0.045	0.007

The STD of the residuals is high and the number of outliers is large because the asteroids with $1 < D < 2.5$ km have a poorly determined absolute magnitude. Both accuracy of the fit and large residuals are due to the fit pushed down to small diameters, because the family is not cut by a resonance on the low a side, and is affected by the 3/1 J resonance on the high a side, but only for $D < 1$ km. The V-base is small and positive (Table 6.8). The internal structure of family 20 is further discussed in Section 6.6.1.

Vesta

The Vesta family has a complex structure, which is discussed in Section 6.6.2: thus the presence of two different slopes on the two sides (Figure 6.5 and Table 6.7) can be interpreted as measuring the age of two different collisional events, the one forming the high a boundary of the family being older. In theory two additional slopes exist, for the outer boundary of the inner subfamily and for the inner boundary of the outer family, but they cannot be measured because of the significant overlap of the two substructures. Thus the negative V-base has no meaning.

The family is cut sharply by the 3/1 resonance with Jupiter on the high a side and by the 7/2 on the low a side. As a result the outer side slope fit is poor, because the range of sizes is not large enough. That the slope is lower (the age is older) on the high a side is likely, but the ratio is only roughly estimated.

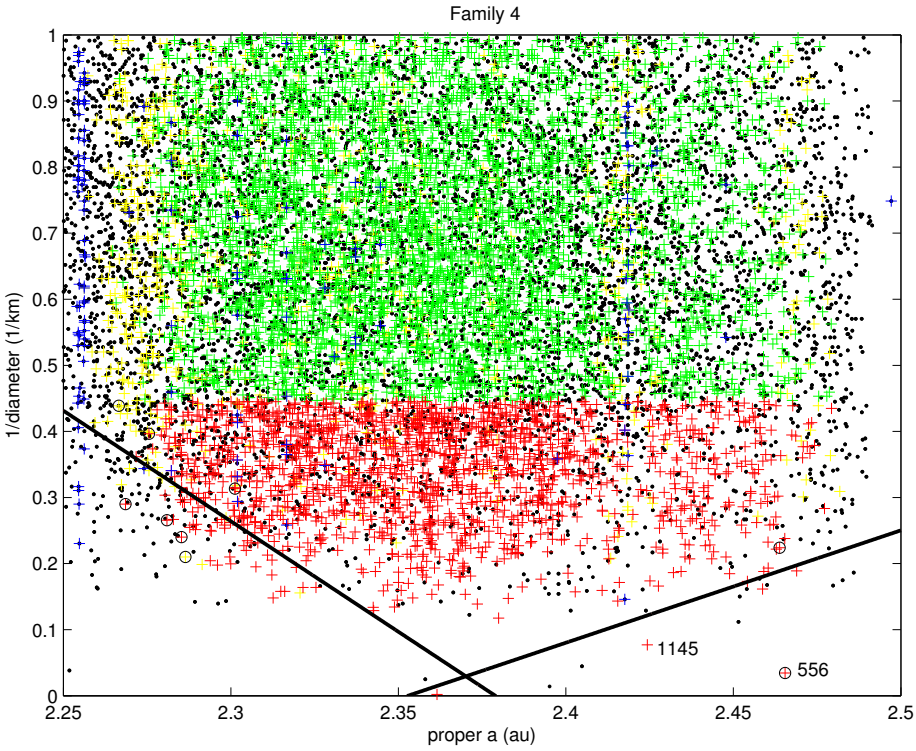

Figure 6.5: V-shape of the family 4. The lines identified by the fit have different slopes on the two sides; for the explanation see Section 6.6.2.

The calibration constant should be similar for the two subfamilies with the same composition (with only a small difference due to the relative difference in a), thus the age computed from the outer side is older, but we do not have a reliable estimate of this ratio.

For the computation of the barycenter (Table 6.8) it is important to remove the interlopers (556) and (1145), which clearly stick out from the V-shape on the outer side, although (1145) is not rejected automatically by the fit[19].

Eunomia

The slope on the outer side in Figure 6.6 is affected by the 8/3 resonance with Jupiter, forcing us to cut the fit already at $D = 5.9$ km. The fit on the inner side has been cut at $D > 4.5$ km, because the 3/1 J resonance is eating up the family at lower diameters. The inner and outer V-shape slopes for Eunomia are different by 23%, but this difference is very poorly constrained.

[19]By using the smaller WISE albedos, these two are even larger than shown in Figure 6.5.

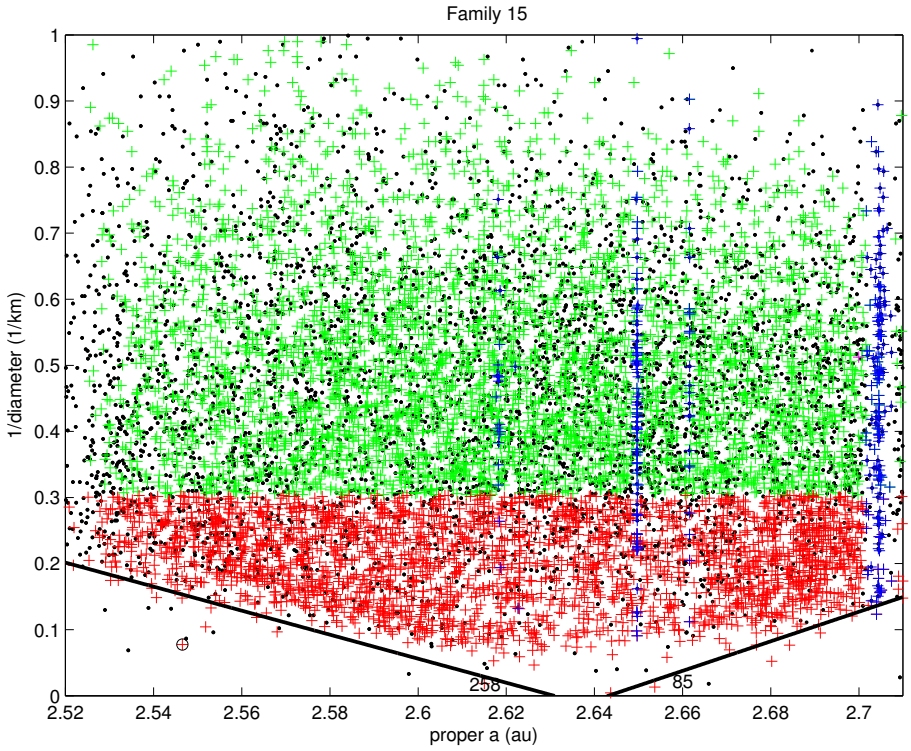

Figure 6.6: V-shape of the family 15: asteroids (85) and (258) are interlopers.

The possibility of an internal structure, affecting the interpretation of the slopes and ages, is discussed in Section 6.6.4: thus the small, positive V-base (Table 6.8) may not be significant.

For the computation of the barycenter (Table 6.8) it is important to remove the interlopers (85) and (258) which stick out from the V-shape, on the right and on the left, respectively, with the largest diameters after (15), see Figure 6.6[20].

Koronis

The Koronis family has a V-shape sharply cut by the 5/2 resonance with Jupiter on the low a side, by the 7/3 on the high a side (Figure 6.7), hence a short range of diameters usable to compute the slope: on the low a side, we have been forced to cut the fit at $D = 7.8$ km. This is the consequence of a well known phenomenon, by which leakage by Yarkovsky effect from family 158 into the 5/2 resonance occurs even for comparatively large objects

[20]Moreover, the albedo of (85) Io is well known (both from IRAS and from WISE) to be incompatible with (15) Eunomia as parent body.

Table 6.8: Cratering families: family, proper a, e and $\sin I$ of the barycenter, position of the barycenter with respect to the parent body, V-base, center of the V-base and escape velocity from the parent body. The barycenter is computed by removing the parent body, the interlopers and the outliers.

family	a_b	e_b	$\sin I_b$	$a_b - a_0$	$e_b - e_0$	$\sin I_b - \sin I_0$	V-base	center of V-base	v_e (m/s)
20	2.4061	0.1621	0.0252	-0.0026	0.0003	0.0004	0.005	2.4112	102
4	2.3637	0.1000	0.1153	0.0022	0.0012	0.0039	-0.026		363
4 (N≠1145)	2.3620	0.0993	0.1153	0.0005	0.0005	0.0040			
4 low e	2.3434	0.0936	0.1169	-0.0181	-0.0051	0.0056			
4 high e	2.3951	0.1094	0.1124	0.0336	0.0106	0.0010			
15	2.6346	0.1528	0.2276	-0.0090	0.0042	0.0010	0.012	2.6370	176
15 (N≠85, 258)	2.6295	0.1496	0.2282	-0.0141	0.0011	0.0015			
15 low a	2.6050	0.1495	0.2298	-0.0386	0.0009	0.0032			
15 high a	2.6805	0.1499	0.2247	0.0368	0.0013	-0.0019			

Milani and Farinella [1995]; Vokrouhlický et al. [2001]. The low fit accuracy can explain the discrepancy by 29% of the two slopes, which corresponds to only a little more than the STD uncertainty. We have no evidence for substructures which could affect the V-shape[21].

Agnia

The family of (847) Agnia has a prominent subfamily forming a V-shape inside the wider V-shape of the entire family (Figure 6.4). We call this structure the subfamily of (3395) Jitka. A possible interpretation is that Jitka is the largest fragment of a catastrophic fragmentation of an Agnia family member.

There are some problems if we use the WISE albedo data for the members of the dynamical family 847: there are 114 albedos with $S/N > 3$, which introduces some risk of small number statistics. Anyway, they indicate that the two subgroups, the 3395 subfamily and the rest of the 847 dynamical family, have a similar distribution of albedos, including dark interlopers. However, the albedo of (847) Agnia 0.147 ± 0.012 is lower than most family members, while (3395) Jitka has 0.313 ± 0.045 which is more compatible with the family. Thus it is not clear whether (847) Agnia is the largest remnant or an interloper. Also the choice of the common albedo is not obvious. We have used all the albedo data cited above, including the ones belonging to the 3395 subfamily, to compute an average (after discarding tails with albedo

[21]There is a well known substructure, the subfamily of (832) Karin, which is perfectly visible in Figure 6.7, but does not affect the two sides of the V-shape.

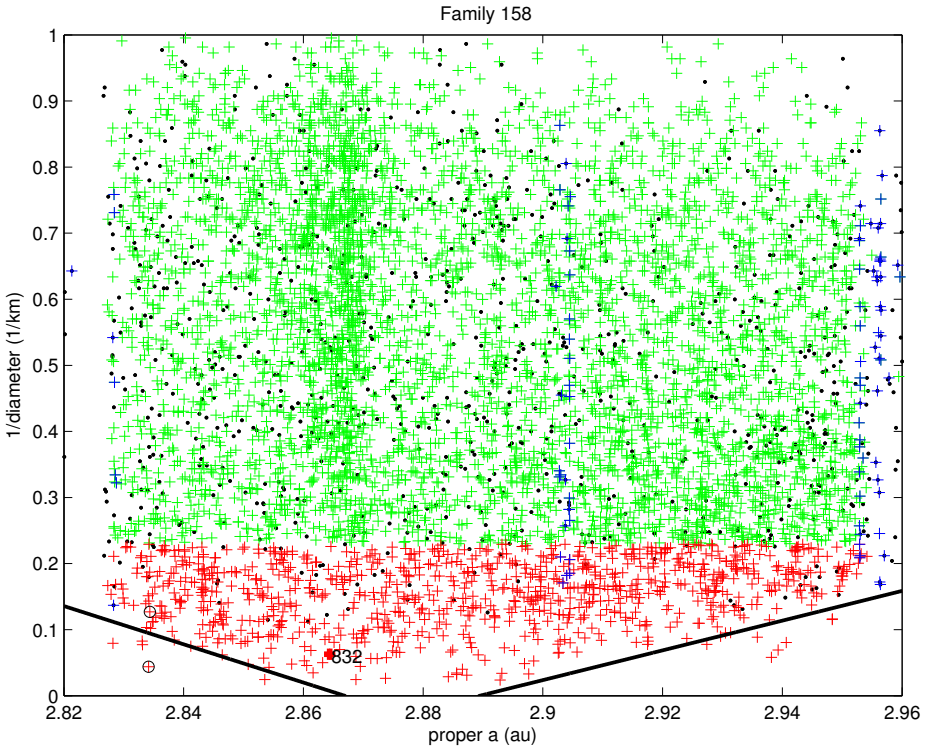

Figure 6.7: V-shape of the family 158. The Karin subfamily is clearly visible above the point marked 832.

< 0.1 and > 0.35), and got the mean value of Table 6.7.

Then we have computed 4 slopes, 2 for the entire dynamical family 847 and 2 specifically for the Jitka subgroup (by selecting only the members with $2.762 < a < 2.82$). For the entire family, consistent values (within the formal uncertainty) of the slopes on the two sides (Table 6.7) appear to correspond to the much older age of a wider and less dense family.

The fit for the Jitka slopes resulted in a large number of outlier rejections, because on the exterior of the V-shape there are Agnia members which do not belong to the Jitka subgroup, but are much more dense than the background. Nevertheless, the fit was good as shown by the two consistent slopes of the Jitka subfamily, with inverse slopes lower by a factor > 7. The V-base is negative in both cases (Table 6.9).

The Jitka subfamily shows in the V-shape plot (Figure 6.4) a depletion of the central portion, which should correspond to obliquities ϕ not far from 90°. This can be interpreted as a signature of the YORP effect Vokrouhlický et al. [2006b], in that most members with $\phi \sim 90°$ would have had their spin axes evolved by YORP towards one of the two stable states, $\phi = 0°, 180°$.

Table 6.9: Fragmentation families: family, proper a, e, $\sin I$ of the barycenter, V-base and center of the V-base. The barycenter is computed by removing the outliers.

family	a_b	e_b	$\sin I_b$	V-base	center of V-base
158	2.8807	0.0488	0.0371	0.023	2.8782
847	2.7799	0.0715	0.0664	-0.017	2.7759
847 (w/o 3395)	2.7450	0.0724	0.0651		
3395	2.7925	0.0727	0.0667	-0.004	2.7911

Yarkovsky effect calibration and family age estimation

Recalling that there is not a single measurement of the Yarkovsky effect for the main belt asteroids, thus also for the families, we can perform the calibration only by using the measurements for Near Earth Asteroids.

Thus, here the age estimation is obtained by scaling the results for the asteroid for which there is the best Yarkovsky effect determination 3, namely the low-albedo asteroid (101955) Bennu, with scaling taking into account the different values of D, a, e, ρ and A, where ρ is the density and A is the Bond albedo. The da/dt value for (101955) Bennu has a $S/N = 197.7$, thus a relative uncertainty $< 1\%$. The scaling formula we have used is:

$$\frac{da}{dt} = \left.\frac{da}{dt}\right|_{Bennu} \frac{\sqrt{a}_{(Bennu)}(1-e^2_{Bennu})}{\sqrt{a}(1-e^2)} \frac{D_{Bennu}}{D} \frac{\rho_{Bennu}}{\rho} \frac{\cos(\phi)}{\cos(\phi_{Bennu})} \frac{1-A}{1-A_{Bennu}}$$

where $D = 1$ km used in this scaling formula is not the diameter of an actual asteroid, but is due to the use of the inverse slope and $\cos(\phi) = \pm 1$, as explained in the description of the method above.

It may appear that the use of the Yarkovsky effect measurements for asteroids more similar in composition to the considered families than Bennu would be more appropriate. So, for example, the asteroid (2062) Aten has the best determined da/dt value of all S-type asteroids ($S/N = 6.3$), but the obliquity ϕ is not known. Thus, using an S-class asteroid for scaling may not result in a better calibration, because the S-type asteroids are not all the same, e.g., densities and thermal properties may be different.

For the family of (4) Vesta one would expect that the Yarkovsky measurement for asteroid (3908) Nyx, presumably of V-type Binzel et al. [2004], should represent a natural choice for calibration. In fact, the same authors warn that this asteroid belongs to a small group of objects with "sufficiently unusual or relatively low S/N spectra", thus the taxonomic class may be different from nominal. This suspicion is further strengthened by the value of geometric albedo of only 0.16 ± 0.06 reported by Benner et al. [2002], significantly lower than the typical value (~ 0.35) for a Vestoid. (3908) Nyx is

of extremely low density Farnocchia et al. [2014]: it has too many properties inconsistent with Vestoids.

Thus we have used (101955) Bennu as benchmark to be scaled for the Yarkovsky calibration of all families, because it is the known case with both the best estimate of Yarkovsky and best known properties, including obliquity, density, and size.

As shown in the formula above, for the calibration we need an estimate for the density of asteroids in the size range contributing to the V-shape, that is down to the minimum value of D used in the fit (given in Table 6.7). A large compilation of asteroid densities has been published by Carry [2012], but for main belt asteroids they are accurate and reliable only for very large diameters. Thus we have used the following method: having selected the asteroids (704), (4), (6) as representative of the taxonomic classes B, V, S respectively (for family 15 we have used the density of (15)) with good density estimates and expected negligible porosity, we take their densities ρ from Carry [2012]. Then we compute the porosity of Bennu as $p = 0.36$ from the density 1.26 estimated by 4, and apply the same porosity to all the taxonomic classes, e.g, to a Vestoid we assign a density $(1-p)\,\rho(Vesta)$. The porosity, and the correlated change in thermal conductivity with size, are the main sources of uncertainty in the calibration. We do not yet have enough information to derive a formal standard deviation for the calibration, but the relative uncertainty should be approximately 0.3.

Table 6.10: Family age estimation: family, da/dt for $D = 1$ km obtained using (101955) Bennu for the calibration, for the two sides of the V-shape, corresponding family age, standard deviation due only to the propagation of the formal fit uncertainty.

family		density g/cm^3	da/dt (10^{-10} au/y)	Δt (My)	$STD(\Delta t)$ (My)
20	IN	2.45	-3.54	161	8
20	OUT		3.46	153	12
4	IN	2.30	-3.44	869	131
4	OUT		3.30	1 800	759
15	IN	2.28	-3.66	1 500	232
15	OUT		3.55	1 300	141
158	IN	2.45	-3.04	1 100	296
158	OUT		3.00	1 500	267
847	IN	2.45	-3.28	1 100	213
847	OUT		3.24	979	154
3395	IN	2.45	-3.26	147	21
3395	OUT		3.24	139	22

The results of our age computation for the considered families are given in Table 6.10, for the two sides of the V-shape. The standard deviation of the age reported there is only the portion due to the fit of the slope. We need to stress that in most cases the main uncertainty in the age is due to the uncertainty of the calibration.

The estimations of the age of Massalia family from the two slopes are very close; they are also in good agreement with results obtained with a quite different method by Vokrouhlický et al. [2006b].

The Vesta family case is particularly interesting as the lower age appears to be compatible with the estimated age of one of the two largest craters on Vesta, Rheasilvia ($\sim$ 1 Gy) Marchi et al. [2012]. An age for the other big crater, Veneneia, has not been estimated, although it must be older because this crater is below the other. Our result that there is another, older collisional family is interesting, although there is no way to compare ages with the Veneneia crater.

The difference of the values of the inner and outer slopes of the V-shape for the Eunomia could be interpreted as the age of two different events, see Section 6.6.4. There is no previous estimate of the age of Eunomia we are aware of, a "young age" being suggested on the basis of simulations of size distribution evolution by Michel et al. [2001].

The estimation of the age of the Koronis family as inferred from the longer outer side of the V-shape is consistent with the age (≤ 2 Gy) reported previously by Marzari et al. [1995], based on the observed size distribution of larger members, and by Chapman et al. [1996], based on the crater count on the surface of the Koronis family member (243) Ida. Bottke et al. [2001] give 2.5 ± 1 Gy, which is also consistent.

The age estimate for the Agnia family of < 140 My, provided by Vokrouhlický et al. [2006a], is consistent with our result for the Jitka subfamily; the older age for the entire Agnia family has not been found previously because the low a component identified by us was not included in the family.

The two youngest according to our estimates, family 20 and subfamily 3395, have in common the presence of a lower density central region of the V-shape, more pronounced for Jitka, barely visible for Massalia. This suggests that the time scale for the YORP effect to reorient the rotation axis to either $\phi = 0°$ or $\phi = 180°$ is smaller than the time scale for randomization of a significant fraction of the spin states, which would fill the central gap.

Collisional Models and the interpretation of V-shapes

The method we have proposed for the computation of family ages has the advantage of using an objective measurement of the family V-shape, rather

than using a line placed "by eye" on a plot. However, because two parameters are fit for each boundary line, that is the slope and the intersection with the a-axis, whenever both sides are accessible the output is a set of four parameters: the inverse slopes on both sides (Table 6.7), the V-base and the center of V-base (Tables 6.8, and 6.9). To force the lines to pass from a single vertex on the horizontal axis would remove one fit parameter, to assign also the proper a of this vertex (e.g., at the value of some barycenter) would remove two parameters: this would bias the results and contradict the claimed objectivity of the procedure, to be defined by the family membership only[22].

On the other hand, our procedure does not use the V-base and its center to estimate the family age. Only the slopes of the leading edge of family members (for either high or low a) are used for the ages. This leads to two questions: which information is contained in the two parameters we are not using, and is it appropriate to obtain, e.g., a negative V-base, or is this an indication of a poor fit for at least one of the two lines?

The interpretation of the V–shape plots is not straightforward, because they are the outcome of a game involving three major players, each one producing its own effect. These players are: (1) the collisional history of a family, including the possible presence of overlapping multi-generation events; (2) the Yarkovsky effect, which in turn is influenced by the YORP effect; (3) the original field of fragment ejection velocities at the epoch of family formation. In addition, also the possible presence of strong nearby resonances plays an important role. Note also that in the present list of families several ones have been created by a cratering and not by a catastrophic disruption.

As for the effect (3), the existence of a correlation between the size and the dispersion in semi-major axis of family members has been known for several years. In the past, pre–Yarkovsky era (and with most of the recognized families resulting from catastrophic events), this correlation was assumed to be a direct consequence of the distribution of original ejection velocities, with smaller fragments being ejected at higher speeds Cellino et al. [1999]. The ejection velocities derived from observed proper element differences, however, turned out to be too high to be consistent with the experiments, since they implied collisional energies sufficient to thoroughly pulverize the parent bodies.

Later, the knowledge of the Yarkovsky effect and the availability of more detailed hydrodynamic simulations of catastrophic fragmentation family–

[22]Assumptions on the V-base were contained in most previous attempts at estimating family ages, although this is not easy to recognize because of the prevalent usage of coordinates (a, H) instead of $(a, 1/D)$.

forming events (see, for instance, Michel et al. [2001]) suggested a different scenario: most family members would be reaccumulated conglomerates, issued from merging of many fragments ejected at moderate velocities. In this scenario, the original ejection velocities give a moderate contribution to the observed dispersion of proper elements. Then the V–shape plots discussed in the previous subsections would be essentially a consequence of such Yarkovsky–driven evolution (see Bottke et al. [2002b] for a general reference). The extension of the above scenario to families formed by craterization events is not obvious, nor –at the present time– supported by numerical simulations, which are not yet capable to reach the required resolution Jutzi et al. [2013]. However, the interpretation of the V–shape as a consequence of Yarkovsky effect should hold also for them.

Unfortunately, a satisfactory interpretation of the observed V–shape plots can hardly be achieved in a purely Yarkovsky–dominated scenario: the original ejection velocities of fragments cannot be totally disregarded. For the Eos family Brož and Morbidelli [2013], Vokrouhlický et al. [2006c], assume, for $D = 5$ km, average asymptotic relative velocities $v_\infty \sim 90$ m/s. This is even more true for the families formed by cratering events on very large asteroids, since ejection velocities v_0 must be $> v_e$ (escape velocity) as to overcome the gravitational well of the parent body, and the v_∞ of the family members are both large and widely dispersed (see Section 6.6).

Due to the original dispersion of the family members, we cannot expect that the two sides of any given V–plot exactly intersect on the horizontal axis, as one might expect for a "pure" Yarkovsky model. The original extension of the family depends on the ejection velocities v_∞ of the bodies, while the Yarkovsky effect on every body of a given size depends on the orientation of the spin vector. If velocities and spin vectors are not correlated, the two terms should combine as independent distributions. If the Yarkovsky term is the dominant signal, the original velocities provide a noise term; the noise/signal value is certainly significant for large objects, thus the two lines of the "V" should not intersect at $1/D = 0$, but in the half plane $D < 0$. The "V–base" has therefore to be positive. Yet, this is not the case in some of the examples presented in this paper. How to possibly explain this?

A more physical explanation may be tentatively suggested, based on an argument which has been previously discussed in the literature La Spina et al. [2005], Paolicchi and Micheli [2008] but not yet fully explored. According to the results of some laboratory fragmentation experiments Fujiwara et al. [1989], Holsapple et al. [2002] the fragments ejected from a catastrophic disruption rotate, and the sense of spin is related to the ejection geometry: the fragments rotate away from the side of higher ejection velocity. Such behavior is clearly represented in [Fujiwara et al., 1989, Fig. 1]. This experimental

evidence was used in developing the so-called semi-empirical model Paolicchi et al. [1989, 1996], assuming that fragment rotations are produced by the anisotropy in the velocity ejection field.

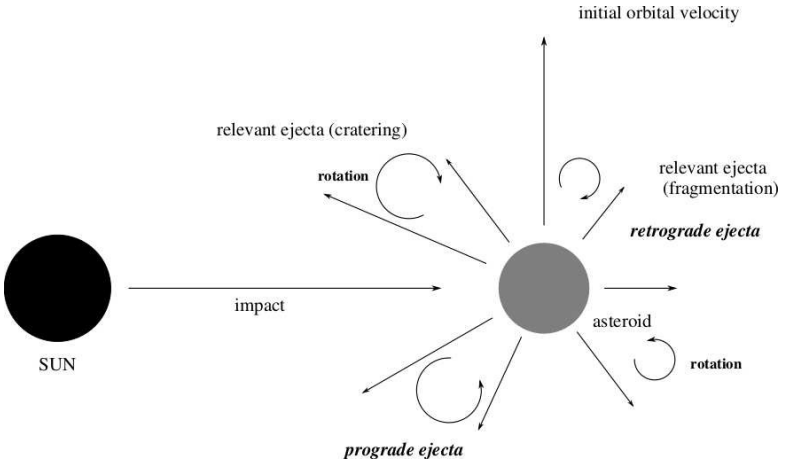

Figure 6.8: The possible correlation spin–ejection velocity for a radial impact from the interior of the Solar System. This is a projection on the orbital plane. For a cratering impact the ejecta are in the same hemisphere as the impact point, while for a catastrophic disruption the crater zone is pulverized, most sizable fragments are ejected from the antipodal hemisphere. In both cases the ejection velocity decreases with the angular distance from the impact point. If the rotation is connected to the velocity shear the fragment with a positive along track velocity (top of the figure) have a retrograde (clockwise) rotation, and conversely. This is true both for the front side ejecta (cratering) and for the rear side fragments (fragmentation). In this case the correlation between the initial Δa and $\cos\phi$ is negative, and the Yarkovsky effect tends initially to shrink the family in a.

In this scenario, the rotation of fragments created in a catastrophic process can be strongly correlated with the ejection velocity. For what concerns cratering events, as far as we know, there is not in this respect any experimental evidence mentioned in the literature. However, also in cratering events the ejection velocity field is strongly anisotropic (see, for instance, the popular Z–model by Maxvell [1997]), and a similar correlation between ejection velocity and spin rate can be expected for the fragments. It is not obvious how significantly the reaccumulation of ejecta (a process which certainly is very important after catastrophic events) can affect this correlation. There are very few simulations taking into account the rotation of fragments recorded in the literature Richardson et al. [2009], Michel and Richardson [2013], they are all about fragmentations, and their results do not solve the present question. However, if the fragments which stick together were ejected from nearby

regions of the parent body, an original correlation might be preserved.

If this is the case, different impact geometries will result in different evolutions of the semi-major axis spread of the family. To model the geometry of the impact, let us call *crater radiant* the normal $\hat{n}$ to the smoothed terrain before the crater is excavated (at the impact point). What matters are the angles between $\hat{n}$ and the directions $\hat{v}$ of the orbital velocity of the parent body, and $\hat{s}$ towards the Sun (both at the epoch of the impact).

If $\hat{n} \cdot \hat{s} > 0$ (impact on the inner side) with $\hat{n} \cdot \hat{v} \simeq 0$ (impact radiant close to normal to the velocity) there are preferentially retrograde fragments on the side where ejection velocity adds up with orbital velocity, thus giving rise to larger a of fragments, preferentially prograde on the opposite, lower a side. This implies that the spread in proper a of the family initially decreases (ejection velocity and Yarkovsky term act in the opposite sense), then increases again, and the V-base is negative.

If $\hat{n} \cdot \hat{s} < 0$ (impact on the outer side) with $\hat{n} \cdot \hat{v} \simeq 0$ there are preferentially prograde fragments at larger a, preferentially retrograde at lower a. This results in a large spread, even after a short time, of the family in proper a (ejection velocity and Yarkovsky term add), and the V-base is positive.

Finally, in case of negligible $\hat{n} \cdot \hat{s}$, the original ejection velocities and Yarkovsky drift add up as a noise terms, the latter dominating in the long run; the V-base is positive but small. Note that, as shown by Figure 6.8, this argument applies equally to cratering and to fragmentation cases.

Thus, in principle, the properties of the V-base and of the family barycenter (Tables 6.8, and 6.9) contain information on the impact geometry and on the original distribution of v_∞. However, the interpretation of these data is not easy. A quantitative model of the ejection of fragments, describing the distribution of v_∞, the direction of v_∞, $\cos\phi$, and D, taking into account all the correlations, is simply not available. We have just shown that some of these correlations (between direction and $\cos\phi$) are not negligible at all, but all the variables can be correlated. Even less we have information on shapes, which are known to be critical for the YORP effect.

This does introduce error terms in our age estimates. The main problem is the dependence on D of the Yarkovsky drift in a, averaged over very long times. According to the basic YORP theories (see Bottke et al. [2006] for a general reference) the bodies should preferentially align their rotation axes close to the normal to the orbital plane (both prograde and retrograde), with a timescale strongly dependent on the size, approximately as $1/D^2$. This result is also supported by the recent statistical work on the spin vector catalog Paolicchi and Kryszczyńska [2012]. Consequently, there should be a substantial fraction of the small bodies moving towards the borders of the V–plot, especially after times long with respect to the time scale for

the YORP-driven evolution to the spin up/spin down stable states. Using a different database Vokrouhlický et al. [2006b] have found, for most families, a number density distribution in accordance to this idea. However, the maxima are not at the edges, but somewhere in between the symmetry axis of the V-shape and the edges: e.g., see Figure 6.4. It is not easy to draw conclusions from this, because in most families the portions near the extreme values of proper a are affected by resonances and/or by the merging of step 3 families as satellites.

There are many models proposed in the literature to account for a form of randomization of the spin state, resulting in something like a Brownian motion along the a axis over very long time scales; e.g., Statler [2009] and Cotto-Figueroa et al. [2013] show that the YORP effect can be suddenly altered. Thus after a long enough time span, most family members may be random-walking between the two sides of the V-shape, and the central area is never emptied. However, what we are measuring is not the evolution in a of the majority of family members, but the evolution of the members fastest in changing a. Our method, indeed any method using only the low and high a boundaries of the family, should be insensitive to this effect for large enough families. In a random effect a portion of the family with a spin state remaining stable at $\cos\phi \simeq \pm 1$ will be maintained for a very long time, and this portion is the one used in the V-shape fit.

Our method is mathematically rigorous in extracting from the family data two components of the evolution of proper a after the family formation, a term which is constant in time (from the original distribution of velocities) and independent from D, and a term which is proportional to $1/D$ and to the time elapsed. If the situation is much more complicated, with a larger number of terms with different dependence on both D and t, we doubt that the current dataset is capable of providing information on all of them, whatever the method used. Moreover, some terms may not be discriminated at all, such as an $1/D$ dependency not due to a pure Yarkovsky term $\Delta t/D$.

6.4.3 Size distributions

Another use of the diameters deduced from absolute magnitudes assuming uniform albedo is the possibility of computing a size distribution. This can be done by fitting a slope in a log-log plot of an histogram as a function of D, but it is a delicate computation. The numbers of members at too small diameters are affected by incompleteness, while too large diameters are affected by small number statistics, especially for cratering events.

In Figure 6.9 we show the result of a size distribution power law fit for family 20, by using the range from $D = 1.5$ to 5 km, thus excluding (20)

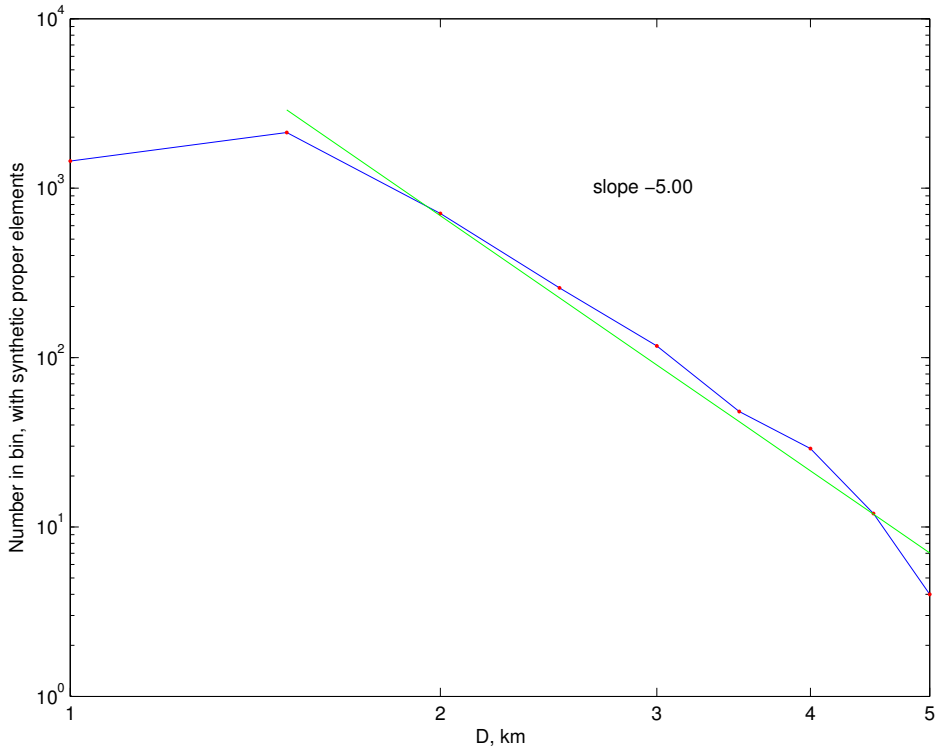

Figure 6.9: Size distribution for the family of (20) Massalia using the range $1.5 < D < 5$ km.

and the two outliers identified above as well as two others above 5 km. The resulting best fit differential power law is proportional to $1/D^5$, that is the cumulative distribution is proportional to $1/D^4$; this value suggests that the fragments are not yet in collisional equilibrium, thus supporting a comparatively young age for the family. The figure shows well the decline in numbers at both extremes of the range in D, the inner one due to incompleteness of the asteroid catalogs for $D < 1.5$ km. Note, however, that if the slope of the differential size distribution exceeds 4 the total volume of the fragments diverges at the low end. Thus the "real" slope has to decrease below some unknown value of D. It is not possible to discriminate between the observational bias and a possible detection of this change of slope.

The interpretation of the other change of slope in the region of large fragments is not obvious; maybe it resides in some geometrical constraint, such as the impossibility of creating fragments larger than a given fraction of the crater depth, in analogy with the well known findings concerning the catastrophic case Durda et al. [2007]; Tanga et al. [1999].

The same computation was done for the size distribution power law fit for

family 4, by using as a common albedo 0.35. We have used the range from $D = 1.5$ to 8 km, thus excluding (4) and the interlopers (556) and (1145) as well as another member marginally larger than $D = 8$. The differential power law is $1/D^{4.5}$, that is the cumulative is $1/D^{3.5}$, with concavities similar to those represented in Figure 6.9. The slope suggests that collisional equilibrium has not been reached, but the complex structure of the family (as proposed in Section 6.6.2) makes a complete interpretation difficult.

6.5 Refinement with physical data

The data from physical observations of asteroids, especially if they are available in large and consistent catalogs like WISE and SDSS, are very useful to solve some of the problems left open by purely dynamical classifications such as the one discussed above. This happens with enough consistent and quality controlled data, and when the albedo and/or colors can discriminate, either between subsets inside a family, or between a family and the local background, or between nearby families. (Other examples in Section 6.6.)

6.5.1 The Hertha–Polana–Burdett complex family

The most illustrative example of discrimination inside a dynamical family is in the family with lowest numbered asteroid (135) Hertha; when defined by dynamical parameters only, it is the largest family with 11 428 members. Its shape is very regular in the $a, sinI$ proper element projection, but has a peculiar >-shape in the a, e projection (Figure 6.10), which has been strongly enhanced by the addition of the smaller asteroids of the satellite families (in yellow).

Already by using absolute magnitude information some suspicion arises from the V-shape plot, from which it appears possible to derive a consistent "slope" neither from the inner nor for the outer edge. Problems arise in this family from the very top, that is (142) Polana which is dark (WISE albedo 0.045) and diameter $D \simeq 60$ km, and (135) Hertha which is of intermediate albedo 0.152 and $D \simeq 80$ km, also known to be an M type asteroid, but exhibiting the 3 μm spectral feature of hydrated silicates Rivkin et al. [2000].

By using systematically the WISE albedo, limited to the asteroids for which the albedo uncertainty is less than 1/3 of the nominal value (1 247 such data points in the 135 dynamical family), we find the sharply bimodal distribution of Figure 6.11. (142) Polana is by far the largest of the "dark" population (for the purpose of this discussion defined as albedo < 0.09, 611 asteroids) as well as the lowest numbered. The "bright" population (albedo

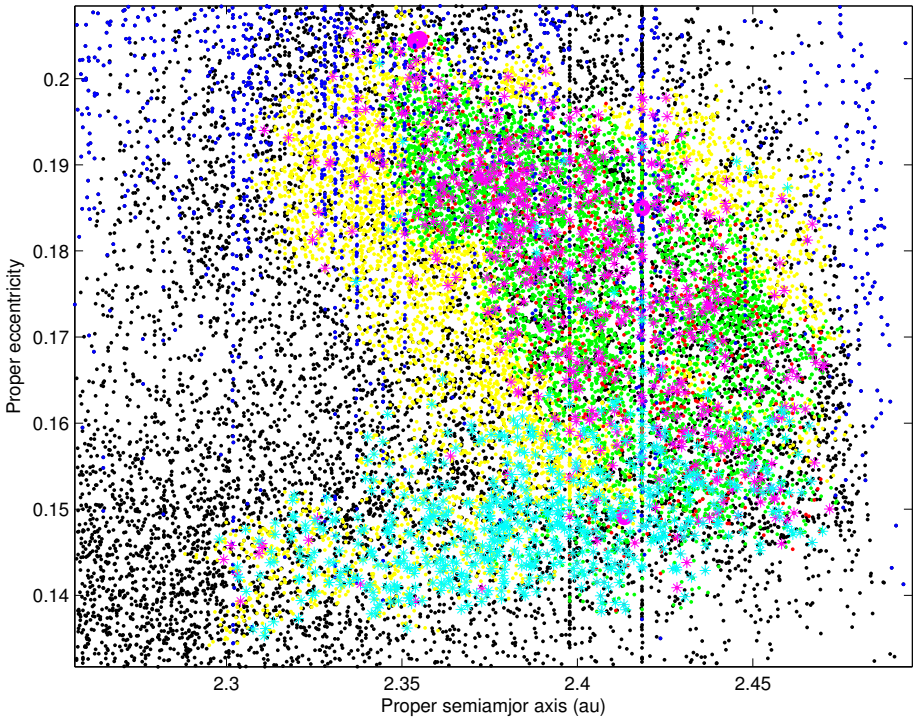

Figure 6.10: The Hertha dynamical family in proper a, e plane. Bright objects (magenta stars) and dark objects (cyan stars) forming a characteristic >-shape indicate two partly overlapping collisional families.

> 0.16, 568 asteroids) does not have a dominant large member, the largest being (3583) Burdett (albedo 0.186 ± 0.02, $D \simeq 7.6$ km)[23]

In Figure 6.10 we have plotted with magenta stars the "bright", with cyan stars the "dark": it shows that they are distributed in such a way that the >-shape in the proper a, e plane is explained by the presence of two separate collisional families, the "Polana" family and the "Burdett" family, with a significant overlap in the high a, low e portion of the Hertha dynamical family. Because the WISE dataset is smaller than the proper elements dataset, we cannot split the list of members of the 135 dynamical family into Polana and Burdett, because such a list would contain an overwhelming majority of "don't know". Erosion of the original clouds of fragments by the 3/1 resonance with Jupiter must have been considerable, thus we can see only a

[23]The asteroid (878) Mildred was previously used as namesake of a family in the same region: it is likely to be "bright", but the WISE albedo is inaccurate ($= 0.40 \pm 0.22$), and is quite small ($D \simeq 2.5$ km). (878) was imprudently numbered in 1926 and then lost: this is why a low numbered asteroid is so small.

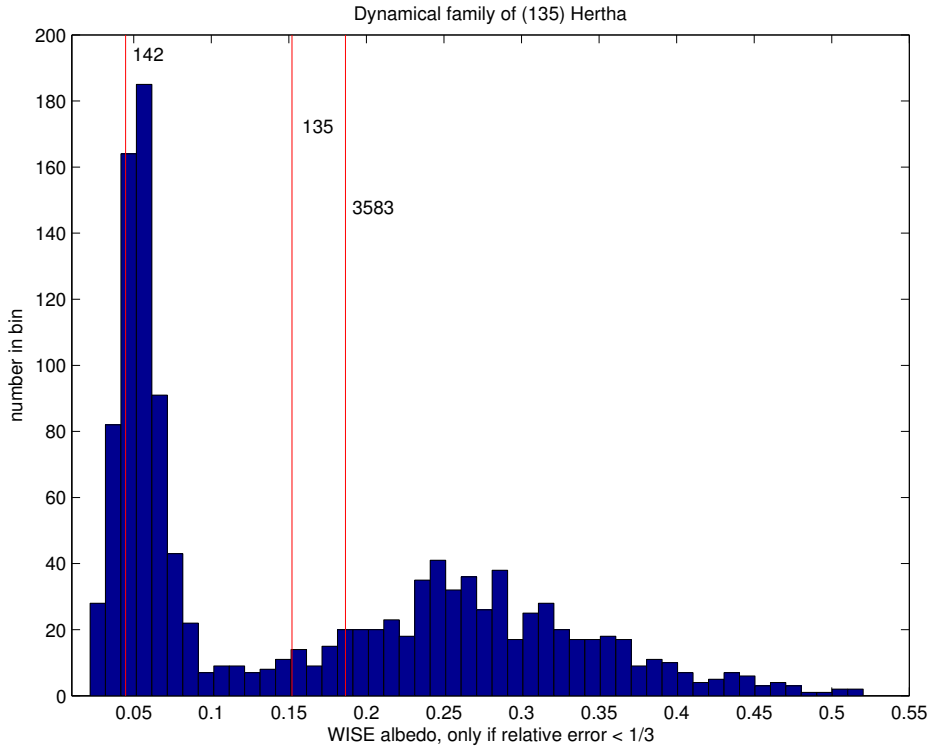

Figure 6.11: The distribution of WISE albedos for the 135 dynamical family with the locations of the three namesakes indicated by red lines. The distribution is clearly bimodal supporting the scenario with two collisional families.

portion of each of the two clouds of fragments. Based on the total volume of the objects for which there are good albedo data, the parent body of Polana must have had $D > 76$ km, the one of Burdett $D > 30$ km.

Note that we could get the same conclusion by using the a^* parameter of the SDSS survey: among the 1 019 asteroids in the 135 dynamical family with SDSS colors and a^* uncertainty less than 1/3 of the nominal value, 184 have $-0.3 < a^* < -0.05$ and 835 have $+0.05 < a^* < 0.3$, thus there is also a bimodal distribution, which corresponds to the same two regions marked in magenta and cyan in Figure 6.10, with negative a^* corresponding to low albedo and positive a^* corresponding to high albedo, as expected [Parker et al., 2008, Figure 3]. The lower fraction of "dark" contained in the SDSS catalog, with respect to the WISE catalog, is an observation selection effect: dark objects are less observable in visible light but well observable in the infrared.

Because of its very different composition (135) Hertha can be presumed to belong to neither the one nor the other collisional family. However, this

conclusion cannot be proven from the data we are using, listed in Section 2, but requires some additional information (e.g., taxonomic classification of Hertha) and suitable modeling (e.g., excluding that a metallic asteroid can be the core of a parent body with ordinary chondritic mantle). All these conclusions are a confirmation, based on a statistically very significant information, of the results obtained by Cellino et al. [2001] on the basis of a much more limited dataset (spectra of just 20 asteroids). Other authors Masiero et al. [2013] have first split the asteroids by albedo then formed families by proper elements: they get the same conclusion on two overlapping families, but their total number of family members is lower by a factor ~ 3.

6.5.2 Watsonia and the Barbarians

The family of (729) Watsonia had been already identified in the past by Novaković et al. [2011], who adopted a proper element data base including also a significant number of still unnumbered, high-inclination asteroids, not considered in our present analysis. This family is interesting because it includes objects called "Barbarians", see Cellino et al. [2006], which are known to exhibit unusual polarization properties. Two of us (AC and BN) have recently obtained VLT polarimetric observations Cellino et al. [2014] showing that seven out of nine observed members of the Watsonia family exhibit the Barbarian behavior. This result strongly confirms a common origin of the members of the Watsonia family. However, the story is somewhat more complicated: for more details on this interesting example of using complementary datasets, see Cellino et al. [2014].

6.6 Cratering families

As a result of the procedure adding many smaller asteroids to the largest families, our classification contains a large fraction of families formed by cratering events. Cratering events on the same asteroid occur multiple times over the age of the solar system, since the target keeps the same impact cross section. The outcomes can appear as structures inside a dynamical family.

Modeling of the formation of cratering families needs to take into account the escape velocity v_e from the parent body, which results in the parent body not being at the center of the family as seen in proper elements space. This is due to the fact that fragments which do not fall back on the parent body need to have an initial relative velocity $v_0 > v_e$, and because of the formula giving the final relative velocity $v_\infty = \sqrt{v_0^2 - v_e^2}$ the values of v_∞ have a wide distribution even for a distribution of v_0 peaking just above v_e. The

mean value of v_∞ is expected to be smaller than v_e, at most of the same order. Thus immediately after the cratering event, the family appears in the proper elements space as a region similar to an ellipsoid, which is centered at a distance d of the order of v_e from the parent body. Of course this effect is most significant for the very largest parent bodies.

We use as criterion for identification of a cratering family that the fragments should add up to $\leq 10\%$ of the parent body volume; we have tested only the large and medium families, and used the common albedo hypothesis to compare volumes. In this way 12 cratering families have been identified with the asteroids (2), (3), (4), (5), (10), (15), (20), (31), (87), (96), (110), (179), and (283) as parent bodies. Other large asteroids do not appear to belong to families. We will discuss some interesting examples.

6.6.1 The Massalia family

Although the V-shape plot (Figure 6.3) does not suggest any internal structure for the family 20, the inspection of the shape of the family in the space of all three proper elements suggests otherwise.

The distribution of a is symmetrical with respect to (20) Massalia, while these of e and I are rather asymmetrical. The e distribution is skewed towards higher e (third moment positive), this is apparent from Figure 6.1 as a decrease of number density for $e < 0.157$; the I one is skewed towards lower I (third moment negative).

Thus the barycenter of the ejected objects appears quite close to the parent body (20), see Table 6.8: if the differences in $e, \sin I$ are scaled by the orbital velocity they correspond to about 7 m/s, much smaller than the escape velocity. For a single cratering event, the center of mass of the ejecta has to move in a direction close to the crater radiant, for a barycenter that close to the parent body multiple craterings with different crater radiants are needed. This suggests a multiple collision origin of the dynamical family. At $e < 0.157$ there is a portion of a family with less members which does not overlap the other, more dense collisional family. The more dense family has been ejected in a direction such that e increases and $\sin I$ decreases, the other in a direction with roughly opposite effect.

However, the presence of the low e subfamily does not affect the age computation, which only applies to the high e subfamily, due to the fact that the extreme values of a are reached in the high e region. Thus there are two concordant values for the slopes on the two sides, and a single value of the age we can compute, which refers only to the larger, high e subfamily.

6.6.2 The Vesta family substructures

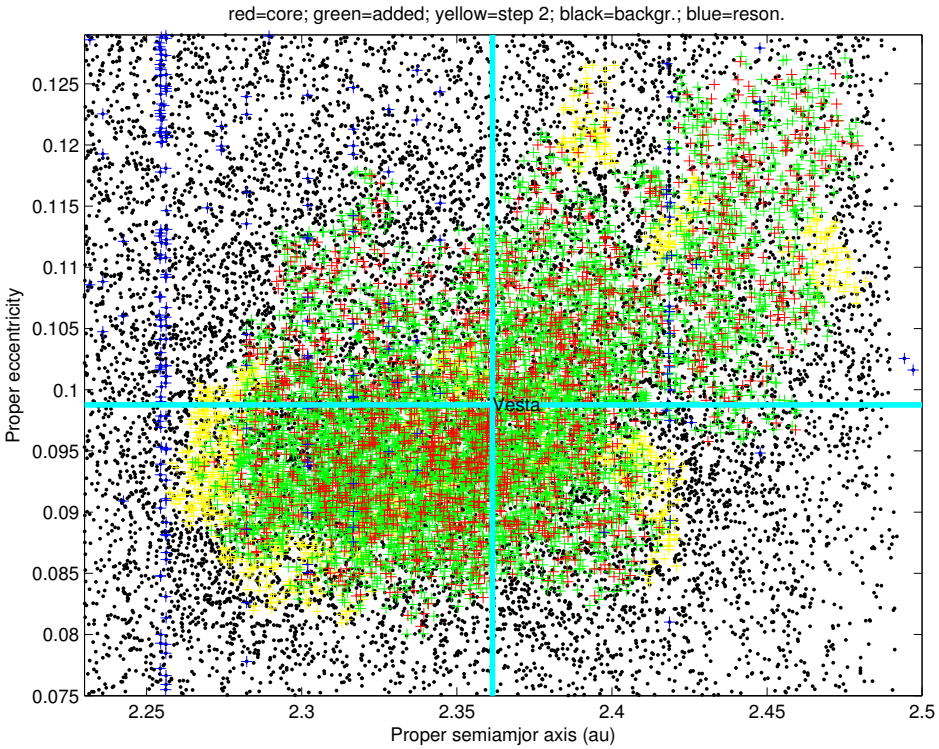

Figure 6.12: The family 4 shown in the proper a, e plane. The satellite families merged in step 5 of our procedure (yellow dots) extend the family closer to the 3/1 resonance with Jupiter on the right and to the 7/2 resonance on the left. The position of (4) Vesta is indicated by the cyan cross, showing that the parent body is at the center of neither of the two subfamilies, at lower e and at higher e.

The Vesta family has a curious shape in the proper a, e plane (Figure 6.12), even more if we consider the position of (4) Vesta in that plane.

In proper a, this family is bound by the 3/1 resonance with Jupiter on the outside and by the 7/2 inside. Closer inspection reveals the role the 1/2 resonance with Mars at $a \simeq 2.417$ au: the low e portion of the family has the outside boundary at the 1/2 resonance with Mars. By stressing the position of Vesta with the cyan cross in Figure 6.12, we can appreciate the existence of a oval shape group with proper e lower than, or only slightly above, the one of Vesta (which is 0.099). We can define a "low e subfamily" as the family 4 members with $a < 2.417$ and $e < 0.102$, conditions satisfied by 5 324 members.

By assuming that albedo and density are the same, we compute the center

of mass of this low e group, which is at $a = 2.3435$ and $e = 0.0936$. To get to such values the relative velocity components after escape from Vesta should have been -76 and -98 m/s, respectively[24]. Since the escape velocity from Vesta surface is ~ 363 m/s, this is compatible with the formation of the low e subfamily from a single cratering event, followed by a Yarkovsky evolution.

What is then the interpretation of the rest of the family 4? We shall call "high e subfamily" all the members not belonging to the low e portion defined above, excluding the interlopers (556) and (1145). This leaves 2 538 members, with size $D < 8$ km. It is also possible to compute a center of mass: the necessary relative velocities after escape are larger by a factor ~ 2, still comparable to the escape velocity from Vesta, although this estimate is contaminated by the inclusion of low e, low a members into the low e subfamily. Anyway, the shape of this subfamily is not as simple as the other one, thus there could have been multiple cratering events to generate it.

This decomposition provides an interpretation of the large discrepancy, by a factor roughly 2, between the age as computed from the low a side and from the high a side of the V-shape in $a, 1/D$. Indeed, if the low e subfamily ends for $a < 2.417$, while the high e subfamily ends at $a \sim 2.482$, then the right side of the V-shape belongs to the high e subfamily. From Figure 6.12 we see that the low a side of the family is dominated by the low e subfamily.

By this model, the two discordant ages computed in Section 6.4.2 belong to two different cratering events. This is consistent with the expectation that large cratering events occur multiple times on the same target.

As for the uncertainties of these ages, they are dominated by the poor a priori knowledge of the Yarkovsky calibration constant c for the Vesta family. Still the conclusion that the two ages should be different by a factor ~ 2 appears robust. From the DAWN images, the age of the crater Rheasilvia on Vesta has been estimated at about 1 Gy Marchi et al. [2012], while the underling crater Veneneia must be older, its age being weakly constrained. Thus both the younger age and the ratio of the ages we have estimated in Section 6.4.2 are compatible with the hypothesis that the low e subfamily corresponds to Rheasilvia, the high e subfamily (or at least most of it) corresponds to Veneneia. We are not claiming to have a proof of this identification.

Unfortunately, for now there are no data to disentangle the portions of the two collisional families which overlap in the proper elements space. Thus we can compute only with low accuracy the barycenter of the two separate collisional families, and to model the initial distributions of velocities would be too difficult. However, there are some indications Bus [2013] that discrim-

[24]The negative sign indicates a direction opposite to the orbital velocity for a, and a direction, depending upon the true anomaly at the collision, resulting in decrease of e.

ination of the two subfamilies by physical observations may be possible.

In conclusion, the current family of Vesta has to be the outcome of at least two cratering events on Vesta, not including even older events which should not have left visible remnants in the family region as we see it today.

6.6.3 Vesta Interlopers and lost Vestoids

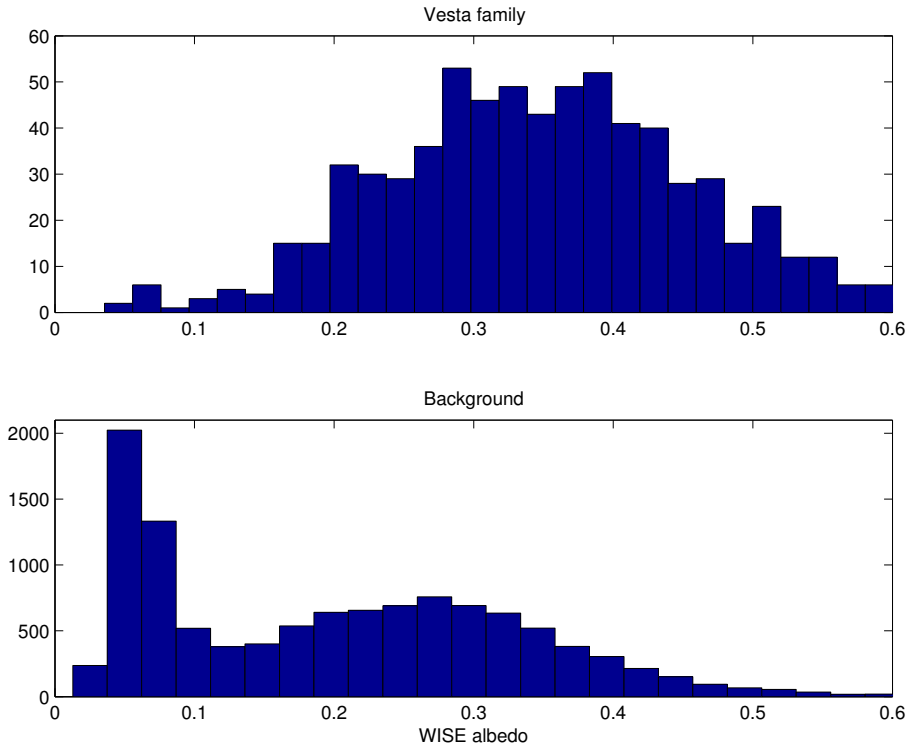

Figure 6.13: Histogram of albedo measured by WISE with $S/N > 3$: above for the asteroids belonging to family 4; below for the background asteroids with $2.2 <$ proper $a < 2.5$ au. The uneven distribution of "dark" asteroids (albedo < 0.1) is apparent. The asteroids with $0.27 <$ albedo < 0.45, corresponding to the bulk of the family 4, are present, but as a smaller fraction, in the background population.

Another possible procedure of family analysis is to find interlopers, that is asteroids classified as members of a dynamical family, not belonging to the same collisional family, because of discordant physical properties; see as an example of this procedure Figure 25 and Table 3 of Milani et al. [2010].

In the dynamical family of (4) Vesta there are 695 asteroids with reasonable (as before) WISE albedo data. We find the following 10 asteroids with albedo < 0.1: (556), (11056), (12691), (13411), (13109), (17703), (92804),

(96672), (247818), (253684); the first is too large ($D \simeq 41$ km) and was already excluded, the next 3 are larger than 7.5 km, that is marginally too large for typical Vestoids; we had also excluded in Section 6.4.1 (1145), which has an intermediate albedo but is also too large ($D \simeq 23$ km). We think these 11 are reliably identified as interlopers, of which 10 belong to the C-complex. By scaling to the total number 7 865 of dynamic family members, we would expect a total number of interlopers belonging to the C-complex $\simeq 120$.

The problem is how to identify the interlopers belonging to the S-complex, which should be more numerous. For this the WISE albedo data are not enough, as shown by Figure 6.13. The albedos of most family members are between 0.16 and 0.5, which overlaps the values for the S-complex and for V-types. Among the background asteroids, with $2.2 < a < 2.5$ au and with significant WISE albedos, 34% have albedo < 0.1, but the majority have albedos compatible with the S-complex, a large fraction also with V-type.

The estimated value of the albedo is derived from a measured absolute magnitude, which typically has an error of 0.3 magnitudes (or worse). This propagates to a relative error of 0.3 in the albedo. Thus the values of albedo for S and V type are mixed up as a result of the measurement errors, both in the infrared and in the visible photometry.

The only class of objects which are clearly identified from the albedo data are the dark C-complex ones, because the main errors in the albedo are relative ones, thus an albedo estimated at < 0.1 cannot correspond to an S-type, even less to a V-type.

In conclusion, by using the albedo there is no way to count the S-complex interlopers in the Vesta family; it is also not possible to identify "lost Vestoids", originated from Vesta but not in the dynamical family.

The question arises whether it would be possible to use the SDSS data to solve these two problems. According to [Parker et al., 2008, Figure 3] the V-type objects should correspond to the region with $a^* > 0$ and $i-z < -0.15$ in the plane of these two photometric parameters. However, these lines are not sharp boundaries, just probabilistic ones. Thus this criterion is suitable to reliably identify neither family 4 interlopers, nor lost Vestoids.

The Parker et al. criterion can be used to estimate the V-type population in a statistical sense. The asteroids which have a large probability of being V-type need to have $a^* - 2\,STD(a^*) > 0$ and $i - z + 2\,STD(i - z) < -0.15$; we find 1 758 asteroids, of which 55 with $a > 2.5$ au; they are plotted on the proper a, e plane in Figure 6.14. The number of asteroids of V-type beyond the 3/1 resonance with Jupiter should be very small, anyway 55 is an upper bound on the number of false positive for the V-type criterion in that region.

Of the V-type with $a < 2.5$ au, 504 are members of the dynamical family 4 and 1 199 are not. In conclusion, even taking into account the possible

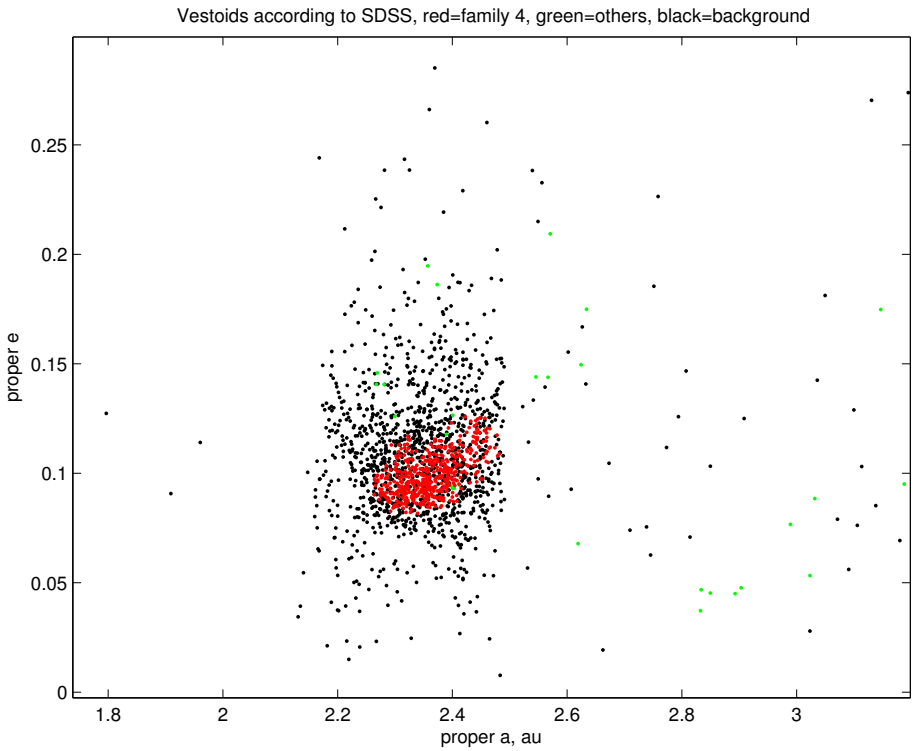

Figure 6.14: Asteroids complying with the Parker et al. [2008] criterion for V-type. Red points: members of family 4, green: members of other families, black: background asteroids. The "halo", in the sense defined by Brož and Morbidelli [2013], is formed by background asteroids apparently matching the color properties of Vestoids: they are, among objects with significant SDSS data, at least twice more numerous than the family 4 members with the same colors.

number of false positive, there are at least twice as many V-types in the inner belt outside of the dynamical family rather than inside the Vesta family.

Conversely, if we define "non-V type" by either $a^* + 2\,STD(a^*) < 0$ or $i-z-2\,STD(i-z) > -0.15$ we find in the inner belt $a < 2.5$ as many as 8 558 non-V, out of which only 42 belong to the dynamical family 4, which means the number of S-type interlopers is too small to be accurately estimated, given the possibility of "false negative" in the V-type test.

This gives an answer to another open question: where are the "lost Vestoids", remnants of cratering events on Vesta which occurred billions of years ago? The answer is everywhere, as shown by Figure 6.14, although much more in the inner belt than in the outer belt, because the 3/1 barrier deflects most of the Vestoids into planet crossing orbits, from which most end up in the Sun, in impacts on the terrestrial planets, etc. Still there is no

portion of the asteroid main belt which cannot be reached, under the effect of Gy of Yarkovsky effect and chaotic diffusion combined. We should not even try to find families composed with them, because they are too widely dispersed. All but the last two family-forming cratering events have completely disappeared from the Vesta family, as it can be found by HCM.

6.6.4 The Eunomia Family

The number frequency distributions of the family members' proper elements indicate that some multiple collisions interpretation is plausible: the distribution of semimajor axes exhibits a gap around $a = 2.66$ au, close to where Eunomia itself is located. The distribution of family members on all sides of the parent body for all three proper elements, and the barycenter of the family (not including Eunomia) very close to (15), are discordant with the supposed anisotropic distribution of velocities of a single cratering event.

These pieces of evidence indicate that a single collisional event is not enough to explain the shape of the dynamical family 15. Then the discrepancy in the slopes on the two sides could be interpreted as the presence of two collisional families with different ages. Since the subfamily with proper $a > 2.66$ dominates the outer edge of the V-shape, while the inner edge is made only from the rest of the family, we could adopt the younger age as that of the high a subfamily, the older as the age of the low a subfamily. However, the lower range of diameters, with $D > 6.7$ km on the outer edge, and the ratio of ages too close to 1 result in a poorly constrained age difference.

Still the most likely interpretation is that the Eunomia dynamical family was generated by two cratering events, with roughly opposite crater radiants, such that one of the two collisional families has barycenter at $a > a(Eunomia)$, the other at $a < a(Eunomia)$, see Table 6.8.

The WISE albedo distributions of the two subfamilies are practically the same, which helps in excluding more complex models with different parent bodies.

In conclusion, our interpretation is similar to the one of the Vesta family.

6.6.5 The missing Ceres family

(1) Ceres in our dynamical classification does not belong to any family, still there could be a family originated from Ceres. The escape velocity from Ceres is $v_e \sim 510$ m/s, while the QRL velocity used to form families in zone 3 was 90 m/s. An ejection velocity v_0 just above v_e would results in a velocity at infinity larger than 90 m/s: $v_0 = 518$ m/s is enough.

Thus every family moderately distant from Ceres, such that the relative velocity needed to change the proper elements is much less than v_e, is a candidate for a family from Ceres. Family 93 is one such candidate[25]. By computing the distance d between the proper element set of (1) and all the family 93 members, we find the minimum possible $d = 153$ m/s for the distance (in terms of the standard metric) between (1) and (28911). The relationship between d and v_∞ is not a simple one (depending upon the true anomaly at the impact), anyway v_∞ would be of the same order as d, corresponding to $v_0 \sim 532$ m/s.

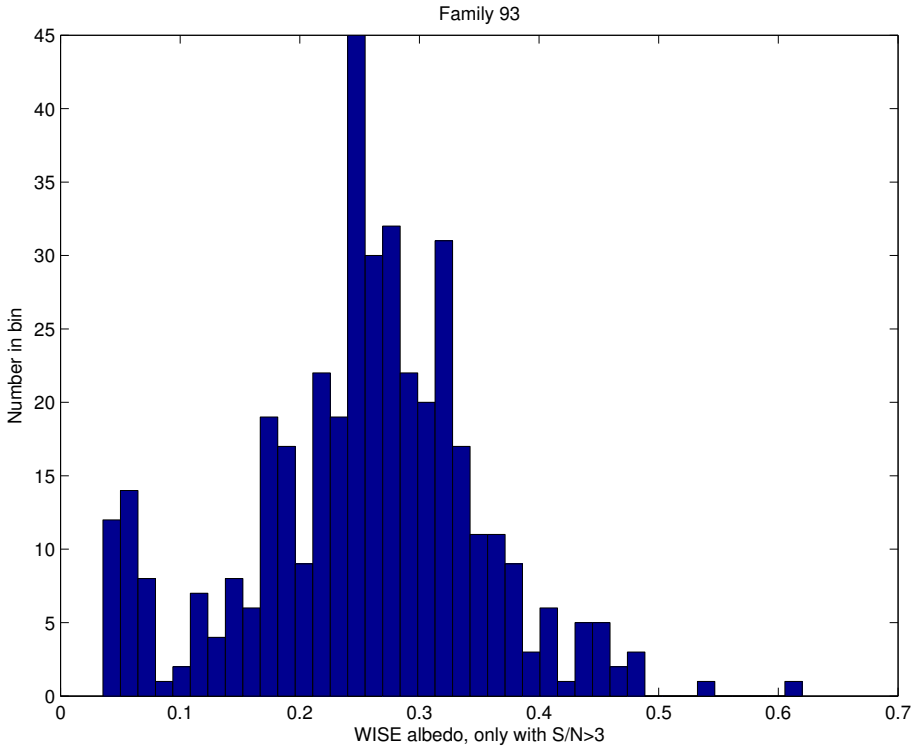

Figure 6.15: Histogram of the albedos measured by WISE with $S/N > 3$ among the members of the family 93. There is an obvious "dark" subgroup with albedo < 0.1 and a large spread of higher estimated albedos. Most members have intermediate albedos typical of the S-complex.

This is a hypothesis, for which we seek confirmation by using absolute magnitudes and other physical observations, and here comes the problem.

According to Li et al. [2006], the albedo of (1) Ceres is 0.090 ± 0.0033;

[25]There are family classifications, including Zappalà et al. [1995], in which (1) is a member of a family largely overlapping with our family 93.

the surface has albedo inhomogenities, but the differences do not exceed 8% of the value.

The WISE albedos of the family 93 (by using only the 403 data with $S/N > 3$) are much brighter than that of Ceres, apart from a small minority: only 37, that is 9%, have albedo < 0.1. (93) has albedo 0.073 from IRAS, but we see no way to eject a $D \sim 150$ km asteroid in one piece from a crater; also (255) belongs to the dark minority, and is too large for a crater ejecta. No other family member, for which there are good WISE data, has diameter $D \geq 20$ km. Actually, from Figure 6.15 the albedo of Ceres is a minimum in the histogram. By using the SDSS data we also get a large majority of family 93 members in the S-complex region.

We cannot use V-shape diagrams composed with the same method used in Section 6.4.2, because the assumption of uniform albedo is completely wrong, as shown by Figure 6.15. By studying the shape of the family in the proper $a, \sin I$ plane and in the proper a, e plane, taking into account the albedo, there is no obvious concentration of objects with low/intermediate albedo. Thus there appears to be no "Ceres family", just a family of comparatively bright asteroids, having to do neither with (1), nor with (93), nor with (255).

The family 93 is the only one suitable, for its position in proper elements space, to be a cratering family from Ceres. However, physical observations (albedo and colors) contradict this origin for an overwhelming majority of family members. Thus we need to accept that the bright/intermediate component of family 93 is the result of a catastrophic fragmentation of some S-complex asteroid, and the fact of being very near Ceres is just a coincidence. We can assign 366 "bright and intermediate" (with albedo > 0.1 measured by WISE with $S/N > 3$) members of family 93 to a collisional family, with the lowest numbered member (1433) Gerantina, which has albedo 0.191 ± 0.017, from which $D \simeq 15$. The volume of these 366 is estimated at 49 000 km^3, equivalent to a sphere with $D \simeq 45$ km; the parent body must have been an S-complex asteroid with a diameter $D > 60$ km, given that a good fraction of the fragments has disappeared in the 5/2 resonance.

However, why Ceres does not have any family? This could not be explained by assuming that Ceres has been only bombarded by much smaller projectiles than those impacting on (2), (4), (5) and (10): Ceres has an impact cross section comparable to the sum of all these four others.

Before attempting an explanation let's find out how significant are our family classification data. This leads to a question, to which we can give only a low accuracy answer: which is the largest family from Ceres which could have escaped our classification? This has to be answered in two steps: first, how large could be a family resulting from cratering on Ceres superimposed to the family 93? 37 dark interlopers out of 403 with good WISE data could

be roughly extrapolated to 168 out of 1 833 members of family 93[26].

Second, how large could be a Ceres family separate from 93 and not detected by our classification procedure? In the low proper I zone 3, the three smallest families in our classification have 93, 92 and 75 members. Although we do not have a formal derivation of this limit, we think that a family with about 100 members could not be missed by our HCM procedure, unless it is so dispersed that there is no way to assess its existence.

By combining these two answers, families from Ceres cratering with up to about 100 members could have been missed. The comparison with the family of (10) Hygiea, with 2 402 members, and the two subfamilies of Vesta, the smallest with $> 2,538$ members, suggests that the loss in efficiency in the generation of family members in the specific case of Ceres is by a factor > 20, possibly much more.

Thus an explanation for the missing Ceres family needs to be some physical mechanism preventing most fragments which would be observable, currently those with $D > 2$ km, either from being created by a craterization, or from being ejected with $v_0 > 510$ m/s, or from surviving as asteroids. We are aware of only two possible models.

One model can be found in [Li et al., 2006, section 6.3]: "The lack of a dynamical family of small asteroids associated with Ceres, unlike Vesta's Vestoids, is consistent with an icy crust that would not produce such a family." We have some doubts on the definition of an "icy" crust with albedo < 0.1, thus we generalize this model by assuming a comparatively thin crust, with whatever composition is compatible with the measured albedo, effectively shielding the mantle volatiles. When Ceres is impacted by a large asteroid, $20 < D < 50$ km, the crust is pierced and a much deeper crater is excavated in an icy mantle. Thus the efficiency in the generation of family asteroids (with albedo similar to the crust) is decreased by a factor close to the ratio between average crater depth and crust thickness. The ejected material from the mantle forms a family of main belt comets, if they have enough water content they quickly dissipate. This rare event would be one of the most spectacular events of solar system history[27]. Thus a crust thickness of few km would be enough to explain a loss of efficiency by a factor > 20 and a possible Ceres family could be too small to be found.

A second possible model is that there is a critical value for the ejection velocity v_0 beyond which asteroids with $D > 2$ km cannot be launched without going into pieces. If this critical velocity v_c is > 363 m/s for V-type

[26]This is an upper bound, since some dark interlopers need to be there: in the range $2.66 < a < 2.86$ au we find that 59% of background asteroids have albedo < 0.1.

[27]The exceptional presence of some 10 000 comets could perhaps be detected in an extrasolar planetary system, but we know too few of these.

asteroids, but is < 510 m/s for the composition of Ceres ejecta (presumably with much lower material strength), then Vesta can have a family but Ceres can not. Of course it is also possible that the number of large ejecta with $v_0 > 510$ is not zero but very small. Thus even a very large impact on Ceres does generate few observable objects, it does not matter whether they are asteroids or comets, leading to a family too small to be detected. However, if the crater is deeper than the crust, Ceres itself behaves like a main belt comet for some time, until the crater is "plugged" by dirt thick enough to stop sublimation. This would be spectacular too.

The fact is, little is known of the composition and geological structure of Ceres. This situation is going to change abruptly in 2015, with the visit by the DAWN spacecraft. Then what these two models would predict for the DAWN data?

With both models, larger impacts would leave only a scar, resulting from the plugging of the mantle portion of the crater (because Ceres does not have large active spots). What such a big scar looks like is difficult to be predicted, it could be shallow if the mantle restores the equilibrium shape, but still be observable as albedo/color variations.

If there is a thin crust, then craters should have low maximum depth and a moderate maximum diameter. At larger diameters only scars would be seen[28].

If the family generation is limited by the maximum ejection velocity, the crust could be thicker: there would be anyway craters and scars, but the craters can be larger and the scars would be left only by the very large impact basins.

6.7 Couples

One step of our family classification procedure is the computation of the distance in proper elements space between each couple of asteroids; the computation is needed only if the distance is less than some control d_{min}. If the value of d_{min} is chosen to be much smaller than the QRL values used in the family classification, a new phenomenon appears, namely the *very close couples*, with differences in proper elements corresponding to few m/s.

A hypothesis for the interpretation of asteroid couples, very close in proper elements, has been proposed long ago, see Milani [1994][p. 166-167]. The idea, which was proposed by the late P. Farinella, is the following: the

[28]Küppers et al. [2014] recently announced that Herschel observations detected water vapor connected with Ceres, and tentatively identified the sources with small exposed patches of ice. This appears to support the thin crust model.

pairs could be obtained after *an intermediate stage as binary*, terminated by a low velocity escape through the so-called fuzzy boundary, generated by the heteroclinic tangle at the collinear Lagrangian points.

Table 6.11: Very close couples among the numbered asteroids, with distance $d < 0.4$ m/s.

name	H	name	H	d	$\delta a_p/a_p$	δe_p	$\delta \sin I_p$
92652	15.11	194083	16.62	0.1557213	0.0000059	-0.0000011	0.0000011
27265	14.72	306069	16.75	0.2272011	0.0000076	0.0000021	-0.0000029
88259	14.86	337181	16.99	0.2622311	-0.0000091	0.0000019	-0.0000011
180906	17.41	217266	17.44	0.2649047	0.0000069	-0.0000049	-0.0000013
60677	15.68	142131	16.05	0.3064294	0.0000090	0.0000021	0.0000052
165389	16.31	282206	16.85	0.3286134	0.0000019	0.0000080	0.0000022
188754	16.29	188782	16.90	0.3384864	-0.0000059	-0.0000019	0.0000087
21436	15.05	334916	18.14	0.3483815	-0.0000041	-0.0000081	0.0000016

The procedure to actually prove that a given couple is indeed the product of the split of a binary is complex, typically involving a sequence of filtering steps, followed by numerical integrations (with a differential Yarkovsky effect, given the differences in size) to find an epoch for the split and confirm that the relative velocity was very small. Our goal is not to confirm a large number of split couples, but just to offer the data for confirmation by other authors, in the form of a very large list of couples with very similar proper elements.

Currently we are offering a dataset of 14 627 couples with distance < 10 m/s, available from AstDyS[29].

To assess the probability of finding real couples in this large sample, it is enough to draw an histogram of the distance d. It shows the superposition of two components, one growing quadratically with d and one growing linearly. Since the incremental growth of volume is quadratic in d, these components correspond to the random couples and to the ones from a low velocity split, followed by a linear drift in a due to differential Yarkovsky. From the histogram it is possible to compute that, out of 14 627 couples, about half belong to the "random" sub-population, half to the linear growth component. If it was possible to confirm such a large fraction of couples as split binaries, this would provide information on the difference in the fraction of binaries between families and background[30].

[29] http://hamilton.dm.unipi.it/~astdys2/propsynth/numb.near

[30] This cannot be obtained from the known binaries, because they are too few: e.g., a current total of 88 identified binary systems is given by R. Johnston at the URL http://johnstonsarchive.net/astro/asteroidmoons.html

6.8 Conclusions and Future Work

By performing an asteroid family classification with a very enlarged dataset the results are not just "more families", but there are interesting qualitative changes. These are due to the large number statistics, but also to the larger fraction of smaller objects contained in recently numbered asteroids and to the accuracy allowing to see many structures inside the families.

Another remarkable change is that we intend to keep this classification up to date, by the (partially automated) procedures we have introduced.

In this section we summarize some of these changes, and also identify the most productive future research efforts. Note that we do not intend to do all this research ourselves: given our open data policy this is not necessary.

6.8.1 How to use HCM

The size increase of the dataset of proper elements has had a negative effect on the perception about the HCM method, because of the chaining effect which tends to join even obviously distinct families. Thus some authors have either reduced the dataset by requiring physical observations, or used QRL values variable for each family, or even reverted to visual methods.

We believe that this paper shows that there is no need to abandon the HCM method, provided a multistep procedure is adopted. In short, our procedure amounts to using a truncation QRL for the larger members of the core family different from the one used for smaller members. This is statistically justified, because the smaller asteroids have larger number density.

We are convinced that our method is effective in adding many smaller asteroids to the core families, without expanding the families with larger members. As a result we have a large number of families with very well defined V-shapes, thus with a good possibility of age estimation. We have also succeeded in identifying many families formed only with small asteroids, or at most with very few large ones, as expected for cratering.

We intend to work more on the step 5 of the procedure, merging, which is still quite subjective (even visual inspection plays a significant role).

6.8.2 Stability of the classification

We have established a procedure to maintain our family classification up to date, by adding the newly discovered asteroids, as soon as their orbital elements are stable enough because determined with many observations. First the proper elements catalogs are updated, then we attribute some of the new

entries as new members to the already known families. This step 6 is performed in an automatic way, by running the same computer code used for steps 2 and 4. Some changes in the classification such as mergers are not automatic, thus we are committed to apply them when appropriate.

We already have done this for the proper elements catalog update of April 2013, and we continue with periodic updates. The results are available, as soon as computed, on the AstDyS information system. The classification is methodologically stable but frequently updated in the dataset. In this way, the users of our classification can download the current version.

6.8.3 Magnitudes

As shown in Table 6.1, the absolute magnitudes computed with the incidental photometry could contribute a good fraction of the information used in family classification and analysis. However, the accuracy is poor, in most cases not estimated; better data are available for samples too small for statistical purposes.

This does not affect the classification, but has a negative impact on the attempt to compute ages, size distributions, and volumes; also on the accuracy of the albedos, and the population models.

The question is what should be done to improve the situation. One possibility would be a statistically rigorous debiasing and weighting of the photometry collected with the astrometry. The problem is, the errors in the photometry, in particular the ones due to difference in filters and star/asteroid colors, are too complex for a simple statistical model, given that we have no access to a complete information on the photometric reduction process.

Thus the best solution is to have an optimally designed photometric survey, with state of the art data processing, including the new models of the phase effect Muinonen et al. [2010]. This requires a large number (of the order of 100) photometric measurements per asteroid per opposition, with a wide filter, and with enough S/N for most numbered main belt asteroids. These appear tough requirements, and a dedicated survey does not appear a realistic proposal. However, these requirements are the same needed to collect enough astrometry for a NEO "Wide survey", aiming at discovering asteroids/comets on the occasion of close approaches to the Earth. Thus a "magnitude survey" could be a byproduct of a NEO discovery survey.

6.8.4 Yarkovsky effect and ages

One of our main results is that for most families, large enough for statistically significant analysis of the shape, the V-shape is clearly visible.

We have developed a method to compute ages, which is more objective and takes into account the error in the diameter estimate by the common albedo hypothesis, which is substantial.

We believe this method tackles in an appropriate way all the difficulties of the age estimation discussed in Section 6.4.2, but for one: the Yarkovsky calibration. The difficulty in the calibration estimate, due to the need to extrapolate from NEAs with measured da/dt to main belt asteroids, is in most cases the main term in the error budget of the age estimation.

Thus the research effort which could most contribute to the improvement of age estimation (for a large set of families) would be either the direct measurement of Yarkovsky effect for some family members (with known obliquity) or the measurement of the most important unknown quantities affecting the scaling from NEA, such as thermal conductivity and/or density. These appear ambitious goals, but they may become feasible by using advanced observation techniques, in particular from space, and radar from the ground.

6.8.5 Use of physical observations

In this paper we have made the choice of using the dynamical data first, to build the family classification, then use all the available physical data to check and refine the dynamical families.

This is best illustrated by the example of the Hertha/Polana/Burdett complex dynamical family, in which the identification of the two collisional families Polana and Burdett can be obtained only with the physical data.

The use of dynamical parameters first is dictated by the availability and accuracy of the data. We would very much welcome larger catalogs of physical data, including smaller asteroids and with improved S/N for those already included. However, this would require larger aperture telescopes.

6.8.6 Cratering vs. Fragmentation

Our procedure, being very efficient in the addition of small asteroids to the core families, has allowed to identify new cratering families and very large increases of membership for the already known ones.

As a result of the observational selection effect operating against the cratering families, because they contain predominantly small asteroids (e.g., $D < 5$ km), in the past the cratering events have been less studied than the catastrophic fragmentations. On the contrary, there should be more cratering than fragmentation families, because the target of a cratering remains available for successive impacts, with the same cross section.

As the observational bias against small asteroids is progressively mitigated, we expect that the results on cratering will become more and more important.

This argument also implies that multiple cratering collisional families should be the rule rather than the exception. They necessarily intersect because of the common origin but do not overlap completely because of the different crater radiants. Although we have studied only some of the cratering families (listed in Section 6.6), all the examples we have analyzed, namely the families of (4), (20), (15), show a complex internal structure.

For the catastrophic fragmentation families, the two examples we have analyzed, (158) and (847), appear to contain significant substructures (named after Karin and Jitka). The general argument could be used that fragments are smaller, thus should have collisional lifetimes shorter than the parent body of the original fragmentation family. Thus we should expect that as fragmentation families become larger in membership and include smaller asteroids, substructures could emerge in most of the families.

A full fledged collisional model for the ejection velocities and rotations of fragments from both cratering and fragmentation needs to be developed, possibly along the lines of the qualitative model of Section 6.4.2. This will contribute both to the age determination and to the understanding of the family formation process.

6.8.7 Comparison with space mission data

When on-site data from spacecraft, such as DAWN, become available for some big asteroid, a family classification should match the evidence, in particular from craters on the surface. For Vesta the main problem is the relationship between the dynamical family 4 and the two main craters Rheasilvia and Veneneia. The solution we are suggesting is that the two subfamilies found from internal structure of family 4 correspond to the two main craters. We have found no contradiction with this hypothesis in the data we can extract from the family, including ages. However, to prove this identification of the source craters requires more work: more accurate age estimates for both subfamilies and craters, and more sophisticated models of how the ejecta from a large crater are partitioned between ejecta reaccumulated, fragments in independent orbits but too small, and detected family members.

Because the problem of the missing Ceres family is difficult, due to apparently discordant data, we have tried to discuss a consistent model, with an interpretation of the dynamical family 93 (without the namesake) and two possible physical explanations of the inefficiency of Ceres in generating families. We are not claiming these are the the only possible explanations,

but they appear plausible. The data from DAWN in 2015 should sharply decrease the possibilities and should lead to a well constrained solution.

Chapter 7

Asteroid families ages

7.1 Introduction

One of the main purposes for collecting large datasets on asteroid families is to constrain their ages, that is the epoch of the impact event generating a collisional family. A collisional family not always coincides with the dynamical family detected by density contrast in the proper elements space. More complicated cases occur, such as a dynamical family to be decomposed in two collisional families, or the opposite case in which a collisional family is split in two density contrast regions by some dynamical instability.

Although other methods are possible, currently the most precise method to constrain the age of a collisional family (for the ages older than ~ 10 My) exploits non-gravitational perturbations, mostly the Yarkovsky effect [Vokrouhlický et al., 2000b]. These effects generate secular perturbations in the proper elements of an asteroid which are affected not just by the position in phase space, but also by the Area/Mass ratio, which is inversely proportional to the asteroid diameter D. Thus, the main requirements are to have a list of family members with a wide range of values in D, enough to detect the differential effect in the secular drift of the proper elements affecting the shape of the family, and to have a large enough membership, to obtain statistically significant results.

Recently Milani et al. [2014] have published a new family classification by using a large catalog of proper elements (with $> 330,000$ numbered asteroids) and with a classification method improved with respect to past methods. This method is an extension of the Hierarchical Clustering Method (HCM) [Zappala et al., 1990], with special provisions to be more efficient in including large numbers of small objects, while escaping the phenomenon of chaining. Moreover, the new method includes a feature allowing to (almost)

automatically update the classification when new asteroids are numbered and their proper elements have been computed. This has already been applied to extend the classification to a source catalog with $\sim 384,000$ proper elements, obtaining a total of $\sim 97,400$ family members [Knežević et al., 2014]. In this paper we are going to use the classification of Milani et al. [2014], as updated by Knežević et al. [2014], and the data are presently available on AstDyS[1].

This updated classification has 21 dynamical families with $> 1,000$ members and another 24 with > 250 members. The goal of this paper can be simply stated as to obtain statistically significant age constraints for the majority of these 45 families. Computing the ages for all would not be a realistic goal because there are several difficulties. Some families have a very complex structure, for which it is difficult to formulate a model, even with more than one collision: these cases have required or need dedicated studies. Some families are affected by particular dynamical conditions, such as orbital resonances with the planets, which result in more complex secular perturbations: these shall be the subject of continuing work. The results for families with only a moderate number of members (such as $250 - 300$) might have a low statistical significance.

The age estimation includes several sources of uncertainty which cannot be ignored. The first source appears in the formal accuracy in the least square fit used in our family shape estimation methods. The uncertainty depends upon the noise resulting mostly from the inaccuracy of the estimation of D from the absolute magnitude H. The second source of error occurs in the conversion of the inverse slope of the family boundaries into age, requiring a Yarkovsky calibration: this is fundamentally a relative uncertainty, and in most cases it represents the largest source of uncertainty in the inferred ages. In Sec. 7.4.1 we give an estimate of this uncertainty between 20% and 30%.

As a result of the current large relative uncertainty of the calibration, we expect that this part of the work will be soon improved, thanks to the availability of new data. Thus the main result of this paper are the inverse slopes, because these are derived by using a consistent methodology and based upon large and comparatively accurate data set. Still we believe we have done a significant progress with respect to the previous state of the art by estimating 37 collisional family ages, in many cases providing the first rigorous age estimate, and in all cases providing an estimated standard deviation. The work can continue to try and extend the estimation to the cases which we have found challenging.

Since this paper summarizes a complex data processing, with output needed to fully document our procedures but too large, we decided to in-

[1] http://hamilton.dm.unipi.it/astdys/index.php?pc=5

clude only the minimum information required to support our analysis and results. Supplementary material, including both tables and plots, is available from the web site `http://hamilton.dm.unipi.it/astdys2/fam_ages/`.

7.2 Least squares fit of the V-shape

Asteroids formed by the same collisional event take the form of a V in the (proper a - $1/D$) plane. The computation of the family ages can be performed by using this V-shape plots if the family is old enough and the Yarkovsky effect dominates the spread of proper a, as explained in [Milani et al., 2014, Sec. 5.2]. The key idea is to compute the diameter D from the absolute magnitude H, assuming a common geometric albedo p_v for all the members of the family. The common geometric albedo is the average value of the known WISE albedos [Mainzer et al., 2011b; Wright et al., 2010] for the asteroids in the family. Then we use the least squares method to fit the data with two straight lines, one for the low proper a (IN side) and the other for the high proper a (OUT side), as in Milani et al. [2014], with an improved outlier rejection procedure, see [Carpino et al., 2003] and Sec. 7.2.4.

7.2.1 Selection of the Fit Region

Most families are bounded on one side or on both sides by resonances. Almost all these resonances are strong enough to eject most of the family members that fell into the resonances into unstable orbits. In these cases the sides of the V are cut by vertical lines, that is by values of a, which correspond to the border of the resonance. For each family we have selected the fit region taking into account the resonances at the family boundaries. The fit of the slope has to be done for values of $1/D$ below the intersection of one of the sides of the V affected by the resonance and the resonance border value of proper a. In Table 7.1 we report the values for a and D, and the cause of each selection.

The *cause* of each cut in proper a is a mean motion resonance, in most cases a 2-body resonance with Jupiter, in few cases either a 2-body resonance with Mars or a 3-body resonance with Jupiter and Saturn. When no resonance with this role has been identified, we use the label FB (for Family Box) to indicate that the family ends where the HCM procedure does not anymore detect a significant density contrast (with respect to the local background). This is affected by the depletion of the proper elements catalog due to the completeness limit of the surveys: the family may actually contain many smaller asteroids beyond the box limits, but they have not been discovered

Table 7.1: Fit region: family number and name, explanation of the choice, minimum value of proper a, minimum value of the diameter selected for the inner and the outer side.

number/ name	cause	min proper a	min D IN	cause	max proper a	min D OUT
158 Koronis	5/2	2.82	7.69	7/3	2.96	5.00
24 Themis	11/5	3.075	25.00	2/1	3.24	16.67
847 Agnia	8/3	2.70	4.55	5/2	2.82	6.67
3395 Jitka	FB	2.76	1.33	5/2	2.82	1.33
1726 Hoffmeister	3-1-1	2.75	5.00	5/2	2.82	4.00
668 Dora	3-1-1	2.75	5.88	5/2	2.815	8.33
434 Hungaria	5/1	1.87	1.25	4/1	2.00	1.25
480 Hansa	3/1?	2.54	5.00	FB	2.71	6.67
808 Merxia	8/3	2.7	2.50	FB	2.80	2.00
3330 Gantrisch	FB?	3.13	6.67	5-2-2	3.17	6.67
10955 Harig	FB	2.67	1.43	FB	2.77	1.82
293 Brasilia	5/2	2.83	2.50	FB	2.88	2.00
569 Misa	FB	2.62	3.33	FB	2.70	3.33
15124 $2000EZ_{39}$	FB	2.62	2.00	FB	2.70	2.50
1128 Astrid	FB?	2.755	2.22	5/2	2.82	2.22
845 Naema	FB	2.91	2.86	7/3	2.96	5.00
4 Vesta	7/2	2.25	2.50	3/1	2.50	2.94
15 Eunomia	3/1?	2.52	5.00	8/3	2.71	5.00
20 Massalia	10/3	2.33	1.00	3/1	2.50	0.91
10 Hygiea	11/5	3.07	7.14	2/1	3.25	7.69
31 Euphrosyne	11/5	3.07	6.67	2/1	3.25	6.67
3 Juno	FB?	2.62	2.00	8/3	2.70	2.50
163 Erigone	10/3	2.33	2.50	2/1M	2.42	2.50
3815 König	FB	2.56	2.20	FB	2.585	2.20
396 Aeolia	FB	2.73	1.67	FB	2.755	2.00
606 Brangane	FB	2.57	1.67	FB	2.595	1.67
1547 Nele	FB	2.64	1.67	FB	2.648	1.67
18405 $1993FY_{12}$	FB	2.83	2.50	FB	2.85	2.00
170 Maria	3/1?			FB	2.665	4.00
93 Minerva	FB	2.71	4.00	5/2		
2076 Levin	7/2			FB	2.34	2.50
3827 Zdenekhorsky	8/3	2.7	2.00	1-1C		
1658 Innes	3/1?			11/4	2.645	2.00
375 Ursula	FB	3.1	12.50	2/1		

yet. On the contrary when the family range in proper a is delimited by strong resonances, the family members captured in them can be transported far in proper e (and to a lesser extent in proper $\sin I$) to the point of not being recognizable as members; over longer time spans, they can be transported to planet-crossing orbits and removed from the main belt altogether.

The tables in this paper are sorted in the same way: there are four parts, dedicated to families of the types fragmentation, cratering, young, one-sided; inside each group the families are sorted by decreasing number of members. In some cases the tables have been split in four sub-tables, one for each type.

In two cases we have already defined the fit region in such a way that we can include two families in a single V-shape. This *family join* is justified later, in Section 7.3, by showing that the two dynamical families can be generated by a single collision. This applies to the join of 10955 with 19466 and to the join of 163 with 5206. Note that the join of two families, justified by the possibility to fit together in a single V-shape with a common age, is conceptually different from the *merge* of two families due to intersections, discussed in [Knežević et al., 2014; Milani et al., 2014]; however, the practical consequences are the same, namely one family is included in another one and disappears from the list of families.

For one-sided families we are also indicating the "cause" of the missing side. E.g., for 2076 the lack of the IN side of the V-shape is due to the 7/2 resonance; on the other hand, the dynamical family 883 could be the continuation of 2076 at proper a lower than the one of the resonance. However, the V-shape which would be obtained by this join would have two very different slopes, thus it can be excluded that they are the same collisional family.

For most families the "cause" of the delimitation in proper a, in the sense above, can be clearly identified. However, some ambiguous cases remain: e.g., for family 1128 the outer boundary could be due to the 3-body resonance 3-1-1 (the three integer coefficients apply to the mean motions of Jupiter, Saturn and the asteroid, respectively); for family 3 the inner boundary could be due to 4-3-1. For family 3330 a 3-body resonance (not identified) at $a = 3.129$ could be the cause of the inner boundary.

For the one-sided family 3827 we do not know the cause of the missing OUT side, although we suspect it has something to do with (1) Ceres, given that the proper a of Ceres is very close to the upper limit of the family box.

The family of (3395) Jitka is a subfamily of the dynamical family 847. The family of (15124) 2000 EZ_{39} is a subfamily of the dynamical family 569.

With 3/1? we are indicating 2 cases (480, 15) in which the families could be delimited on the IN side by the 3/1 resonance (also 170, 1658 in which the 3/1 could be the cause of the missing IN side), but the lower bound on proper a appears too far from the Kirkwood gap. This is a problem which needs to be investigated.

7.2.2 Binning and fit of the slopes

Next we divide the $1/D$ axis into bins, as in Figures 7.1 and 7.2. The partition is done in such a way that each bin contains roughly the same number of members.

The following points explain the main features of the method used to create the bins:

1. the maximum number of bins N is selected for each family, depending upon the number of members of the family;

2. the maximum value of the standard deviation of the number of members in each bin is decided depending upon the number of members of the family;

3. the region between 0 and the maximum value of $1/D$ is divided in N bins;

4. the difference between the number of members in two consecutive bins is computed:

   4.1 if the difference is less than the standard deviation, the bins are left as they are;

   4.2 if the difference is greater than the standard deviation, the first bin is divided into smaller bins and then the same procedure is applied to the new bins.

This procedure is completely automatic, and it is the same both for the inner and the outer side of a V-shape. In the example of the Figures, namely the family of (20) Massalia, in the IN side there are 84 bins with a mean of 19 members in each, with a STD of this number 13. In the OUT side there are 82 bins with mean 19 and STD 11.

In the case of the low a side we select the minimum value of proper a and the corresponding $1/D$ in each bin, as in Fig. 7.1. For the other side we select the maximum value of the proper semimajor axis and the corresponding $1/D$, as in Fig. 7.2. These are the data to be fit to determine the slopes of the V-shapes: thus it is important to have enough bins to properly cover the range in proper a.

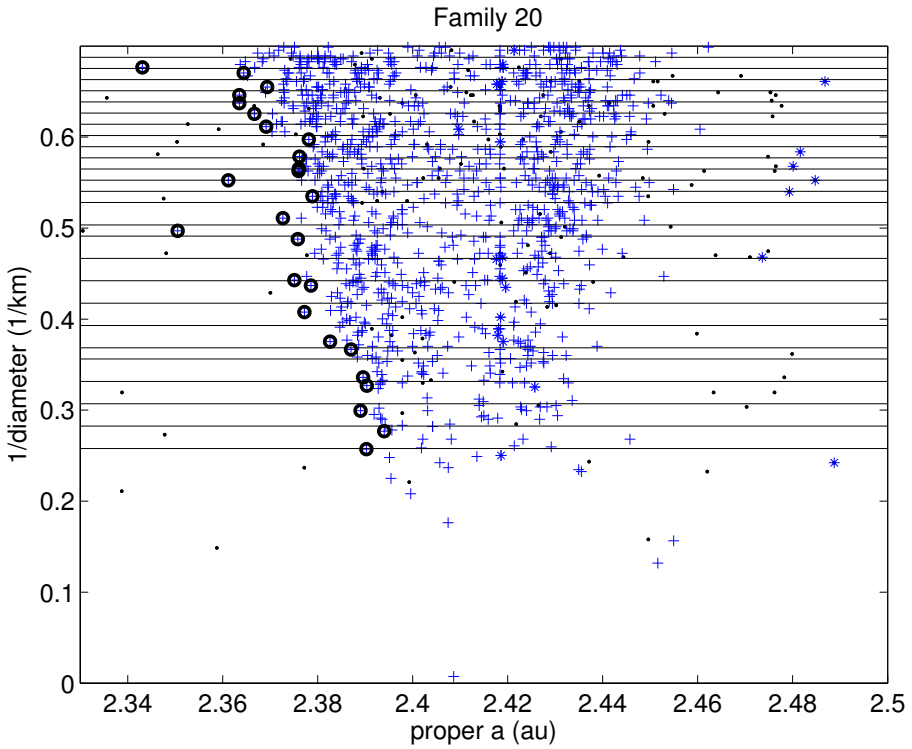

Figure 7.1: Blow up of the bins for the inner side of the family of (20) Massalia. Crosses are the members of the family, points are background asteroids, stars are affected by the resonances. Circles are members of the family of (20) Massalia with the minimum value of proper a and the corresponding $1/D$ in each bin.

7.2.3 Error Model and Weights

The least squares fit, especially if it includes an outlier rejection procedure, requires the existence of an error model for the values to be fit. Until now there are no error models for the absolute magnitude and the albedo, which are available for a large enough catalog of asteroids.

We have built a simple but realistic error model for $1/D$ computed from the absolute magnitude H (the formula is $D = 1\,329 \times 10^{-H/5} \times 1/\sqrt{p_v}$) by combining the effect of two terms in the error budget: the error in the absolute magnitude with STD σ_H and the one in the geometric albedo with STD σ_{p_v}. The derivatives of $1/D$ with respect to these two quantities are:

$$\frac{\partial(1/D)}{\partial H} = \frac{log(10)}{5} \times \frac{1}{D} \qquad \frac{\partial(1/D)}{\partial p_v} = \left(\frac{1}{2 \times p_v}\right) \times \frac{1}{D} \ ,$$

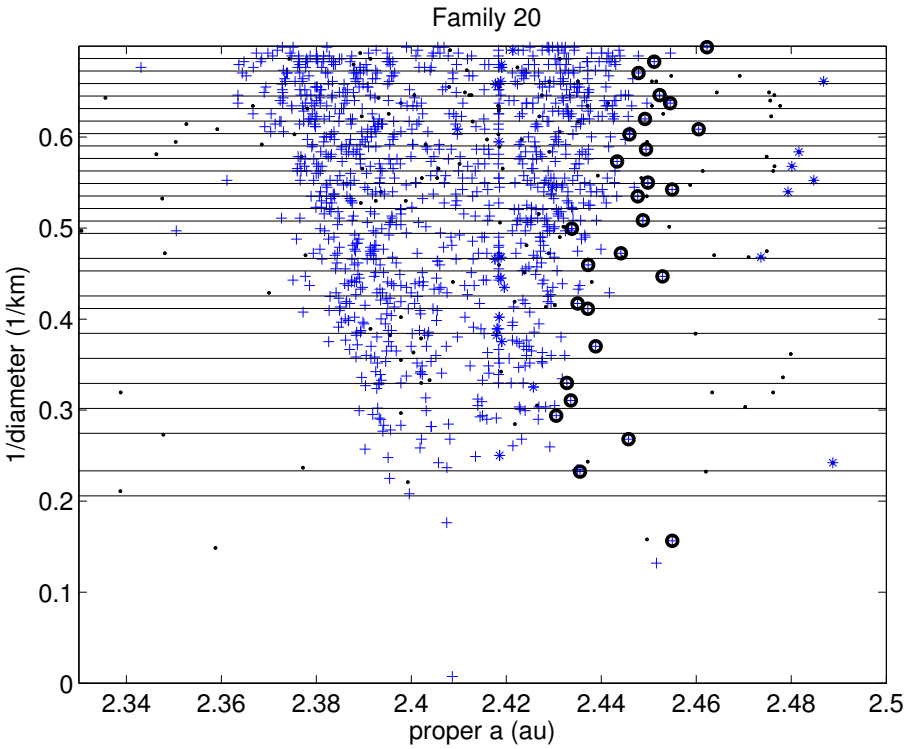

Figure 7.2: Blow up of the bins for the outer side of the family of (20) Massalia. Circles are members of the family of (20) Massalia with the maximum value of proper a and the corresponding $1/D$ in each bin on the left side. Crosses, points and stars as in Fig. 7.1.

then the combined error has STD

$$\sigma_{1/D} = \sqrt{\left(\frac{\partial(1/D)}{\partial H}\,\sigma_H\right)^2 + \left(\frac{\partial(1/D)}{\partial p_v}\,\sigma_{p_v}\right)^2}\,.$$

To compute this error model we need to select three values: 1) the common geometric albedo p_v for all the family members, 2) the dispersion with respect to this common albedo σ_{p_v}, 3) the uncertainty in the absolute magnitude σ_H.

For the first two, we select all the "significant" WISE albedos , that is the values of the albedos greater than 3 times their standard deviations (with $S/N > 3$). Then we cut the tails of this distribution (see Figure 7.3): p_v is the mean and σ_{p_v} is the standard deviation of the values of the albedo without the tails. For the third value σ_H we use the same for all the families and the chosen value is 0.3, see the discussion in 6.1 and in [Pravec et al., 2012].

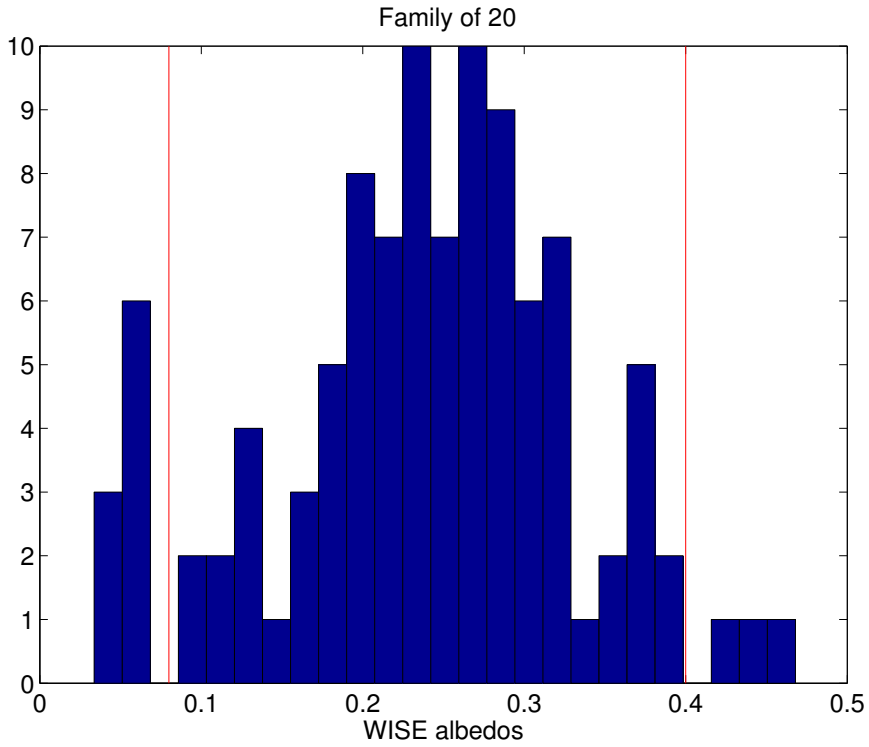

Figure 7.3: Histogram of the "significant" WISE albedos for the dynamical family of (20) Massalia. The vertical lines show the values of the albedos used for the cut, leaving out values which should correspond to interlopers. In this and in many other cases the selection of the interlopers is simple: albedo < 0.1 indicates C-complex asteroids and > 0.4 values are likely to be affected by large errors.

The histograms such as Figure 7.3 are available for all the families listed in Table 7.2 at the Supplementary material web site.

In Table 7.2 we show the albedo value of the namesake asteroid, with its uncertainty and the appropriate reference: W for WISE data [Masiero et al., 2011], I for IRAS, S for [Shepard et al., 2008], and A for AKARI. In some cases albedo data are not available. The columns 5 and 6 contain the value of the albedo used for the cut of the tails, and the last two columns are the mean albedo and the standard deviation.

Two discordant results from the albedo analysis of the dynamical families are easily appreciated from Table 7.2. (93) Minerva and (293) Brasilia are interlopers in the dynamical families for which they are namesake, as shown by albedo data outside of the family range. Indeed, in the following of this paper we are going to speak of the family 1272 (Gefion) instead of 93, and of the family 1521 (Seinajoki) instead of 293; both are obtained by removing

Table 7.2: Family albedos: number and name of the family, albedo of the parent body with standard deviation and code of reference, maximum and minimum value for computing mean, mean and standard deviation of the albedo

number/ name	albedo value	largest STD	ref	family min	family max	albedo mean	albedo STD
158 Koronis	0.144	0.009	W	0.07	0.50	0.240	0.061
24 Themis	0.064	0.016	W		0.12	0.069	0.019
847 Agnia	0.147	0.012	W	0.10	0.40	0.242	0.056
1726 Hoffmeister	0.036	0.007	W		0.10	0.048	0.013
668 Dora	0.073	0.009	W		0.10	0.058	0.014
434 Hungaria	0.380		S			0.380	0.100
480 Hansa	0.249	0.024	I	0.10	0.45	0.286	0.068
808 Merxia	0.165	0.021	W	0.10	0.40	0.248	0.055
3330 Gantrisch	0.048	0.010	W			0.047	0.012
10955 Harig						0.251	0.068
293 Brasilia	0.033	0.007	W	0.10	0.27	0.174	0.042
569 Misa	0.030	0.001	I		0.10	0.058	0.016
1128 Astrid	0.046	0.018	W			0.052	0.014
845 Naema	0.072	0.019	W		0.10	0.065	0.014
4 Vesta	0.423	0.053	I	0.15	0.60	0.355	0.099
15 Eunomia	0.206	0.055	W		0.50	0.260	0.083
20 Massalia	0.210	0.030	I	0.08	0.40	0.249	0.070
10 Hygiea	0.058	0.005	W	0.02	0.15	0.073	0.022
31 Euphrosyne	0.045	0.045	W		0.10	0.061	0.015
3 Juno	0.238	0.025	I	0.10	0.40	0.253	0.055
163 Erigone	0.033	0.004	W		0.10	0.055	0.013
3815 König	0.056	0.004	W		0.15	0.051	0.014
396 Aeolia	0.139	0.025	W			0.106	0.028
606 Brangane	0.089	0.012	W			0.121	0.028
1547 Nele	0.313	0.040	A	0.15		0.355	0.064
18405 $1993FY_{12}$				0.10		0.184	0.042
170 Maria	0.160	0.007	I			0.261	0.084
93 Minerva	0.073	0.004	I	0.10	0.50	0.277	0.096
2076 Levin	0.557	0.318	W	0.10	0.40	0.202	0.070
3827 Zdenekhorsky	0.104	0.008	W		0.12	0.074	0.020
1658 Innes	0.224	0.037	W	0.10	0.43	0.264	0.064
375 Ursula	0.049	0.001	A		0.10	0.062	0.015

interlopers selected because of albedo data, and the namesake is the lowest numbered after removing the interlopers.

For many families we have proceeded in the same way, that is removing interlopers clearly indicated by an albedo discordance. The list of these interlopers for each family is in the Supplementary material.

In some cases we have joined two dynamical families for the purpose

of mean albedo computation: 2076 includes 298, 163 include 5026, 10955 includes 19466[2]. Family 847 includes the subfamily 3395: the same mean albedo was used for both, although (847) has albedo 0.147 ± 0.01 and (3395) 0.313 ± 0.05, which are on the opposite side of the mean. Also 569 in Table 7.2 includes the subfamily 15124.

The family of (434) Hungaria is a difficult case: some WISE data exist for its family members, but they are of especially poor quality. Thus we have used for all the albedo derived from radar data [Shepard et al., 2008], and assumed a quite large dispersion (0.1).

7.2.4 Outlier Rejection and Quality Control

The algorithm for differential corrections used for the computation of the slopes includes an automatic outlier rejection scheme, as in [Carpino et al., 2003]. Both the use of an explicit error model for the observations and the fully automatic outlier rejection procedure are implemented in the free software OrbFit[3] and are used for the orbit determination of the asteroids included in the NEODyS and AstDyS information systems[4]. Thus, although the application of these methods to the computation of family ages is new, this is a very well established procedure on which we have a lot of experience.

In practice, outlier rejection is performed in an iterative way. At each iteration, the program computes the residuals of all the observations, their expected covariance and the corresponding χ^2 value. If we can assume that the observation errors have a normal distribution, to mark an observation as an outlier we can compare the χ^2 value of the post-fit residual with a threshold value χ^2_{rej}: the observation is discarded if $\chi^2_i > \chi^2_{rej}$. At each iteration it is also necessary to check if a given observation, that we have previously marked as an outlier, should be recovered. Therefore, the program selects an outlier to be recovered if for the non-fitted residual $\chi^2_i < \chi^2_{rec}$. The current values for χ^2_{rej} and χ^2_{rec} are 10 and 9, respectively.

During each iteration of the linear regression we compute the residuals, the outliers, the RMS of the weighted residuals and the Kurtosis of the same weighted residuals. Our method converges if there is an iteration without additional outliers. All these data are reported in Table 1 of the Supplementary material. Besides the automatic outlier rejections, some *interlopers* have been manually removed when there was a specific evidence that they do

[2]However, there is only 1 significant WISE albedo among members of family 19466.

[3]Distributed at http://adams.dm.unipi.it/orbfit/

[4]http://newton.dm.unipi.it/neodys/ and http://hamilton.dm.unipi.it/astdys/ respectively.

not belong to the collisional family, e.g., based upon WISE data: also these manual rejections are detailed in the Supplementary material.

7.3 Results

7.3.1 Fragmentation Families

The results of the fit for the slopes of the V-shape are described in Table 7.3 for the families of the fragmentation type. To define fragmentation families, we have used the (admittedly conventional) definition that the volume of the family without the largest member has to be more than 12% of the total. This computation has been done after removing the interlopers (by physical properties) and the outliers (removed in the fit), and is based on D computed with the mean albedo p_v. Comments for some of the cases are given below.

- For family 158 (Koronis) the values of the inverse slope $1/S$ on the two sides are consistent, that is the ratio is within a standard deviation from 1: this indicates that we are measuring the age of a single event. The well known subfamily of (832) Karin, with a recent age, does not affect the slopes.

- Family 24 (Themis) has the well known subfamily of (656) Beagle near the center of the V-shape, thus it does not affect the slopes. The values IN and OUT are not the same but the difference has very low statistical significance. The low accuracy of the IN slope determination is due to the fact that the 11/5 resonance cuts the V-shape too close to the center, sharply reducing the useful range in D.

- For family 847 (Agnia) we have estimated also the slopes for the subfamily 3395. 847 has discordant slope values on the two sides, but the OUT one has too few points, being affected by 3395. Thus we consider as the true value the one obtained on the IN side. 3395 has a very good fit but with many outliers, which can be explained as members of 847 but not 3395. Anyway the inverse slopes are significantly lower for 3395; since the ages are proportional to the inverse slopes, this indicates an age younger by a factor 7.42 ± 2.06 (based upon the IN values).

- Family 1726 (Hoffmeister) has an especially complicated dynamics on the IN side, due to both the nonlinear secular resonance $g + s - g_6 - s_6$ and the proximity with (1) Ceres, see the discussion in 6.3.1. However, the results on the two slopes are perfectly consistent: this is in agreement with what was claimed by Delisle and Laskar [2012], namely that

Table 7.3: Slopes of the V-shape for the fragmentation families: family number/name, number of dynamical family members, side, slope (S), inverse slope ($1/S$), standard deviation of the inverse slope, ratio OUT/IN of $1/S$, and standard deviation of the ratio.

number/ name	no. members	side	S	$1/S$	STD $1/S$	ratio	STD ratio
158 Koronis	6130	IN	-1.647	-0.608	0.089		
		OUT	1.755	0.570	0.069	0.94	0.18
24 Themis	4329	IN	-0.720	-1.390	0.385		
		OUT	0.477	2.096	0.326	1.51	0.48
847 Agnia	2395	IN	-2.882	-0.347	0.072		
		OUT	4.381	0.228	0.034	0.66	0.17
3395 Jitka		IN	-21.387	-0.047	0.009		
		OUT	21.214	0.047	0.008	1.01	0.26
1726 Hoffmeister	1560	IN	-5.026	-0.199	0.028		
		OUT	5.212	0.192	0.025	0.96	0.18
668 Dora	1233	IN	-3.075	-0.325	0.053		
		OUT	3.493	0.286	0.086	0.88	0.30
434 Hungaria	1187	IN	-14.855	-0.067	0.006		
		OUT	15.293	0.065	0.003	0.97	0.10
480 Hansa	960	IN	-3.710	-0.270	0.109		
		OUT	3.064	0.326	0.040	1.21	0.51
808 Merxia	924	IN	-8.400	-0.119	0.010		
		OUT	8.963	0.112	0.008	0.94	0.10
3330 Gantrisch	723	IN	-3.986	-0.251	0.061		
		OUT	3.552	0.282	0.075	1.12	0.40
10955 Harig &	517	IN	-6.515	-0.154	0.027		
19466 Darcydiegel	153	OUT	5.853	0.171	0.050	1.11	0.38
1521 Seinajoki	545	IN	-8.454	-0.118	0.023		
		OUT	23.507	0.043	0.005	0.36	0.08
569 Misa	441	IN	-5.0376	-0.199	0.151		
		OUT	6.5380	0.153	0.052	0.77	0.64
15124 $2000EZ_{39}$		IN	-14.422	-0.069	0.006		
		OUT	14.337	0.070	0.007	1.01	0.14
1128 Astrid	436	IN	-11.339	-0.088	0.006		
		OUT	11.434	0.088	0.007	0.99	0.10
845 Naema	286	IN	-11.715	-0.085	0.011		
		OUT	10.741	0.093	0.004	1.09	0.15

the Yarkovsky effect prevails over the chaotic effects induced by close approaches (also by the 1-1 resonance) with Ceres, in the range of sizes which is relevant for the fit.

- For the family 480 (Hansa) the slope for the IN side has lower quality, probably due to 3/1 resonance. It is a marginal fragmentation with 14% of the total volume, excluding (480) Hansa itself.

- Family 808 (Merxia) is a fragmentation with a dominant largest member (64% in volume), thus (808) must not be included in the fit.
- For the family 3330 (Gantrisch) it has been difficult to compute a slope for the IN side, because of the irregular shape of the low a border resulting in few data to be fit.
- Family 10955 (Harig) can be joined with family 19466: in this way two one-sided families form a single V-shape: this join is confirmed by the two slopes being consistent. Thus one collisional family is obtained from two dynamical families. This merge was already suggested in 6.3.3, based on the family box overlap (by 40%).
- Family 1521 (Seinajoki) appears to have two discordant slopes: in the projection $(a, \sin I)$ a bimodality appears in the family shape. We draw from this the conclusion that there are two collisional families, the one on the IN side being older.
- The family 569 (Misa) is a marginal fragmentation (fragments account for 19% of the total volume). The ratio of the IN and OUT slopes is not significantly different from 1, mostly because of the low accuracy of the IN value. (15124) 2000 EZ_{39} appears to be the largest fragment of a fragmentation subfamily inside the family 569: the inverse slopes are significantly lower, indicating an age younger by a factor 2.19 ± 0.78 with respect to 569 (based upon the OUT values).

7.3.2 Cratering Families

The results of the fit for the slopes of the V-shape are described in Table 7.4 for the families of the cratering type, defined by a volume of the family without the largest member $< 12\%$ of the total. Comments for some of the cases are given below.

- Family 4 (Vesta) has two discordant slopes on the IN and OUT sides. As already suggested in 6.6, this should be interpreted as the effect of two distinct collisional families, with significantly different ages. The estimated ratio of the slopes provides a significant estimate of the ratio of the ages, because the Yarkovsky calibration is common to the two subfamilies, corresponding to two craters on Vesta.
- Family 15 (Eunomia) has a subfamily which determines the OUT slope, the ratio of the slopes gives a good estimate of the ratio of the ages, because of the common calibration. The interpretation as two collisional families, proposed in 6.6, is thus confirmed.

Table 7.4: Slope of the V-shape for the cratering families. Columns as in Table 7.3.

number/ name	no. members	side	S	$1/S$	STD $1/S$	ratio	STD ratio
4 Vesta	8620	IN	-2.983	-0.335	0.040		
		OUT	1.504	0.665	0.187	1.98	0.61
15 Eunomia	7476	IN	-1.398	-0.715	0.057		
		OUT	2.464	0.406	0.020	0.57	0.05
20 Massalia	5510	IN	-15.062	-0.066	0.003		
		OUT	14.162	0.071	0.006	1.06	0.10
10 Hygiea	2615	IN	-1.327	-0.754	0.079		
		OUT	1.329	0.752	0.101	1.00	0.17
31 Euphrosyne	1137	IN	-1.338	-0.747	0.096		
		OUT	1.507	0.663	0.081	0.89	0.16
3 Juno	960	IN	-5.261	-0.190	0.038		
		OUT	7.931	0.126	0.049	0.66	0.29
163 Erigone &	429	IN	-7.045	-0.142	0.035		
5026 Martes	380	OUT	6.553	0.153	0.013	1.08	0.28

- Family 10 (Hygiea) has a shape (especially in the proper (a, e) projection) from which we could suspect two collisional events, but the IN and OUT slopes not just consistent but very close suggest a single collision.

- For family 3 (Juno) the IN and OUT slopes are discordant, but due to the low relative accuracy of the slopes the difference is marginally significant. The number density as a function of proper a is asymmetric, more dense on the OUT side.

- Family 163 (Erigone) can be joined with 5026 (Martes), with (163) as parent body for both (marginally within the cratering definition, fragments forming 11% of the total volume). This is confirmed by similar albedo (dark in a region dominated by brighter asteroids) and by very consistent slopes of the IN side (formed by family 163) and of the OUT side (formed by 5026), see Figure 7.4. There is a very prominent gap in the center, which explains why we have found no intersections; it should be due to the YORP effect; see Section 7.5.2. Again one collisional family is obtained from two dynamical families.

7.3.3 Young Families

We define as *young families* those with an estimated age of < 100 My; thus the inverse slopes are much lower than those of the previous tables. These can

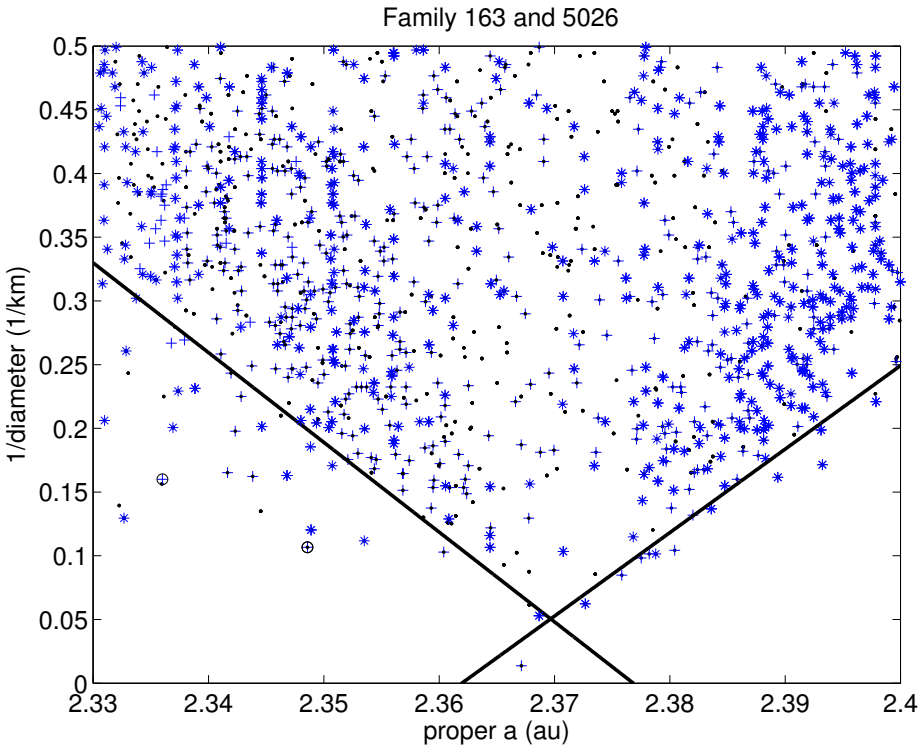

Figure 7.4: V-shape fit for the join of families of (163) Erigone and (5026) Martes. The IN slope is fit to members of 163, the OUT slope to members of 5026, but the two values are consistent. The central depleted region explains why the two families have no intersection: they are *joined* but not *merged*.

be both fragmentations and craterings. The results of the fit are described in Table 7.5.

These families have a comparatively low number of members, but because they also have a small range of proper a values a significant slope fit is possible. In particular we have introduced the three last families in the Table with < 250 members.

Few comments: families 396 (Aeolia) and 606 (Brangane) are craterings, all the others are fragmentations. The family 1547 (Nele) is a marginal fragmentation, with 19% of volume outside (1547); it is known to be very young [Nesvorný et al., 2003], it has been included to test the applicability of the V-shape method to recent families (see Sec. 7.4.2).

Table 7.5: Slope of the V-shape for the young families. Columns as in Table 7.3.

number/ name	no. members	side	S	$1/S$	STD $1/S$	ratio	STD ratio
3815 König	340	IN	-31.892	-0.031	0.004		
		OUT	31.364	0.032	0.004	1.02	0.17
396 Aeolia	306	IN	-32.358	-0.031	0.005		
		OUT	35.556	0.028	0.005	0.91	0.22
606 Brangane	192	IN	-54.027	-0.019	0.002		
		OUT	60.374	0.017	0.003	0.89	0.17
1547 Nele	152	IN	-201.336	-0.005	0.0008		
		OUT	187.826	0.005	0.002	1.07	0.44
18405 $1993FY_{12}$	102	IN	-34.189	-0.029	0.01		
		OUT	34.456	0.029	0.005	0.99	0.36

7.3.4 One Side

The one-sided families are those for which we cannot identify one of the two sides of the V-shape. The results of the fit are described in Table 7.6.

The families of this type can be due to fragmentations and craterings: in most cases there is no dominant largest fragment, and they might have had parent bodies disappeared in the resonance which also wiped out one of the sides, thus we do not really know.

Table 7.6: Slopes of the V-shape for the one-sided families: family number/name, number of dynamical family members, side, slope (S), inverse slope ($1/S$), standard deviation of the inverse slope.

number/ name	no. members	side	S	$1/S$	STD $1/S$
170 Maria	1431	OUT	1.487	0.672	0.059
1272 Gefion	1341	IN	-2.594	-0.386	0.094
2076 Levin	1237	OUT	7.080	0.141	0.023
3827 Zdenekhorsky	794	IN	-10.871	-0.092	0.009
1658 Innes	606	OUT	6.006	0.167	0.011
375 Ursula	335	IN	-0.516	-1.938	0.426

- The family 170 (Maria) has a possible subfamily for low proper a (no effect on the OUT slope). There is no dominant largest fragment, thus it could be either a fragmentation or a cratering, in the latter case with parent body removed by the 3/1 resonance.

- For the family 1272 (Gefion) there is no dominant largest fragment,

thus the same argument applies, with possible parent body removal by the 5/2 resonance.

- For family 2076 (Levin) the possibility of merging with families 298 (Baptistina) and 883 has been discussed in 6.3.1. Joining Baptistina does not change the slopes; joining 883 would result in a two-sided V-shape, with a gap due to the 7/2 resonance in between; however, the two slopes would be very different. All three dynamical families (for which we already have some intersections) could be considered as a single complex dynamical family, but still they would belong to different collisional families with different ages. The slope (thus the age) we have computed belongs to the event generating only the 2076 family. There are not enough significant physical data on the members of these families[5], not even on the comparatively large (298), to help us in disentangling this complex case.

- Family 1658 (Innes) is the largest fragment but it is not dominant in size, thus we cannot distinguish between fragmentation and cratering with parent body removed by the 3/1 resonance.

- (375) Ursula is an outlier in the fit for the IN slope of 375. This can have two interpretations. Either (375) is the largest fragment of a marginal fragmentation (fragments are 23% of total volume), in which case it is correct not to include it in the slope fit, or (375) is an interloper and the family could have had a parent body later disappeared in the 2/1 resonance. Unfortunately, it is difficult to use albedo data to help on this, because there is no albedo contrast with the background.

7.4 Age Estimation

7.4.1 Yarkovsky Calibrations

The method we use to convert the inverse slopes from the V-shape fit into family ages has been established in 6.4.2, and consists in finding a *Yarkovsky calibration*, which is the value of the Yarkovsky driven secular drift da/dt for an hypothetical family member of size $D = 1$ km and with spin axis obliquity (with respect to the normal to the orbital plane) 0° for the OUT side and 180° for the IN side. Since the inverse slope is the change $\Delta(a)$ accumulated over the family age by a family member with unit $1/D$, the age is just $\Delta(t) = \Delta(a)/(da/dt)$.

[5]E.g., (2076) has WISE data $p_v = 0.56 \pm 0.32$.

The question is how to produce the Yarkovsky calibration. As discussed in 6.4.2, this can be done in different ways depending upon which data are available. Unfortunately for main belt asteroids there are too few data to compute any calibration: indeed, a measured da/dt is available for not even one main belt object. The solution we have used was to extrapolate from the data available for Near Earth Asteroids. The best estimate available for da/dt is the one of asteroid (101955) Bennu, with a $S/N \simeq 200$ [Chesley et al., 2014]. By suitable modeling of the Yarkovsky effect, by using the available thermal properties measurements, the density of Bennu has been estimated as $\rho_{Bennu} = 1.26 \pm 0.07$ g/cm^3. Bennu is a B-type asteroid, thus it is possible to compute its porosity by comparison with the very large asteroid (704) Interamnia which is of the same taxonomic type and has a reasonably well determined bulk density [Carry, 2012].

Table 7.7: Benchmark asteroids for the density of a taxonomic type: number/name, taxonomic type, densities as in [Carry, 2012] with their uncertainties, densities at 1 km.

number/ name	tax type	ρ	$STD(\rho)$	ρ (1 km)
4 Vesta	V	3.58	0.15	2.30
10 Hygiea	C	2.19	0.42	1.41
15 Eunomia	S	3.54	0.20	2.275
216 Kleopatra	Xe	4.27	0.15	2.75
704 Interamnia	B	1.96	0.28	1.26

In Table 7.7 we list the data on benchmark large asteroids with known taxonomy and density. For the other taxonomic classes we estimate the density at $D = 1$ km by assuming the same porosity of Bennu and the same composition as the largest asteroid of the same taxonomic class. Thus in the Table the density at $D = 1$ km for B class is the one of Bennu from [Chesley et al., 2014], the ones for the other classes are obtained by scaling.

Once an estimate of the density ρ is available, the scaling formula can be written as:

$$\frac{da}{dt} = \left.\frac{da}{dt}\right|_{Bennu} \frac{\sqrt{a}_{(Bennu)}(1-e^2_{Bennu})}{\sqrt{a}(1-e^2)} \frac{D_{Bennu}}{D} \frac{\rho_{Bennu}}{\rho} \frac{\cos(\phi)}{\cos(\phi_{Bennu})} \frac{1-A}{1-A_{Bennu}}$$

where $D = 1$ km used in this scaling formula is not the diameter of an actual asteroid, but it is the reference value corresponding to the inverse slope; we also assume $\cos(\phi) = \pm 1$, depending upon the IN/OUT side.

The additional terms which we would like to have in the scaling formula are thermal properties, such as thermal inertia or thermal conductivity: the

problem is that these data are not available. To replace the missing thermal parameters with another scaling law would not give a reliable result, also because of the strong nonlinearity of the Yarkovsky effect as a function of the conductivity, as shown in [Vokrouhlický et al., 2000b][Figure 1].

We are not claiming this is the best possible calibration for each family. However, for generating a homogeneous set of family ages, we have to use a uniform method for all. To improve the calibration (thus to decrease the uncertainty of the age estimate) for a specific family is certainly possible, but requires a dedicated effort in both acquiring observational data and modeling. E.g., the Yarkovsky effect could be measured from the orbit determination for a family member (going to be possible with data from the astrometric mission GAIA), thermal properties could be directly measured with powerful infrared telescopes, densities can be derived for binaries by using radar observations, for the cases with missing taxonomy it could be obtained by spectrometry/infrared/polarimetry. A good example is given by a very recent event: on January 26, 2015 the asteroid (357439) 2004 BL_{86} had a very close approach to the Earth, with minimum distance 0.008 au. Thus it has been possible by radar to confirm that it has a satellite, and to measure its diameter; infrared observations allowed to assign this asteroid to the taxonomic class V. When all the data are analyzed and published, we expect to have for (357439) an estimated density (from the satellite orbit and the volume, both from the radar data). This could provide a Yarkovsky calibration, specifically for the Vesta families, significantly better than the one of this paper.

This implies that the main results of this paper are the inverse slopes, from which the ages can continue to be improved as better calibration data become available.

In Table 7.8 we are summarizing the data used to compute the calibration. The eccentricity used in the calibration is selected, separately for the IN and OUT side, as an approximate average of the values of proper eccentricity for the family members with proper semimajor axis close to the limit. It is clear that the extrapolation from Near Earth to main belt asteroids introduces a model uncertainty, which is not the same in all cases. If a family has a well determined taxonomic type, which corresponds to one of the benchmark asteroids, our computation of the calibration is based on actual data and we assign to this case a comparatively low relative calibration STD of 0.2; these cases are labeled with the code "m". We have also estimated the Bond albedo A, which is used in the scaling, from the mean geometric albedo p_v by WISE. For subfamilies 3395 (inside 847) and 15124 (inside 569) we have assumed the same taxonomy as the larger family.

Then there are cases in which the taxonomic class is similar, but not

Table 7.8: Data for the Yarkovsky calibration: family number and name, proper semimajor axis a and eccentricity e for the inner and the outer side, 1-A, density value ρ at 1 km, taxonomic type, a flag with values m (measured) a (assumed) g (guessed), and the relative standard deviation of the calibration.

number/ name	proper a IN	proper e IN	proper a OUT	proper e OUT	1-A	ρ (1 km)	tax. type	flag m	rel. STD
158 Koronis	2.83	0.044	2.93	0.06	0.92	2.275	S	m	0.20
24 Themis	3.085	0.14	3.23	0.135	0.98	1.41	C	m	0.20
847 Agnia	2.73	0.07	2.81	0.07	0.92	2.275	S	m	0.20
3395 Jitka	2.762	0.07	2.81	0.07	0.92	2.275	S	m	0.20
1726 Hoffmeister	2.76	0.05	2.8	0.046	0.98	1.41	C	a	0.25
668 Dora	2.76	0.19	2.8	0.197	0.98	1.41	C	a	0.25
434 Hungaria	1.92	0.07	1.97	0.07	0.87	2.75	Xe	g	0.30
480 Hansa	2.55	0.04	2.69	0.035	0.91	2.45	S	m	0.20
808 Merxia	2.71	0.135	2.78	0.13	0.92	2.45	S	m	0.20
3330 Gantrisch	3.13	0.195	3.16	0.198	0.98	1.41	C	g	0.30
10955 Harig &	2.67	0.016			0.92	2.275	S	g	0.30
19466 Darcydiegel			2.77	0.009	0.92	2.275	S	g	0.30
1521 Seinajoki	2.84	0.12	2.866	0.123	0.94	2.275	S	g	0.30
569 Misa	2.63	0.177	2.69	0.175	0.98	1.41	C	a	0.25
15124 $2000EZ_{39}$	2.64	0.178	2.67	0.177	0.98	1.41	C	a	0.25
1128 Astrid	2.767	0.048	2.81	0.048	0.98	1.41	C	m	0.20
845 Naema	2.92	0.035	2.95	0.036	0.98	1.41	C	m	0.20
4 Vesta	2.27	0.09	2.44	0.11	0.88	2.3	V	m	0.20
15 Eunomia	2.53	0.15	2.69	0.15	0.92	2.275	S	m	0.20
20 Massalia	2.35	0.162	2.46	0.162	0.92	2.275	S	m	0.20
10 Hygiea	3.08	0.13	3.24	0.11	0.98	1.41	C	m	0.20
31 Euphrosyne	3.11	0.17	3.2	0.21	0.98	1.41	C	m	0.20
3 Juno	2.62	0.235	2.69	0.235	0.92	2.275	S	m	0.20
163 Erigone &	2.34	0.208			0.98	1.41	C	m	0.20
5026 Martes			2.37	0.207	0.98	1.41	C	m	0.20
3815 König	2.57	0.13	2.58	0.14	0.98	1.41	C	a	0.25
396 Aeolia	2.735	0.168	2.743	0.167	0.97	2.75	Xe	a	0.25
606 Brangane	2.579	0.18	2.59	0.18	0.96	2.275	S	m	0.20
1547 Nele	2.64	0.269	2.646	0.269	0.88	2.275	S	g	0.30
18405 $1993FY_{12}$	2.83	0.106	2.86	0.106	0.94	2.275	S	g	0.30
170 Maria			2.65	0.08	0.91	2.275	S	m	0.20
1272 Gefion	2.74	0.13			0.92	2.275	S	a	0.25
2076 Levin			2.31	0.14	0.93	2.275	S	g	0.30
3827 Zdenekhorsky	2.71	0.087			0.98	1.41	C	m	0.20
1658 Innes			2.61	0.17	0.91	2.275	S	g	0.30
375 Ursula	3.13	0.08			0.98	1.41	C	m	0.20

identical to the one of the benchmark. (1726) is of type Cb, (668) of type Ch in the SMASSII classification, both assimilated to a generic C type; (808) is Sq, (1272) is SI in SMASSII, (1658) is AS in the Tholen classification, all assimilated to a generic S type. These are labeled with the code "a" and we have assigned a relative STD of 0.25.

Finally we have 7 cases in which we do not have taxonomic data at all, but just used the mean WISE albedo of Table 7.2 to guess a simplistic classification into a C vs. S complex. These are labeled "g" and have a relative STD of 0.3. Thus these are the worst cases from the point of view of age uncertainty, but they are the easiest to improve by observations.

7.4.2 Ages and their Uncertainties

The results on the ages are presented in Tables 7.9–7.12, each containing the Yarkovsky calibration, computed with the data of Table 7.8, the estimated age and three measures of the age uncertainty.

The first uncertainty is the standard deviation of the inverse slope, as output from the least square fit, divided by the calibration. The second is the age uncertainty due to the calibration uncertainty from the last column of Table 7.8: this relative uncertainty is multiplied by the estimated age. The third is the standard deviation of the age, obtained by combining quadratically the STD from the fit with the STD from the calibration.

The first uncertainty is useful when comparing ages which can use the same calibration, such as ages from the IN and from the OUT side (as shown in the last two columns of Tables 7.3–7.6); this can be applied also to the cases of subfamilies. The third uncertainty is applicable whenever the absolute age has to be used, as in the case in which the ages of two different families, with independent calibration errors, are to be compared.

Among the figures, not included in this paper but available in the Supplementary material site, there are all the V-shape plots, which can be useful to better appreciate the robustness of our conclusions.

In this Section we also comment on ages for the same families found in the scientific literature, with the warning that for some families there are multiple estimates, including discordant ones, in some cases published by the same authors at different times. Thus we think it is important to have a source of ages computed with a uniform and well documented procedure, such as this paper. Compilations of ages, such as [Brož et al., 2013b; Nesvorný et al., 2005], are useful for consultation, but have the limitation of mixing results obtained with very different methods, sometimes even with methods not specified. We use the terminology *consistent* when one nominal value is within the STD of the other, *compatible* when difference of nominal values is

Table 7.9: Age estimation for the fragmentation families: family number and name, da/dt, age estimation, uncertainty of the age due to the fit, uncertainty of the age due to the calibration, and total uncertainty of the age estimation.

number/ name	side IN/OUT	da/dt 10^{-4} au/My	Age My	STD(fit) My	STD(cal) My	STD(age) My
158 Koronis	IN	-3.40	1792	262	358	444
	OUT	3.34	1708	206	342	399
24 Themis	IN	-5.68	2447	678	489	836
	OUT	5.54	3782	588	756	958
847 Agnia	IN	-3.46	1003	207	201	288
	OUT	3.41	669	100	134	167
3395 Jitka	IN	-3.44	136	25	27	37
	OUT	3.41	138	24	28	37
1726 Hoffmeister	IN	-5.90	337	47	84	96
	OUT	5.86	328	42	82	92
668 Dora	IN	-6.11	532	87	133	159
	OUT	6.08	471	141	118	184
434 Hungaria	IN	-3.23	208	19	62	65
	OUT	3.18	205	8	62	62
480 Hansa	IN	-3.53	763	310	153	346
	OUT	3.44	950	117	190	223
808 Merxia	IN	-3.52	338	28	68	73
	OUT	3.47	321	24	64	69
3330 Gantrisch	IN	-5.75	436	105	131	168
	OUT	5.73	492	131	148	197
10955 Harig &	IN	-3.48	441	78	132	154
19466 Darcydiegel	OUT	3.42	500	146	150	209
1521 Seinajoki	IN	-3.50	338	66	101	121
	OUT	3.49	122	15	37	40
569 Misa	IN	-6.23	319	242	80	255
	OUT	6.15	249	85	62	105
15124 $2000EZ_{39}$	IN	-6.22	111	10	28	29
	OUT	6.18	113	11	28	30
1128 Astrid	IN	-5.89	150	11	30	32
	OUT	5.85	150	11	30	32
845 Naema	IN	-5.73	149	19	30	35
	OUT	5.70	163	8	33	34

less than the sum of the two STD, *discordant* otherwise.

Ages of fragmentation families

The ages results are in Table 7.9; comments on specific families follow.

158 (Koronis): the present estimate increases somewhat the result we reported in Chap. 6[Table 10] of 1500 My for the OUT side (the result for

the IN side was considered of lower quality), but within the fit uncertainty. Now the results from the two sides are not just consistent but very close, and the fit uncertainty has slightly improved (in Table 10 of the previous paper the calibration uncertainty was not included). The earliest estimates in the literature were just upper bounds of ≤ 2 Gy [Chapman et al., 1996; Marzari et al., 1995], followed by [Farinella et al., 1996; Greenberg et al., 1996] who give ~ 2 Gy; Brož et al. [2013b] give 2.5 ± 1 Gy, which is consistent with our results: our improvement in accuracy is significant.

24 (Themis): the two sides give different values which are not discordant, but are affected by large uncertainties. This is one of the oldest families, for which there are few ages estimates in the literature: [Marzari et al., 1995] give 2 Gy.

847 (Agnia): the new result is consistent with the one of Chap. 6[Table 10] for the IN side; the OUT side is anyway degraded by the presence of the 3395 subfamily.

3395 (Jitka): the results are almost the same as in 6[Table 10]. In the literature there are estimates for the age of Agnia, in [Vokrouhlický et al., 2006a] of 100^{+30}_{-20} My, but from their Figure 1 it is clear that their Agnia family is restricted to our Jitka subfamily, apart from the addition of (847) Agnia itself. Also in [Brož et al., 2013b] there is an estimate for 847 of 200 ± 100 My. Thus our results on the age are consistent with all the others, even if we disagree on the name of the family.

1726 (Hoffmeister): our result is consistent with the one in [Brož et al., 2013b; Nesvorný et al., 2005], giving 300 ± 200 My, but with significantly lower uncertainty. The fact that the perturbations from (1) Ceres do not appear to disturb an evolution model based on the Yarkovsky secular drift is a confirmation of the statement by Delisle and Laskar [2012]: chaotic perturbations from other asteroids are less effective in shifting the semimajor axis than Yarkovsky for the objects with $D < 40$ km.

668 (Dora): the OUT result is somewhat degraded by the 5/2 resonance, thus the IN is better, but anyway they are consistent. [Brož et al., 2013b] give 500 ± 200 My, in good agreement, notwithstanding the much lower distance cutoff used to define the family (60 m/s vs. our 90).

434 (Hungaria): with a similar but less rigorous method, Milani et al. [2010] find 274 My, which is higher but practically consistent with the current result. Warner et al. [2009] give ~ 500 My, but with a low accuracy method.

480 (Hansa): in the literature we find only [Brož et al., 2013b; Carruba, 2010] giving as upper bound < 1.6 Gy. Our result is much more informative, especially from the OUT side.

808 (Merxia): our results are consistent with both [Brož et al., 2013b] 300 ± 200 My, and [Nesvorný et al., 2005] 500 ± 200, but significantly more

precise.

3330 (Gantrisch): we have found nothing in the literature on the age of this family, thus the result is useful even if the relative accuracy is poor.

10955 (Harig), including 19466: a well determined slope, consistent between the two sides, thus confirming the join. The absolute age is of limited accuracy because of the lack of physical observations. No previous estimates found in the literature.

1521 (Seinajoki) has two significantly different ages, younger for the OUT side. This is an additional case of a dynamical family containing two collisional families. [Nesvorný et al., 2005] gives 50 ± 40 My, which is compatible with our estimate for the OUT side.

1128 (Astrid) has a perfect agreement on the two sides, which appears as a coincidence since the uncertainty is much higher. Nesvorný et al. [2005] give 100 ± 50 which is consistent, our estimate being more precise.

845 (Naema) has a good agreement on the two sides. Nesvorný et al. [2005] give 100 ± 50 which is compatible, our estimate being more precise.

Ages of cratering families

The ages results are in Table 7.10; comments on each family follow.

Table 7.10: Age estimation for the cratering families. Columns as in Table 7.9.

number/ name	side IN/OUT	da/dt 10^{-4} au/My	Age My	STD(fit) My	STD(cal) My	STD(age) My
4 Vesta	IN	-3.60	930	112	186	217
	OUT	3.49	1906	537	381	659
15 Eunomia	IN	-3.66	1955	155	391	421
	OUT	3.55	1144	57	229	236
20 Massalia	IN	-3.81	174	7	35	35
	OUT	3.73	189	16	38	41
10 Hygiea	IN	-5.67	1330	139	266	300
	OUT	5.50	1368	183	274	329
31 Euphrosyne	IN	-5.71	1309	169	262	312
	OUT	5.72	1160	142	232	272
3 Juno	IN	-3.46	550	110	110	156
	OUT	3.41	370	143	74	161
163 Erigone &	IN	-6.68	212	53	42	68
5026 Martes	OUT	6.64	230	46	19	50

4 (Vesta): the idea that Vesta might have suffered two large impacts generating two families Sec. 6.6 is quite natural given that cratering does not decrease the collisional cross section, and has been proposed long ago

[Farinella et al., 1996]. The new error model and outlier rejection procedure have reduced the fit uncertainty, especially for the OUT side, thus the ratio of values on the two sides has increased its level of significance (see Table 7.4). The good agreement of the age from the IN side with the cratering age of the Rheasilvia basin, 1 Gy according to Marchi et al. [2012] is very interesting. Only a rough lower bound age of ~ 2 Gy is available for the Veneneia basin because of the disruption due to the impact forming Rheasilvia [O'Brien et al., 2014]. Thus our age estimate from the OUT side is an independent constraint to the age of Veneneia.

15 (Eunomia): in Chap. 6[Table 10] the difference in the slopes for the two sides was much smaller and the fit uncertainty for the OUT side much larger, thus the existence of two separate ages was proposed as possible. The improved results provide a ratio very significantly different from 1, thus the existence of two collisional families inside the single dynamical family 15 is now supported by high S/N evidence. Nesvorný et al. [2005] give 2.5 ± 0.5 Gy as age for the entire family, which is compatible with our IN side age.

20 (Massalia): our new results are very similar to the ones of our previous paper as well as consistent with [Vokrouhlický et al., 2006b], giving as most likely an age between 150 and 200 My. On the contrary [Nesvorný et al., 2003] give 300 ± 100 which is marginally compatible.

10 (Hygiea): the interesting point is that this dynamical family appears to have a single age, a non-trivial result since the family has a bimodal shape in the proper (a, e) projection, and (10) has almost the same impact cross section as (4) Vesta. In the literature we found only [Nesvorný et al., 2005] giving a consistent, but low accuracy, 2 ± 1 Gy.

31 (Euphrosine): This high proper $\sin I$ family is crossed by many resonances, nevertheless the age can be estimated. In the literature, we found only the upper bound < 1.5 Gy in [Brož et al., 2013b].

3 (Juno): the two ages IN and OUT are not consistent but only compatible; more data are needed to assess the possibility of multiple collisions. In the literature we found only an upper bound < 700 My in [Brož et al., 2013b].

163 (Erigone): another very good example of join of two dynamical families, 163 and 5026, into a collisional family with all the properties expected, including age estimates consistent (within half of STD) and a lower number density in a central strip. [Vokrouhlický et al., 2006b] give an age of 280 ± 112 My, which is higher but consistent; [Bottke et al., 2015] by a different method give an age 170^{+25}_{-30}, which is lower but consistent with the IN side. From the figures we can deduce that in both papers their family 163 also includes our 5026.

Table 7.11: Age estimation for the young families. Columns as in Table 7.9.

number/ name	side IN/OUT	da/dt 10^{-4} au/My	Age My	STD(fit) My	STD(cal) My	STD(age) My
3815 König	IN	-6.21	51	6	13	14
	OUT	6.21	51	6	13	14
396 Aeolia	IN	-3.09	100	18	25	31
	OUT	3.08	91	15	23	27
606 Brangane	IN	-3.82	48	4	10	10
	OUT	3.81	44	7	9	11
1547 Nele	IN	-3.61	14	2	4	5
	OUT	3.61	15	5	5	7
18405 1993FY$_{12}$	IN	-3.50	83	28	25	37
	OUT	3.48	83	13	25	28

Ages of young families

The ages results are in Table 7.11. We are interested in finding a lower limit for the ages we can compute with the V-shape method. For most of these asteroids there are in the literature only either upper bounds or low relative accuracy estimates of the ages [Brož et al., 2013b]. In order of estimated age:

1547 (Nele): for this family Brož et al. [2013b] give an age < 40 My; Nesvorný et al. [2003] give a constraint ≤ 5 My on the age of the Iannini cluster, which he identified as composed of 18 members not including (1547). Our estimate (for a family with $152 - 3 = 149$ members, including (4652) Iannini) is higher, but such a young age could be too much affected by the effect of the initial velocity field, which is apparent in the anti-correlation between proper a, e. From this example we conclude that probably 15 My is too young to be an accurate estimate by the V-shape method; this family should be dated by a method using also the evolution of the angles ϖ, Ω.

3815 (König): we have a precise estimate, in the literature we have found only an upper bound < 100 My [Brož et al., 2013b].

606 (Brangane): also a precise estimate, in good agreement with 50 ± 40 in [Brož et al., 2013b]. We do not have a ground truth to assess the systematic error due to contamination from the initial velocity spread, which for these ages may not be negligible[6].

396 (Aeolia): also a precise estimate, consistent with the upper bound < 100 My in [Brož et al., 2013b]. 18405 (1993FY$_{12}$): Brož et al. [2013b] give an age < 200 My. Our estimate is precise and not just consistent, but the same on the two sides. For this range of ages around 100 My the initial

[6]A size independent velocity spread is removed by our fit method, but there may well be a $1/D$ dependency in this spread.

velocity field should not matter.

From these examples we can conclude that the V-shape method is applicable to *young* families with ages below 100 My, but there is some lower age limit t_{min} such that younger ages are inaccurately estimated from the V-shape. The cases we have analyzed suggest that $t_{min} > 15$ My, but we do not have enough information to set an upper bound for t_{min}.

Ages of one-sided families

The ages results are in Table 7.12; these ages are based upon the assumption that only one side of the family V-shape is preserved. Of course if this was not the case, ages younger by factor roughly 2 would be obtained. For each case, comments on the justification of the one-side assumption are given below.

Table 7.12: Age estimation for the one-sided families. Columns as in Table 7.9.

number/ name	side IN/OUT	da/dt 10^{-4} au/My	Age My	STD(fit) My	STD(cal) My	STD(age) My
170 Maria	OUT	3.48	1932	169	386	422
1272 Gefion	IN	-3.50	1103	270	276	386
2076 Levin	OUT	3.86	366	59	110	125
3827 Zdenekhorsky	IN	-5.99	154	14	31	34
1658 Innes	OUT	3.59	464	31	139	143
375 Ursula	IN	-5.56	3483	765	697	1035

170 (Maria): the very strong 3/1 resonance with Jupiter makes it impossible for asteroids of the IN side of the family to have survived in the main belt, moreover the shape of the family in the $(a, 1/D)$ plane is unequivocally one sided. This is an ancient family, and our age estimate is compatible with 3 ± 1 Gy given in [Nesvorný et al., 2005], but we have significantly decreased the estimate, to the point that this cannot be a "LHB" family, as suggested by [Brož et al., 2013b].

1272 (Gefion): the very strong 5/2 resonance with Jupiter makes it impossible for most asteroids of the OUT side of the family to have survived in the main belt. Thus there is no OUT side in the V-shape[7]. Nesvorný et al. [2005] give an age 1.2 ± 0.4 Gy, in good agreement with ours, while [Nesvorný et al., 2009][Figure 1] show a one-sided model, giving a discordant age of 480 ± 50 My.

2076 (Levin): as discussed in Section 7.3, this could be just a component of a complex family, possibly including 298 and 883. The OUT slope, thus

[7]See the figure 1272_vshapea.eps in the Supplementary material.

the age we have estimated, refers to the event generating 2076, while 298 and 883 have too few members for a reliable age. In the literature there are ages for the family of (298) Baptistina: e.g., Bottke et al. [2007] give a discordant age of 160^{+30}_{-20} My, but they refer to a two-sided V-shape including our 883, with an enormous number of outliers.

3827 (Zdenekhorsky): the family shape is obviously asymmetric, with much fewer members on the OUT side[8]. This prevents a statistically significant determination of the OUT slope. The family is not abruptly truncated, possibly because the effect of (1) Ceres is weaker than the one of the main resonances with Jupiter.

1658 (Innes): the shape of the family in the $(a, 1/D)$ plane is clearly one-sided. The family ends on the IN side a bit too far from the 3/1 resonance, thus the dynamics of the depletion on the IN side remains to be investigated.

375 (Ursula): the strongest 1/2 resonance with Jupiter makes it impossible for most asteroids of the OUT side of the family to have survived in the main belt. This prevents a statistically significant determination of the OUT slope. With an age estimated at $\sim 3.5 \pm 1$ Gy, this family could be the oldest for which we have an age. Brož et al. [2013b] give the upper bound < 3.5 Gy.

7.5 Conclusions and future work

In this paper we have computed the ages of 37 collisional families[9]. The members of these collisional families belong to 34 dynamical families, including 30 of those with > 250 members. Moreover, we have computed uncertainties based on a well defined error model: the standard deviations for the ages are quite large in many cases, but still the signal to noise ratio is significantly > 1.

7.5.1 Main results

In Figure 7.5 we have placed the families on the horizontal axis with the same order used in the Tables, separated in four categories[10].

On the vertical axis (in a logarithmic scale) we have marked the estimated age with a 1 STD error bar. To avoid overcrowding of the Figure, for the

[8] See the figure 3827_vshapea.eps in the supplementary material.

[9] Plus one possible, a second age for the family 3 (Juno) with a moderate significance in the slope ratio, see Table 7.4.

[10] To locate these families in the asteroid belt, the best way is to use the graphic visualizer of asteroid families provided by the AstDyS site at http://hamilton.dm.unipi.it/astdys2/Plot/

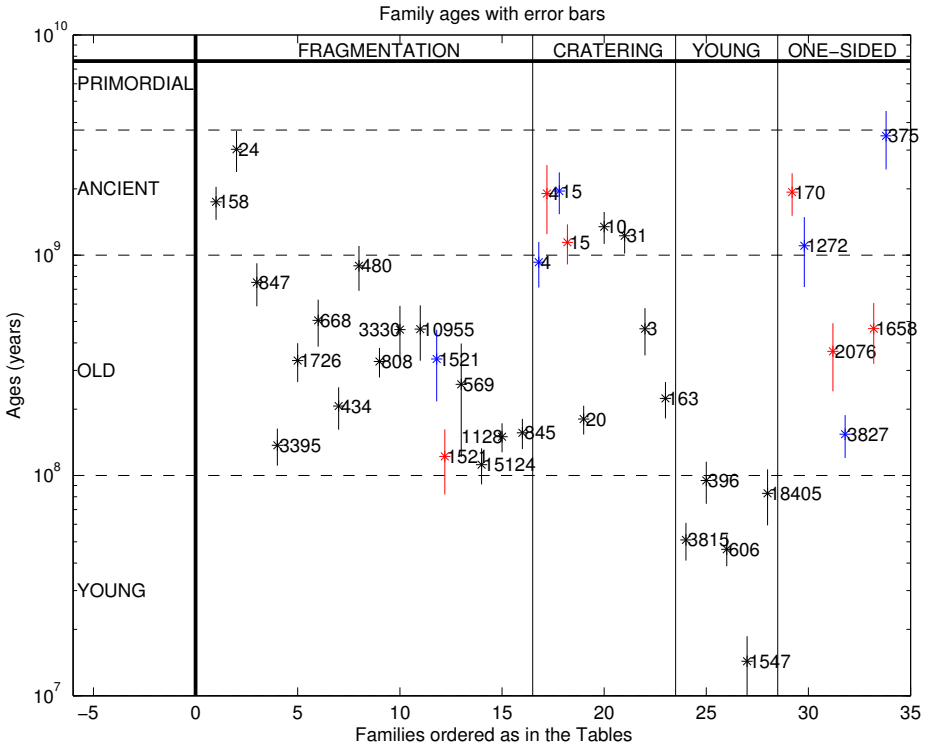

Figure 7.5: Family ages and their uncertainties computed in this paper. If two ages of the same family are incompatible, the figure shows both ages; this applies to families 4, 15, 1521. The horizontal dashed lines separate the conventional age groupings, the vertical solid lines separate the family types, for the definitions see in the text.

families with compatible ages from the IN and OUT side we have used the average (weighted with the inverse square of the STD) as the nominal with an error bar $\sigma = \sqrt{\sigma_{IN}^2 + \sigma_{OUT}^2}/2$. If the two ages are incompatible we have plotted the two estimates with the corresponding bars[11]. We have also used an informal terminology by which families are rated by their age: *primordial* with age > 3.7 Gy, *ancient* with age between 1 and 3.7 Gy, *old* with age between 0.1 and 1 Gy, and finally the adjective *young*, as used previously, is for ages < 0.1 Gy.

By looking at Figure 7.5 it is apparent that we have been quite successful in computing ages for old families, we have significant results for both young and ancient, while we have little, if any, evidence for primordial families. This should not be rated as a surprise: already Brož et al. [2013b], while specifically searching for primordial families, found a very short list of can-

[11]For 847 we have used the IN age and STD, as discussed in Section 7.3.

didates, out of which 4, 10, 15, 158 and 170 we are showing to be ancient, but not primordial. From our results, only two families could be primordial, 24 and 375, although they are more likely to be just ancient. Thus we agree with the conclusion by Vokrouhlický et al. [2010] that most of the primordial families, which undoubtedly have existed, have been depleted of members to the point of not being recognized by statistically significant number density contrast: our results indicate that this conclusion applies not only to the Cybele region (beyond the 2/1 resonance) but to the entire main belt.

Figure 7.5 also shows that our results allow many statistically significant absolute age comparisons between different families. Although the results should be improved, especially by obtaining more accurate Yarkovsky calibrations, this can be the beginning of a real asteroid belt chronology. The large compilations of family ages, such as Brož et al. [2013b]; Nesvorný et al. [2005] are very useful to confirm that our results are reasonable. When available, the uncertainties reported in these compilations are generally larger; often only upper/lower bounds are given. However, the literature as analyzed in Section 7.4.2 shows that often results obtained with different methods, even by the same authors, can be discordant. Thus the comparison of ages for different families should not be done with the ages listed in a compilation, but only from a list of ages computed with a single consistent method, including a single consistent calibration scheme, as in this paper.

In Chap. 7 we have introduced the distinction between dynamical and collisional families; out of the 5 dynamical families we analyzed as examples, we found 3 cases in which a dynamical family corresponds to at least 2 collisional ones. In this paper we report on the results of a systematic survey of the largest (by number of members) dynamical families, monitoring whether the 1 to 1 correspondence with collisional families does or does not apply.

We have found two examples, for which we use the definition of *family join*, in which two separate dynamical families together form a single V-shape, with consistent slopes, thus indicating a single collisional event: this applies to families 10955 and 19466, 163 and 5026. Note that this is distinct from a *family merge* which can arise when two families, as a result of adding new members with recently computed proper elements, acquire some members in common [Knežević et al., 2014].

We have also found at least three examples of dynamical families containing multiple collisional families: 4, 15 and 1521. For these we have obtained discordant slopes from the IN and the OUT side of the V-shape, resulting in distinct ages, see Figure 7.5. We have found a dubious case, family 3, and there are several other cases already either known or suspected.

Finally, we have found two cases of families containing a conspicuous subfamily, with a sharp number density contrast, such that it is possible to

measure the slope of a distinct V-shape for the subfamily, thus the age of the secondary collision: the subfamily 3395 of 847, and 15124 of 569. There are several cases of subfamilies, with a separate collisional age, already reported in the literature, but they are mostly from recent (< 10 My of age) collisions: we have identified subfamilies with ages of ~ 100 My.

From the above discussion, we think a new paradigm emerges: whenever a family age computation is performed, the question on the minimum number of collisional events capable of generating the observed distribution of members of the family in the classification space has to be analyzed. This needs to take also into account other families in the neighborhood (in the classification space). In our case, the classification space is the 3-dimensional proper elements space because we use dynamical families, but note that the same argument applies also to other classifications made in different spaces, such as the ones containing also physical observations data: separate collisional families may well have the same composition.

7.5.2 Open problems

On other issues we have accumulated data, useful to constrain the asteroid families evolution, but we do not have a full model.

An example is the fact already known that many families have a central gap, in the sense of a bimodal number frequency distribution of members as a function of proper a. The interpretation of this gap as a consequence of the interaction between the YORP and the Yarkovsky effect, as proposed in [Vokrouhlický et al., 2006b], is plausible and widely accepted, but a model capable of predicting the timescales of this evolution is not available.

We have observed the presence and depth of the gap for all the families having, in our best estimate, < 600 My.

- Ages between 10 and 100 My: the gap does not occur in the youngest 1547 and the one near the upper limit of 100 My, that is 396, but occurs in 18405 which has an age similar to 396, and in the two with ages ~ 50 My, 3815 and 606.

- Ages between 100 and 200 My: the gap occurs consistently in families such as 3395, 15124, 1128, 845, and less deep in 20.

- Ages between 200 and 400 My: there are three families with gap (434, 808, 163) and two without (1726, 3).

- Ages between 400 and 600 My: 10955 has a gap and 668 does not.

- Ages > 600 My: among the ancient families only 158 and maybe 31 show some small dip in density at the center.

These results do not contradict the interpretation that YORP moves the rotation axes towards the spin up/spin down position, but takes quite some time to achieve a strong bimodality which gradually empties the gap. Over longer time scales, spin axis randomization can reverse the process. However, our set of examples above shows that the time scales for such processes are not uniform, but may substantially change from family to family.

Another open problem results from the fact that several families on the outer edge of the 3/1 resonance gap appear to have a boundary close to, but not at the Kirkwood gap. This happens to the IN side of families 480 and 15; there are also families 170 and 1658 which are one-sided because of the missing IN side, with the family not touching the gap. This might require a dedicated study to find a plausible explanation.

7.5.3 Family ages left to be computed

Of the dynamical families in the current classification, there are 11 with > 300 members for which we have not yet computed a satisfactory age. The motivations are as follows.

- There are five complex families: 135, known to have at least two collisional families, with incompatible physical properties, difficult to disentangle; see e.g., 6.10; 221, complex both for dynamical evolution [Vokrouhlický et al., 2006c] and suspect of multiple collisions; 145, which appears to have at least 2 ages; 25, corresponding to a stable region surrounded by secular resonances, could have many collisional families; 179, a cratering family which is difficult to be interpreted.

- There are another four families strongly affected in their shape in proper element space by resonances: 5, 110, 283 with secular resonances, and 1911 inside the 3/2 resonance.

- Two others: 490, well known to be of recent age [Nesvorný et al., 2003; Tsiganis et al., 2007]; 1040, at large proper $\sin I$ and also quite large e; both are strongly affected by 3-body resonances.

We are convinced that for many of these it will be possible to estimate the age, but this might require ad hoc methods, different from case to case. In this paper we have included all the ages which we have up to now been able to estimate by a uniform method.

Other families with marginal number of members for the V-shape fit (between 100 and 300 in the current classification) could become suitable as new proper elements are computed and the classification is automatically updated, especially in the zones where the number density is low, such as the high I region, and the Cybele region, beyond the 2/1 resonance.

Chapter 8

Shadowing Lemma and chaotic orbit determination

Chaotic dynamical systems are characterized by the existence of a predictability horizon in time, beyond which the information on the state available from the initial conditions is not enough for meaningful predictions. Thus it appears a difficult task to perform an orbit determination for a chaotic dynamical system, at least when the observations are spread over a timespan longer than the predictability horizon.

Nevertheless there are practical problems of orbit determination in which the system is chaotic and the time-span of the observations is very long. It is important to understand the behaviour of the solutions, with their estimated uncertainties, in particular when the variables to be solved for include not just the initial conditions but also some dynamical parameters. If the number of available observations grows, but simultaneously the time interval over which they are spread grows up to values comparable to the predictability horizon, does the solution become more accurate, and is the iterative procedure of differential corrections [Milani and Gronchi, 2010, Chap. 5] to find the least squares solution still possible?

In this paper we use a model problem, namely the discrete dynamical system defined by the standard map of the pendulum, with just one dynamical parameter, the μ coefficient appearing in equation (8.1). We also set up an observation process in which both coordinates of the standard map are observed after each iteration. In the observations we include a simulated random noise with a normal distribution. Then, each experiment of orbit determination is also a concrete computation of a segment limited to n iterations (of the map and of its inverse) of a ε shadowing orbit for the δ pseudo trajectory defined by the observation process. The Shadowing Lemma (see Section 8.2) provides a mathematically rigorous result on the availability of

shadowing orbits, but thanks to the orbit determination process we make explicit the relationship between ε and δ (see Section 8.2.1), and we explicitly compute the ε-shadowing orbit.

At the same time, each experiment provides an estimate of the standard deviation of each of the variables, including initial conditions and the parameter. These estimates can be plotted as a function of n, thus showing the relationship between accuracy, number of observations and time interval, measured in Lyapounov times (see Section 8.3).

Of course the numerical experiments are limited to a finite number of iterations, while the Shadowing Lemma refers to an infinite orbit. However, the maximum number of iterations is controlled by another time limit, the computability horizon due to round off error. This limit can be estimated approximately by a simple formula, and it is found in numerical experiments as a function of both the initial conditions and the numeric precision used in the computations.

Wisdom hypothesis

In 1987 J. Wisdom was discussing the chaotic rotation state of Hyperion, when he claimed that numerical experiments indicated that *the knowledge gained from measurements on a chaotic dynamical system grows exponentially with the timespan covered by the observations* Wisdom [1987]. This pertained in particular the information on dynamical parameters like the moments of inertia ratios for Hyperion, as well as the rotation state at the midpoint of the time interval covered by the observations, which he proposed would be determined with exponentially decreasing uncertainty.

Therefore Wisdom suggests that the orbit determination for a chaotic system might be in fact more effective than for a non-chaotic one. It is clear from the context that he was referring to numerical results, thus his statement can only be verified with finite computations as close as possible to a realistic data processing of observations of a chaotic system with dynamical parameters to be determined.

We have set as a goal in this paper to test the behavior of the uncertainty in the dynamical parameter of our model problem. We shall discuss the implications for Wisdom's claim in Section 8.4.

Application to planet-crossing asteroids

In our solar system there are planet-crossing minor bodies, including asteroids and comets, by definition such that their orbits can, at some times, intersect the orbit of the major planets. In particular many of the Near Earth

Asteroids (NEAs) can intersect the orbit of the Earth. These orbits are necessarily chaotic, at least over the timespan accessible to accurate numerical computations.

Unfortunately, these orbits are especially important and necessary to be studied because of the very reason of chaos, namely close approaches to the major planets including the Earth: these approaches may, in some cases, be actual impacts on a finite size planet.

The attempt to predict possibility of impacts by NEAs, in particular on our planet, is called Impact Monitoring, and it is indeed a form of orbit determination for chaotic orbits. There is a subset of cases of NEAs for which non-gravitational perturbations, such as the ones resulting from the Yarkovsky effect, are not negligible in terms of Impact Monitoring because of the exponential divergence of nearby orbits which amplifies initially very small perturbations (see Farnocchia and Chesley [2014]; Farnocchia et al. [2013a], and Chap. 4 and 5).

Thus the Impact Monitoring for these especially difficult cases is an instance of orbit determination of a chaotic system, with as parameters the 6 initial conditions and at least one dynamical parameter, such as a Yarkovsky effect coefficient to be solved for. We shall show in Section 8.5 that the weak determination of the dynamical parameter is a key feature of these cases.

8.1 Orbit determination for the standard map

The simplest example of a conservative dynamical system which has both chaotic and ordered orbits can be built by means of an area preserving map of a two dimensional manifold:

$$S_\mu(x_k, y_k) = \left\{ \begin{array}{rcl} x_{k+1} & = & x_k + y_{k+1} \\ y_{k+1} & = & y_k - \mu \sin x_k \end{array} \right. \tag{8.1}$$

where μ is the perturbation parameter, and S is the standard map. The system has more regular orbits for small μ, and more chaotic orbits for large μ. We choose an intermediate value of μ, e.g. $\mu = 0.5$, in such a way that ordered and chaotic orbits are both present. Figure 8.1 shows the strongly chaotic region around the hyperbolic fixed point, and a few regular orbits on both sides.

The advantage of such example is that the least square parameter estimation process can be performed by means of an explicit formula.

First we compute the linearized map

$$DS = \begin{pmatrix} \frac{\partial x_{k+1}}{x_k} & \frac{\partial x_{k+1}}{y_k} \\ \frac{\partial y_{k+1}}{x_k} & \frac{\partial y_{k+1}}{y_k} \end{pmatrix} = \begin{pmatrix} 1 - \mu\cos(x_k) & 1 \\ -\mu\cos(x_k) & 1 \end{pmatrix}$$

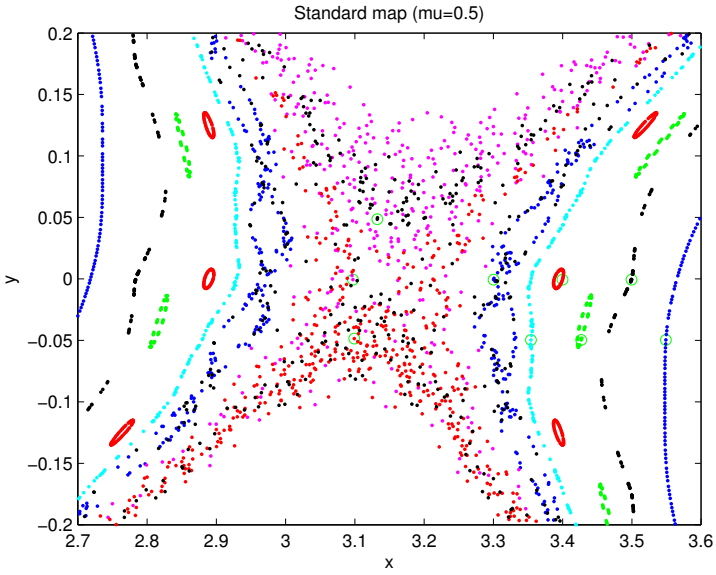

Figure 8.1: Orbits of the standard map for the perturbation parameter $\mu = 0.5$. Plotted is a blow up of the central region around the hyperbolic fixed point, showing the strongly chaotic region and a few regular orbits on both sides.

and from this the linearized state transition matrix

$$A_k = \frac{\partial(x_k,\ y_k)}{\partial(x_0,\ y_0)}$$

which is the solution of the variational equation (for infinitesimal displacement in the initial conditions), and given by the recursion:

$$A_{k+1} = DS\ A_k \quad ; \quad A_0 = I\ .$$

The variational equation for the derivatives with respect to the model parameter μ is:

$$\begin{aligned} \frac{\partial(x_{k+1},\ y_{k+1})}{\partial\mu} &= DS\ \frac{\partial(x_k,\ y_k)}{\partial\mu} + \frac{\partial S_\mu}{\partial\mu} \\ &= DS\ \frac{\partial(x_k,\ y_k)}{\partial\mu} + \begin{pmatrix} -\sin(x_k) \\ -\sin(x_k) \end{pmatrix} \end{aligned}$$

Then we set up an observation process, in which both coordinates x and y are observed at each iteration, and the observations are Gaussian random variables with mean x_k (y_k respectively) and standard deviation σ: we use the notation $x_k(\mu_0, \sigma)$ to indicate that the probability density function of the

observation x_k is the normal $\mathcal{N}(x_k(\mu_0), \sigma^2)$ one, and similarly for y_k. The residuals are:

$$\left\{ \begin{array}{rcl} \xi_k & = & x_k(\mu_0, \sigma) - x_k(\mu_1) \\ \bar{\xi}_k & = & y_k(\mu_0, \sigma) - y_k(\mu_1). \end{array} \right. \tag{8.2}$$

for $k = -n, \ldots, n$. In (8.2) $x_k(\mu_0, \sigma)$ and $y_k(\mu_0, \sigma)$ are the observations at each iteration, μ_0 is the "true" value and $\mu_1 = \mu_0 + d\mu$ is the current guess.

Then the least squares fit is obtained from the normal equations:

$$C = \sum_{k=-n}^{n} B_k^T B_k \quad ; \quad D = -\sum_{k=-n}^{n} B_k^T \begin{pmatrix} \xi_k \\ \bar{\xi}_k \end{pmatrix} \tag{8.3}$$

$$B_k = \frac{\partial(\xi_k, \bar{\xi}_k)}{\partial(x_0, y_0, \mu)} = -\left(A_k | \frac{\partial(x_k, y_k)}{\partial \mu} \right).$$

The least squares solution for both, the parameter μ and the initial conditions, is:

$$\begin{pmatrix} \delta x \\ \delta y \\ \delta \mu \end{pmatrix} = \Gamma D, \quad \Gamma = C^{-1}$$

with Γ the covariance matrix of the result. This is enough to find the least squares solution by iteration of the above differential correction. However, to assess the uncertainty of the result, weights should be assigned to the residuals consistently with the probabilistic model, in this case each residual needs to be divided by its standard deviation σ; then the distribution of the result (x, y, μ) is a normal distribution with covariance matrix $\sigma^2 \Gamma$.

8.2 Shadowing Lemma

The shadowing problem is that of finding a deterministic orbit as close as possible to a given noisy orbit. The so-called Shadowing Lemma is the main result about shadowing near a hyperbolic set of a diffeomorphism. Anosov [1967] and Bowen [1975] proved the existence of arbitrarily long shadowing solutions for invertible hyperbolic maps. Here we give an overview of these classical results, as in Pilyugin [1991].

Let (X, d) be a metric space and let Φ be a homeomorphism mapping X onto itself. A δ-pseudotrajectory of the dynamical system Φ is a sequence of points $\zeta = \{x_k \in X : \ k \in \mathbf{Z}\}$ such that the following inequalities

$$d(\Phi(x_k), x_{k+1}) < \delta. \tag{8.4}$$

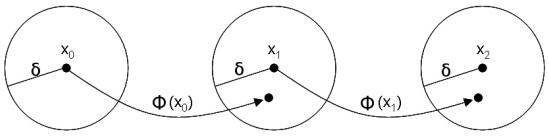

Figure 8.2: A δ-pseudotrajectory.

hold. For a graphical description of a δ-pseudotrajectory, see Fig. 8.2. Usually, a δ-pseudotrajectory is considered as the result of using a numerical method to compute orbits of the dynamical system Φ, e.g., because of round off error. We say that a point $x \in X$ (ε, Φ)-*shadows* a pseudotrajectory $\zeta = \{x_k\}$ if the inequalities

$$d(\Phi^k(x), x_k) < \varepsilon \tag{8.5}$$

hold (see Figure 8.3). If only one dynamical system Φ is considered, we

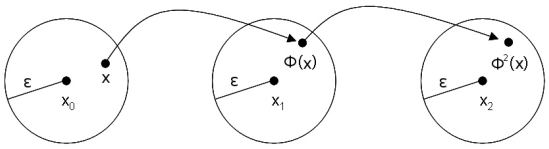

Figure 8.3: An ε-shadowing.

will usually write ε-shadows ζ. The existence of a shadowing point for a pseudotrajectory ζ means that ζ is close to a real trajectory of Φ.

The following statement is usually called the Shadowing Lemma.

Theorem 8.2.1. *If Λ is a hyperbolic set for a diffeomorphism Φ, then there exists a neighborhood W of Λ such that for all $\varepsilon > 0$ there exists $\delta > 0$ such that for any δ-pseudotrajectory with initial conditions $\zeta \in W$ there is a point x that ε-shadows ζ.*

The Anosov shadowing requires the existence of a hyperbolic set. It means that at each point there are two directions where the motion is either exponentially expanding (stable manifold) or exponentially contracting (unstable manifold).

Definition 8.2.1. We say that a set Λ is hyperbolic for a diffeomorphism $\Phi \in C^1(\mathbf{R}^n)$ if:

(a) Λ is compact and Φ-invariant;

(b) there exist constants $C > 0$, $\lambda_0 \in (0,1)$, and families of linear subspaces $S(p)$, $U(p)$ of $\mathbf{R}^n$, $p \in \Lambda$, such that

(b.1) $S(p) \oplus U(p) = \mathbf{R}^n$;

(b.2) $D\Phi(p)T(p) = T(\Phi(p))$, $p \in \Lambda$, $T = S, U$;

(b.3)

$$|D\Phi^m(p)v| \leq C\lambda_0^m |v| \ for \ v \in S(p), \ m \geq 0;$$
$$|D\Phi^{-m}(p)v| \leq C\lambda_0^m |v| \ for \ v \in U(p), \ m \geq 0;$$

The definition of a hyperbolic set is strictly related to the one of Lyapounov exponents: for each orbit inside a hyperbolic set, the Lyapounov exponents must be either $> \log(\lambda_0)$ or $< -\log(\lambda_0)$.

8.2.1 Shadowing Lemma and orbit determination

Our goal is to connect the Shadowing Lemma with the chaotic orbit determination, involving the least squares fit and the differential corrections.

First of all we build a δ-pseudotrajectory by using a simulated observations process. In Section 8.1 we have set up such an observations process, with observations $(x_k(\mu_0, \sigma), y_k(\mu_0, \sigma))$. We claim that a sequence $\zeta = \{(x_k(\mu_0, \sigma), y_k(\mu_0, \sigma))\}$ is a δ-pseudotrajectory for the dynamical system $S_{\mu^*}(x_0, y_0)$, with $\delta = \sqrt{2}|\mu^* - \mu_0| + \mathcal{K}\sigma$, $\mathcal{K} \in \mathbf{R}$. To obtain this result we compute the Euclidean distance:

$$d(S_{\mu^*}(x_k(\mu_0, \sigma), y_k(\mu_0, \sigma)), (x_{k+1}(\mu_0, \sigma), y_{k+1}(\mu_0, \sigma))) \tag{8.6}$$

For the sake of simplicity $(\bar{x}_{k+1}, \bar{y}_{k+1})$ are the observations, i.e. Gaussian random variables with mean x_{k+1} (y_{k+1}, respectively), and standard deviation σ, as in Sec. 8.1, and $S_{\mu^*}(\bar{x}_k, \bar{y}_k) = (\tilde{x}_{k+1}, \tilde{y}_{k+1})$. Using these notations, (8.6) turns into

$$d(S_{\mu *}(\bar{x}_k, \bar{y}_k), (\bar{x}_{k+1}, \bar{y}_{k+1})) = \sqrt{(\tilde{x}_{k+1} - \bar{x}_{k+1})^2 + (\tilde{y}_{k+1} - \bar{y}_{k+1})^2}$$

We compute separately the two differences.

$$\begin{aligned} |\tilde{y}_{k+1} - \bar{y}_{k+1}| &= |\bar{y}_{k+1} - \mu^* \sin \bar{x}_k - y_{k+1} - \mathcal{N}(0, \sigma^2)| \\ &= |\mathcal{N}(0, 2\sigma^2) - \mu^* \sin x_k \cos(\mathcal{N}(0, \sigma^2)) + \mu^* \sin(\mathcal{N}(0, \sigma^2)) \cos x_k + \mu_0 \sin x_k| \\ &< \mathcal{N}(0, 2\sigma^2) + |\mu_0 - \mu^*| \end{aligned} \tag{8.7}$$

To allow the last estimate, we need to solve a technical problem: the Shadowing Lemma uses a uniform norm, that is the maximum of the distance

between the δ-pseudotrajectory and the ε-shadowing. On the contrary, the natural norm for the residuals of the fit is the Euclidean norm with the square root of the sum of the squares. However, since the number of residuals is not only finite but sharply limited by the numerical phenomena discussed in Section 8.3, in a given experiment we can just take the maximum absolute value of the residuals and it is going to be $\mathcal{K}\sigma$, with $\mathcal{K}$ a number which in practice cannot be too large, e.g., in our experiment $\mathcal{K} = 5.9$.

Then we can approximate the quantities $\mathcal{O}(\sigma)$ and smaller, e.g., $\cos(\mathcal{N}(0, \sigma^2)) \sim 1$ and $\sin(\mathcal{N}(0, \sigma^2)) \sim 0$. The x coordinate gives a similar result:

$$|\tilde{x}_{k+1} - \bar{x}_{k+1}| = |\bar{x}_{k+1} + \tilde{y}_{k+1} - x_k - y_{k+1} - \mathcal{N}(0, \sigma^2)|$$

$$< \mathcal{N}(0, \sigma^2) + \mathcal{N}(0, 2\sigma^2) + |\mu_0 - \mu^*| = \mathcal{N}(0, 3\sigma^2) + |\mu_0 - \mu^*| \tag{8.8}$$

Putting together (8.7) and (8.8) we obtain

$$\begin{aligned} \sqrt{(\tilde{x}_{k+1} - \bar{x}_{k+1})^2 + (\tilde{y}_{k+1} - \bar{y}_{k+1})^2} < \\ < \sqrt{(\mathcal{N}(0, 3\sigma^2) + |\mu_0 - \mu^*|)^2 + (\mathcal{N}(0, 2\sigma^2) + |\mu_0 - \mu^*|)^2} < \\ < \sqrt{2}|\mu_0 - \mu^*| + \sqrt{(\mathcal{N}(0, 3\sigma^2))^2 + (\mathcal{N}(0, 2\sigma^2))^2} < \sqrt{2}|\mu_0 - \mu^*| + \mathcal{K}\sigma \end{aligned} \tag{8.9}$$

with $\mathcal{K} \in \mathbf{R}$.

Therefore the sequence generated by the observations is a δ-pseudotrajectory for the dynamical system S_{μ^*} with $\delta = \sqrt{2}|\mu_0 - \mu^*| + \mathcal{K}\sigma$.

Figure 8.4 is an example of observations as a δ-pseudotrajectory. The observations are built with $\sigma = 10^{-3}$ and $\mu_0 = 0.5$, and the dynamical system is S_{μ^*}, with $|\mu^* - \mu| = 10^{-1}$; the circles have radius δ.

The solution of the least squares fit (to the observations from $-n$ to n), obtained by convergent differential corrections, is a finite ε-shadowing, valid for the iterations from $-n$ to n.

We choose a value $\varepsilon > 0$, that is a boundary on the maximum of the residuals. Then we choose $\sigma < \varepsilon/\mathcal{K}$ and we set up the observations process. Next, we create a first guess: a new orbit obtained with a small change of the initial conditions and of the dynamical parameter μ: $\{(x_k(\mu_g), y_k(\mu_g))\} = S_{\mu_g}(x_g, y_g)$, with $x_g = x_0 + dx$, $y_g = y_0 + dy$, and $\mu_g = \mu_0 + d\mu$. Then we apply the differential corrections to the orbit. If the iterations converge, that is the last correction is very small, the maximum of the norm of the residuals is less than ε (because the individual residuals are less than 3σ).

At convergence, we obtain an initial condition (x^*, y^*) and a value of the dynamical parameter μ^*, such that (x^*, y^*) is the (ε, S_{μ^*})-shadowing for the

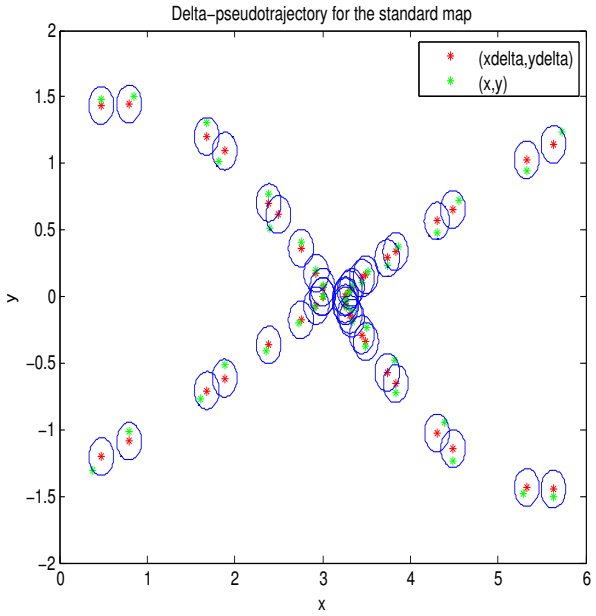

Figure 8.4: An example of a δ-pseudotrajectory. Initial conditions are $x_0 = 3$, $y_0 = 0$, $\mu_0 = 0.5$. $\delta\mu = 10^{-1}$, and $\sigma = 10^{-3}$.

δ-pseudotrajectory with $\delta = \sqrt{2}|\mu^* - \mu_0| + \mathcal{K}\sigma$, for all the points used in the fit.

The most important requirement is the convergence of the differential corrections, otherwise we cannot obtain the ε-shadowing. This is far from trivial, because the chaotic divergence of the orbits introduces enormous nonlinear effects, for which the linearized approach of differential corrections may fail. To guarantee convergence, first we select the initial conditions x_0, y_0 to be at the center of the observed interval, otherwise the initial conditions would be essentially undetermined along the stable manifold of the initial conditions. Second, we use a progressive solution approach, namely, given the solution with $2n + 1$ observations with indexes between $-n$ and n, we use the convergent solution x_0^*, y_0^*, μ^* for n as first guess for the solution with $2n + 3$ observations (between $-n - 1$ and $n + 1$). Then the initial guess is actually used only for the solution with 3 observations, for which the nonlinearity is negligible. Still the convergence of the differential corrections depends critically upon the number n of iterations of the map, as explained in Section 8.3.

8.3 Numerical results

The experiment was performed with the initial conditions at $x_0 = 3$ and $y_0 = 0$, and the value of the dynamical parameter $\mu_0 = 0.5$. The dynamical context for this orbit can be appreciated from Figure 8.1, showing that the initial conditions are indeed in a portion of the initial conditions space containing mostly chaotic orbits. For the observation noise we have used a standard deviation $\sigma = 10^{-10}$.

8.3.1 Computability horizon

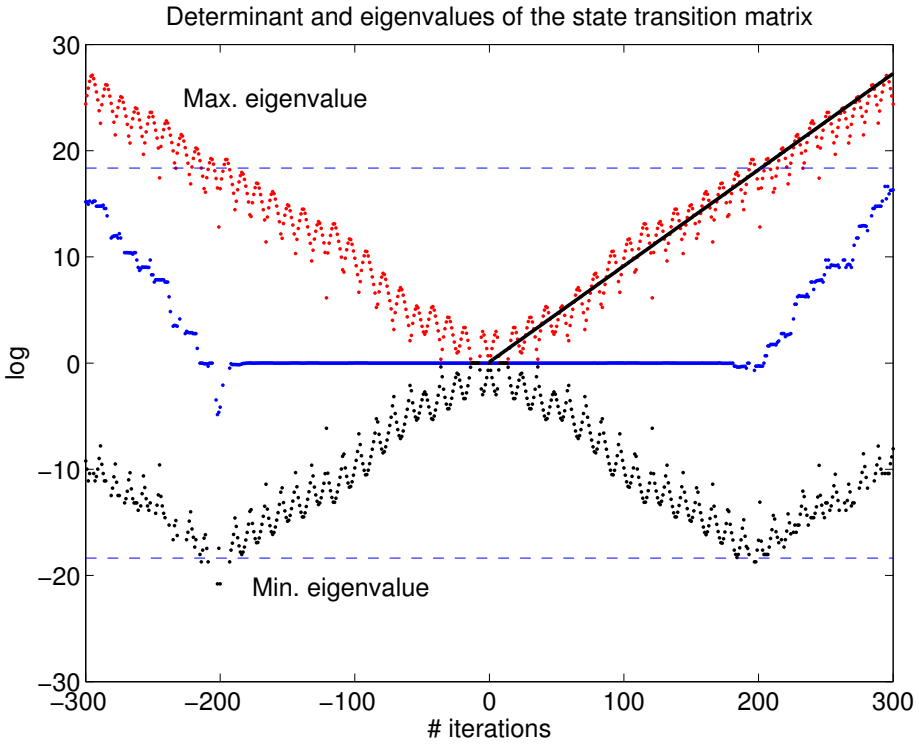

Figure 8.5: The eigenvalues and the determinant of the state transition matrix in a semilogarithmic scale, as a function of the number of iterations. Also shown is the linear fit to the large eigenvalue based on the first 180 iteration, with slope +0.091. The computation is in double precision and the number of iterations of the standard map n is 300 with the map and 300 with its inverse. The determinant of the state transition matrix would be 1, for all n, in an exact computation. The numerical instability occurs when the eigenvalues reach the critical values $\sqrt{\varepsilon_d}, \sqrt{1/\varepsilon_d}$ marked by the dotted lines.

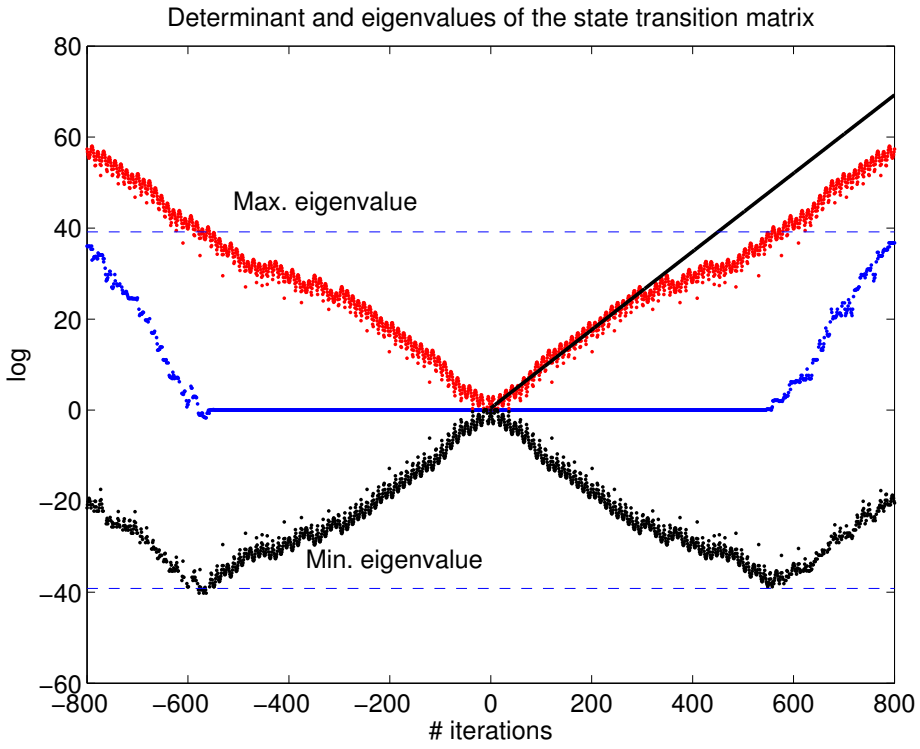

Figure 8.6: The eigenvalues and the determinant of the state transition matrix in a semilogarithmic scale, as a function of the number of iterations. Also shown is the linear fit to the large eigenvalue based on the first 300 iteration, with slope +0.086. The computation is in quadruple precision and the number of iterations of the standard map n is 800 with the map and 800 with its inverse. The numerical instability occurs when the eigenvalues reach the critical values $\sqrt{\varepsilon_q}$, $\sqrt{1/\varepsilon_q}$ marked by the dotted lines.

Figure 8.5 and 8.6 show the absolute value of the eigenvalues of the state transition matrix forward and backward. The product of two eigenvalues should be 1 in exact arithmetic. When the condition number of the matrix becomes larger than the inverse of the machine rounding off error, the computation of the matrix becomes numerically impossible, and the computed value of the determinant is far from 1.

In Figure 8.5 the computations are performed in the standard double precision, that is with a mantissa of 52 binary digits and a round off relative error of $\varepsilon_d = 2^{-53} = 1.1 \times 10^{-16}$. We observe a numerical instability after $\simeq 180$ iterations: the determinant deviates from the exact value of 1 and the small eigenvalue starts increasing; the large eigenvalue keeps increasing, but there is a slight change of slope. Then we fit the slope of the large eigenvalue

curve for the first 180 iterations, and get a Lyapounov indicator +0.091: it approximates the maximum Lyapounov exponent χ for the orbit to which our differential corrections converge[1].

The Lyapounov time is $T_L = 1/\chi$, in this example $T_L \simeq 11$. To reach a ratio of eigenvalues of the state transition matrix of $1/\varepsilon_d$ we need a number of Lyapounov times $\log(1/\sqrt{\varepsilon_d})$, in this case $\simeq 18.4\,T_L \simeq 202$ iterations of the map. At about this number of iterations the maximum and minimum eigenvalues of A_n are so widely apart in size that a bad conditioning horizon is reached, and the computation of the state transition matrix becomes numerically inaccurate. Hence near $\pm 18.4\,T_L$ we observe the numerical instability in the computation of the determinant and of the eigenvalues of the state transition matrix.

Figure 8.6 shows the same computations, with the same initial condition, but in quadruple precision, with a 112 bit mantissa and $\varepsilon_q = 2^{-113} = 9.6 \times 10^{-35}$. The change of slope in the eigenvalues curves occurs after $\simeq 300$ iterations, while a full blown numerical instability occurs after $\simeq 550$ iterations. The fit to the large eigenvalue for the first 300 iterations gives a Lyapounov indicator +0.086, not very different from the one obtained in double precision. Thus we would expect the numerical instability to occur after $\log(1/\sqrt{\varepsilon_q})\,T_L \simeq 39.2\,T_L = 455$ iterations. It appears that the rate of divergence decreases after 300 iterations, as shown by the change in slope, allowing to maintain at least the determinant near the exact value for about 100 more iterations beyond the value predicted above.

The computability horizon represents the maximum number of iterations we can reach, before the computation becomes numerically unstable. The computability horizon strongly depends on the chaoticity of the system: more chaos, that is larger χ, more instability; but also upon the precision of the computations.

Thus, in the following we perform the numerical experiments in quadruple precision, in order to mitigate the problem of the numerical instability. We compute 500 iterations forwards and backwards, but we use only the first 300 iterations for the linear fits, to avoid the possibility that changes in slope, such as the ones apparent in Figure 8.6, contaminate our experimental results.

The compatibly horizon is a hard limit in that it is not practically possible

[1]There is no way to rigorously compute the Lyapounov exponents: in practice Lyapounov indicators extracted from finite propagations are used to assess, but not rigorously prove, the chaotic nature of the orbits. Note that it is a numerically well documented phenomenon that the indicators are not constant, but actually depend upon the time interval over which they are computed, although in most cases these changes are not very large and the conclusion that an orbit is chaotic is reliable.

to increase the number of iterations to a much higher value. E.g., to push the horizon by a factor 10 above the value for double precision, we would need computations performed with real numbers represented with 800 bytes[2].

The conclusion is that the practical problem of chaotic orbit determination is meaningful only for a finite number of iterations, and the accuracy of the results can be tested only within the boundary of the computability horizon.

8.3.2 Chaotic case

Figure 8.7 shows the results in quadruple precision of the full 3-parameter fit: the 3 parameters are the initial conditions and the dynamical parameter μ. The determination of μ is indeed not possible without simultaneous determination of the initial conditions.

Even in quadruple precision we find a maximum value of n beyond which the iterative solution of the nonlinear least squares problem is divergent. This maximum turns out to be 599 in this experiment: it is close to what we have called the computability horizon, that is this limitation is due to the difficulty of computing the state transition matrix when the condition number is too large.

The curves in Fig. 8.7 represent both the formal standard deviation and the actual error of the solutions of the least squares fit, as a function of n in a semilogarithmic plot. Both the formal standard deviation and the actual error of μ do not decrease exponentially. Indeed, in Fig. 8.8 we have the same behavior of the curves that we have already seen in Fig. 8.7, but in a log-log plot, in which a constant slope a would imply a power law proportional to n^a. The slopes of the lines that fit the uncertainties are: -0.675 for the dynamical parameter μ, -0.833 and -12.030 for the initial conditions x and y, respectively. This plot in logarithmic scale shows that the uncertainty for μ and x does not decrease exponentially. It is also apparent that one of the initial conditions (y) is better determined than the other one (x), with an improvement as a function of n which could be exponential. This is a property of the specific initial condition we have used, for other choices we can get three parameters determined with comparable accuracy, none of them with exponential improvement[3].

Figure 8.9 shows the results for the standard deviation and the actual error when solving only for the initial condition. The 2x2 portion of the normal

[2]Software to perform arithmetic computations with an arbitrary number of digits is available, but the algorithms are too slow to be used even for our simple example.

[3]This depends upon the orientation of the stable and unstable directions at the initial condition.

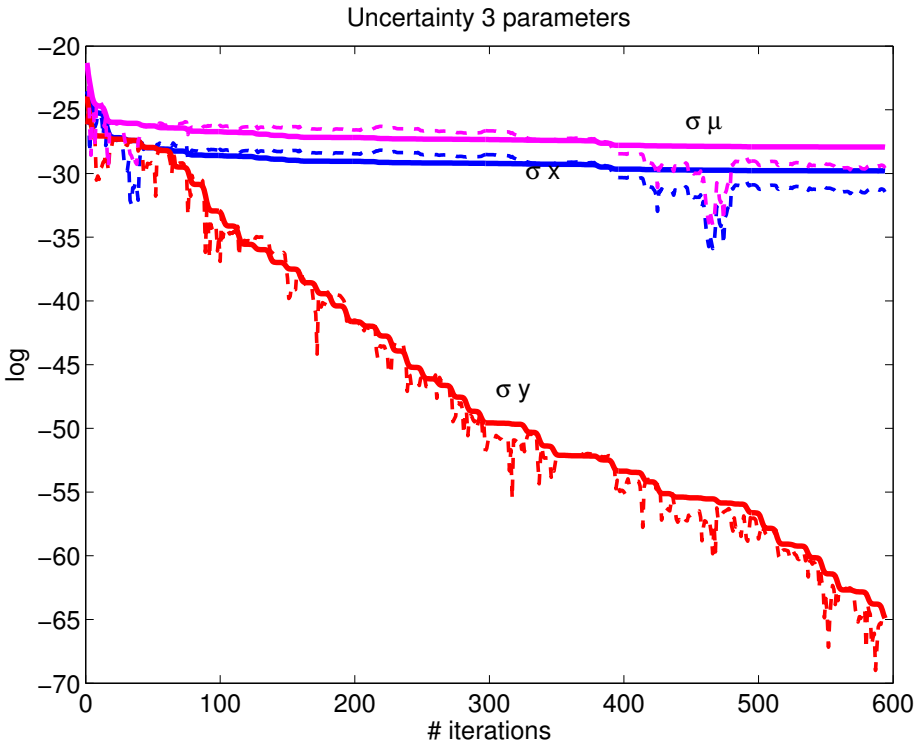

Figure 8.7: Standard deviation of the solutions for the initial conditions and for the dynamical parameter μ (continuous lines), and actual error (nominal solution of the fit minus real value used in the simulation, dashed lines), as a function of the number of iterations.

matrix which refers only to the initial conditions is not badly conditioned. Also as a result of this, we are able to get convergence of the differential corrections up to ± 742 iterations, which is even beyond the numerical stability boundary. If the fit is done by using only up to 300 iterates, to avoid the apparent slope change, the slopes shown in this Figure are -0.084 for x and -0.083 for y; note that the Lyapounov indicator for the same interval is $+0.086$. Thus exponentially improving determination of the initial conditions only is possible, and the exponent appears to be very close to the opposite of the Lyapounov exponent.

8.3.3 Ordered case

An ordered case can be obtained with a change of the initial conditions. For the numerical experiments we have chosen $x_0 = 2$, $y_0 = 0$ and $\mu_0 = 0.5$. In the ordered case we have not the problem of the computability horizon and

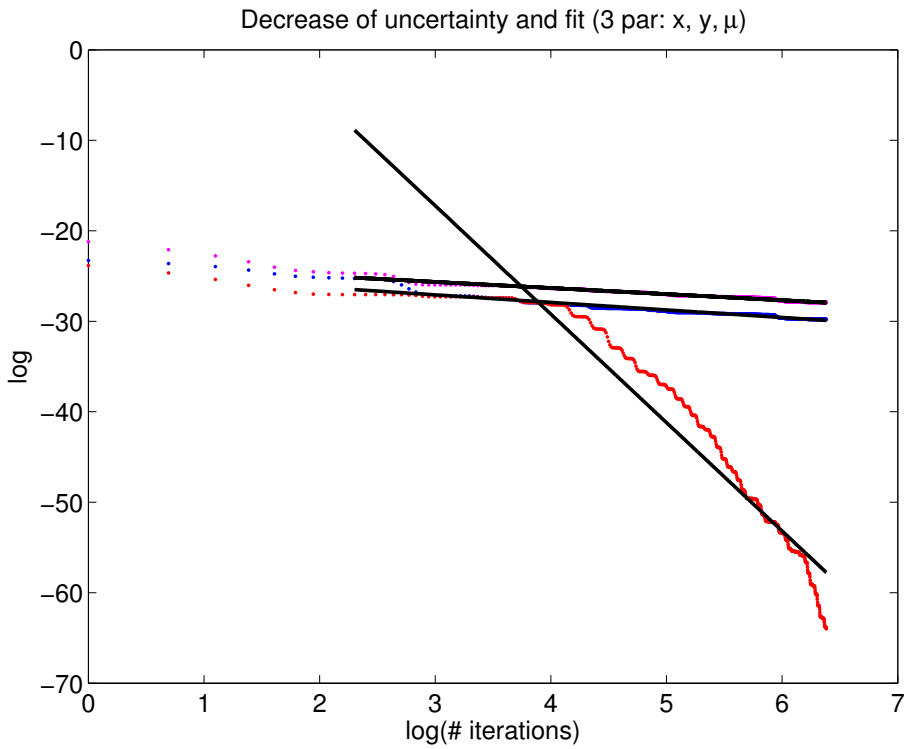

Figure 8.8: Uncertainty of the solution of the least squares fit for the initial conditions and for the dynamical parameter μ in a logarithmic scale.

the Lyapounov exponent is very small: actually, it could be zero if we are on a Moser invariant curve. Thus we have computed 5000 iterations.

Figure 8.10 gives a summary of our numerical experiment in the ordered case. The Lyapounov indicator is very small ($\simeq 10^{-4}$), and can be made even smaller by continuing the experiment for larger values of n. As a consequence, the state transition matrix is not badly conditioned, and the computability horizon is much beyond the number of iterations we have used (if it exists at all). Thus the lack of chaoticity implies the practical absence of the computability horizon, and we can determine all the parameters with very good accuracy, even if we are not in exact arithmetic. The values of the slopes of the fit to the uncertainty are -0.504 for μ, -0.504 and -0.488 for x and y respectively, the corresponding regression lines are shown in the log-log plot on the bottom right. As it is clear by comparing the top right and the bottom left plot, the standard deviation for the solution with only 2 parameters have very much the same behavior, indeed in a log-log plot (not shown) we can get slopes -0.511 for x, -0.481 for y.

All these power laws are close to the inverse square root of the number of

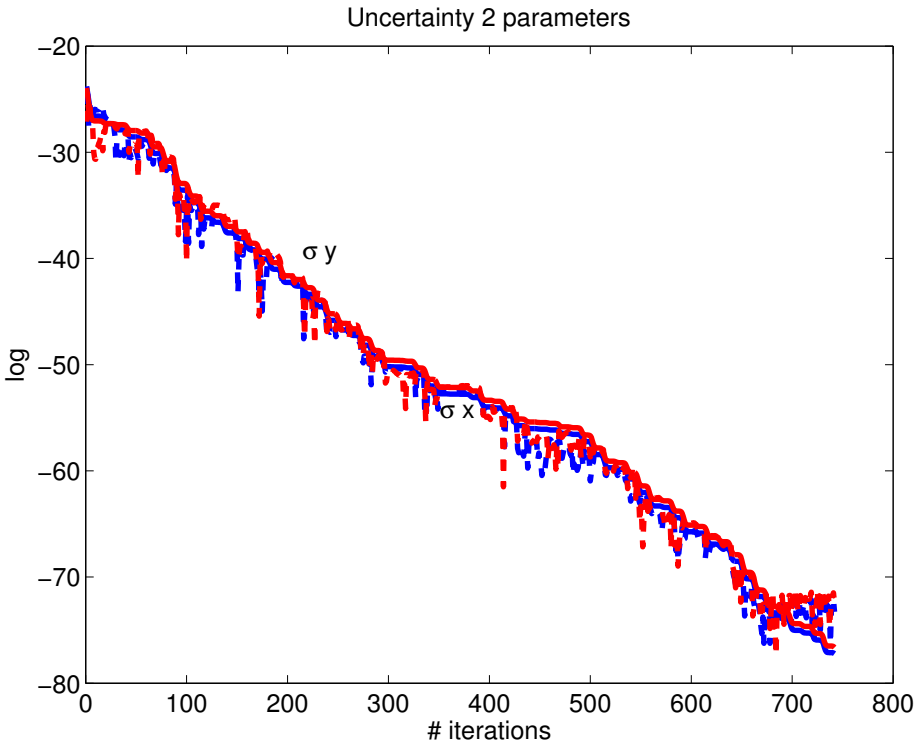

Figure 8.9: Standard deviation of the solutions for the initial conditions (continuous lines), true errors for the same 2 parameters (dashed lines).

iterations, namely the same rule as the standard deviation in the computation of a mean. We do not have a formal proof of this, but we conjecture that for an orbit on a Moser invariant curve (for which the Lyapounov exponents are exactly zero) the standard deviations for all the parameters decrease as $1/\sqrt{n}$.

8.4 Discussion on the Wisdom hypothesis

The statement by Wisdom, as a practical rule for concrete orbit determination, appears to be first limited by the computability horizon. Second, the actual decrease of the uncertainty, going as far as it can be done numerically, is not exponential, but polynomial, as n^a, with a negative and rather small, although we have found that the value of a depends upon the initial conditions[4]. Note that the orbit determinations in which the only parameters

[4]We are showing figures and giving data only for one initial condition, but of course we have run many tests.

to be solved are the 2 initial coordinates show an exponential decrease as $\exp(-\alpha\, n)$, where α appears to be close to the Lyapounov exponent χ, but the strong correlations appearing when 3 parameters are solved degrade the result in a very substantial way.

This needs to be compared to the regular case, shown in Figure 8.10, where the standard deviations for each of the 3 fit parameters decrease approximately according to an $1/\sqrt{n}$ law, as prescribed by the standard rule for the estimate of the mean with errors having a normal distribution. Indeed it is possible that the determination of μ for some chaotic cases, including the example shown in Figure 8.8, decreases faster than for an ordered case, but the decrease is anyway polynomial, proportional to n^a with some different negative a, thus the difference is not very large, given the tight constraint on the maximum possible value of n.

8.5 Examples from Impact Monitoring

One feature of our results is that adding a dynamical parameter to the list of parameters to be determined results in degradation in the normal matrix, thus in much slower decrease of the uncertainties as the number of observations grows. The problems of orbit determination for NEA undergoing several close approaches to the Earth (or other planets) is more complex than our simple model, but we have found that the phenomenon described above does occur in a remarkably similar way.

In Figure 8.11 we show two probability distributions, as derived from the orbit determination of the asteroid (410777) 2009 FD. The narrow peaked distribution corresponds to an orbit determination with 6 parameters, the initial conditions only: the standard deviation is 6×10^4 km. The much wider distribution corresponds to a fit with 7 parameters, including the constant A_2 appearing in the transverse acceleration due to the Yarkovsky effect: the STD is $\simeq 2.3 \times 10^6$ km. The Yarkovsky effect is a form of non-gravitational perturbation due to thermal radiation emitted anisotropically by the asteroid, and is indeed very small. However, when the uncertainty resulting from the covariance matrix of the orbit determination is propagated for $\sim$ 170 years after the last observation available, not only the Yarkovsky effect has a long enough time to accumulate but it is also enhanced by the exponential divergence of nearby orbits, the Lyapounov time being about 15.3 years [Spoto et al., 2014][Figure 5].

The practical consequence of this increase of the uncertainty arises from the fact that the Target Plane of 2009 FD for 2815 includes some keyholes, small portions corresponding to impacts with the Earth (either at that time

or a few years later, until 2196). With the 7 parameters solutions these keyholes are within the range of outcomes with a significant value of the Probability Density Function, thus the impacts have a non-negligible probability, the largest being an Impact Probability of $\simeq 1/370$ for 2185. If on the contrary the orbit was estimated with 6 parameters only, then the probability would appear to be even larger for an impact in 2190, and all the other keyholes (including the one for 2185) would correspond to negligible impact probabilities. Given that the impact, if it was to occur, would release an energy equivalent to $3,700$ MegaTons of TNT, this difference is practically relevant. In fact, the solution including the Yarkovsky effect leads to a more reliable estimate of the Impact Probabilities, because the Yarkovsky effect exists and needs to be taken into account.

Is the discrepancy in the uncertainties with and without the dynamical parameter in the fit essentially the same phenomenon we have found in our simple model? We do not know the answer to this question, but we shall investigate this issue in the future.

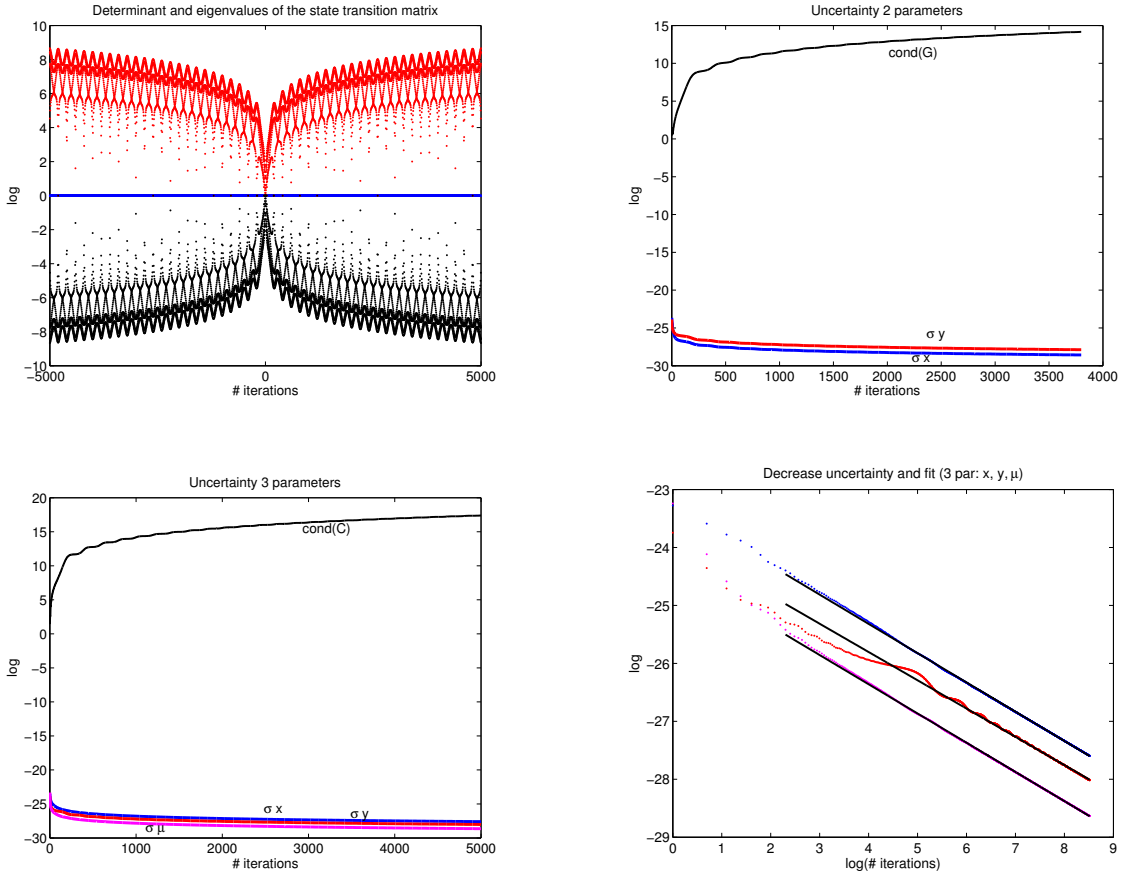

Figure 8.10: Top left: eigenvalues of the state transition matrices, for the chosen regular initial conditions and for ± 5000 iterations. Top right: solutions for the initial condition only, condition number of the normal matrix, standard deviation of y and for x. Bottom left: solutions for three parameters, condition number, standard deviation of x, of y, of μ. Bottom right: log-log plot of the 3 standard deviations, with very similar slopes.

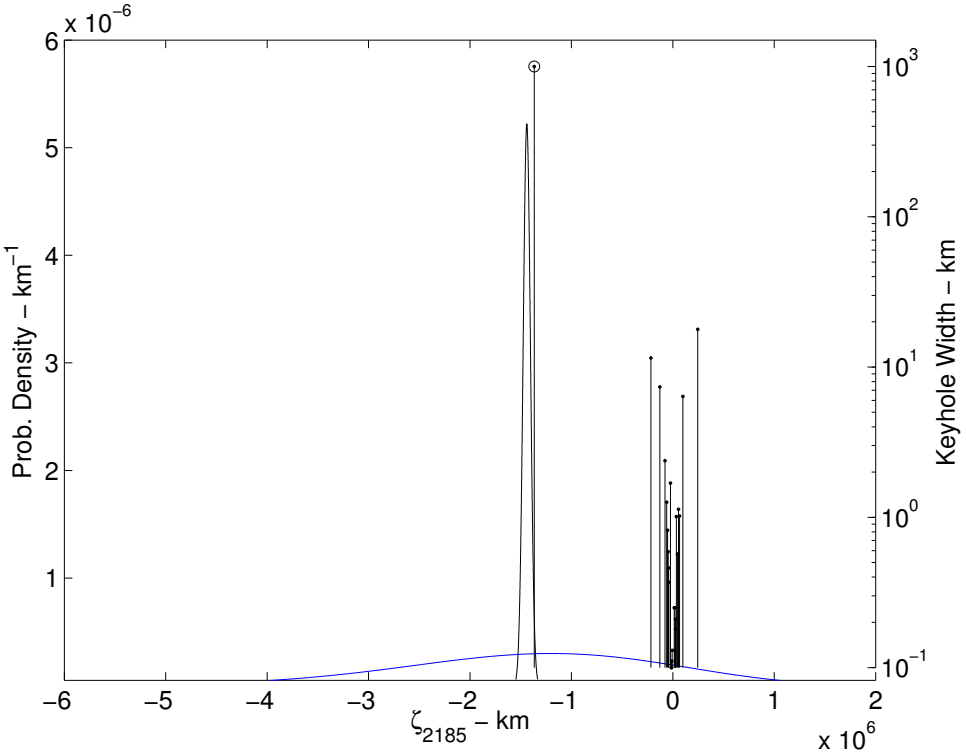

Figure 8.11: Two different Probability Density Functions (PDF) for the trace of possible solutions on the Target Plane of the close approach of asteroid (410777) 2009 FD to the Earth in the year 2185. Superimposed and on a different vertical scale are the keyholes relative to impacts in different years between 2185 and 2196; the height of the bar is proportional to the width of the keyhole, thus the Impact Probability can be computed as product of the width and the PDF.

Chapter 9

Effect of parallax cadence on asteroid impact probabilities

The past quarter century has witnessed an exponential increase in the number of known near Earth objects accompanied by a concomitant improvement in the ability to calculate their impact probabilities with Earth. The job of identifying the largest and most hazardous NEOs, those larger than about 1 km diameter, has mostly been accomplished and asteroid surveys are now focussing on the individually less hazardous but far more numerous smaller asteroids. The large asteroids can be detected at great distances years to centuries in advance of their impact but the smaller asteroids may only be detected on their final approach, if at all, since about 40% of them must approach from the direction of the Sun in daylight sky. This work quantifies how the impact probability and warning time evolve in the impact apparition for the smaller asteroids as a function of their size, time after discovery, and observing cadence. In particular, we examine whether the parallax afforded by observations at nearly the same time from two independent observatories provides leverage in improving the impact probability calculation or increasing the impact warning time.

The Catalina Sky Survey [CSS, Larson et al., 1998] and the Panoramic Survey Telescope and Rapid Response System prototype [Pan-STARRS 1; *e.g.* Hodapp et al., 2004; Kaiser et al., 2002] currently dominate the field of NEO discovery — almost 90% of all NEOs and about 75% of all potentially hazardous objects[1] (PHO) were discovered by these two surveys in calendar years 2012 and 2013. The known population of NEOs larger than 1 km diameter is more than 90% complete [Mainzer et al., 2011b] so the discovery

[1] PHOs are NEOs that have a minimum orbital intersection distance [*e.g.* Gronchi, 2005] with Earth less than 0.05 au and absolute magnitude $H < 22$

rate of NEOs in this size range has decreased by about a factor of 6 from a peak of 93 in the year 2000 to about 15/year in the last two years.

Despite the success of the surveys in the past few decades it remains the case that the most likely warning time for an impact is *zero* — contemporary surveys are unlikely to detect smaller but still dangerous asteroids because they do not survey the entire sky deeply or regularly enough to identify the next impactor. The surveys are further limited by the simple fact that ground-based facilities can not survey during the day and about 40% of all impactors will approach from the direction of the Sun. These problems were spectacularly highlighted by the Chelyabinsk impact on the morning of 15 February 2013 [*e.g.* Borovička et al., 2013; Brown et al., 2013] — with absolutely no warning a ~ 17 m diameter object blew up in the atmosphere with an energy equivalent to about 500 kilotons of TNT, damaging buildings 50 km away in the city of Chelyabinsk and injuring about 1,500 people.

The impact risk associated with the unknown objects larger than 1 km diameter is now comparable to the impact risk with the much more numerous, but individually less destructive, objects with diameters less than 1 km. The new balance in the impact risk, along with the realization that smaller impacts may be more numerous but less destructive than anticipated a decade ago [*e.g.* Brown et al., 2013], has contributed to an increased interest and funding for the NEO survey programs in recent years. *e.g.* NASA's NEO Observations (NEOO) program office now solicits[2] proposals for surveys that 'provide capability to detect the subset of 90% of PHOs down to 140 meters in size'

The smaller NEOs are more difficult to detect than the larger ones. They are detected closer to Earth (*if* they are detected), and consequently have shorter observational arcs. The limited time range of the set of detections can make it difficult to identify real impactors even during the apparition in which the impact will take place. This was not the case for the few-meter diameter asteroids 2008 TC_3[*e.g.* Jenniskens et al., 2009] and 2014 AA[3], the only natural objects to be discovered before striking Earth. The very smallest objects will be discovered so close to Earth that, if individual detections of the object can be associated with one another as a 'tracklet' [Denneau et al., 2013], the non-linear motion of the detections on the sky-plane due to topocentric parallax can provide enough leverage in the orbit solution to predict an impact.

The observable characteristics of NEOs that will impact Earth can be quite different from those of other NEOs [*e.g.* Chesley and Spahr, 2004;

[2] ROSES 2011 NEOO solicitation section C.9.1.1.

[3] Minor Planet Electronic Circular 2014-A02

Farnocchia et al., 2012; Vereš et al., 2009]. For instance, their observable steady-state distribution on the sky-plane is a function of their size and time before impact. Decades before impact they tend to be concentrated in 'sweet spots' near the ecliptic and within about 120° of the Sun. As the time until impact decreases from weeks to days they spread out over most of the sky but they are still concentrated in the direction towards and away from the Sun. An object on its 'death plunge' must be moving directly towards Earth in a geocentric reference frame so that about a week before impact its apparent rate of motion may be small — likely mimicking the rate of motion of much more distant and totally harmless asteroids, and perhaps not triggering followup that would allow an impact probability calculation.

The techniques employed for the impact probability calculation have evolved dramatically over the past few decades with the realization that asteroid impacts have shaped the Moon's surface and influenced the evolution of life on Earth. Indeed, it was only 34 years ago that Alvarez et al. [1980] proposed that the KT extinction was the result of an asteroid impact and, even though Opik [1952] stated that "Over a dozen meteor craters are at present known on the earth's surface", it was only in 1960 that Chao et al. [1960] found strong physical evidence that Meteor Crater in Arizona, USA, was formed in an impact event.

Opik [1952]'s estimated collision rates using the 'Theory of Probabilities' for the entire NEO population were surprisingly good given that only six NEOs were known at the time. His collision probability formulae formed the basis of much of the impact collision work in the next decades [*e.g.* Bottke et al., 1996; Kessler, 1981] but were eventually supplanted by new numerical techniques [Milani et al., 2002]. The two primary operational asteroid impact warning systems, the Jet Propulsion Laboratory's Sentry system and the NEODyS CLOMON2 system, calculate the collision probability by generating synthetic 'Virtual Asteroids' (VA) on orbits that are consistent with the known set of observations and propagating all of them into the future with an N-body integrator to search for impacts [Milani et al., 2005a]. These impact warning systems are based on a geometric sampling technique for which the identification of the Virtual Impactors (VI) is performed on the line-of-variation [LOV, Milani et al., 2005b], thus avoiding the poor efficiency inherent to the Monte Carlo methods, especially when the collision probability is small.

Impact predictions are extremely sensitive to the orbit accuracy that depends on many factors, but the primary drivers are the length of the observational arc and the astrometric accuracy of the detections [*e.g.* Desmars et al., 2013]. The longer the arc, and the better the astrometry, the more accurate the orbit. The latter effect is best illustrated by radar detection of

asteroids that provide exquisite range and range-rate information, thereby dramatically improving the impact probability accuracy and/or extending the time frame during which the impact probability can be calculated [Ostro et al., 2002].

Impactors can be either direct or resonant [Milani et al., 1999]. Direct impactors collide with Earth during their first known encounter and must be discovered far away to have a large warning time. The warning time for small impactors can be significantly less than one orbital period because they have to be close to Earth to be detected. On the other hand, resonant impactors experience intervening Earth encounters before collision. The intervening encounters are the main source of non-linearity in the dynamics and usually prevent a conclusive assessment of the impact threat, but provide additional observational opportunities to detect and constrain their orbits and the impact threat.

In this work we focus on the evolution of the collision probability with time for a single survey and concentrate on direct Earth impactors that are detected in the apparition during which the impact occurs. The smaller the asteroid the more likely this scenario, as the likelihood that small asteroids will be detected in earlier apparitions is 1) small and, even if they are detected, 2) it is unlikely that they will be recoverable in future apparitions because of the large uncertainties in their ephemeris based on the short observational arcs in the discovery apparition. Thus, we concentrate on collision probability evolution with time for 300 m, 100 m, 50 m and 10 m diameter impactors.

We also explore whether the collision probability calculation benefits from simultaneous or nearly-simultaneous parallax measurements from two observatories. The heliocentric motion of the impactor and Earth, as well as the topocentric rotation of the observer about the geocenter, produce parallax between successive observations of the same object, even from the same site. For very close objects that will impact within days of discovery there may be benefits from the two-site scenario — especially in rapidly identifying the object as an impactor.

Finally, we measure the single-system impact warning time as a function of impactor diameter. We expect the warning time to be longer for larger objects but the exact relationship between diameter and warning time is not intuitively obvious. The larger objects are discovered at greater distances where their rate of motion is similar to the much more distant main belt objects and the impact probability will be much smaller. If the impact probability is too small it may not cross the threshold to flag the object as an imminent impactor.

9.1 Method

9.1.1 Synthetic asteroid populations

Our study considers three different classes of asteroids that might be identified soon after discovery as impactors:

- Impactors

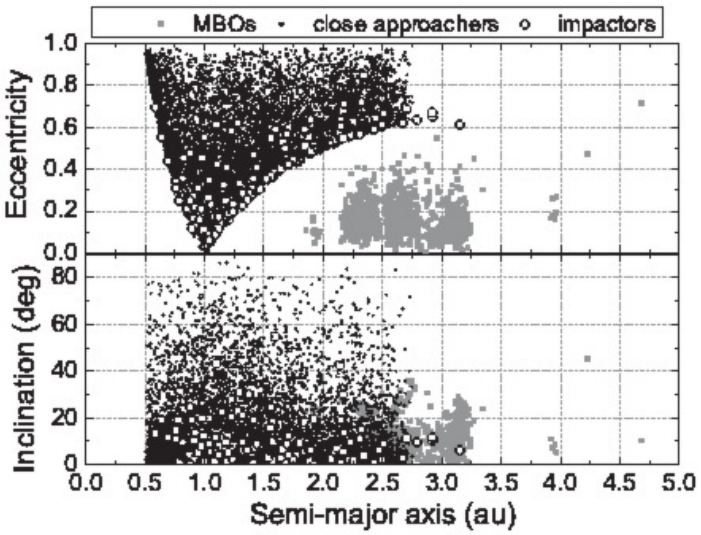

Figure 9.1: Eccentricity (top) and inclination (bottom) vs. semi-major axis for synthetic impactors (circles), close-approachers (black dots) and main belt objects (grey squares).

We used a 133 member subset of the population of Earth impactors developed for Vereš et al. [2009] that strike the Earth in a 12 month period beginning at the same time as the 12 month survey simulation described below (§9.1.2). The impactors' orbit elements are drawn from a realistic population of NEOs [Bottke et al., 2002a] and tend to have perihelia or aphelia that lie near Earth's geocentric distance of about 1 au (fig: 9.1). These types of orbits are nearly tangent to Earth's orbit so they spend more time available for impact. There is also an enhancement with small inclinations for the same reason.

- Close Approachers

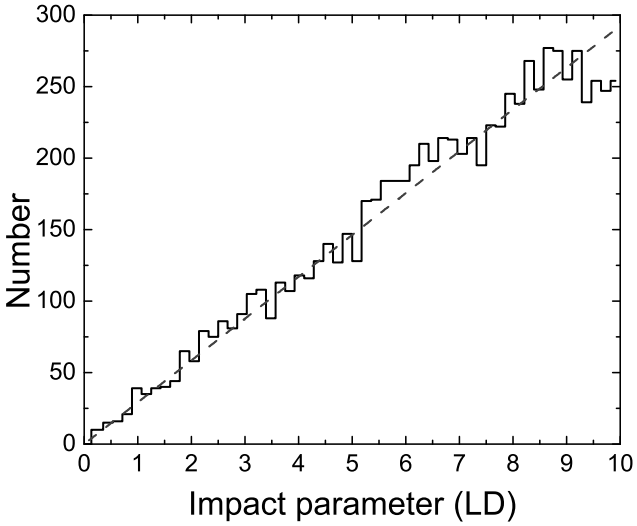

Figure 9.2: Impact parameters (closest approach distance to Earth) of the synthetic close-approaching asteroids. The dashed straight line is a linear fit to the data.

We generated 8,275 synthetic asteroids from the Bottke et al. [2002a] NEO model that approach Earth to within 10 LD (lunar distance, ~ 0.028 au) during the one year simulated survey (§9.1.2). The orbit distribution of the close approachers is more representative of the underlying NEO population (Fig. 9.1) and has a higher mean eccentricity and inclination compared to the impactors. This leads to them having higher speeds relative to Earth and higher apparent rates of motion as viewed from ground-based observatories (compared to the impactors). The number of close-approachers increases linearly with the impact parameter because the area of annuli of fixed width increases linearly with the annuli diameter (Fig. 9.2).

- Main Belt Objects (MBO)
  There are about one million asteroids larger than 1 km diameter in the main belt with semi-major axes between about 2.0 au and 3.5 au (Fig. 9.1). By definition, they can not approach within ~ 0.7 au of Earth, but tens of thousands will be within the detection limits of the survey that we model below (§9.1.2), and many of them will not be known objects (at least in the beginning of the survey). We will show that the objects' rates of motion are typical of some incoming

impactors and we wanted to determine if a relatively large astrometric uncertainty could generate false, non-zero, impact probabilities for these distant objects. We used a sample of about 14,000 synthetic main belt asteroids selected from the Grav et al. [2011] solar system model that have minimum perihelion magnitudes[4] detectable in our synthetic survey with $V_q < 20$). We used the absolute magnitudes (H) from the Grav et al. [2011] model that were assigned randomly according to a realistic size-frequency distribution.

9.1.2 Survey simulation

We simulated the detection of small incoming impacting asteroids with the in-development ATLAS [Tonry, 2011] system because of its all-sky every-night survey capabilities. The smaller the asteroid the more likely it is that it will not be brighter than any of the contemporary or planned survey system's limiting magnitudes until a few days before impact, so that detecting the object requires nearly all-sky coverage over that time interval. ATLAS achieves all-sky coverage by using small telescopes with wide fields-of-view (FOV) and large-format CCD cameras. Thus, it has a relatively large pixel scale (and astrometric uncertainty) and brighter limiting magnitude than other surveys.

The two primary purposes of this study were to 1) measure the time-evolution of the impact probability of asteroids detected with a realistic survey and 2) measure the effect of parallax on the impact probability precision.

To address the first issue we generated synthetic observations of each of our synthetic asteroids for a simulated one year ATLAS survey. Our low-fidelity instantiation of the survey covered the entire dark sky each night without regard for the Moon, weather, galaxy and clouds. The survey does account for the changing duration of the night through the year and geometrical constraints from the horizon. The fidelity of the simulation is not critical to the two primary purposes of this study but will have an impact on *e.g.* the calculated detection efficiency for small objects.

We addressed the second issue by using the synthetic survey to simulate the performance of two ATLAS surveys located at observatory sites F51 and 568 (respectively, the locations of the Pan-STARRS 1 facility on Haleakala, Maui, Hawaii, and the University of Hawaii 2.2 m telescope on Mauna Kea, Hawaii). These locations are amongst the best ground-based astronomical sites in the world with typically more than 75% clear nights, dark sky, high

[4] The minimum perihelion magnitude is the apparent magnitude an object would have if observed at opposition from Earth when the object is at perihelion.

altitude, sub-arcsecond seeing, and a number of other nearby operational observatories and instruments. The sites are separated by $\sim 130\,\mathrm{km}$ to enable parallax measurements for nearby asteroids. For instance, an asteroid at 10 LD can have a parallax of up to ~ 6.5" from the two sites — about an order of magnitude larger than the system's astrometric uncertainty. Increasing the distance between the two observatories would enhance the parallax effect. However, the meteorological correlation would be lower and it would be less likely that both sites could observe. Furthermore, the greater the separation between the two sites the more difficult it is to survey the same fields. Finally, two separate sites introduce additional cost and management issues.

To create the survey we divided the sky into 'square' tiles (or fields) with each square having an area equal[5] to that of an ATLAS camera's FOV of $\sim 40\,\mathrm{deg}^2$. The tile centers were equally spaced at about the width of the ATLAS FOV along lines of latitude. They were also spaced in latitude by the width of the ATLAS FOV. This pattern is not optimal because it results in significant field overlap at high latitudes but it was simple to implement and the details of the survey pattern will have little impact on the results. We used the *Tools for Automated Observing optimization* (TAO) package[6] to schedule the nightly surveying of the tiles and maximize the number of fields exposed each night with the desired cadence subject to the survey's limitations. Each tile was visited 4 times per night with roughly a Transient Time Interval (TTI) of 15 minutes between visits. We did not account for the Moon, galactic plane, planets, bright stars or weather (Fig. 9.3) but did account for the camera readout and telescope slew times. The fields were observed only when the Sun was more than 12° below the horizon and the field centers were more than 30° above the horizon (*i.e.* above 2 airmasses). We imposed a southern declination limit of $-30°$ that will have the effect of decreasing the detection efficiency for the imminent impactors that are concentrated towards opposition, but will provide more time for surveying the 'sweet spots' [Chesley and Spahr, 2004] at small solar elongations where the sky-plane density of future and larger impactors is highest. The strategy of surveying the sweet spots is a likely scenario for actual surveys that are rightfully more concerned with the long-term advance notice of larger impactors rather than the short-term notice for smaller objects.

We used the Pan-STARRS 1 Moving Object Processing System [MOPS, Denneau et al., 2013] to generate the synthetic asteroid detections in our simulated survey and to link detections within a tile on one night into 'track-

[5] Some of the values for the ATLAS system characteristics used in this work represent early expectations for the system. The exact values have no impact on our general conclusions.

[6] Paolo Holvorcem, `http://sites.mpc.com.br/holvorcem/tao/readme.html`

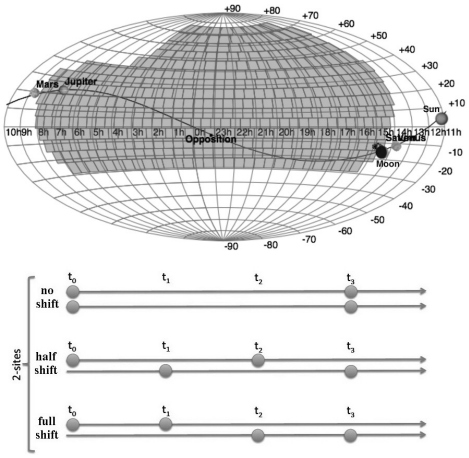

Figure 9.3: (Top) One night of the synthetic ATLAS survey covering the entire night sky visible from Haleakala, Maui, Hawaii. Each shaded 'square' represents one bore site that is imaged 4 times/night. The dark solid line represents the ecliptic, and the positions of some of the planets, Sun and Moon are represented with their images. The declination limit of $-30°$ is roughly $40°$ above the horizon as observed from Haleakala. (Bottom) Time series for detections in tracklets for the 2-site 'no-shift', 'half-shift' and 'full-shift' scenarios. Each of the time steps represent a transient time interval (TTI).

lets'. MOPS employes an N-body integrator and the DE406 ephemerides [Standish, 1998] to compute the position and brightness of every synthetic detection. In practice, we set the absolute magnitude of each synthetic object to $H = 0$ and turned off the MOPS system's capability of adding astrometric and photometric uncertainty to each detection so that we could modify those values *post hoc* as described below.

9.1.3 Photometric & astrometric uncertainty

Each synthetic MOPS detection had a calculated apparent magnitude m_0 corresponding to the value if the object's absolute magnitude (H) was zero. We could then assign any other absolute magnitude to the object and its *actual* apparent magnitude corresponding to that detection would then be $m^* = m_0 + H$. We then used a *reported* apparent magnitude $m = m_0 + H + \Delta m$ where $\Delta m = \texttt{max}\{0.01, G[0, \sigma(m^*)]\}$ and G represents a randomly generated number from a normal (Gaussian) distribution with a mean of zero and width $\sigma(m^*) = 0.02 \times 2^{(m^*-16)}$ appropriate for the ATLAS system. The `max` function limits the minimum photometric uncertainty to 0.01 mag.

We did not account for the effect of trailing of the detections due to the

motion of the object during an exposure [*e.g.* Vereš et al., 2012]. The neglect is justified because the large ATLAS plate scale of about 2"/pixel means that detections trail by less than 1 pixel for rates of up to 1.6°/day and the majority of the impactors that are larger than 10 m diameter move slower than this rate when they are first detected (Fig. 9.5). Main belt objects are not trailed at all because they typically move fastest near opposition at rates of about 0.25°/day. The close-approachers can move much faster but here we assume that ATLAS will apply a trail finding and fitting algorithm to maintain astrometric and photometric integrity for objects with faster rates motion.

The impact probability calculation depends on the reported astrometric uncertainty that, in turn, depends on the apparent brightness of the detections and the system's pixel scale. The reported astrometric position of each synthetic detection was 'fuzzed' by an offset $\Delta = \texttt{max}\{0.1", G[0, \sigma_p(m^*)]\}$ where the sub-script 'p' represents 'positional' uncertainty and $\sigma_p(m^*) = 2"/10^{8.5-0.4m^*}$ appropriate to the ATLAS system's 2" pixel scale and photometric performance. The `max` function ensures that the minimum astrometric uncertainty is always larger than 0.1".

9.1.4 Survey cadence

One of the main goals of this study was to demonstrate how two survey sites could improve the impact probability determination in comparison with a single site, but there are many different survey cadences that could be implemented in either scenario. We decided that a fair comparison between the two scenarios required maintaining the same combined tracklet arc-length (*i.e.* time from first to last observation) and studied three different 2-site visit cadences (see Fig. 9.3):

- **1-site (quads)**
  4 images acquired with roughly a TTI between each
- **2-site no-shift**
  2 images acquired at each site with roughly 3 TTI between them
- **2-site half-shift**
  2 images acquired at each site with roughly 2 TTI between them interleaved with the other site
- **2-site full-shift**
  2 images acquired at each site with roughly a TTI between them sequential with the other site

We will show in §9.2.3 that there is little difference in performance between the cadences, but there is a marginal benefit to the 2-site full-shift scenario and we adopt it as the nominal cadence unless otherwise specified.

9.1.5 Observability windows

For a fair comparison between the observation circumstances of our synthetic close-approachers and impactors we only considered observations of close-approachers *before* the moment of closest approach. This requirement is symmetric with the impactors because it is impossible to obtain observations of an impactor after impact.

Furthermore, because our simulated survey was only one year in duration instead of infinite, we were careful to consider only those impactors of different sizes that could be detected *before* impact. Letting D represent the impactor diameter, we defined an D-dependent 'observability window', $t_{window}(D)$. Then, letting t_{begin} and t_{end} represent the simulated survey's starting and finishing time respectively, we require that the time of impact of an object with diameter D, $t_{impact}(D)$, satisfy $t_{begin} + t_{window}(D) \leq t_{impact}(D) \leq t_{end}$, *i.e.* we require that the time of impact *and* the entire observability window be in the simulated survey time.

We defined $t_{window}(D)$ using our simulated survey and synthetic objects from which we could measure the number of days between the first detection and impact as a function of the impactor diameter (Fig. 9.4). If $\bar{t}_{first}(D)$ represents the average value as a function of diameter, and $\sigma_{first}(D)$ the standard deviation of the distribution, then we set $t_{window}(D) = \bar{t}_{first}(D) + \sigma_{first}(D)$. This time observability window encompasses the actual observability window of about 84% of the objects at each diameter but will eliminate the $\sim 16\%$ of the sample with the longest observability times. The choice reflects a balance between increasing the time observability windows and keeping more objects in the analysis — longer windows mean fewer objects satisfy the requirement. No window was applied for main belt asteroids.

9.1.6 Orbit determination and impact probability

Orbit determination is the process of identifying the best-fit least-squares orbit to an object's astrometric dataset. We used the standard differential correction procedure [Milani and Gronchi, 2010, Chap. 5] with the objects' synthetically generated orbit as the starting point. The use of the synthetic orbit as the initial orbit in the fit will skew our orbit determination and impact probability calculation towards more accurate values than could be

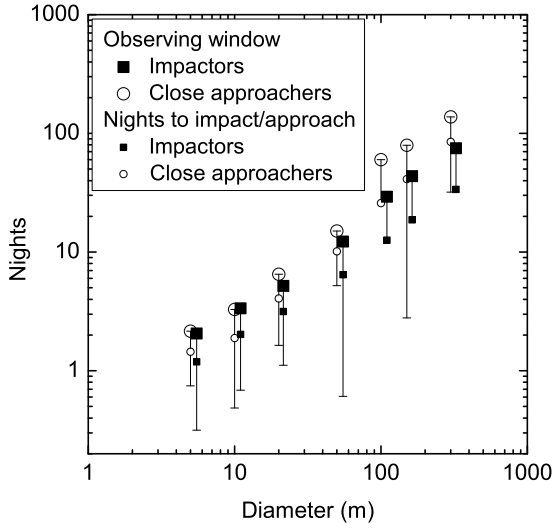

Figure 9.4: (large circles and squares) Observing window duration implemented in this study for close-approachers and impactors on their final approach. (small circles and squares) Average number of nights to closest approach or impact. By definition, the upper limits of the error bars on these data points corresponds to the observing window durations (§9.1.5).

expected from the single-survey performance in our study. We do not consider this an important issue because the NEO candidate followup community rapidly provides additional astrometry for initial orbit determination by the Minor Planet Center. It is also worth noting that we assume a high efficiency and accuracy for linking detections of the same object into tracklets and then linking the tracklets into 'tracks' [Milani and Gronchi, 2010, Chap. 8]. This is justified because the MOPS has better than 99.5% efficiency at performing this function [Denneau et al., 2013].

After an orbit was computed along with its corresponding uncertainty we computed the probability of an Earth impact. The analysis of close encounters is typically a strongly non-linear problem whose solution requires sophisticated methods [*e.g.*, Milani et al., 2005a] but we adopted a simplified approach to the calculation of the impact probability since this study only assesses its evolution in the days and weeks before impact. First we search for upcoming close approaches and then we perform a linear mapping of the orbital uncertainty region to the close encounter b-plane and compute the impact probability corresponding to the intersection between the mapped uncertainty region and Earth's cross section [Valsecchi et al., 2003]. The short-term propagation and the lack of intervening planetary encounters justifies the adoption of the simplified linear approach.

We updated the orbit determination and risk assessment night-by-night within the simulation to assess the time evolution of the impact probability. *i.e.* we incrementally added each tracklet to an object's astrometric data set and then recalculated the orbit and associated impact probability each night.

9.2 Results & Discussion

We tested the performance of the ATLAS survey for impactors and close approachers of 5, 10, 20, 50, 100, 150, and 300 meters diameter because we expected there to be a size-dependency on the ability to rapidly calculate impact probabilities. Large objects will typically be detected at larger distances where the effects of parallax are small and the lever arm to impact is large, making it difficult to assign a high probability to a possible impact. Small objects will be detected close to Earth so parallax will provide some power in the orbit solution and impact probability calculation.

9.2.1 Observable characteristics of the impactor population

The mean apparent rate of motion of impactors on the first night of detection is about 0.25 ± 0.05(rms) deg/day, essentially matching both the mean rate and distribution of typical main belt asteroids moving at 0.19 ± 0.06(rms) deg/day (Fig. 9.5).

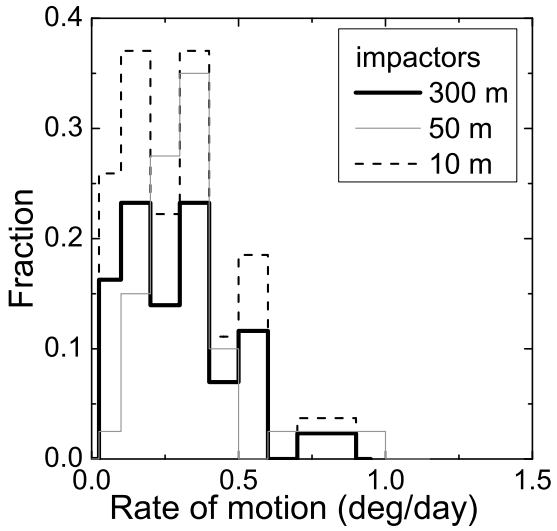

The fastest impactor rates of $\gtrsim 0.5$ deg/day mimic that of the perfectly harmless Hungaria asteroids. The Hungarias are on the inner edge of the main belt [*e.g.* Jedicke, 1996; Rabinowitz, 1991] and can have high rates of motion in ecliptic latitude because of their high inclinations. On the other hand, the Earth-grazing close-approachers typically have high apparent fly-by speeds even on their night of first detection. Their angular rate of motion extends to ~ 10 deg/day while less than 2% move slower than 0.5 deg/day.

Figure 9.6 illustrates several features of the detected impactors' sky plane motion. First, smaller objects are visible for much less time than the larger impactors, the impactors typically move westwards and mostly in longitude, and they are first detected near the system's limiting magnitude and increase in brightness as they move closer to Earth. The larger objects can be discovered almost everywhere on the night sky but the smaller objects tend to be discovered towards opposition where the reduction in apparent brightness due to phase angle effects is smallest.

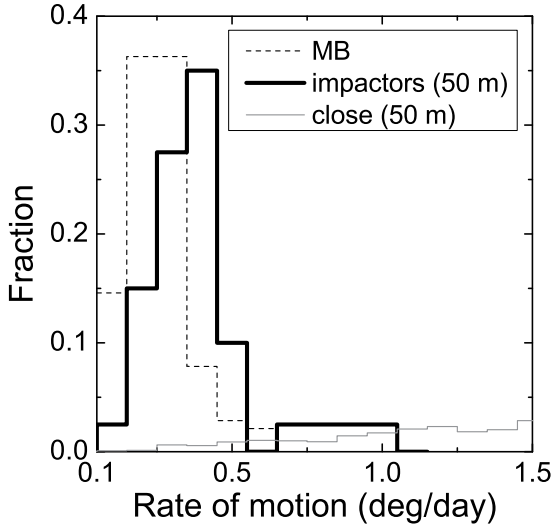

Figure 9.5: (left) Apparent rate of motion on the first night of observation for impactors with diameters of 10 m, 50 m and 300 m. (right) Apparent rate of motion on the first night of observation for impacting, close-approaching and main belt asteroids. The impactors and close-approachers both have diameters of 50 m but the main belt asteroids have a realistic size-frequency distribution.

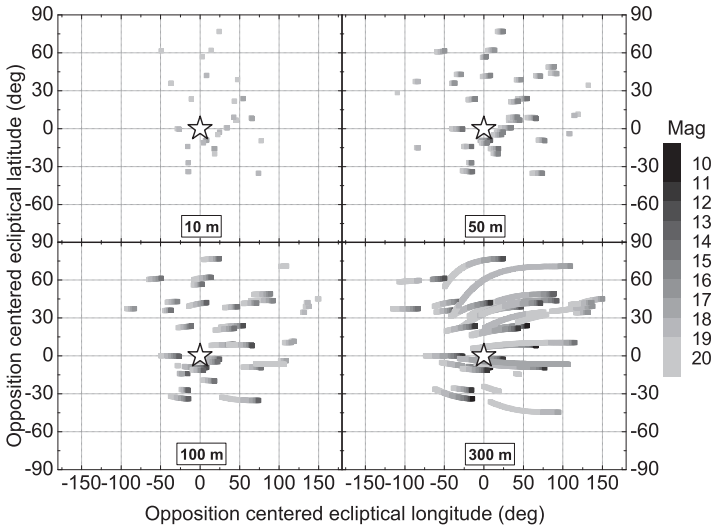

Figure 9.6: Time evolution of the sky plane position and apparent V magnitude for all the detected synthetic impactors at 4 different sizes: 10 m, 50 m, 100 m and 300 m. The coordinates are ecliptic opposition-centric with west to the right. The star symbol in the center represents opposition.

9.2.2 Detection efficiency & rates

The ATLAS pre-impact detection efficiency (Fig. 9.2.2, left) plateaus due to geometrical reasons at a maximum of about 50% even for the largest objects — ATLAS only surveys about half the sky but detects everything brighter than its limiting magnitude. The efficiency decreases for smaller objects with a particularly dramatic drop from 10 m to 5 m. *i.e.* it decreases by about half, to about 25%, from 300 m to 10 m diameter — nearly 3 orders of magnitude in the impactors cross-sectional area — but then decreases by another 50% from just 10 m to 5 m diameter (only a factor of 4 in cross-section). In this size range the objects are typically fainter than the survey system's limiting magnitude and even a nightly cadence is not sufficient to catch the objects in the brief time they are bright enough to be detected before impact.

The behavior of the detection efficiency as a function of diameter is different for close-approaching asteroids (Fig. 9.2.2, left). Remembering that for a direct comparison to the impactors we only considered close-approachers detected *before* closest approach, the detection efficiencies are identical at the largest sizes we considered. The close-approacher detection efficiency would have been much higher if we had allowed them to be detected after

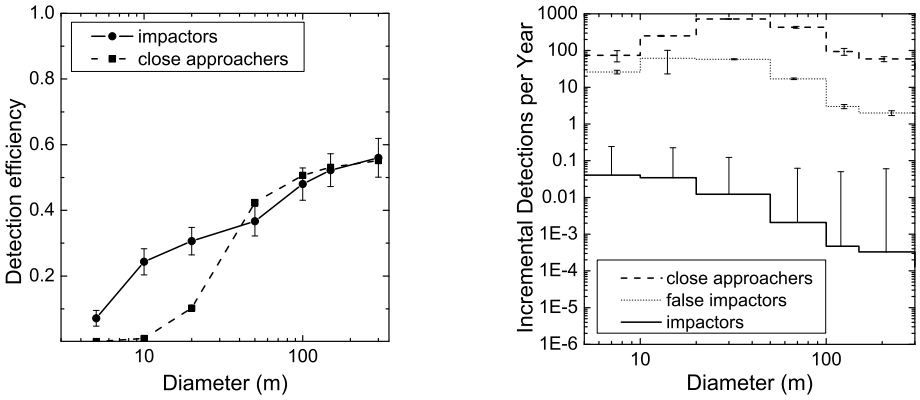

Figure 9.7: (left) Detection efficiency for synthetic impactors and close approachers as a function of object diameter and (right) our predicted incremental number of detections per year of impactors, close-approachers, and false impactors (close-approachers with a residual impact probability higher than 10^{-6} on the day of closest approach — see Fig. 9.11). Our calculation of the discovery rates used the Brown et al. [2013] impactor size-frequency distribution and impact rate. Note that the close-approacher statistics only includes objects *before* closest approach for direct comparison to the impactors.

close-approach because there would be much more time to detect them, and because objects that approach in daylight from the direction of the Sun are likely to depart and be detectable in the night time sky. The detection efficiency is slightly higher for the close-approachers in the 50 m to 150 m diameter range because these objects will be bright enough and detectable longer than the impactors. On the other hand, close-approachers smaller than 50 m diameter are detected less efficiently than the impactors because they are usually too far away and therefore too faint to be detected — 1% of the close approachers in our simulation come no closer than 1 LD while all the impactors do so by definition.

Figure 9.2.2 (right) illustrates that it is unlikely that ATLAS will detect impactors larger than 5 m diameter. There are simply not enough of them and the detection efficiency for the smaller, most frequent, impactors is less than 10%. It is dangerous to extrapolate ATLAS's ability to detect even smaller impactors in the 1-2 m diameter size range like 2008 TC_3 [*e.g.* Jenniskens et al., 2009] because the detection efficiency becomes particularly sensitive to the observing cadence and subtleties of image processing *e.g.* trail detection. However, assuming that the detection efficiency drops to just 1% for a 1 m diameter object, ATLAS might detect one impactor every few

years.

On the other hand, ATLAS will detect 100s or 1,000s of close approaching asteroids to within 10 LD because there are far more of them than impactors (scaling like the ratio of the cross sectional area of a circle with radius equal to the close-approach distance and the cross sectional area of Earth). Most of the detected close approachers will be in the 20 m to 50 m diameter range (Fig. 9.2.2, right) but there will still be 10s to 100s of detected objects outside that range. We will show in §9.2.4 that ATLAS alone can not establish that all the close-approachers are not impactors — 100s of the closest approaching objects will always have a residual non-zero impact probability unless additional observations are acquired with other optical or radar facilities.

9.2.3 Impact probability evolution for impacting asteroids

The impact probability for an impacting asteroid depends on the observed arc length and the object's distance from Earth and both depend on the size of the impactor (see Fig. 9.8). Longer arc lengths provide better orbit precision and a higher impact probability because all these objects are actually impactors. However, when an object is far from Earth the integration to the impact epoch stretches the orbital uncertainty and decreases the impact probability. The impact probability is smaller for larger diameter impactors at the same number of nights after discovery because smaller objects are likely to be observed when close to Earth and therefore closer to their impact time. The topocentric parallax in the detections and deviation from great-circle motion allow a better orbit determination, and the small amount of time to impact provides a higher impact probability.

The typically monotonically increasing impact probability that asymptotically approaches unity (Fig. 9.8) is the expected behavior though we were surprised that the single-system astrometry required about a week to reach $\sim$ 100% for the 50 m diameter impactors and a month to reach the same values at 100 m. The impact probability reached 99% an average of 2.0 ± 0.5(rms), 4.5 ± 1.8(rms), 8.9 ± 4.7(rms) and 29 ± 16(rms) days before impact for impactors of 10 m, 50 m, 100 m, and 300 m diameter at mean geocentric distances of 0.6 ± 0.4(rms) LD, 1.0 ± 0.5(rms) LD, $1.9 \pm 1.0(rms)$ LD and 5.5 ± 1.5(rms) LD respectively. Thus, even though a 300 m diameter object has nearly $1,000$ times the cross-sectional area of a 10 m diameter object, and is therefore about a $1,000$ times brighter ($\sim$ 7.5 mag) at the same topocentric distance, an imminent impact becomes definitive with only about 10 times more warning time when the larger object is only $\sim$ 5 times

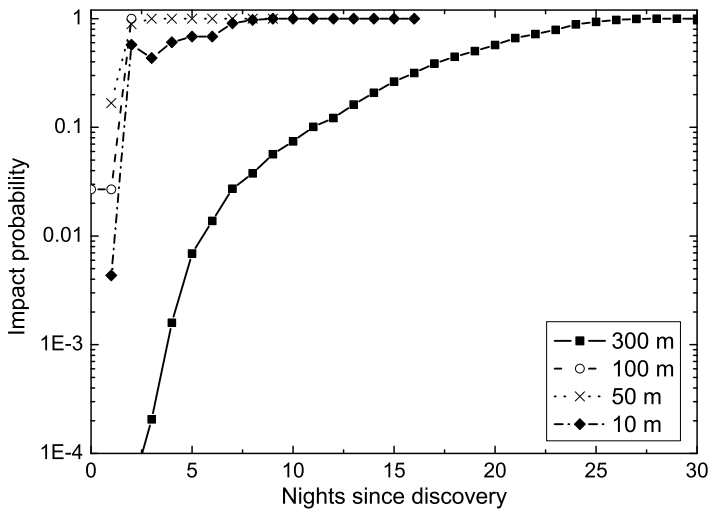

Figure 9.8: Impact probability time evolution for four synthetic objects of 10 m, 50 m, 100 m and 300 m diameter.

further away.

Of course, our calculated impact probabilities rely only on the detections from a single survey with relatively large astrometric uncertainty compared to contemporary standards (because of its all-sky coverage as described in §9.1.3). In some cases there will be nights with particularly bad astrometric error that temporarily decrease the impact probability as illustrated by the 100 m diameter example in Fig. 9.8. The detection of a real impactor with even a 10^{-6} impact probability would certainly trigger high-precision ground-based optical and radar followup that would improve the orbit determination and impact probability.

None of the four objects represented in Fig. 9.8 had an impact probability calculated on the first night. This does not mean that the impact probability was zero, only that with just one night's data the orbit determination could not converge on a full 6-parameter orbit (even when we *start* with the correct initial orbit) and its covariance matrix, but both are required for the impact probability calculation. While short-arc orbit determination methods are available they have not yet been extensively tested in their ability to provide reliable hazard assessments [*e.g.* Chesley, 2005; Milani and Knežević, 2005; Virtanen et al., 2001]. With our single survey simulation there is a $\sim 14\%$ efficiency for calculating an impact probability on the first night for 10 m diameter objects with the efficiency *decreasing* with diameter to just 2% for

300 m impactors. Therefore, it is critical to have rapid follow-up observations from other observatories to achieve a better efficiency in recognizing impactors on the discovery night — but there may be nothing particularly noteworthy about the tracklet to flag it as worthy of immediate follow-up.

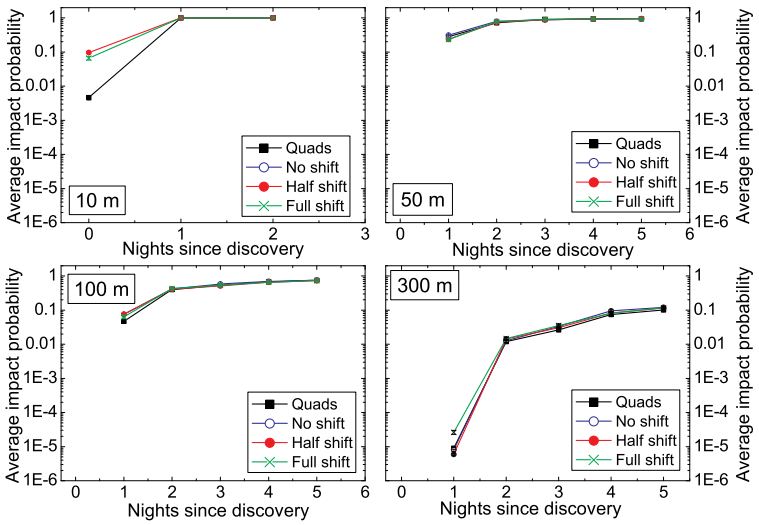

Figure 9.9: Average impact probability as a function of the number of nights since discovery for impactors of 10 m, 50 m, 100 m and 300 m diameter. The four curves correspond to the cadence scenarios illustrated in fig. 9.3 and discussed in §9.1.4. The missing data points for night zero indicates that it was not possible to calculate the impact probability on the discovery night: this is not the same as claiming the objects have zero impact probability.

The average impact probability as a function of time for an ensemble of impactors of a specific diameter (Fig. 9.9) behaves much the same as the individual examples illustrated in Fig. 9.8. The four survey cadences (§9.1.4) are essentially equivalent in terms of the numerical value and efficiency of the impact probability calculation beginning on the second night after discovery. While the efficiency for calculating an impact probability on the first night is small (discussed above), the 2-site full-shift scenario is always superior, so that combining observations from different stations does provide better constraints on the orbit and allows for an impact probability calculation. Again, we stress that this is true only on the first night of discovery and only for the small fraction of objects for which an impact probability can be calculated, so the benefits of parallax in the impact probability calculation afforded by a 2-site scenario is limited to a small fraction of the least danger-

ous impactors. We recognize that the 2-site scenario offers other advantages such as increased immunity to weather shutdowns (one site can still survey if the other is not operational) and natural disasters (such as lava flows) but at the expense of having to maintain two sites.

We define the impact warning time as the time interval between the impact epoch and the epoch at which an object's Palermo Scale [Chesley et al., 2002] ranking becomes higher than -2. We used the Palermo Scale because it is a standard tool to communicate the risk posed by a possible impact, and selected the -2 threshold as it corresponds to cases that 'merit careful monitoring'.[7]. The warning time increases with the impactor diameter as $t_{warn} \propto D^{1.1\pm0.2}$ (Fig. 9.10) — *detected* impactors *with* an orbit determination that are smaller than ~ 20 m diameter typically have less than a couple of days of warning time, 50 m diameter objects provide about one week notice, and the warning time is weeks to months for objects larger than 100 m diameter. Including those objects that were detected, but for which an orbit was impossible to calculate (even starting with the correct orbit as the initial value in the fitting procedure), the warning time increases with diameter as $t_{warn} \propto D^{1.3\pm0.1}$.

The time to impact from first detection (Δt) should increase linearly with diameter D because the geocentric distance (ρ_{limit}) at which an asteroid becomes brighter than a system's limiting magnitude (m_{limit}) is given by

$$5 \log_{10} \rho_{limit} = m_{limit} - H + \phi(r, \rho_{limit}) \tag{9.1}$$

where ϕ is a 'phase function' that depends on an object's geocentric and heliocentric (r) distance [Bowell et al., 1988]. Furthermore, $H \propto \log_{10} D$ [Pravec and Harris, 2007] so it follows that $\rho_{limit} \propto D$ assuming that ϕ is roughly constant (which is justified given that the heliocentric distance is nearly constant during the final approach ($r \sim 1$), and because ϕ depends on the phase angle which does not change much during an impacting object's final approach to Earth). Since $\rho_{limit} = v\Delta t$, where v is the speed of the impactor relative to Earth, it follows that $\Delta t \propto D$.

However, v depends on the diameter because smaller objects are detected closer to Earth where they are moving faster because they have accelerated in Earth's gravity well. Assuming that impactors fall towards Earth with similar initial v_∞ then it is not difficult to show that the speed at discovery goes roughly as $v \propto D^{1/2}$ and that $\Delta t \propto D^{3/2}$.

The impact warning time t_{warn} as we have defined it is related, but not identical to, and always $\leq \Delta t$. Thus, we expect that $t_{warn} \propto D^x$ with $1 < x < 1.5$ in agreement with our measured value of 1.3 ± 0.1. To put this

[7] http://neo.jpl.nasa.gov/risk/doc/palermo.html

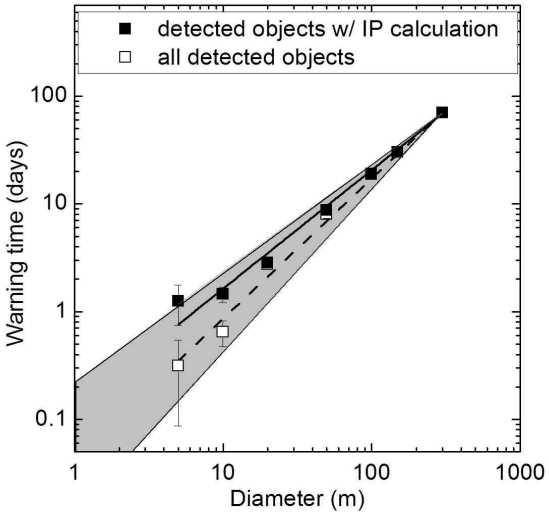

Figure 9.10: Impact warning time t_{warn} as a function of impactor diameter (D) for the ATLAS survey using the full-shift cadence (see Fig. 9.3 and §9.1.4). The error bars represent the standard error on the mean and are equal to or smaller than the data points for all but the two leftmost values. (dashed line) The fit to the data for all detected impactors (*i.e.* including those without calculated orbits and impact probabilities) with warning time given by $\log_{10}(t/\text{days}) = (1.3 \pm 0.1)\ \log_{10}(D/\text{meters}) - (1.4 \pm 0.2)$. (solid line) The fit to the objects with calculated impact probability is $\log_{10}(t/\text{days}) = (1.1 \pm 0.2)\ \log_{10}(D/\text{meters}) - (1.0 \pm 0.4)$. The grey area represents the expected range with slopes in the range $[1.0, 1.5]$ (see §9.2.3) when anchored at 300 m diameter.

in perspective, a Chelyabinsk-like impactor of 20 m diameter would typically only have a 2 day warning time *if* it was detected by an ATLAS-like survey.

9.2.4 Impact probability evolution for main belt and close-approaching asteroids

We included a sample of main belt and close-approaching asteroids to assess the survey's ability to distinguish them from impactors. The problem may be difficult when only a short arc of observations is available, in which case the orbital uncertainty is large and there may be multiple and very different initial orbits [Milani et al., 2008] consistent with the observations, some of which lead to a least-square solution far from the actual orbit.

The inclusion of the distant, slow-moving main belt asteroids may seem surprising but Fig. 9.5 illustrates that the rate of motion of impacting asteroids can be similar to that of main belt objects. Despite the similarity in their rates of motion we never found a non-zero impact probability for a synthetic main belt object with ≥ 2 days of arc. It is worth noting once again that we used the actual main belt orbit as the starting point to obtain the orbit solution — this process biases our results towards decreasing the calculated impact probability a short time after discovery.

The most likely false impactors must be PHOs that experience a close-approach to Earth. These objects might be identified as they approach Earth and the astrometric uncertainties and orbit integration may combine to produce non-zero impact probabilities. Indeed, about 30% of the close-approaching objects in our synthetic population had an impact probability higher than 10^{-6} at some time during the simulation[8] but none of the impact probabilities ever exceeded 3%.

With our single-system survey simulation (*i.e.* one or two sites) we find that even large objects, those ≥ 50 m diameter, can have non-zero impact probabilities just a few days before impact (Fig. 9.11). About 3 to 5% of the 50 m and 100 m diameter close-approachers have a persistent impact risk *on* the day of (false) impact which means that follow-up observations from other stations are critical to establish the lack of danger from these objects. A persistent impact risk remains on the day of impact for about 75% of the 10 m diameter close approachers but perhaps this is not too worrisome since they are unlikely to make it through Earth's atmosphere and cause serious ground damage. On the other hand, the opportunity for scientific study of more 2008 TC_3-like events [Jenniskens et al., 2009] is tremendous if the false

[8] 10^{-6} is the threshold typically used by NASA to rule out an impact. *e.g.* `http://www.jpl.nasa.gov/asteroidwatch/newsfeatures.cfm?release=2013-017`

alarm rate is small enough so, once again, follow-up observations are required for all these objects.

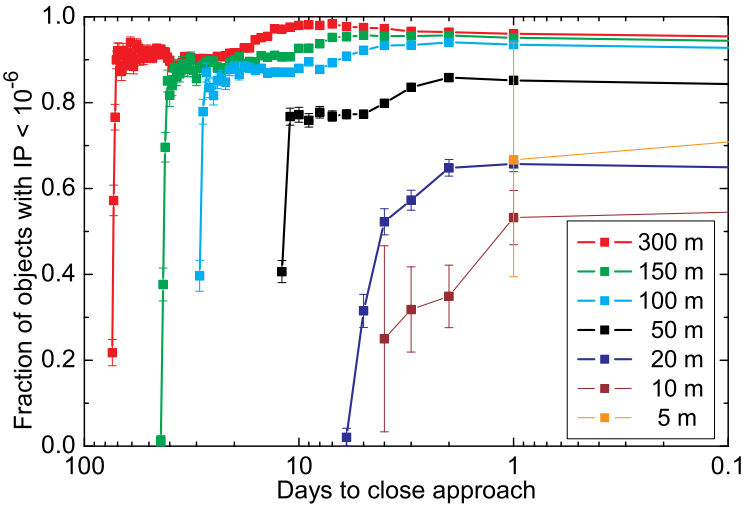

Figure 9.11: Fraction of close-approaching asteroids for which an impact is ruled out (impact probability less than 10^{-6}) as a function of the number of days before close-approach for 7 different asteroid diameters. The 'noisy' behavior on the left, corresponding to long times before impact, is mostly due to low number statistics.

We estimated the false impactor rate (fig:9.2.2, right) with the single-survey system using the [Brown et al., 2013] PHO size frequency distribution appropriate for objects in this size range, our calculated close-approacher survey efficiency (Fig. 9.2.2, left), and the fraction of them that retain a non-zero impact probability on the (false) impact date (Fig. 9.11). We find that the single all-sky survey system will generate 100s of false impactors per year for objects of $\lesssim$ 100 m diameter. Thus, rapid astrometric followup with other optical and radar facilities is imperative to reduce the false impactor rate to zero.

9.3 Conclusions

We have performed a simulation of a single all-sky asteroid survey to study the time evolution of the calculated impact probability for both real and false impactors. We also studied the utility of using two observatories at

different locations to perform the survey to take advantage of the parallactic displacement in the detections of the same object.

As expected, the impact probability for impactors typically increases monotonically with time after discovery and is larger at the time of discovery for small objects that are detected closer to Earth and with less time to impact. We found that the impact warning time, the time interval between when the impact probability reaches -2 on the Palermo Scale and when the impact takes place, increases with diameter according to $t_{warn} \propto D^{1.3}$, and developed a simple mathematical argument that the exponent should be in the range $[1.0, 1.5]$.

Close approaching asteroids can almost always be unambiguously identified as non-impactors but a small percentage will have a non-zero impact probability even on the day of (false) impact. *i.e.* the simulated survey on its own is unable to eliminate the impact risk. The fraction of objects for which a persistent impact risk exists at the time of impact increases with decreasing diameter of the object because the small objects have smaller observational arc lengths and concomitantly less precise orbit elements. The combination of the PHO size-frequency distribution with the probability of detecting false impactors suggests that the single all-sky system alone will generate 100s of potential impactors that must be ruled out with other followup facilities.

The calculated impact probability can take surprisingly long to reach $\sim 100\%$ with just the results from a single low-precision astrometric survey. The impact probability may reach 100% only a few days before impact even for 300 m diameter objects detected a month in advance and imaged nightly thereafter.

Our simulations suggest that a 2-site survey is unnecessary, at least in terms of the incremental benefit in improving the impact probability calculation. The parallax afforded by this scenario only improves the impact probability calculation for a small fraction of the smallest asteroids detected shortly before impact. The 2-site survey offers many different cadence options and some can provide more efficient impact probability calculations than others. The derived impact probability was ~ 10 times higher (*i.e.* better) on the discovery night using the 'full-shift' cadence compared to the other two cadences. This suggests that a real survey that implements the 2-site scenario should carefully test different cadences to select one that maximizes the efficiency and accuracy of the impact probability on the discovery night. The effect of survey cadence on the impact probability calculation is negligible on successive nights.

Chapter 10

Appendix

10.1 Finding the best power law to model the Yarkovsky effect

We want to find the value of d such that the transverse acceleration $A_T(r/r_0)^{-d}$, $r_0 = 1$ au, provides the best match to the Yarkovsky acceleration acting on Bennu. We can neglect the seasonal component of the Yarkovsky effect. In fact, the diurnal component is usually the dominant one [Vokrouhlický et al., 2000b]. Moreover, the obliquity of Bennu is 175° and the seasonal component vanishes when the spin axis is normal to the orbital plane [Bottke et al., 2006]. For the diurnal component of the Yarkovsky effect we have that the transverse acceleration is [Vokrouhlický, 1998a]

$$a_t = \frac{4(1-A)}{9}\phi(r)f(\Theta)\cos(\gamma)\ ,\ f(\Theta) = \frac{0.5\Theta}{1+\Theta+0.5\Theta^2} \tag{10.1}$$

where A is the Bond albedo, ϕ the standard radiation force factor at heliocentric distance r, Θ the thermal parameter, and γ the obliquity.

The dependence on r is contained in $\phi(r) \propto r^{-2}$ and $f(\Theta)$. As a matter of fact, Θ depends on the subsolar temperature $T_\star$, and $T_\star$ depends on r:

$$\Theta = \frac{\Gamma}{\epsilon\sigma T_\star^3}\sqrt{\frac{2\pi}{P}}\ ,\ T_\star = \sqrt[4]{\frac{(1-A)G_S}{\sigma\epsilon}\left(\frac{1\text{ au}}{r}\right)^2} \tag{10.2}$$

where Γ is the thermal inertia, ϵ the emissivity, σ the Stefan-Boltzmann constant, $G_S = 1365\,\mathrm{W/m^2}$ is the solar constant, and P the rotation period. Thus, $\Theta \propto r^{3/2}$.

We want to approximate $f(\Theta)$ with a power law $(r/r_0)^\psi$:

$$f(\Theta) \simeq c(r/r_0)^\psi \Longrightarrow \log f(\Theta) \simeq \log c + \psi\log(r/r_0)\ . \tag{10.3}$$

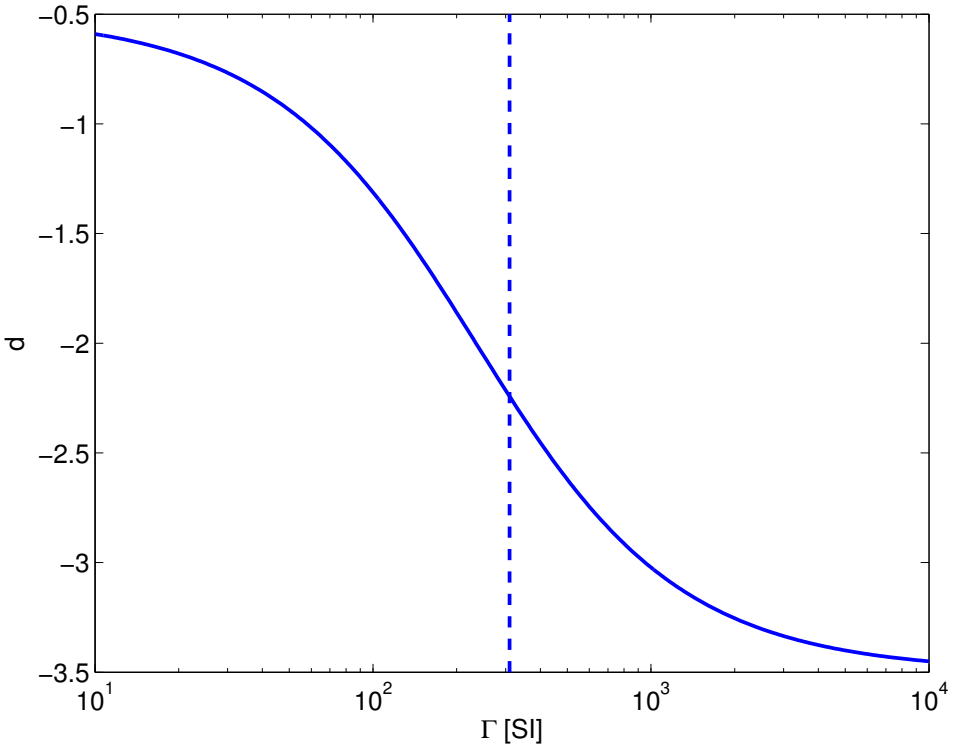

Figure 10.1: Dependency of transverse acceleration exponent d on thermal inertia Γ for Bennu.

By differentiating with respect to r we find:

$$\psi = r \left. \frac{\partial \log f(\Theta)}{\partial r} \right|_{r=r_0} . \tag{10.4}$$

From the chain rule we obtain

$$\frac{\partial \log f(\Theta)}{\partial r} = \frac{1}{f(\Theta)} \frac{\partial f(\Theta)}{\partial \Theta} \frac{\partial \Theta}{\partial r} \tag{10.5}$$

Evaluating this equation for $r = r_0$ and using the physical quantities as in Table 4.4 yield $\psi \simeq -0.24$. Therefore, $d \simeq 2.24$, which is in good agreement with the value 2.25 found numerically in Sec. 5.2.

10.2 An analytic estimate of the resonant returns cascade

We can make an analytic estimate of the range of semimajor axes of the possible post-2185 orbits [Valsecchi et al., 2003]; in doing so, we will use the b-plane coordinates ξ, which correspond to the local MOID with sign, and ζ, which is related to the timing of the encounter, as well as the values of the unperturbed geocentric velocity U (in units of the Earth orbital velocity), and of the angle θ between the velocity of the Earth and the unperturbed geocentric velocity of 2009 FD at the encounter of 2185. We assume the values of the 2185 VI, $U = 0.533$ and $\theta = 97.^{\circ}7$.

We then compute $c = m_{\oplus}/U^2$, where $m_{\oplus}$ is the mass of the Earth in units of the solar mass; c is the value of the impact parameter leading to a rotation of the geocentric velocity by 90°, and plays the role of a characteristic length for each NEA. In the case of 2009 FD $c = 0.25\ r_{\oplus}$, where $r_{\oplus}$ is the Earth radius.

The gravitational cross section of the Earth seen by 2009 FD is a disk of radius $b_{\oplus}$ [Valsecchi et al., 2003],

$$b_{\oplus} = r_{\oplus}\sqrt{1 + \frac{2c}{r_{\oplus}}} = 1.22\, r_{\oplus};$$

thus, the b-plane distance corresponding to a grazing Earth encounter is $1.22\, r_{\oplus}$.

We now turn to the possible post-encounter values of the orbital semimajor axis a' of 2009 FD, which is given by

$$a' = \frac{1}{1 - U^2 - 2U\cos\theta'};$$

in fact, as discussed by [Valsecchi et al., 2003], a' is maximum when $\cos\theta'$ is maximum, and a' is minimum when $\cos\theta'$ is minimum. We can therefore consider the expression for $\cos\theta'$ as a function of the b-plane coordinates:

$$\cos\theta' = \frac{(\xi^2 + \zeta^2 - c^2)\cos\theta + 2c\zeta\sin\theta}{\xi^2 + \zeta^2 + c^2}.$$

We use the wire approximation of [Valsecchi et al., 2003], so that ξ can be considered constant, like all other quantities in the expression, except ζ. We therefore take the partial derivative with respect to ζ,

$$\frac{\partial\cos\theta'}{\partial\zeta} = \frac{2c[2c\zeta\cos\theta + (\xi^2 - \zeta^2 + c^2)\sin\theta]}{(\xi^2 + \zeta^2 + c^2)^2},$$

and look for the zeroes $\zeta_\pm$ of its numerator:

$$\begin{aligned} 0 &= \zeta^2 \sin\theta - 2c\zeta\cos\theta - (\xi^2 + c^2)\sin\theta \\ \zeta_\pm &= \frac{c\cos\theta \pm \sqrt{c^2 + \xi^2 \sin^2\theta}}{\sin\theta}. \end{aligned}$$

Making the appropriate substitutions ($c = 0.25\, r_\oplus, |\xi| = 0.52\, r_\oplus, \theta = 97^\circ\!.7$), we get $\zeta_+ = 0.54\, r_\oplus$ and $\zeta_- = -0.61\, r_\oplus$; both values lead to values smaller than $b_\oplus$, implying that the maximum and minimum possible values for a' are obtained for grazing encounters taking place at $\zeta = \pm\sqrt{b_\oplus^2 - \xi^2} = \pm 1.11\, r_\oplus$. Thus, the maximum post-encounter a' and the related maximum orbital period P' are

$$a'_{max} = 2.10 \text{ au} \quad \textit{and} \quad P'_{max} = 3.05 \text{ yr},$$

and the minimum post-encounter a' and the related minimum orbital period P' are

$$a'_{min} = 0.82 \text{ au} \quad \textit{and} \quad P'_{min} = 0.74 \text{ yr}.$$

This range of post-2185 orbital periods for 2009 FD makes a number resonant of returns within 2196 possible, the year after which the secular increase in the MOID precludes the possibility of additional collisions with the Earth at the same node. The list of resonances is given in Table 10.1; the lines in boldface describe cases in which actual VIs are found numerically.

In Table 10.1 the columns shows, from left to right: the year of impact of the potential VI; the associated mean motion resonance; the value of the resonant post-2185 semimajor axis a'; the ζ coordinate of the keyhole center; $\partial\zeta''/\partial\zeta$, i.e., the partial derivative of the ζ coordinate on the post-2185 b-plane, taken with respect to the ζ coordinate on the 2185 b-plane; and finally an estimate of the maximum possible impact probability P_{max} for the potential VI in question. Both ζ and $\partial\zeta''/\partial\zeta$ are computed according to [Valsecchi et al., 2003]; in practice, $\partial\zeta''/\partial\zeta$ can be seen as the factor by which the stretching increases in the interval of time between the first and the second encounter.

The values of P_{max} are computed by multiplying the PDF by the maximum possible chord (i.e., the diameter of the circle of radius $b_\oplus$), and thus has to be seen as an upper limit; in this respect, it should not be considered too surprising that the potential VIs in the two top rows of Table 10.1 are not found by either of the numerical procedures described in the paper, since it may well be that the real values of the probability are significantly smaller than P_{max} because of small chords. In the same spirit, the good agreement between the values of P_{max} in Table 10.1 and those in the risk tables should not be overestimated because of the very simple dynamical model with which the analytical estimates are computed.

Table 10.1: The resonances with the mean motion of the Earth made accessible to 2009 FD by the 2185 close encounter. The lines in boldface show the resonances for which actual VIs are found numerically.

year	reson.	a' (au)	ζ (km)	$\partial\zeta''/\partial\zeta$	P_{max}
2194	7/9	1.1824	246116	8.8×10^2	2.7×10^{-6}
2189	3/4	1.2114	98818	2.5×10^3	1.1×10^{-6}
2196	8/11	1.2365	66047	1.5×10^4	1.9×10^{-7}
2192	5/7	1.2515	55426	1.4×10^4	2.1×10^{-7}
2195	7/10	1.2684	47028	2.8×10^4	1.0×10^{-7}
2188	2/3	1.3104	34570	1.5×10^4	1.9×10^{-7}
2196	7/11	1.3517	27698	8.9×10^4	3.3×10^{-8}
2193	5/8	1.3680	25736	7.5×10^4	3.9×10^{-8}
2190	3/5	1.4057	22199	6.3×10^4	4.7×10^{-8}
2197	7/12	1.4324	20288	1.8×10^5	1.6×10^{-8}
2192	4/7	1.4522	19089	1.2×10^5	2.5×10^{-8}
2194	5/9	1.4797	17667	1.8×10^5	1.7×10^{-8}
2196	6/11	1.4979	16850	2.4×10^5	1.2×10^{-8}
2187	1/2	1.5874	13820	6.3×10^4	4.7×10^{-8}
2196	5/11	1.6915	11524	4.8×10^5	6.2×10^{-9}
2194	4/9	1.7171	11083	4.2×10^5	7.0×10^{-9}
2192	3/7	1.7592	10431	3.6×10^5	8.2×10^{-9}
2197	5/12	1.7926	9970	6.7×10^5	4.4×10^{-9}
2190	2/5	1.8420	9361	3.1×10^5	9.6×10^{-9}
2193	3/8	1.9230	8511	5.7×10^5	5.3×10^{-9}
2196	4/11	1.9629	8146	8.3×10^5	3.6×10^{-9}
2188	1/3	2.0801	7220	2.6×10^5	1.2×10^{-8}
2188	4/3	0.8255	-7389	1.2×10^5	2.5×10^{-8}
2192	9/7	0.8457	-8493	2.6×10^5	1.1×10^{-8}
2189	5/4	0.8618	-9413	1.4×10^5	2.2×10^{-8}
2194	11/9	0.8748	-10204	2.8×10^5	1.1×10^{-8}
2190	6/5	0.8856	-10899	1.5×10^5	2.1×10^{-8}
2191	7/6	0.9023	-12069	1.5×10^5	2.0×10^{-8}
2192	8/7	0.9148	-13023	1.6×10^5	1.9×10^{-8}
2193	9/8	0.9245	-13819	1.7×10^5	1.8×10^{-8}
2194	10/9	0.9322	-14494	1.8×10^5	1.7×10^{-8}
2195	11/10	0.9384	-15075	1.9×10^5	1.6×10^{-8}
2196	12/11	0.9436	-15580	1.9×10^5	1.6×10^{-8}
2186	**1/1**	**1.0000**	$\mathbf{-22947}$	$\mathbf{9.2 \times 10^3}$	$\mathbf{3.3 \times 10^{-7}}$
2197	11/12	1.0597	-39074	4.2×10^4	7.4×10^{-8}
2196	10/11	1.0656	-41704	3.4×10^4	9.1×10^{-8}
2195	9/10	1.0728	-45365	2.6×10^4	1.2×10^{-7}
2194	**8/9**	**1.0817**	$\mathbf{-50811}$	$\mathbf{1.9 \times 10^4}$	$\mathbf{1.6 \times 10^{-7}}$
2193	7/8	1.0931	-59775	1.2×10^4	2.5×10^{-7}
2192	**6/7**	**1.1082**	$\mathbf{-77314}$	$\mathbf{6.6 \times 10^3}$	$\mathbf{4.8 \times 10^{-7}}$
2191	**5/6**	**1.1292**	$\mathbf{-127134}$	$\mathbf{2.1 \times 10^3}$	$\mathbf{1.6 \times 10^{-6}}$
2196	**9/11**	**1.1431**	$\mathbf{-215975}$	$\mathbf{1.4 \times 10^3}$	$\mathbf{2.6 \times 10^{-6}}$
2190	**4/5**	**1.1604**	$\mathbf{-1366152}$	$\mathbf{1.6 \times 10^1}$	$\mathbf{3.0 \times 10^{-4}}$

Bibliography

Alvarez, L. W., Alvarez, W., Asaro, F., and Michel, H. V. (1980). Extraterrestrial Cause for the Cretaceous-Tertiary Extinction. *Science*, 208:1095–1108.

Anosov, D. V. (1967). Geodesic flows on closed Riemannian manifolds with negative curvature. In *Proceeding of Stecklov Math. Institute*, volume 90 of *Proceeding of Stecklov Math. Institute*, pages 1–235.

Baer, J. and Chesley, S. R. (2008). Astrometric masses of 21 asteroids, and an integrated asteroid ephemeris. *Celestial Mechanics and Dynamical Astronomy*, 100:27–42.

Baer, J., Chesley, S. R., and Matson, R. D. (2011a). Astrometric Masses of 26 Asteroids and Observations on Asteroid Porosity. *The Astronomical Journal*, 141:143.

Baer, J., Chesley, S. R., and Matson, R. D. (2011b). Astrometric Masses of 26 Asteroids and Observations on Asteroid Porosity. *The Astronomical Journal*, 141:143.

Beekman, G. (2006). I.O Yarkovsky and the discovery of 'his' effect. *J. Hist. Astron.*, 37:71–86.

Benner, L. A. M., Ostro, S. J., Hudson, R. S., Rosema, K. D., Jurgens, R. F., Yeomans, D. K., Campbell, D. B., Chandler, J. F., and Shapiro, I. I. (2002). Radar Observations of Asteroid 3908 Nyx. *Icarus*, 158:379–388.

Bien, R. and Schubart, J. (1987). Three characteristic parameters for the Trojan group of asteroids. *Astronomy & Astrophysics*, 175:292–298.

Binzel, R. P., Rivkin, A. S., Stuart, J. S., Harris, A. W., Bus, S. J., and Burbine, T. H. (2004). Observed spectral properties of near-Earth objects: results for population distribution, source regions, and space weathering processes. *Icarus*, 170:259–294.

Borovička, J., Spurný, P., Brown, P., Wiegert, P., Kalenda, P., Clark, D., and Shrbený, L. (2013). The trajectory, structure and origin of the Chelyabinsk asteroidal impactor. *Nature*, 503:235–237.

Bottke, W. F., Morbidelli, A., Jedicke, R., Petit, J.-M., Levison, H. F., Michel, P., and Metcalfe, T. S. (2002a). Debiased Orbital and Absolute Magnitude Distribution of the Near-Earth Objects. *Icarus*, 156:399–433.

Bottke, W. F., Vokrouhlický, D., Rubincam, D. P., and Broz, M. (2002b). The Effect of Yarkovsky Thermal Forces on the Dynamical Evolution of Asteroids and Meteoroids. In Bottke, W. F., Cellino, A., Paolicchi, P., and Binzel, R. P., editors, *Asteroids III*, pages 395–408. Univ. Arizona Press, Tucson.

Bottke, W. F., Vokrouhlický, D., Broz, M., Nesvorný, D., and Morbidelli, A. (2001). Dynamical Spreading of Asteroid Families by the Yarkovsky Effect. *Science*, 294:1693–1696.

Bottke, W. F., Vokrouhlický, D., and Nesvorný, D. (2007). An asteroid breakup 160Myr ago as the probable source of the K/T impactor. *Nature*, 449:48–53.

Bottke, W. F., Vokrouhlický, D., Walsh, K., Delbò, M., Michel, P., Lauretta, D., Campins, H., Connolly, H. J., Scheeres, D., and Chesley, S. (2015). In search of the source of asteroid (101955) Bennu: Applications of the stochastic YORP model. *Icarus*, 245:191–217.

Bottke, Jr., W. F., Nolan, M. C., Melosh, H. J., Vickery, A. M., and Greenberg, R. (1996). Origin of the Spacewatch Small Earth-Approaching Asteroids. *Icarus*, 122:406–427.

Bottke, Jr., W. F., Vokrouhlický, D., Rubincam, D. P., and Nesvorný, D. (2006). The Yarkovsky and Yorp Effects: Implications for Asteroid Dynamics. *Annual Review of Earth and Planetary Sciences*, 34:157–191.

Bowell, E., Hapke, B., Domingue, D., Lumme, K., Peltoniemi, J., and Harris, A. (1988). *Asteroids II*, pages 399–433. University of Arizona Press, Tucson.

Bowell, E., Hapke, B., Domingue, D., Lumme, K., Peltoniemi, J., and Harris, A. W. (1989). Application of photometric models to asteroids. In Binzel, R. P., Gehrels, T., and Matthews, M. S., editors, *Asteroids II*, pages 524–556.

Bowen, R. (1975). ω-limit sets for axiom a diffeomorphisms. *J. Diff. Eqs.*, 18:333–356.

Broucke, R. A. and Cefola, P. J. (1972). On the Equinoctial Orbit Elements. *Celestial Mechanics*, 5:303–310.

Brouwer, D. (1951). Secular variations of the orbital elements of minor planets. *The Astronomical Journal*, 56:9–32.

Brož, M. and Morbidelli, A. (2013). The Eos family halo. *Icarus*, 223:844–849.

Brož, M., Morbidelli, A., Bottke, W. F., Rozehnal, J., Vokrouhlický, D., and Nesvorný, D. (2013a). Constraining the cometary flux through the asteroid belt during the late heavy bombardment. *Astronomy & Astrophysics*, 551:A117.

Brož, M., Morbidelli, A., Bottke, W. F., Rozehnal, J., Vokrouhlický, D., and Nesvorný, D. (2013b). Constraining the cometary flux through the asteroid belt during the late heavy bombardment. *Astronomy & Astrophysics*, 551:A117.

Brož, M., Vokrouhlický, D., Morbidelli, A., Nesvorný, D., and Bottke, W. F. (2011). Did the Hilda collisional family form during the late heavy bombardment? *Monthly Notices of the Royal Astronomical Society*, 414:2716–2727.

Brown, P. G., Assink, J. D., Astiz, L., Blaauw, R., Boslough, M. B., Borovička, J., Brachet, N., Brown, D., Campbell-Brown, M., Ceranna, L., Cooke, W., de Groot-Hedlin, C., Drob, D. P., Edwards, W., Evers, L. G., Garces, M., Gill, J., Hedlin, M., Kingery, A., Laske, G., Le Pichon, A., Mialle, P., Moser, D. E., Saffer, A., Silber, E., Smets, P., Spalding, R. E., Spurný, P., Tagliaferri, E., Uren, D., Weryk, R. J., Whitaker, R., and Krzeminski, Z. (2013). A 500-kiloton airburst over Chelyabinsk and an enhanced hazard from small impactors. *Nature*, 503:238–241.

Brozović, M., Ostro, S. J., Benner, L. A. M., Giorgini, J. D., Jurgens, R. F., Rose, R., Nolan, M. C., Hine, A. A., Magri, C., Scheeres, D. J., and Margot, J.-L. (2009). Radar observations and a physical model of Asteroid 4660 Nereus, a prime space mission target. *Icarus*, 201:153–166.

Bus, S. J. (2013). A Record of Multiple Cratering Events in the Vesta Asteroid Family. In *AAS/Division for Planetary Sciences Meeting Abstracts*,

volume 45 of *AAS/Division for Planetary Sciences Meeting Abstracts*, page #208.05.

Busch, M. W., Giorgini, J. D., Ostro, S. J., Benner, L. A. M., Jurgens, R. F., Rose, R., Hicks, M. D., Pravec, P., Kusnirak, P., Ireland, M. J., Scheeres, D. J., Broschart, S. B., Magri, C., Nolan, M. C., Hine, A. A., and Margot, J.-L. (2007). Physical modeling of near-Earth Asteroid (29075) 1950 DA. *Icarus*, 190:608–621.

Campins, H., Morbidelli, A., Tsiganis, K., de León, J., Licandro, J., and Lauretta, D. (2010). The Origin of Asteroid 101955 (1999 RQ_{36}). *The Astrophysical Journal Letters*, 721:L53–L57.

Čapek, D. and Vokrouhlický, D. (2004). The YORP effect with finite thermal conductivity. *Icarus*, 172:526–536.

Čapek, D. and Vokrouhlický, D. (2005). Accurate model for the Yarkovsky effect. In Knežević, Z. and Milani, A., editors, *IAU Colloq. 197: Dynamics of Populations of Planetary Systems*, pages 171–178.

Carbognani, A. (2011). Lightcurves and Periods of Eighteen NEAs and MBAs. *Minor Planet Bulletin*, 38:57–63.

Carpino, M., Milani, A., and Chesley, S. R. (2003). Error statistics of asteroid optical astrometric observations. *Icarus*, 166:248–270.

Carpino, M., Milani, A., and Nobili, A. M. (1987). Long-term numerical integrations and synthetic theories for the motion of the outer planets. *Astronomy & Astrophysics*, 181:182–194.

Carruba, V. (2009). An analysis of the region of the Phocaea dynamical family. *Monthly Notices of the Royal Astronomical Society*, 398:1512–1526.

Carruba, V. (2010). The stable archipelago in the region of the Pallas and Hansa dynamical families. *MNRAS*, 408:580–600.

Carruba, V., Domingos, R. C., Nesvorný, D., Roig, F., Huaman, M. E., and Souami, D. (2013). A multidomain approach to asteroid families' identification. *Monthly Notices of the Royal Astronomical Society*, 433:2075–2096.

Carruba, V. and Michtchenko, T. A. (2007). A frequency approach to identifying asteroid families. *Astronomy & Astrophysics*, 475:1145–1158.

Carry, B. (2012). Density of asteroids. *Planetary and Space Science*, 73:98–118.

Cellino, A., Bagnulo, S., Tanga, P., Novaković, B., and Delbò, M. (2014). A successful search for hidden Barbarians in the Watsonia asteroid family. *Monthly Notices of the Royal Astronomical Society*, 439:L75–L79.

Cellino, A., Belskaya, I. N., Bendjoya, P., Di Martino, M., Gil-Hutton, R., Muinonen, K., and Tedesco, E. F. (2006). The strange polarimetric behavior of Asteroid (234) Barbara. *Icarus*, 180:565–567.

Cellino, A., Bus, S. J., Doressoundiram, A., and Lazzaro, D. (2002). Spectroscopic Properties of Asteroid Families. *Asteroids III*, pages 633–643.

Cellino, A., Gil-Hutton, R., Dell'Oro, A., Bendjoya, P., Cañada-Assandri, M., and Di Martino, M. (2012). A new calibration of the albedo-polarization relation for the asteroids. *Journal of Quantitative Spectroscopy and Radiative Transfer*, 113:2552–2560.

Cellino, A., Michel, P., Tanga, P., Zappalà, V., Paolicchi, P., and Dell'Oro, A. (1999). The Velocity-Size Relationship for Members of Asteroid Families and Implications for the Physics of Catastrophic Collisions. *Icarus*, 141:79–95.

Cellino, A., Zappalà, V., Doressoundiram, A., Di Martino, M., Bendjoya, P., Dotto, E., and Migliorini, F. (2001). The Puzzling Case of the Nysa-Polana Family. *Icarus*, 152:225–237.

Chao, E. C. T., Shoemaker, E. M., and Madsen, B. M. (1960). First Natural Occurrence of Coesite. *Science*, 132:220–222.

Chapman, C. R., Ryan, E. V., Merline, W. J., Neukum, G., Wagner, R., Thomas, P. C., Veverka, J., and Sullivan, R. J. (1996). Cratering on Ida. *Icarus*, 120:77–86.

Chesley, S. R. (2005). Very short arc orbit determination: the case of asteroid 2004 FU_{162}. In Knežević, Z. and Milani, A., editors, *IAU Colloq. 197: Dynamics of Populations of Planetary Systems*, pages 255–258.

Chesley, S. R. (2006). Potential impact detection for Near-Earth asteroids: the case of 99942 Apophis (2004 MN 4). In Lazzaro, D., Ferraz-Mello, S., and Fernández, J. A., editors, *Asteroids, Comets, Meteors*, volume 229 of *IAU Symposium*, pages 215–228.

Chesley, S. R., Baer, J., and Monet, D. G. (2010). Treatment of star catalog biases in asteroid astrometric observations. *Icarus*, 210:158–181.

Chesley, S. R., Chodas, P. W., Milani, A., Valsecchi, G. B., and Yeomans, D. K. (2002). Quantifying the Risk Posed by Potential Earth Impacts. *Icarus*, 159:423–432.

Chesley, S. R., Farnocchia, D., Nolan, M. C., Vokrouhlický, D., Chodas, P. W., Milani, A., Spoto, F., Rozitis, B., Benner, L. A. M., Bottke, W. F., Busch, M. W., Emery, J. P., Howell, E. S., Lauretta, D. S., Margot, J.-L., and Taylor, P. A. (2014). Orbit and bulk density of the OSIRIS-REx target Asteroid (101955) Bennu. *Icarus*, 235:5–22.

Chesley, S. R., Milani, A., Tholen, D., Bernardi, F., Chodas, P., and Micheli, M. (2009). An Updated Assessment Of The Impact Threat From 99942 Apophis. In *AAS/Division for Planetary Sciences Meeting Abstracts #41*, volume 41 of *AAS/Division for Planetary Sciences Meeting Abstracts*, page #43.06.

Chesley, S. R., Nolan, M. C., Farnocchia, D., Milani, A., Emery, J., Vokrouhlický, D., Lauretta, D. S., Taylor, P. A., Benner, L. A. M., Giorgini, J. D., Brozovic, M., Busch, M. W., Margot, J.-L., Howell, E. S., Naidu, S. P., Valsecchi, G. B., and Bernardi, F. (2012). The Trajectory Dynamics of Near-Earth Asteroid 101955 (1999 RQ36). *LPI Contributions*, 1667:6470.

Chesley, S. R., Ostro, S. J., Vokrouhlický, D., Čapek, D., Giorgini, J. D., Nolan, M. C., Margot, J.-L., Hine, A. A., Benner, L. A. M., and Chamberlin, A. B. (2003). Direct Detection of the Yarkovsky Effect by Radar Ranging to Asteroid 6489 Golevka. *Science*, 302:1739–1742.

Chesley, S. R. and Spahr, T. B. (2004). Earth impactors: orbital characteristics and warning times. In *Mitigation of Hazardous Comets and Asteroids*, pages 22–37.

Chesley, S. R., Vokrouhlický, D., Ostro, S. J., Benner, L. A. M., Margot, J.-L., Matson, R. L., Nolan, M. C., and Shepard, M. K. (2008). Direct Estimation of Yarkovsky Accelerations on Near-Earth Asteroids. *LPI Contributions*, 1405:8330.

Chodas, P. W. (1999). Orbit uncertainties, keyholes, and collision probabilities. In *Bulletin of the American Astronomical Society*, volume 31 of *Bulletin of the American Astronomical Society*, page 1117.

Chodas, P. W. and Yeomans, D. K. (1999). Predicting close approaches and estimating impact probabilities for near-Earth objects. Paper AAS 99-462, AAS/AIAA Astrodynamics Specialists Conference, Girdwood, Alaska.

Clark, B. E., Binzel, R. P., Howell, E. S., Cloutis, E. A., Ockert-Bell, M., Christensen, P., Barucci, M. A., DeMeo, F., Lauretta, D. S., Connolly, H., Soderberg, A., Hergenrother, C., Lim, L., Emery, J., and Mueller, M. (2011). Asteroid (101955) 1999 RQ36: Spectroscopy from 0.4 to 2.4 μm and meteorite analogs. *Icarus*, 216:462–475.

Consolmagno, G., Britt, D., and Macke, R. (2008). The significance of meteorite density and porosity. *Chemie der Erde / Geochemistry*, 68:1–29.

Cotto-Figueroa, D., Statler, T. S., Richardson, D. C., and Tanga, P. (2013). Killing the YORP Cycle: A Stochastic and Self-Limiting YORP Effect. In *AAS/Division for Planetary Sciences Meeting Abstracts*, volume 45 of *AAS/Division for Planetary Sciences Meeting Abstracts*, page #106.09.

Damour, T., Soffel, M., and Xu, C. (1994). General-relativistic celestial mechanics. IV. Theory of satellite motion. *Physical Review D*, 49:618–635.

De Angelis, G. (1995). Asteroid spin, pole and shape determinations. *Planetary and Space Science*, 43:649–682.

Delbó, M., Dell'Oro, A., Harris, A. W., Mottola, S., and Mueller, M. (2007). Thermal inertia of near-Earth asteroids and implications for the magnitude of the Yarkovsky effect. *Icarus*, 190:236–249.

Delbó, M., Harris, A. W., Binzel, R. P., Pravec, P., and Davies, J. K. (2003). Keck observations of near-Earth asteroids in the thermal infrared. *Icarus*, 166:116–130.

Delbò, M. and Michel, P. (2011). Temperature History and Dynamical Evolution of (101955) 1999 RQ 36: A Potential Target for Sample Return from a Primitive Asteroid. *The Astrophysical Journal Letters*, 728:L42.

Delisle, J.-B. and Laskar, J. (2012). Chaotic diffusion of the Vesta family induced by close encounters with massive asteroids. *Astronomy & Astrophysics*, 540:A118.

Dell'Oro, A., Cellino, A., and Paolicchi, P. (2012). Non-destructive collisions and the evolution of the orbits of binary asteroid systems in the Main Belt. *Monthly Notices of the Royal Astronomical Society*, 425:1492–1503.

DeMeo, F. E., Binzel, R. P., Slivan, S. M., and Bus, S. J. (2009). An extension of the Bus asteroid taxonomy into the near-infrared. *Icarus*, 202:160–180.

Denneau, L., Jedicke, R., Grav, T., Granvik, M., Kubica, J., Milani, A., Vereš, P., Wainscoat, R., Chang, D., Pierfederici, F., Kaiser, N., Chambers, K. C., Heasley, J. N., Magnier, E. A., Price, P. A., Myers, J., Kleyna, J., Hsieh, H., Farnocchia, D., Waters, C., Sweeney, W. H., Green, D., Bolin, B., Burgett, W. S., Morgan, J. S., Tonry, J. L., Hodapp, K. W., Chastel, S., Chesley, S., Fitzsimmons, A., Holman, M., Spahr, T., Tholen, D., Williams, G. V., Abe, S., Armstrong, J. D., Bressi, T. H., Holmes, R., Lister, T., McMillan, R. S., Micheli, M., Ryan, E. V., Ryan, W. H., and Scotti, J. V. (2013). The Pan-STARRS Moving Object Processing System. *Publications of the Astronomical Society of the Pacific*, 125:357–395.

Desmars, J., Bancelin, D., Hestroffer, D., and Thuillot, W. (2013). Statistical and numerical study of asteroid orbital uncertainty. *Astronomy & Astrophysics*, 554:A32.

Drummond, J. D. and Wisniewski, W. Z. (1990). The rotational poles and shapes of 1580 Betulia and 3908 (1980PA) from one apparition. *Icarus*, 83:349–359.

Durda, D. D., Bottke, W. F., Enke, B. L., Merline, W. J., Asphaug, E., Richardson, D. C., and Leinhardt, Z. M. (2004). The formation of asteroid satellites in large impacts: results from numerical simulations. *Icarus*, 170:243–257.

Durda, D. D., Bottke, W. F., Nesvorný, D., Enke, B. L., Merline, W. J., Asphaug, E., and Richardson, D. C. (2007). Size-frequency distributions of fragments from SPH/ N-body simulations of asteroid impacts: Comparison with observed asteroid families. *Icarus*, 186:498–516.

Ďurech, J., Vokrouhlický, D., Baransky, A. R., Breiter, S., Burkhonov, O. A., Cooney, W., Fuller, V., Gaftonyuk, N. M., Gross, J., Inasaridze, R. Y., Kaasalainen, M., Krugly, Y. N., Kvaratshelia, O. I., Litvinenko, E. A., Macomber, B., Marchis, F., Molotov, I. E., Oey, J., Polishook, D., Pollock, J., Pravec, P., Sárneczky, K., Shevchenko, V. G., Slyusarev, I., Stephens, R., Szabó, G., Terrell, D., Vachier, F., Vanderplate, Z., Viikinkoski, M., and Warner, B. D. (2012). Analysis of the rotation period of asteroids (1865) Cerberus, (2100) Ra-Shalom, and (3103) Eger - search for the YORP effect. *Astronomy & Astrophysics*, 547:A10.

Ďurech, J., Vokrouhlický, D., Kaasalainen, M., Higgins, D., Krugly, Y. N., Gaftonyuk, N. M., Shevchenko, V. G., Chiorny, V. G., Hamanowa, H., Hamanowa, H., Reddy, V., and Dyvig, R. R. (2008a). Detection of the

YORP effect in asteroid (1620) Geographos. *Astronomy & Astrophysics*, 489:L25–L28.

Ďurech, J., Vokrouhlický, D., Kaasalainen, M., Weissman, P., Lowry, S. C., Beshore, E., Higgins, D., Krugly, Y. N., Shevchenko, V. G., Gaftonyuk, N. M., Choi, Y.-J., Kowalski, R. A., Larson, S., Warner, B. D., Marshalkina, A. L., Ibrahimov, M. A., Molotov, I. E., Michałowski, T., and Kitazato, K. (2008b). New photometric observations of asteroids (1862) Apollo and (25143) Itokawa - an analysis of YORP effect. *Astronomy & Astrophysics*, 488:345–350.

Emery, J. P., Fernández, Y. R., Kelley, M. S., Hergenrother, C., Ziffer, J., Lauretta, D. S., Drake, M. J., and Campins, H. (2010). Thermophysical Characterization of Potential Spacecraft Target (101955) 1999 RQ36. In *Lunar and Planetary Institute Science Conference Abstracts*, volume 41 of *Lunar and Planetary Institute Science Conference Abstracts*, page 2282.

Emery, J. P., Fernandez, Y. R., Kelley, M. S. P., Warden, K. T., Hergenrother, C. W., Lauretta, D. S., Drake, M. J., Campins, H., and Ziffer, J. (2014). Thermal Infrared Observations and Thermophysical Characterization of OSIRIS-REx Target Asteroid (101955) Bennu. *Icarus*. In press.

Emery, J. P., Kelley, M. S., Fernandez, Y. R., Hergenrother, C. W., Crane, K. T., Ziffer, J., Campins, H., Lauretta, D. S., and Drake, M. J. (2012). Thermal and Physical Characterization of the OSIRIS-REx Target Asteroid (101955) 1999 RQ36. In *AAS/Division for Planetary Sciences Meeting Abstracts*, volume 44 of *AAS/Division for Planetary Sciences Meeting Abstracts*, page 102.05.

Farinella, P., Davis, D. R., and Marzari, F. (1996). Asteroid Families, Old and Young. In Rettig, T. and Hahn, J. M., editors, *Completing the Inventory of the Solar System*, volume 107 of *Astronomical Society of the Pacific Conference Series*, pages 45–55.

Farinella, P., Vokrouhlický, D., and Hartmann, W. K. (1998). Meteorite delivery via Yarkovsky orbital drift. *Icarus*, 132:378–387.

Farnocchia, D., Bernardi, F., and Valsecchi, G. B. (2012). Efficiency of a wide-area survey in achieving short- and long-term warning for small impactors. *Icarus*, 219:41–47.

Farnocchia, D. and Chesley, S. R. (2014). Assessment of the 2880 impact threat from Asteroid (29075) 1950 DA. *Icarus*, 229:321–327.

Farnocchia, D., Chesley, S. R., Chodas, P. W., Micheli, M., Tholen, D. J., Milani, A., Elliott, G. T., and Bernardi, F. (2013a). Yarkovsky-driven impact risk analysis for asteroid (99942) Apophis. *Icarus*, 224:192–200.

Farnocchia, D., Chesley, S. R., Tholen, D. J., and Micheli, M. (2014). High precision predictions for near-Earth asteroids: the strange case of (3908) Nyx. *Celestial Mechanics and Dynamical Astronomy*, 119:301–312.

Farnocchia, D., Chesley, S. R., Vokrouhlický, D., Milani, A., Spoto, F., and Bottke, W. F. (2013b). Near Earth Asteroids with measurable Yarkovsky effect. *Icarus*, 224:1–13.

Folkner, W. M. (2011). Planetary ephemeris DE424 for Mars Science Laboratory early cruise navigation. Technical Report IOM 343R-11-003, Jet Propulsion Laboratory.

Folkner, W. M., Williams, J. G., Boggs, D. H., Park, R. S., and Kuchynka, P. (2014). The Planetary and Lunar Ephemerides DE430 and DE431. *Interplanetary Network Progress Report*, 196:C1.

Fujiwara, A., Cerroni, P., Davis, D., Ryan, E., and di Martino, M. (1989). Experiments and scaling laws for catastrophic collisions. In Binzel, R. P., Gehrels, T., and Matthews, M. S., editors, *Asteroids II*, pages 240–265.

Giorgini, J. D., Benner, L. A. M., Ostro, S. J., Nolan, M. C., and Busch, M. W. (2008). Predicting the Earth encounters of (99942) Apophis. *Icarus*, 193:1–19.

Giorgini, J. D., Ostro, S. J., Benner, L. A. M., Chodas, P. W., Chesley, S. R., Hudson, R. S., Nolan, M. C., Klemola, A. R., Standish, E. M., Jurgens, R. F., Rose, R., Chamberlin, A. B., Yeomans, D. K., and Margot, J.-L. (2002). Asteroid 1950 DA's Encounter with Earth in 2880: Physical Limits of Collision Probability Prediction. *Science*, 296:132–136.

Grav, T., Jedicke, R., Denneau, L., Chesley, S., Holman, M. J., and Spahr, T. B. (2011). The Pan-STARRS Synthetic Solar System Model: A Tool for Testing and Efficiency Determination of the Moving Object Processing System. *Publications of the Astronomical Society of the Pacific*, 123:423–447.

Greenberg, R., Bottke, W. F., Nolan, M., Geissler, P., Petit, J.-M., Durda, D. D., Asphaug, E., and Head, J. (1996). Collisional and Dynamical History of Ida. *Icarus*, 120:106–118.

Gronchi, G. F. (2005). An Algebraic Method to Compute the Critical Points of the Distance Function Between Two Keplerian Orbits. *Celestial Mechanics and Dynamical Astronomy*, 93:295–329.

Gwyn, S. D. J., Hill, N., and Kavelaars, J. J. (2012). SSOS: A Moving-Object Image Search Tool for Asteroid Precovery. *PASP*, 124:579–585.

Henrard, J. (1990). A semi-numerical perturbation method for separable Hamiltonian systems. *Celestial Mechanics and Dynamical Astronomy*, 49:43–67.

Hicks, M., Mayes, D., McAuley, A., and Foster, J. (2010). Broadband Photometry of the Potentially Hazardous Asteroid 1999 MN: Suggestive of YORP and/or Tidal Spin-Up? *The Astronomer's Telegram*, 2706:1.

Hirayama, K. (1918). Groups of asteroids probably of common origin. *Astronomical Journal*, 31:185–188.

Hirayama, K. (1923). Families of asteroids. *Japan Journal of Astronomy and Geophysics*, 1:55–93.

Hirayama, K. (1928). Families of asteroids, second paper. *Japan Journal of Astronomy and Geophysics*, 5:137–162.

Hodapp, K. W., Kaiser, N., Aussel, H., Burgett, W., Chambers, K. C., Chun, M., Dombeck, T., Douglas, A., Hafner, D., Heasley, J., Hoblitt, J., Hude, C., Isani, S., Jedicke, R., Jewitt, D., Laux, U., Luppino, G. A., Lupton, R., Maberry, M., Magnier, E., Mannery, E., Monet, D., Morgan, J., Onaka, P., Price, P., Ryan, A., Siegmund, W., Szapudi, I., Tonry, J., Wainscoat, R., and Waterson, M. (2004). Design of the Pan-STARRS telescopes. *Astronomische Nachrichten*, 325:636–642.

Holsapple, K., Giblin, I., Housen, K., Nakamura, A., and Ryan, E. (2002). Asteroid Impacts: Laboratory Experiments and Scaling Laws. *Asteroids III*, pages 443–462.

Hudson, R. S., Ostro, S. J., Jurgens, R. F., Rosema, K. D., Giorgini, J. D., Winkler, R., Rose, R., Choate, D., Cormier, R. A., Franck, C. R., Frye, R., Howard, D., Kelley, D., Littlefair, R., Slade, M. A., Benner, L. A. M., Thomas, M. L., Mitchell, D. L., Chodas, P. W., Yeomans, D. K., Scheeres, D. J., Palmer, P., Zaitsev, A., Koyama, Y., Nakamura, A., Harris, A. W., and Meshkov, M. N. (2000). Radar Observations and Physical Model of Asteroid 6489 Golevka. *Icarus*, 148:37–51.

Ivezić, Ž., Tabachnik, S., Rafikov, R., Lupton, R. H., Quinn, T., Hammergren, M., Eyer, L., Chu, J., Armstrong, J. C., Fan, X., Finlator, K., Geballe, T. R., Gunn, J. E., Hennessy, G. S., Knapp, G. R., Leggett, S. K., Munn, J. A., Pier, J. R., Rockosi, C. M., Schneider, D. P., Strauss, M. A., Yanny, B., Brinkmann, J., Csabai, I., Hindsley, R. B., Kent, S., Lamb, D. Q., Margon, B., McKay, T. A., Smith, J. A., Waddel, P., York, D. G., and SDSS Collaboration (2001). Solar System Objects Observed in the Sloan Digital Sky Survey Commissioning Data. *The Astronomical Journal*, 122:2749–2784.

Jedicke, R. (1996). Detection of Near Earth Asteroids Based Upon Their Rates of Motion. *The Astronomical Journal*, 111:970.

Jenniskens, P., Shaddad, M. H., Numan, D., Elsir, S., Kudoda, A. M., Zolensky, M. E., Le, L., Robinson, G. A., Friedrich, J. M., Rumble, D., Steele, A., Chesley, S. R., Fitzsimmons, A., Duddy, S., Hsieh, H. H., Ramsay, G., Brown, P. G., Edwards, W. N., Tagliaferri, E., Boslough, M. B., Spalding, R. E., Dantowitz, R., Kozubal, M., Pravec, P., Borovicka, J., Charvat, Z., Vaubaillon, J., Kuiper, J., Albers, J., Bishop, J. L., Mancinelli, R. L., Sandford, S. A., Milam, S. N., Nuevo, M., and Worden, S. P. (2009). The impact and recovery of asteroid 2008 TC_3. *Nature*, 458:485–488.

Jewitt, D. and Li, J. (2010). Activity in Geminid Parent (3200) Phaethon. *The Astronomical Journal*, 140:1519–1527.

Jutzi, M., Asphaug, E., Gillet, P., Barrat, J.-A., and Benz, W. (2013). The structure of the asteroid 4 Vesta as revealed by models of planet-scale collisions. *Nature*, 494:207–210.

Kaiser, N., Aussel, H., Burke, B. E., Boesgaard, H., Chambers, K., Chun, M. R., Heasley, J. N., Hodapp, K.-W., Hunt, B., Jedicke, R., Jewitt, D., Kudritzki, R., Luppino, G. A., Maberry, M., Magnier, E., Monet, D. G., Onaka, P. M., Pickles, A. J., Rhoads, P. H. H., Simon, T., Szalay, A., Szapudi, I., Tholen, D. J., Tonry, J. L., Waterson, M., and Wick, J. (2002). Pan-STARRS: A Large Synoptic Survey Telescope Array. In Tyson, J. A. and Wolff, S., editors, *Society of Photo-Optical Instrumentation Engineers (SPIE) Conference Series*, volume 4836 of *Society of Photo-Optical Instrumentation Engineers (SPIE) Conference Series*, pages 154–164.

Kessler, D. J. (1981). Derivation of the collision probability between orbiting objects The lifetimes of Jupiter's outer moons. *Icarus*, 48:39–48.

Knežević, Z. (1989). Asteroid long-periodic perturbations: the second order Hamiltonian. *Celestial Mechanics and Dynamical Astronomy*, 46:147–158.

Knežević, Z. (1993). Minor planet short-periodic perturbations: the indirect part of the disturbing function. *Celestial Mechanics and Dynamical Astronomy*, 55:387–404.

Knežević, Z., Froeschle, C., Lemaitre, A., Milani, A., and Morbidelli, A. (1995). Comparison between two theories of asteroid proper elements. *Astronomy & Astrophysics*, 293:605–612.

Knežević, Z. and Milani, A. (2000). Synthetic Proper Elements for Outer Main Belt Asteroids. *Celestial Mechanics and Dynamical Astronomy*, 78:17–46.

Knežević, Z. and Milani, A. (2003). Proper element catalogs and asteroid families. *Astronomy & Astrophysics*, 403:1165–1173.

Knežević, Z., Milani, A., Cellino, A., Novaković, B., Spoto, F., and Paolicchi, P. (2014). Automated classification of asteroids into families at work. In Knežević, Z. and Lemaitre, A., editors, *Complex Planetary Systems*, Proceedings of the IAU Symposia, Cambridge Univ. Press, pages 130–133.

Konopliv, A. S., Asmar, S. W., Folkner, W. M., Karatekin, Ö., Nunes, D. C., Smrekar, S. E., Yoder, C. F., and Zuber, M. T. (2011). Mars high resolution gravity fields from MRO, Mars seasonal gravity, and other dynamical parameters. *Icarus*, 211:401–428.

Kozai, Y. (1962). Secular perturbations of asteroids with high inclination and eccentricity. *The Astronomical Journal*, 67:591–598.

Kozai, Y. (1979). The dynamical evolution of the Hirayama family. *Asteroids*, pages 334–358.

Küppers, M., O'Rourke, L., Bockelée-Morvan, D., Zakharov, V., Lee, S., von Allmen, P., Carry, B., Teyssier, D., Marston, A., Müller, T., Crovisier, J., Barucci, M. A., and Moreno, R. (2014). Localized sources of water vapour on the dwarf planet (1)Ceres. *Nature*, 505:525–527.

La Spina, A., Paolicchi, P., Kryszczyńska, A., and Pravec, P. (2004). Retrograde spins of near-Earth asteroids from the Yarkovsky effect. *Nature*, 428:400–401.

La Spina, A., Paolicchi, P., and Penco, U. (2005). Yarkovsky-evolved asteroid dynamical families: a correlation between their present properties and the impact geometry? In *AAS/Division for Planetary Sciences Meeting Abstracts #37*, volume 37 of *Bulletin of the American Astronomical Society*, page 641.

Landolt, A. U. (1992). UBVRI photometric standard stars in the magnitude range 11.5-16.0 around the celestial equator. *Astronomical Journal*, 104:340–371.

Larson, S., Brownlee, J., Hergenrother, C., and Spahr, T. (1998). The Catalina Sky Survey for NEOs. In *Bulletin of the American Astronomical Society*, volume 30 of *Bulletin of the American Astronomical Society*, page 1037.

Laskar, J., Gastineau, M., Delisle, J.-B., Farrés, A., and Fienga, A. (2011). Strong chaos induced by close encounters with Ceres and Vesta. *Astronomy & Astrophysics*, 532:L4.

Lemaitre, A. (1993). Proper elements: what are they? *Celestial Mechanics and Dynamical Astronomy*, 56:103–119.

Lemaitre, A. (1994). Hungaria: a potential new family. In Kozai, Y., Binzel, R. P., and Hirayam, T., editors, *Seventy-Five Years of Hirayama Asteroid Families: The Role of Collisions in the Solar System History*, volume 63 of *ASP Conf. Ser.*, pages 140–145.

Lemaitre, A. and Morbidelli, A. (1994). Proper elements for highly inclined asteroidal orbits. *Celestial Mechanics and Dynamical Astronomy*, 60:29–56.

Li, J.-Y., McFadden, L. A., Parker, J. W., Young, E. F., Stern, S. A., Thomas, P. C., Russell, C. T., and Sykes, M. V. (2006). Photometric analysis of 1 Ceres and surface mapping from HST observations. *Icarus*, 182:143–160.

Mainzer, A., Bauer, J., Grav, T., Masiero, J., Cutri, R. M., Dailey, J., Eisenhardt, P., McMillan, R. S., Wright, E., Walker, R., Jedicke, R., Spahr, T., Tholen, D., Alles, R., Beck, R., Brandenburg, H., Conrow, T., Evans, T., Fowler, J., Jarrett, T., Marsh, K., Masci, F., McCallon, H., Wheelock, S., Wittman, M., Wyatt, P., DeBaun, E., Elliott, G., Elsbury, D., Gautier, IV, T., Gomillion, S., Leisawitz, D., Maleszewski, C., Micheli, M., and Wilkins, A. (2011a). Preliminary Results from NEOWISE: An Enhancement to the Wide-field Infrared Survey Explorer for Solar System Science. *The Astrophysical Journal*, 731:53.

Mainzer, A., Bauer, J., Grav, T., Masiero, J., Cutri, R. M., Wright, E., Nugent, C. R., Stevenson, R., Clyne, E., Cukrov, G., and Masci, F. (2014). The Population of Tiny Near-Earth Objects Observed by NEOWISE. *The Astrophysical Journal*, 784:110.

Mainzer, A., Grav, T., Bauer, J., Masiero, J., McMillan, R. S., Cutri, R. M., Walker, R., Wright, E., Eisenhardt, P., Tholen, D. J., Spahr, T., Jedicke, R., Denneau, L., DeBaun, E., Elsbury, D., Gautier, T., Gomillion, S., Hand, E., Mo, W., Watkins, J., Wilkins, A., Bryngelson, G. L., Del Pino Molina, A., Desai, S., Gómez Camus, M., Hidalgo, S. L., Konstantopoulos, I., Larsen, J. A., Maleszewski, C., Malkan, M. A., Mauduit, J.-C., Mullan, B. L., Olszewski, E. W., Pforr, J., Saro, A., Scotti, J. V., and Wasserman, L. H. (2011b). NEOWISE Observations of Near-Earth Objects: Preliminary Results. *The Astrophysical Journal*, 743:156.

Marchi, S., McSween, H. Y., O'Brien, D. P., Schenk, P., De Sanctis, M. C., Gaskell, R., Jaumann, R., Mottola, S., Preusker, F., Raymond, C. A., Roatsch, T., and Russell, C. T. (2012). The Violent Collisional History of Asteroid 4 Vesta. *Science*, 336:690–.

Marchis, F., Descamps, P., Baek, M., Harris, A. W., Kaasalainen, M., Berthier, J., Hestroffer, D., and Vachier, F. (2008a). Main belt binary asteroidal systems with circular mutual orbits. *Icarus*, 196:97–118.

Marchis, F., Descamps, P., Berthier, J., Hestroffer, D., Vachier, F., Baek, M., Harris, A. W., and Nesvorný, D. (2008b). Main belt binary asteroidal systems with eccentric mutual orbits. *Icarus*, 195:295–316.

Marchis, F., Descamps, P., Hestroffer, D., and Berthier, J. (2005). Discovery of the triple asteroidal system 87 Sylvia. *Nature*, 436:822–824.

Marsden, B. G., Sekanina, Z., and Yeomans, D. K. (1973). Comets and nongravitational forces. V. *The Astronomical Journal*, 78:211.

Marzari, F., Davis, D., and Vanzani, V. (1995). Collisional evolution of asteroid families. *Icarus*, 113:168–187.

Masiero, J. R., Mainzer, A. K., Bauer, J. M., Grav, T., Nugent, C. R., and Stevenson, R. (2013). Asteroid Family Identification Using the Hierarchical Clustering Method and WISE/NEOWISE Physical Properties. *The Astrophysical Journal*, 770:7.

Masiero, J. R., Mainzer, A. K., Grav, T., Bauer, J. M., Cutri, R. M., Dailey, J., Eisenhardt, P. R. M., McMillan, R. S., Spahr, T. B., Skrutskie, M. F., Tholen, D., Walker, R. G., Wright, E. L., DeBaun, E., Elsbury, D., Gautier, IV, T., Gomillion, S., and Wilkins, A. (2011). Main Belt Asteroids with WISE/NEOWISE. I. Preliminary Albedos and Diameters. *The Astrophysical Journal*, 741:68.

Maxvell, D. E. (1997). Simple z model of cratering,ejection and the overturned flap; impact and explosion cratering. *Pergamon Press, New York (USA)*, pages 1003–1008.

Michel, P., Benz, W., Tanga, P., and Richardson, D. C. (2001). Collisions and Gravitational Reaccumulation: Forming Asteroid Families and Satellites. *Science*, 294:1696–1700.

Michel, P., Jutzi, M., Richardson, D. C., and Benz, W. (2011). The Asteroid Veritas: An intruder in a family named after it? *Icarus*, 211:535–545.

Michel, P. and Richardson, D. C. (2013). Collision and gravitational reaccumulation: Possible formation mechanism of the asteroid Itokawa. *Astronomy & Astrophysics*, 554:L1.

Micheli, M., Tholen, D. J., and Elliott, G. T. (2012). Detection of radiation pressure acting on 2009 BD. *New Astronomy*, 17:446–452.

Migliorini, F., Zappalà, V., Vio, R., and Cellino, A. (1995). Interlopers within asteroid families. *Icarus*, 118:271–291.

Mignard, F. (2003). Observations of Small Solar System Bodies with GAIA. In *IAU Joint Discussion*, volume 19 of *IAU Joint Discussion*, page 737.

Milani, A. (1994). The Dynamics of the Trojan Asteroids. In Milani, A., di Martino, M., and Cellino, A., editors, *Asteroids, Comets, Meteors 1993*, volume 160 of *IAU Symposium*, page 159.

Milani, A., Cellino, A., Knežević, Z., Novaković, B., Spoto, F., and Paolicchi, P. (2014). Asteroid families classification: Exploiting very large datasets. *Icarus*, 239:46–73.

Milani, A., Chesley, S. R., Chodas, P. W., and Valsecchi, G. B. (2002). Asteroid close approaches: Analysis and potential impact detection. In Bottke, W. F., Cellino, A., Paolicchi, P., and Binzel, R. P., editors, *Asteroids III*, pages 55–69. Univ. Arizona Press, Tucson.

Milani, A., Chesley, S. R., Sansaturio, M. E., Bernardi, F., Valsecchi, G. B., and Arratia, O. (2009). Long term impact risk for (101955) 1999 RQ. *Icarus*, 203:460–471.

Milani, A., Chesley, S. R., Sansaturio, M. E., Tommei, G., and Valsecchi, G. B. (2005a). Nonlinear impact monitoring: line of variation searches for impactors. *Icarus*, 173:362–384.

Milani, A., Chesley, S. R., and Valsecchi, G. B. (1999). Close approaches of asteroid 1999 AN_{10}: resonant and non-resonant returns. *Astronomy & Astrophysics*, 346:L65–L68.

Milani, A. and Farinella, P. (1994). The age of the Veritas asteroid family deduced by chaotic chronology. *Nature*, 370:40–42.

Milani, A. and Farinella, P. (1995). An asteroid on the brink. *Icarus*, 115:209–212.

Milani, A. and Gronchi, G. F. (2010). *Theory of Orbit Determination*. Cambridge University Press.

Milani, A., Gronchi, G. F., Farnocchia, D., Knežević, Z., Jedicke, R., Denneau, L., and Pierfederici, F. (2008). Topocentric orbit determination: Algorithms for the next generation surveys. *Icarus*, 195:474–492.

Milani, A. and Knežević, Z. (1990). Secular perturbation theory and computation of asteroid proper elements. *Celestial Mechanics and Dynamical Astronomy*, 49:347–411.

Milani, A. and Knežević, Z. (1992). Asteroid proper elements and secular resonances. *Icarus*, 98:211–232.

Milani, A. and Knežević, Z. (1994). Asteroid proper elements and the dynamical structure of the asteroid main belt. *Icarus*, 107:219–254.

Milani, A. and Knežević, Z. (1999). Asteroid mean elements: higher order and iterative theories. *Celestial Mechanics and Dynamical Astronomy*, 71:55–78.

Milani, A. and Knežević, Z. (2005). From Astrometry to Celestial Mechanics: Orbit Determination with Very Short Arcs. *Celestial Mechanics and Dynamical Astronomy*, 92:1–18.

Milani, A., Knežević, Z., Novaković, B., and Cellino, A. (2010). Dynamics of the Hungaria asteroids. *Icarus*, 207:769–794.

Milani, A. and Nobili, A. M. (1992). An example of stable chaos in the Solar System. *Nature*, 357:569–571.

Milani, A., Nobili, A. M., and Carpino, M. (1987). Secular variations of the semimajor axes - Theory and experiments. *Astronomy & Astrophysics*, 172:265–279.

Milani, A., Sansaturio, M. E., Tommei, G., Arratia, O., and Chesley, S. R. (2005b). Multiple solutions for asteroid orbits: Computational procedure and applications. *Astronomy & Astrophysics*, 431:729–746.

Mommert, M., Hora, J. L., Farnocchia, D., Chesley, S. R., Vokrouhlický, D., Trilling, D. E., Mueller, M., Harris, A. W., Smith, H. A., and Fazio, G. G. (2014). Constraining the Physical Properties of Near-Earth Object 2009 BD. *The Astrophysical Journal*, 786:148.

Mothé-Diniz, T., Roig, F., and Carvano, J. M. (2005). Reanalysis of asteroid families structure through visible spectroscopy. *Icarus*, 174:54–80.

Moyer, T. D. (2003). *Formulation for Observed and Computed Values of Deep Space Network Data Types for Navigation.* Wiley-Interscience, Hoboken, NJ.

Mueller, M. (2012). Surface Properties of Asteroids from Mid-Infrared Observations and Thermophysical Modeling. *ArXiv e-prints*.

Muinonen, K., Belskaya, I. N., Cellino, A., Delbò, M., Levasseur-Regourd, A.-C., Penttilä, A., and Tedesco, E. F. (2010). A three-parameter magnitude phase function for asteroids. *Icarus*, 209:542–555.

Müller, T. G., O'Rourke, L., Barucci, A. M., Pál, A., Kiss, C., Zeidler, P., Altieri, B., González-García, B. M., and Küppers, M. (2012). Physical properties of OSIRIS-REx target asteroid (101955) 1999 RQ_{36}. Derived from Herschel, VLT/ VISIR, and Spitzer observations. *Astronomy & Astrophysics*, 548:A36.

Müller, T. G., Sekiguchi, T., Kaasalainen, M., Abe, M., and Hasegawa, S. (2005). Thermal infrared observations of the Hayabusa spacecraft target asteroid 25143 Itokawa. *Astronomy & Astrophysics*, 443:347–355.

Nesvorný, D., Bottke, W. F., Levison, H. F., and Dones, L. (2003). Recent Origin of the Solar System Dust Bands. *Astrophys.J*, 591:486–497.

Nesvorný, D., Bottke, W. F., Vokrouhlický, D., Chapman, C. R., and Rafkin, S. (2010). Do planetary encounters reset surfaces of near Earth asteroids? *Icarus*, 209:510–519.

Nesvorný, D., Jedicke, R., Whiteley, R. J., and Ivezić, Ž. (2005). Evidence for asteroid space weathering from the Sloan Digital Sky Survey. *Icarus*, 173:132–152.

Nesvorný, D., Vokrouhlický, D., Morbidelli, A., and Bottke, W. F. (2009). Asteroidal source of L chondrite meteorites. *Icarus*, 200:698–701.

Nolan, M. C., Magri, C., Howell, E. S., Benner, L. A. M., Giorgini, J. D., Hergenrother, C. W., Hudson, R. S., Lauretta, D. S., Margot, J.-L., Ostro, S. J., and Scheeres, D. J. (2013). Shape Model and Surface Properties of the OSIRIS-REx Target Asteroid (101955) Bennu from Radar and Lightcurve Observations. *Icarus*, In press.

Novaković, B., Cellino, A., and Knežević, Z. (2011). Families among high-inclination asteroids. *Icarus*, 216:69–81.

Nugent, C. R., Mainzer, A., Masiero, J., Grav, T., and Bauer, J. (2012a). The Yarkovsky Drift's Influence on NEAs: Trends and Predictions with NEOWISE Measurements. *The Astronomical Journal*, 144:75.

Nugent, C. R., Margot, J. L., Chesley, S. R., and Vokrouhlický, D. (2012b). Detection of Semimajor Axis Drifts in 54 Near-Earth Asteroids: New Measurements of the Yarkovsky Effect. *The Astronomical Journal*, 144:60.

O'Brien, D. P., Marchi, S., Morbidelli, A., Bottke, W. F., Schenk, P. M., Russell, C. T., and Raymond, C. A. (2014). Constraining the cratering chronology of Vesta. *Planetary Space Sci.*, 103:131–142.

Öpik, E. J. (1951). Collision probability with the planets and the distribution of planetary matter. *Proc. R. Irish Acad. Sect. A*, 54:165–199.

Opik, E. J. (1952). Collisions with Heavenly Bodies. *Irish Astronomical Journal*, 2:95.

Ostro, S. J., Hudson, R. S., Benner, L. A. M., Giorgini, J. D., Magri, C., Margot, J. L., and Nolan, M. C. (2002). Asteroid Radar Astronomy. *Asteroids III*, pages 151–168.

Paddack, S. J. (1969). Rotational bursting of small celestial bodies: Effects of radiation pressure. *J. Geophys. Res.*, 74:4379–4381.

Paddack, S. J. and Rhee, J. W. (1975). Rotational bursting of interplanetary dust particles. *Geophys. Res. Lett.*, 2:365–367.

Paolicchi, P., Cellino, A., Farinella, P., and Zappala, V. (1989). A semiempirical model of catastrophic breakup processes. *Icarus*, 77:187–212.

Paolicchi, P. and Kryszczyńska, A. (2012). Spin vectors of asteroids: Updated statistical properties and open problems. *Planetary and Space Science*, 73:70–74.

Paolicchi, P. and Micheli, M. . (2008). The non-gravitational effects on the dynamical evolution and on the rotational properties of the asteroids. *Memorie della Societá Astronomica Italiana Supplementi*, 12:145.

Paolicchi, P., Verlicchi, A., and Cellino, A. (1996). An Improved Semi-Empirical Model of Catastrophic Impact Processes. I: Theory and Laboratory Experiments. *Icarus*, 121:126–157.

Parker, A., Ivezić, Ž., Jurić, M., Lupton, R., Sekora, M. D., and Kowalski, A. (2008). The size distributions of asteroid families in the SDSS Moving Object Catalog 4. *Icarus*, 198:138–155.

Pilyugin, S. Y. (1991). *Shadowing in Dynamical Systems*. Springer.

Pravec, P. and Harris, A. W. (2007). Binary asteroid population. 1. Angular momentum content. *Icarus*, 190:250–259.

Pravec, P., Harris, A. W., Kušnirák, P., Galád, A., and Hornoch, K. (2012). Absolute magnitudes of asteroids and a revision of asteroid albedo estimates from WISE thermal observations. *Icarus*, 221:365–387.

Rabinowitz, D. L. (1991). Detection of earth-approaching asteroids in near real time. *The Astronomical Journal*, 101:1518–1529.

Radzievskii, V. V. (1952a). A mechanism for the disintegration of asteroids and meteorites. *Astron. Zh.*, 29:162–170.

Radzievskii, V. V. (1952b). The influence of anisotropy of re-emited sunlight on the orbital motion of asteroids and meteoroids. *Astron. Zh.*, 29:1952–1970.

Richardson, D. C., Leinhardt, Z. M., Melosh, H. J., Bottke, Jr., W. F., and Asphaug, E. (2002). Gravitational Aggregates: Evidence and Evolution. *Asteroids III*, pages 501–515.

Richardson, D. C., Michel, P., Walsh, K. J., and Flynn, K. W. (2009). Numerical simulations of asteroids modelled as gravitational aggregates with cohesion. *Planetary and Space Science*, 57:183–192.

Rivkin, A. S., Howell, E. S., Lebofsky, L. A., Clark, B. E., and Britt, D. T. (2000). The nature of M-class asteroids from 3-micron observations. *Icarus*, 145:351–368.

Rozitis, B., Duddy, S. R., Green, S. F., and Lowry, S. C. (2013). A thermophysical analysis of the (1862) Apollo Yarkovsky and YORP effects. *Astronomy & Astrophysics*, 555:A20.

Rozitis, B. and Green, S. F. (2012). The influence of rough surface thermal-infrared beaming on the Yarkovsky and YORP effects. *Monthly Notices of the Royal Astronomical Society*, 423:367–388.

Rubincam, D. P. (1995). Asteroid orbit evolution due to thermal drag. *J. Geophys. Res.*, 100:1585–1594.

Rubincam, D. P. (1998). Yarkovsky thermal drag on small asteroids and Mars-Earth delivery. *J. Geophys. Res.*, 103:1725–1732.

Rubincam, D. P. (2000). Radiative spin-up and spin-down of small asteroids. *Icarus*, 148:2–11.

Russell, C. T., Raymond, C. A., Coradini, A., McSween, H. Y., Zuber, M. T., Nathues, A., De Sanctis, M. C., Jaumann, R., Konopliv, A. S., Preusker, F., Asmar, S. W., Park, R. S., Gaskell, R., Keller, H. U., Mottola, S., Roatsch, T., Scully, J. E. C., Smith, D. E., Tricarico, P., Toplis, M. J., Christensen, U. R., Feldman, W. C., Lawrence, D. J., McCoy, T. J., Prettyman, T. H., Reedy, R. C., Sykes, M. E., and Titus, T. N. (2012). Dawn at Vesta: Testing the Protoplanetary Paradigm. *Science*, 336:684–686.

Scheeres, D. J., Benner, L. A. M., Ostro, S. J., Rossi, A., Marzari, F., and Washabaugh, P. (2005). Abrupt alteration of the spin state of asteroid 99942 Apophis (2004 MN4) during its 2029 Earth flyby. *Icarus*, 175:281–283.

Schenk, P., O'Brien, D. P., Marchi, S., Gaskell, R., Preusker, F., Roatsch, T., Jaumann, R., Buczkowski, D., McCord, T., McSween, H. Y., Williams, D., Yingst, A., Raymond, C., and Russell, C. (2012). The Geologically Recent Giant Impact Basins at Vesta's South Pole. *Science*, 336:694–.

Schubart, J. (1982). Three characteristic parameters of orbits of Hilda-type asteroids. *Astronomy & Astrophysics*, 114:200–204.

Schubart, J. (1991). Additional results on orbits of Hilda-type asteroids. *Astronomy & Astrophysics*, 241:297–302.

Schubart, J. and Bien, R. (1987). Trojan asteroids: relations between dynamical parameters. *Astronomy & Astrophysics*, 175:299–302.

Sekiya, M. and Shimoda, A. A. (2013). An iterative method for obtaining a nonlinear solution for the temperature distribution of a rotating spherical body revolving in a circular orbit around a star. *Planetary and Space Science*, 84:112–121.

Sekiya, M. and Shimoda, A. A. (2014). An iterative method for obtaining a nonlinear solution for the temperature distribution of a rotating spherical body revolving in an eccentric orbit. *Planetary and Space Science*, 97:23–33.

Shepard, M. K., Kressler, K. M., Clark, B. E., Ockert-Bell, M. E., Nolan, M. C., Howell, E. S., Magri, C., Giorgini, J. D., Benner, L. A. M., and Ostro, S. J. (2008). Radar observations of E-class Asteroids 44 Nysa and 434 Hungaria. *Icarus*, 195:220–225.

Shepard, M. K., Margot, J.-L., Magri, C., Nolan, M. C., Schlieder, J., Estes, B., Bus, S. J., Volquardsen, E. L., Rivkin, A. S., Benner, L. A. M., Giorgini, J. D., Ostro, S. J., and Busch, M. W. (2006). Radar and infrared observations of binary near-Earth Asteroid 2002 CE26. *Icarus*, 184:198–210.

Shevchenko, V. G. and Tedesco, E. F. (2006). Asteroid albedos deduced from stellar occultations. *Icarus*, 184:211–220.

Sitarski, G. (1992). On the relativistic motion of (1566) icarus. *The Astronomical Journal*, 104:1226–1229.

Sitarski, G. (1998). Motion of the minor planet 4179 toutatis: Can we predict its collision with the earth? *Acta Astronomica*, 48:547–561.

Smirnov, E. A. and Shevchenko, I. I. (2013). Massive identification of asteroids in three-body resonances. *Icarus*, 222:220–228.

Soffel, M., Klioner, S. A., Petit, G., Wolf, P., Kopeikin, S. M., Bretagnon, P., Brumberg, V. A., Capitaine, N., Damour, T., Fukushima, T., Guinot, B., Huang, T.-Y., Lindegren, L., Ma, C., Nordtvedt, K., Ries, J. C., Seidelmann, P. K., Vokrouhlický, D., Will, C. M., and Xu, C. (2003). The IAU 2000 Resolutions for Astrometry, Celestial Mechanics, and Metrology in the Relativistic Framework: Explanatory Supplement. *The Astronomical Journal*, 126:2687–2706.

Spoto, F. and Milani, A. (2015). Shadowing Lemma and Chaotich Orbit Determination. *Celestial Mechanics, under review.*

Spoto, F., Milani, A., Farnocchia, D., Chesley, S. R., Micheli, M., Valsecchi, G. B., Perna, D., and Hainaut, O. (2014). Nongravitational perturbations and virtual impactors: the case of asteroid (410777) 2009 FD. *Astronomy & Astrophysics*, 572:A100.

Spoto, F., Milani, A., and Knežević, Z. (2015). Asteroid family ages. *Icarus.*

Standish, E. M. (1998). JPL Planetary and Lunar Ephemerides, DE405/LE405. Technical report, Jet Propulsion Laboratory, Pasadena.

Standish, E. M. (2000). Recommendation of DE405 for 2001 Mars Surveyor and for Cassini. Technical Report IOM 312.F-00-107b, Jet Propulsion Laboratory.

Standish, E. M. and Hellings, R. W. (1989). A determination of the masses of Ceres, Pallas, and Vesta from their perturbations upon the orbit of Mars. *Icarus*, 80:326–333.

Statler, T. S. (2009). Extreme sensitivity of the YORP effect to small-scale topography. *Icarus*, 202:502–513.

Tanga, P., Cellino, A., Michel, P., Zappalà, V., Paolicchi, P., and Dell'Oro, A. (1999). On the Size Distribution of Asteroid Families: The Role of Geometry. *Icarus*, 141:65–78.

Taylor, P. A., Margot, J.-L., Vokrouhlický, D., Scheeres, D. J., Pravec, P., Lowry, S. C., Fitzsimmons, A., Nolan, M. C., Ostro, S. J., Benner, L. A. M., Giorgini, J. D., and Magri, C. (2007). Spin Rate of Asteroid (54509) 2000 PH5 Increasing Due to the YORP Effect. *Science*, 316:274–.

Tedesco, E. F., Noah, P. V., Noah, M., and Price, S. D. (2002). The Supplemental IRAS Minor Planet Survey. *The Astronomical Journal*, 123:1056–1085.

Tonry, J. L. (2011). An Early Warning System for Asteroid Impact. *Publications of the Astronomical Society of the Pacific*, 123:58–73.

Tsiganis, K., Knežević, Z., and Varvoglis, H. (2007). Reconstructing the orbital history of the Veritas family. *Icarus*, 186:484–497.

Valsecchi, G. B., Milani, A., Gronchi, G. F., and Chesley, S. R. (2003). Resonant returns to close approaches: Analytical theory. *Astronomy & Astrophysics*, 408:1179–1196.

Vereš, P., Farnocchia, D., Jedicke, R., and Spoto, F. (2014). The Effect of Parallax and Cadence on Asteroid Impact Probabilities and Warning Times. *Publications of the Astronomical Society of the Pacific*, 126:433–444.

Vereš, P., Jedicke, R., Denneau, L., Wainscoat, R., Holman, M. J., and Lin, H.-W. (2012). Improved Asteroid Astrometry and Photometry with Trail Fitting. *Publications of the Astronomical Society of the Pacific*, 124:1197–1207.

Vereš, P., Jedicke, R., Wainscoat, R., Granvik, M., Chesley, S., Abe, S., Denneau, L., and Grav, T. (2009). Detection of Earth-impacting asteroids with the next generation all-sky surveys. *Icarus*, 203:472–485.

Virtanen, J., Muinonen, K., and Bowell, E. (2001). Statistical Ranging of Asteroid Orbits. *Icarus*, 154:412–431.

Vokrouhlický, D. (1998a). Diurnal Yarkovsky effect as a source of mobility of meter-sized asteroidal fragments. I. Linear theory. *Astronomy & Astrophysics*, 335:1093–1100.

Vokrouhlický, D. (1998b). Diurnal Yarkovsky effect for metersized asteroidal fragments' mobility II. Non-sphericity effects. *Astronomy & Astrophysics*, 338:353–363.

Vokrouhlický, D. (1999). A complete linear model for the Yarkovsky thermal force on spheric al asteroid fragments. *Astronomy & Astrophysics*, 344:362–366.

Vokrouhlický, D. and Bottke, W. F. (2001). The Yarkovsky thermal force on small asteroids and their fragments. *Astronomy & Astrophysics*, 371:350–353.

Vokrouhlický, D. and Brož, M. (1999). An improved model of the seasonal Yarkovsky force for the regolith-covered asteroid fragments. *Astronomy & Astrophysics*, 350:1079–1084.

Vokrouhlický, D., Brož, M., Bottke, W. F., Nesvorný, D., and Morbidelli, A. (2006a). The peculiar case of the Agnia asteroid family. *Icarus*, 183:349–361.

Vokrouhlický, D., Brož, M., Bottke, W. F., Nesvorný, D., and Morbidelli, A. (2006b). Yarkovsky/YORP chronology of asteroid families. *Icarus*, 182:118–142.

Vokrouhlický, D., Brož, M., Farinella, P., and Knežević, Z. (2001). Yarkovsky-Driven Leakage of Koronis Family Members. I. The Case of 2953 Vysheslavia. *Icarus*, 150:78–93.

Vokrouhlický, D., Brož, M., Morbidelli, A., Bottke, W. F., Nesvorný, D., Lazzaro, D., and Rivkin, A. S. (2006c). Yarkovsky footprints in the Eos family. *Icarus*, 182:92–117.

Vokrouhlický, D., Čapek, D., Chesley, S. R., and Ostro, S. J. (2005a). Yarkovsky detection opportunities. I. Solitary asteroids. *Icarus*, 173:166–184.

Vokrouhlický, D., Čapek, D., Chesley, S. R., and Ostro, S. J. (2005b). Yarkovsky detection opportunities. II. Binary asteroids. *Icarus*, 179:128–138.

Vokrouhlický, D., Chesley, S. R., and Matson, R. D. (2008). Orbital Identification for Asteroid 152563 (1992 Bf) Through the Yarkovsky Effect. *The Astronomical Journal*, 135:2336–2340.

Vokrouhlický, D. and Milani, A. (2000). Direct solar radiation pressure on the orbits of small near-Earth asteroids: observable effects? *Astronomy & Astrophysics*, 362:746–755.

Vokrouhlický, D., Milani, A., and Chesley, S. R. (2000a). Yarkovsky Effect on Small Near-Earth Asteroids: Mathematical Formulation and Examples. *Icarus*, 148:118–138.

Vokrouhlický, D., Milani, A., and Chesley, S. R. (2000b). Yarkovsky Effect on Small Near-Earth Asteroids: Mathematical Formulation and Examples. *Icarus*, 148:118–138.

Vokrouhlický, D., Nesvorný, D., Bottke, W. F., and Morbidelli, A. (2010). Collisionally Born Family About 87 Sylvia. *The Astronomical Journal*, 139:2148–2158.

Walsh, K. J., Delbó, M., Bottke, W. F., Vokrouhlický, D., and Lauretta, D. S. (2013). Introducing the Eulalia and new Polana asteroid families: Re-assessing primitive asteroid families in the inner Main Belt. *Icarus*, 225:283–297.

Walsh, K. J. and Richardson, D. C. (2008). A steady-state model of NEA binaries formed by tidal disruption of gravitational aggregates. *Icarus*, 193:553–566.

Warner, B. D., Harris, A. W., Vokrouhlický, D., Nesvorný, D., and Bottke, W. F. (2009). Analysis of the Hungaria asteroid population. *Icarus*, 204:172–182.

Whipple, F. L. (1983). 1983 TB and the Geminid Meteors. *IAU Circ.*, 3881:1.

Will, C. M. (1993). *Theory and Experiment in Gravitational Physics*. Cambridge University Press.

Williams, J. G. (1969). Secular perturbations in the Solar System. *Ph.D. Thesis, Univ. California*, page 270 pp.

Wisdom, J. (1987). Urey Prize Lecture: Chaotic Dynamics in the Solar System. *Icarus*, 72:241–275.

Wright, E. L., Eisenhardt, P. R. M., Mainzer, A. K., Ressler, M. E., Cutri, R. M., Jarrett, T., Kirkpatrick, J. D., Padgett, D., McMillan, R. S., Skrutskie, M., Stanford, S. A., Cohen, M., Walker, R. G., Mather, J. C., Leisawitz, D., Gautier, III, T. N., McLean, I., Benford, D., Lonsdale, C. J., Blain, A., Mendez, B., Irace, W. R., Duval, V., Liu, F., Royer, D., Heinrichsen, I., Howard, J., Shannon, M., Kendall, M., Walsh, A. L., Larsen, M., Cardon, J. G., Schick, S., Schwalm, M., Abid, M., Fabinsky, B., Naes, L., and Tsai, C.-W. (2010). The Wide-field Infrared Survey Explorer (WISE): Mission Description and Initial On-orbit Performance. *The Astronomical Journal*, 140:1868–1881.

Yarkovsky, I. O. (1901). *The density of luminiferous ether and the resistance it offers to motion*, chapter 1. (in Russian) Bryansk, published privately by the author.

Yeomans, D. K., Antreasian, P. G., Barriot, J.-P., Chesley, S. R., Dunham, D. W., Farquhar, R. W., Giorgini, J. D., Helfrich, C. E., Konopliv, A. S., McAdams, J. V., Miller, J. K., Owen, W. M., Scheeres, D. J., Thomas, P. C., Veverka, J., and Williams, B. G. (2000). Radio Science Results During the NEAR-Shoemaker Spacecraft Rendezvous with Eros. *Science*, 289:2085–2088.

Yeomans, D. K., Barriot, J.-P., Dunham, D. W., Farquhar, R. W., Giorgini, J. D., Helfrich, C. E., Konopliv, A. S., McAdams, J. V., Miller, J. K., Owen, W., Scheeres, D. J., Synnott, S. P., and Williams, B. G. (1997).

Estimating the mass of asteroid 253 Mathilde from tracking data during the NEAR flyby. *Science*, 278:2106–2109.

Yeomans, D. K., Chodas, P. W., Keesey, M. S., Ostro, S. J., Chandler, J. F., and Shapiro, I. I. (1992). Asteroid and comet orbits using radar data. *The Astronomical Journal*, 103:303–317.

Yuasa, M. (1973). Theory of secular perturbations of asteroids including terms of higher order and higher degree. *Publ. Astron. Soc. Japa*, 25:399–445.

Zappalà, V., Bendjoya, P., Cellino, A., Farinella, P., and Froeschlé, C. (1995). Asteroid families: Search of a 12,487-asteroid sample using two different clustering techniques. *Icarus*, 116:291–314.

Zappala, V., Cellino, A., Farinella, P., and Knežević, Z. (1990). Asteroid families. I - Identification by hierarchical clustering and reliability assessment. *Astronomical Journal*, 100:2030–2046.

Zappala, V., Cellino, A., Farinella, P., and Milani, A. (1994). Asteroid families. 2: Extension to unnumbered multiopposition asteroids. *The Astronomical Journal*, 107:772–801.